
Intermolecular energy scales based on aromatic ethers and alcohols

DISSERTATION

zur Erlangung des mathematisch-naturwissenschaftlichen Doktorgrades
„Doctor rerum naturalium“
der Georg-August-Universität Göttingen

im Promotionsprogramm Chemie
der Georg-August-University School of Science (GAUSS)

vorgelegt von

Anja Poblitzki

aus Bremen

Göttingen, 2019

Betreuungsausschuss:

Prof. Dr. Martin A. Suhm, Institut für Physikalische Chemie

Prof. Dr. Ricardo A. Mata, Institut für Physikalische Chemie

Mitglieder der Prüfungskommission:

Referent:

Prof. Dr. Martin A. Suhm, Institut für Physikalische Chemie

Korreferent:

Prof. Dr. Ricardo A. Mata, Institut für Physikalische Chemie

Weitere Mitglieder der Prüfungskommission:

Prof. Dr. Jörg Behler, Institut für Physikalische Chemie

Dr. Oliver Bünermann, Institut für Physikalische Chemie

Dr. Tim Schäfer, Institut für Physikalische Chemie

Prof. Dr. Dietmar Stalke, Institut für Anorganische Chemie

Tag der mündlichen Prüfung: 20.03.2019

Danksagung

Allen voran möchte ich mich bei Prof. Dr. Martin A. Suhm bedanken für die hervorragende Betreuung, das entgegengebrachte Vertrauen und die Chancen, die er mir im Rahmen dieser Doktorarbeit geboten hat. Zudem danke ich Prof. Dr. Ricardo Mata für die freundliche Übernahme des Korreferats, sowie den weiteren Mitgliedern der Prüfungskommission.

Des Weiteren danke ich dem SPP 1807 „Control of London dispersion interactions in molecular chemistry“ und allen Kooperationspartnern, im Besonderen Prof. Dr. Melanie Schnell und Prof. Dr. Samuel Leutwyler für die wertvollen Erfahrungen die ich während der Forschungsaufenthalte sammeln durfte, sowie Prof. Dr. Markus Gerhards. Damit verbunden ist auch ein Dank an die jeweiligen Arbeitskreise, insbesondere Mariyam Fatima und Dr. Richard D. Knochenmuss für die geduldige Einweisung in die Apparaturen, sowie Dominic Bernhard und Fabian Dietrich.

Stellvertretend für alle Mitarbeiter der Werkstätten möchte ich mich bei Herrn Hildebrandt, Herrn Meyer, Herrn Zippert, Herrn Knorr und Herrn Erdmann bedanken, besonders für ihre Ideen und Anregungen zur Entwicklung der V-Düse. Weiterhin danke ich Petra Lawecki, Dr. Markus Hold und Clemens Heymann für die freundliche Unterstützung bei allen Fragen des Universitätsalltags.

Nicht zuletzt möchte ich mich bei allen Mitgliedern des Arbeitskreises Suhm für die stets herzliche Arbeitsatmosphäre bedanken. Dafür, dass man immer jemanden findet wenn man Hilfe braucht, auch wenn ihr selbst gerade wenig Zeit habt. Das Korrekturlesen dieser Arbeit ist dafür nur ein Beispiel von vielen. Besonders möchte ich Jonas Altnöder für die Einarbeitung in das Thema und Hannes Gottschalk für die Zusammenarbeit im Göbench-Projekt danken. Arman Nejad und Manuel Lange danke ich für das Interesse an meiner Forschung im Rahmen ihrer Abschlussarbeiten und dafür, dass ich den *popcorn*-Jet in guten Händen weiß.

Meiner Familie und meinen Freunden danke ich für den Rückhalt während des gesamten Studiums und besonders Tim, dass er einfach für mich da ist, wenn ich ihn brauche.

Contents

1	Introduction	1
2	Experimental and Theoretical Methods	5
2.1	Supersonic Expansion	5
2.2	FTIR Setups	6
2.2.1	<i>popcorn</i> -Jet	7
2.2.2	<i>filet</i> -Jet	18
2.3	Microwave Setup	19
2.4	SEP-R2PI Setup	21
2.5	Multi-spectroscopic Approaches	23
2.6	Theoretical Methods	27
2.6.1	Geometry Optimization	27
2.6.2	Transition State Search	29
3	Clusters of Furans and Alkyl Alcohols	33
3.1	Binding Geometries and Nomenclature	35
3.2	Methylation: Furan, MFuran and DMFuran	37
3.3	π Preference by Enlarging the Alkyl Group	52
3.3.1	2-Ethylfuran	53
3.3.2	2- <i>tert</i> -Butylfuran	59
3.4	Annulated Benzene: 2,3-Benzofuran and Dibenzofuran	63
3.4.1	2,3-Benzofuran	64
3.4.2	Dibenzofuran	71
4	Clusters of Diphenyl Ether and Alkyl Alcohols	89
5	Clusters of Furans and Aromatic Alcohols	101
5.1	1-Naphthol	101
5.2	Phenol	112

6 Discussion	117
6.1 Dispersion Influence	121
6.2 Validation of B3LYP-D3(BJ, abc)/def2-TZVP	123
7 Conclusion	133
A Experimental Parameters	137
B OPUS Macro	138
C Computational Parameters	143
D Complementary Structure Calculations	144
E Complementary Spectra	157
F Data	159
G Box Plot Explanation	163
H List of Spectra	164
I List of Figures	167
J List of Tables	169
K Bibliography	170

1 Introduction

Even though their description dates back to the 1930s,¹ the importance of London dispersion interactions for molecular structure and reactivity has only been fully recognized in recent years.²⁻⁴ Together with electrostatic (Keesom) and inductive (Debye) forces London dispersion interactions make up the attractive part of van der Waals interactions.^{1,2} They arise from electron correlation and can thus not be described classically.⁵ Since London dispersion increases with the number of pairwise interactions, the interaction strength grows faster than the number of atoms in a system.² Hence, London dispersion becomes more important in larger molecular systems. Recent illustrations of the impact of London dispersion interactions are records like the shortest intermolecular CH–HC distance⁶ that even surpasses covalently linked intramolecular competitors or the longest alkane C–C bond, which is stabilized by the interactions between two diamondoid moieties.⁷ Further examples of organic and inorganic molecules and complexes significantly stabilized by dispersion are reviewed in Ref. 4. For a better understanding of dispersion interactions, a priority program on ‘Control of London Dispersion Interactions in Molecular Chemistry’ has been funded by the Deutsche Forschungsgemeinschaft (SPP1807), where this thesis is part of.

Due to their origin in many-body electron correlation, London dispersion interactions are especially challenging to capture by theory.⁸ Errors in the description of these seemingly small contributions accumulate with the number of interactions, which is particularly problematic regarding the increasing size of chemical systems accessible to quantum chemistry. Thus, sufficiently accurate computational methods need to be developed while maintaining reasonable computational cost. For the validation of new computational methods, benchmarking databases are often used, which mainly consist of datapoints obtained by high quality *ab initio* calculations.^{9,10} This results in a decoupling of theoretical chemistry from experiment and major efforts have to be taken on both sides to bring them back together.¹⁰

On the experimental side, molecular balances offer a way to obtain experimental datasets for benchmarking purposes. They consist of two competing molecular conformations, each representing a distinct interaction and connected by a sufficiently low interconversion barrier, whose energetic preference can be tuned by chemical substitution. The terminus has been pioneered by Wilcox in the 1990ies, who introduced a torsional balance system, where the rotation of a biphenyl σ -bond was used to sense aryl edge-to-face interactions.¹¹ Similar torsional intramolecular balances have been designed to investigate various interactions types, *e.g.* CH–O, aromatic CH– π , π stacking as well as biomimetic and dispersion interactions.^{12–14} Besides these torsional balances by σ -bond rotation, other geometrical concepts include larger conformational changes of the molecular backbone, leading to seesaw or gripper like balances.¹⁵ The use of molecular balances for sizing London dispersion has recently been reviewed in Ref. 3. These balances are commonly studied in solution and probed by NMR spectroscopy, measuring the free energy difference (ΔG) between the conformers. Thereby, large activation barriers as the double bond isomerism of cyclooctatetraene^{3,16} can be overcome, but unfortunately solvent effects also compete with the interactions under investigation. This adds to the complexity of the systems, making a quantum chemical description more challenging and limiting the use as benchmarking systems.¹⁰ Low temperature gas-phase conditions as provided by supersonic expansions offer a solution to reduce these complications, as has been applied for the folding of *n*-alkanes¹⁷ or the complexation of *trans*-*N*-methylacetamide *via* the N- or C-terminal carbonyl lone pair¹⁸.

Gas-phase molecular balances consisting of two molecules are less easily defined. They commonly consist of a ‘solute’ molecule with two competing binding sites for a ‘solvent’ molecule, which can freely interact with each other. These systems are more of a scale balance type, weighing the energy of the interactions against each other. Low barriers are needed to reach equilibrium conditions, thus energy differences have to be subtle as well.

An obvious interaction type to compete with dispersion interactions are hydrogen bonds, as these are among the most common and widely studied non-covalent interactions. Furthermore, both play an important role in biorecognition,^{19–21} since their magnitude is suitable for distinct bonding while barriers are low enough for releasing substrates. The understanding and proper description of their interplay is

thus essential for the comprehension of biological phenomena and the development of applications in the fields of biology and material science. Examples comparing hydrogen bonding and dispersion interactions have been studied for the binding of small molecules like nitrogen²²⁻³⁰ or CO^{22,26} to molecules offering a hydrogen bonding site like hydroxy^{22,26-29} or amino groups²²⁻²⁵ and a π system. In most cases, van der Waals binding to the π system was found to be more favorable for nitrogen, with the exception of phenol-N₂, whereas hydrogen bonding is preferred for the examined CO clusters. Due to the small size of these solvent molecules, these molecular scales can test the interactions rather exclusively. Increasing the interaction partner size blurs the dividing line between hydrogen bonded and van der Waals clusters, allowing compromises between them. One example is the strain dispersion can put on a hydrogen bond until ultimately breaking it, as studied in clusters of benzyl alcohol and cyclohexyl methanol.³¹ Other examples are the homodimers of phenol³² and 1-naphthol^{33,34}, where π stacking dominates due to the increased π system, potentially cleaving the classical OH-O hydrogen bond. The distinction between hydrogen bonded and van der Waals clusters is even less applicable regarding weak hydrogen bonds like CH-O or OH- π , since hydrogen bond formation itself involves dispersion as an attractive force.³⁵ Therefore, the juxtaposition of strong, classical OH-O hydrogen bonds and weak OH- π hydrogen bonds can serve as a suitable benchmarking system for the theoretical description and characterization of dispersion interactions, if their energy difference is subtle. For instance, this can be achieved by using furan derivatives as acceptor molecules, where the attractivity of the oxygen site is reduced by delocalizing its electron density within the π system. The applicability as a molecular balance has been demonstrated in the studies of furan-hydrogen halide complexes³⁶, the furan-indole dimer³⁷ and complexes of 2,3-benzofuran with methanol and water.³⁸

In the molecular scales of this thesis OH-O and OH- π hydrogen bonded clusters of furan derivatives and small alkylic alcohols, namely methanol and *tert*-butyl alcohol, are investigated. The furan acceptor is varied by alkylation and annulation of benzene rings. Additionally, diphenyl ether is investigated as a structurally related acceptor molecule, which can be regarded as having a cleaved furan ring. The binding of two aromatic alcohols, 1-naphthol and phenol, to methylated furan is also

examined. The binding energy difference ΔE_0 is the decisive quantity for the tipping of the balance. To identify suitable systems with small energy differences between oxygen and π binding, dispersion corrected density functional theory (DFT) is applied. The complexes are then studied in a supersonic expansion, which is probed by Fourier-transform infrared (FTIR) spectroscopy, making use of the frequency shift and intensity enhancement of the hydroxy stretching vibration upon hydrogen bond formation. Complementary information is gained by cooperations with other research groups of the priority program, providing validation of the assignment (M. Gerhards, IR/UV double resonance spectroscopy), structural information (M. Schnell, microwave spectroscopy) and absolute dissociation energies (S. Leutwyler, SEP-R2PI spectroscopy). The advantages of such multi-spectroscopic approaches for the investigation of benchmarking systems will also be highlighted.

By describing experimental benchmarking systems for theory, this thesis shall help to reduce the diverging gap between experiment and theory. The focus is thus on the identification of molecular systems with small energy differences between OH–O and OH– π hydrogen bonding suitable for benchmarking, characterizing the influence of dispersion interactions and finding systems where dispersion tips the molecular balance towards the seemingly inferior π binding.

2 Experimental and Theoretical Methods

The analysis of the clusters is primarily based on FTIR spectroscopy of supersonic jet expansions, which is described in the following sections. Furthermore, microwave and stimulated emission pumping resonant enhanced two photon ionization (SEPR2PI) spectra were recorded for some systems in cooperation with the groups of M. Schnell in Hamburg and S. Leutwyler in Bern, respectively. Their setups are described briefly as well. The use of such cooperative multi-spectroscopic approaches is outlined in a separate section.

2.1 Supersonic Expansion

For benchmarking purposes, experiments need to be designed to be easily comparable to theoretical data.¹⁰ That means the clusters should be prepared in a way, that they are essentially free of interactions with other molecules and thermal excitation. Supersonic jet expansions offer such conditions with the added advantage of simplifying the spectral analysis.³⁹ Various review articles have been published concerning supersonic jets and their use in spectroscopy, *e.g.* Refs. 40–45, thus only a brief description is given here.

A supersonic jet is formed when a gas is expanded through a nozzle with dimensions much larger than the mean free path of the molecules. The large number of collisions in the vicinity of the nozzle transfers the random movement of the molecules into a directed flow, whereby the velocity distribution is narrowed, resulting in a temperature decrease.^{40,41} As the temperature decreases, the local sonic velocity decreases as well, eventually falling below the increasing particle velocity, hence the expansion is termed ‘supersonic’.⁴¹ Due to the adiabatic conditions in the initial part of the expansion, the translational and internal degrees of freedom equilibrate, cooling the latter. When the lowering of the density prevents further collisions, the molecules freeze in a non-equilibrium state, which can be probed by spectroscopic methods.⁴⁴ The observed temperatures are thus different for each degree of free-

dom, depending on the equilibration rates.^{44,46} The magnitudes are of the order 1 K to 10 K for rotational temperature and 30 K to 100 K for vibrational temperature, respectively.⁴⁰

Commonly, the analyte molecules are seeded in a monoatomic carrier gas, which suppresses the formation of large clusters. Noble gases are chosen as carrier gases due to the absence of spectroscopic features and their efficient cooling because of the lack of vibrational and rotational degrees of freedom.⁴⁴ The cluster formation in the jet is influenced by the nozzle design, larger cross sections leading to larger and more clusters.⁴⁷ In slit nozzles the molecular density and temperature decrease more slowly than in pinhole nozzles, whereby binary and three-body collision rates are increased and thus facilitate cluster formation.^{43,48} For a given design, cluster formation increases with the seeding fraction and stagnation pressure and decreases with initial gas temperature.

The relaxation of higher energy cluster conformations is dependent on the isomerization barrier.⁴⁹ Barriers greater than about 5 kJ mol^{-1} lead to freezing out of the conformers,⁵⁰ similar to the freezing of the rotational and vibrational degrees of freedom. Therefore, the relative abundance of the conformers is given by a Boltzmann distribution at the isomerization temperature, instead of the temperature prior to the expansion, which defines an upper limit.⁵¹ The cooling effect and thus the relaxation can be enhanced by the addition of a heavier carrier gases, but is limited by the undesired formation of clusters with the analyte molecules.^{50,52}

2.2 FTIR Setups

Hydrogen bonding leads to a downshift and an enhanced intensity of the OH stretching vibration. Thus, FTIR spectroscopy provides a powerful tool for studying hydrogen bonded clusters and is used as the main technique in this thesis.^{53,54} The obtained band positions can be assigned by comparison to quantum mechanical calculations. The linear absorption technology offers information about the abundance of each cluster species by integration of the bands. A drawback is the lack of size selectivity, which can partially be overcome by measuring series of differently concentrated gas mixtures (see Sec. 3.2).

Two different setups have been used for this study, which are introduced in the following.

Table 2.2.1: Chemicals used for the FTIR experiments. Data are taken from the manufacturers safety data sheet if not stated otherwise.

substance	CAS	purity	manufacturer	T_{boil} /°C	T_{fus} /°C
methanol	67-56-1	$\geq 99.8\%$	Sigma Aldrich	65	-98
methanol-d1	1455-13-6	99% D	eurisotop		
<i>tert</i> -butyl alcohol	75-65-0	$\geq 99\%$	Roth	82	26
<i>tert</i> -butyl alcohol-d1	3972-25-6	99% D	Cambridge Isotope Laboratories		
1-naphthol	90-15-3	$\geq 99\%$	Sigma Aldrich	278–280	94–97
furan	110-00-9	$\geq 99\%$	Alfa Aesar	32–33	-86
2-methylfuran	534-22-5	$\geq 99\%$	Roth	63–66	-89
2,5-dimethylfuran	625-86-5	99%	Acros Organics	92–94	-62
2- <i>tert</i> -butylfuran	7040-43-9	97%	Sigma Aldrich	119–120	n/a
2-ethylfuran	3208-16-0	$\geq 99\%$	Sigma Aldrich	92–93	n/a
2,3-benzofuran	271-89-6	$\geq 99.0\%$	TCI	175	n/a
dibenzofuran	132-64-9	98%	abcr	287 ⁵⁵	82 ⁵⁶
diphenyl ether	101-84-8	99%	Alfa Aesar	258–260	26–29
helium	7440-59-7	99.996%	Linde		
argon	7440-37-1	99.999%	Air Liquide		

Tab. 2.2.1 lists the chemicals used for these experiments including their boiling (T_{boil}) and melting points (T_{fus}). No further purification has been applied.

2.2.1 popcorn-Jet

The *popcorn*-jet (‘poppet controlled resistively heated nozzle jet’) is designed to measure FTIR spectra of supersonic expansions containing a low-volatility compound. It was originally set up by M. Albrecht in 2006⁵⁷ based on first promising trials by C. Rice.⁵⁸ Fig. 2.2.1 shows a schematic representation of the *popcorn*-jet, more details can be found in Ref. 57,59,60.

Working principle

The low-volatility compound is deposited onto molecular sieve and inserted into the sample compartment between two check valves opening at different differential pressures (70 mbar and 690 mbar). A gas pulse (routinely helium) flowing through

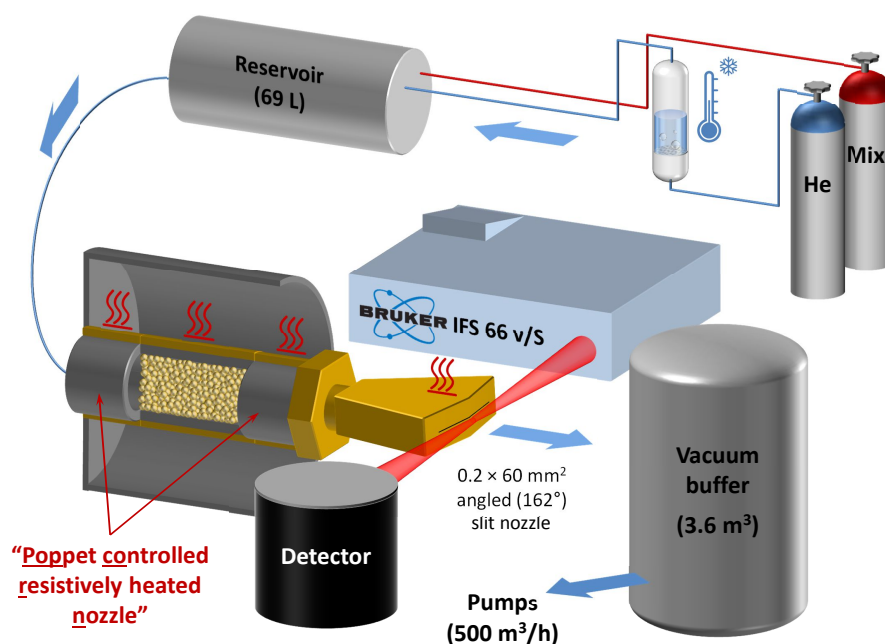


Figure 2.2.1: A schematic representation of the *popcorn-jet*.

the sample compartment from a 69 L reservoir can thereby pick up the sample. This whole part can be resistively heated with three heating sleeves. The ones covering the check valves are usually set 10 °C and 20 °C (upstream and downstream, respectively) warmer than the one covering the sample compartment to prevent condensation. The temperatures given for the spectra refer to the temperature of this middle heating sleeve. The gas mixture is supersonically expanded into vacuum. The gas pulses are produced by two parallel solenoid valves controlled by a ‘IOTA one’ pulse generator. An overview of the different nozzle types is given further below. To keep the background pressure during a gas pulse below 0.5 mbar, the jet chamber opens into a 3.6 m³ buffer volume, which is continuously evacuated by two roots pumps (500 m³ h⁻¹ and 250 m³ h⁻¹) and a rotary piston pump (250 m³ h⁻¹). Between two gas pulses a waiting time of 50 s to 60 s ensures a background pressure below 0.2 mbar before the next pulse.

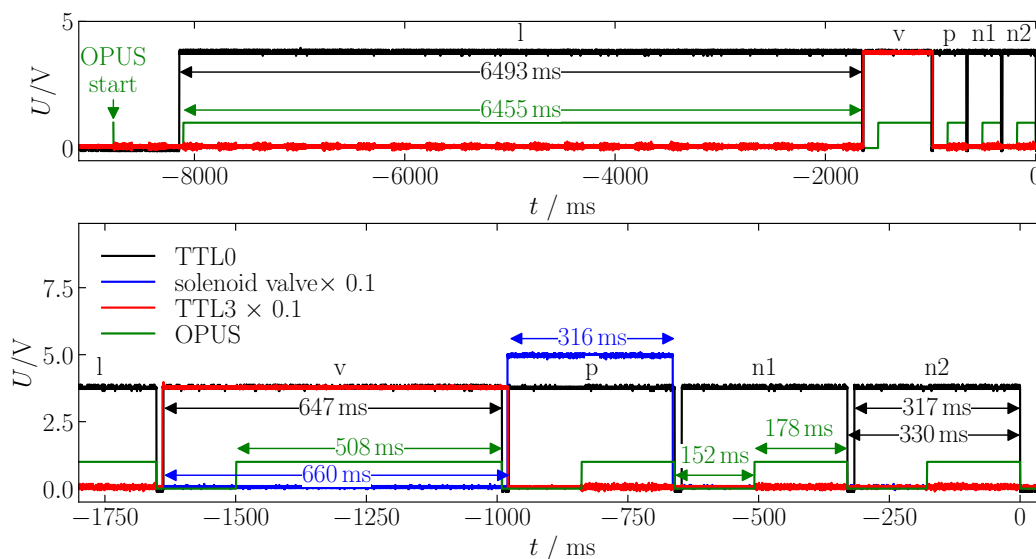


Figure 2.2.2: Pulse sequence for the *popcorn-jet* using the *double sided fast return* method. The whole sequence is shown in the upper panel, the lower shows an enlargement of the last 5 scans. The TTL0 and TTL3 signals are shown in black and red, respectively, as measured using an oscilloscope. The blue signal is the delay and on-time sent from the IOTA one to the solenoid valves. Additionally, the timing reported by OPUS in the *i-file of the spectra is shown in green.

A volatile compound can be added to the gas mixture *via* a coolable saturator prior to the reservoir. To reach even lower concentrations, a gas bottle with a predefined gas mixture can be used, or the carrier gas can be directly added to the reservoir. The opening times of the solenoid valves refilling the reservoir then give an estimate of the dilution.

Each gas pulse is probed by a Bruker IFS 66v/S FTIR spectrometer. A detailed description of the measuring sequence is given below. A typical measurement consists of 25–50 gas pulses and the same amount of probe scans, which are averaged to one spectral block. Overall the spectra are the average of up to 400 probe scans.

Pulse sequence

The pulse sequence for the synchronization of the gas pulse to the spectrometer scan is depicted in Fig. 2.2.2 as measured with an oscilloscope. It is controlled by the TRS method (`'trsfruehpuls.TRS'`)⁵⁷ called by the measuring macro (`'JET_POPCORN-mitVorscans.MTX'`) of the spectrometer operation software OPUS⁶¹.

The spectrometer scan sequence consists of 25 scans. The first 20 scans are averaged to form the background spectrum (*1), followed by two co-averaged pre-scans (*v), one probe scan (*p) and two post-scans (*n1 and *n2). The TTL0 output of the spectrometer is used as a visualization (black signal in Fig. 2.2.2). It is set high before a measuring block in the TRS method and low after its completion. Thereby, the length of the five blocks can be determined to 6493 ms and 647 ms for the *1 and *v blocks, respectively, and 317 ms for *p, *n1 and *n2. All scans are measured in the *double sided fast return* mode, where both sides of the interferogram are measured in the forward movement of the mirror. The data acquisition time of each block reported in OPUS is shown green. It coincides with a noise increase in the TTL3 signal, which thereby provides a measure for the actual acquisition time within the blocks. Furthermore, two of these noise-increased blocks can be observed before the *1 block, starting with $t = 0$ ms of OPUS. With the first pre-scan a TTL-signal (TTL3, red signal in Fig. 2.2.2) is sent to the IOTA one to trigger the solenoid valves for the gas pulse. A waiting time of 660 ms and an opening time of 316 ms have been determined experimentally by M. Albrecht for an optimal overlap of the gas pulse with the probe scan (blue signal in Fig. 2.2.2). This is consistent with the timings given by the TTL0. The discrepancy between the delay time and the time for two scans described by J. Altnöder⁶⁰ is explained by a break of approximately 13.5 ms, that is also contained in the blocks with repeated measuring (e.g. *v block: $2 \times 317 \text{ ms} + 13 \text{ ms} = 647 \text{ ms}$).

The delay and on-time of the solenoid valves have newly been optimized in course of the Master's thesis of M. Lange⁶². Using the latest version of the V-nozzle (hollow) described below, no significant signal loss was observed when shortening the gas pulse to the data acquisition time of the probe scan (delay: 810 ms, on-time: 200 ms). These timings should be taken as the new standard values for this nozzle, regarding the reduced gas throughput.

Nozzle types

Different nozzle types are available for the *popcorn-jet*, which are listed in Tab. 2.2.2. Depending on the nozzle type, different jet-chamber adapters have to be used, which are also stated. The multi-slit nozzles are mounted with the slits perpendicular to the IR beam for best results, whereas the V-nozzles are aligned with the average

Table 2.2.2: Nozzle types available for the *popcorn*-jet and their slit dimensions. Variants used in this thesis are marked bold.

nozzle	length /mm	width /mm	area /mm ²	specifications	jet-chamber adapter
single-slit nozzle	10	1	10		15 cm
single-slit nozzle	10	0.5	5		15 cm
double-slit nozzle	10	0.5	10		15 cm
triple-slit nozzle	10 (5)	0.5	12.5		15 cm
HT-nozzle (double-slit)	10	0.5	10	heatable (500 °C)	15 + 21.5 cm
V-nozzle	60	0.2	12	heatable, conical	21.5 cm
V-nozzle^a	60	0.2	12	heatable, hollow	21.5 cm
V-nozzle	60	0.5	30	heatable, hollow	21.5 cm

^a This version is taken as a new standard.

direction of the photon flux. The double-slit nozzle was used as a standard. Its superiority to the other 10 mm long slit nozzles has been determined by M. Albrecht. Bands in the OH stretching region are more intense than for the single-slit nozzle, while the spectra obtained with the triple-slit nozzle show a broadening of the bands, meaning that the collisional cooling is less sufficient.⁵⁷

The HT-nozzle (high-temperature nozzle) was developed to reach higher concentrations *via* heating of the sample compartment, while keeping the fraction of larger clusters at a minimum.⁵⁹ The nozzle dimensions copy the double-slit nozzle, however the 10 mm² cross section channel length is much longer (200 mm) than for the double-slit nozzle (<1 mm). Therefore, the throughput amounts to 1/3 of the double-slit throughput due to the altered flow resistivity.⁶⁰ This leads to smaller band intensities for the HT-nozzle compared to the double-slit nozzle if all other conditions are unchanged.

To improve the signal-to-noise-ratio a new nozzle type was designed during this thesis ('V-nozzle', see Fig. 2.2.3), based on a related design by R. Medel for a further development of the RESS-Jet⁶⁴. The cross section between the IR beam and the expansion is enhanced by enlarging the slit length to 60 mm, while the width is reduced to 0.2 mm. For a minimum distance between the nozzle and the IR beam, the nozzle is angled (162°) to fit the estimated IR beam focus envelope. The cross section for the gas mixture flow is kept constant and is continuously deformed from a circular shape at the nozzle entrance to a rectangular shape at the nozzle exit.

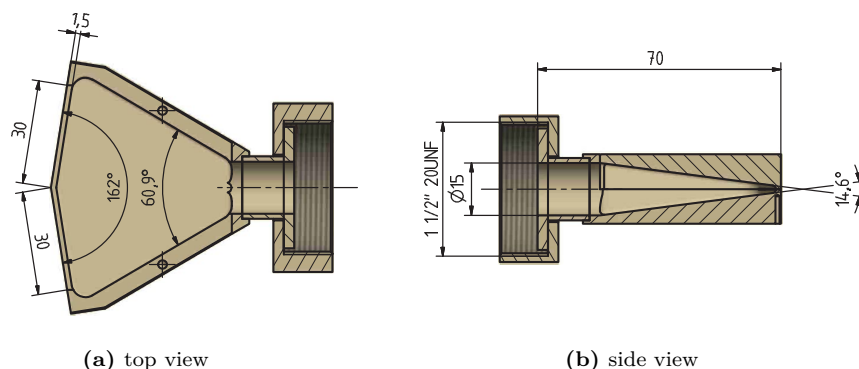


Figure 2.2.3: Technical drawing of the conical V-nozzle.⁶³

Like the HT-nozzle the V-nozzle can be individually heated. This is achieved by four cartridge heaters (Omega, 6.3 mm \times 31 mm, 240 V, 225 W) connected in series at the nozzle exit. Brass is used as the nozzle material to ensure a sufficient heat distribution.

The effect of the nozzle change from the double-slit to the conical V-nozzle can be seen in Fig. 2.2.4 for the test system diphenyl ether–methanol. All parameters are kept identical, the additional cartridge heating of the V-nozzle is set to 130 °C, the same temperature as the prior heating sleeve. The band integral in the CH stretching region, which is mostly unaffected by cluster formation, is enhanced by a factor of 1.6 for the aliphatic methanol and a factor of 2.0 for the aromatic diphenyl ether. Cluster formation is largely inhibited. The broad band (MeOH)_n corresponding to larger clusters is drastically diminished, while methanol trimer ((MeOH)₃) is still visible and methanol dimer ((MeOH)₂) is even slightly enhanced. Mixed cluster bands between those two bands are also reduced. The two mixed dimer bands marked OH– π and OH–O are altered in their relative abundance, the more stable π -bound conformer gains intensity, while the O-bound conformer is almost unaffected. The largest increase is seen for the methanol monomer (MeOH).

Taking this into account, the V-nozzle is clearly superior for the study of monomers, making the double-slit nozzle obsolete for those cases. This is less definite for dimer studies. However, the V-nozzle suppresses the formation of larger clusters and can also enhance the dimer signal – at least for the most stable conformer –, thus, it facilitates the band assignment. Furthermore, while the comparison in Fig. 2.2.4 uses the same temperature settings as in the double slit nozzle experi-

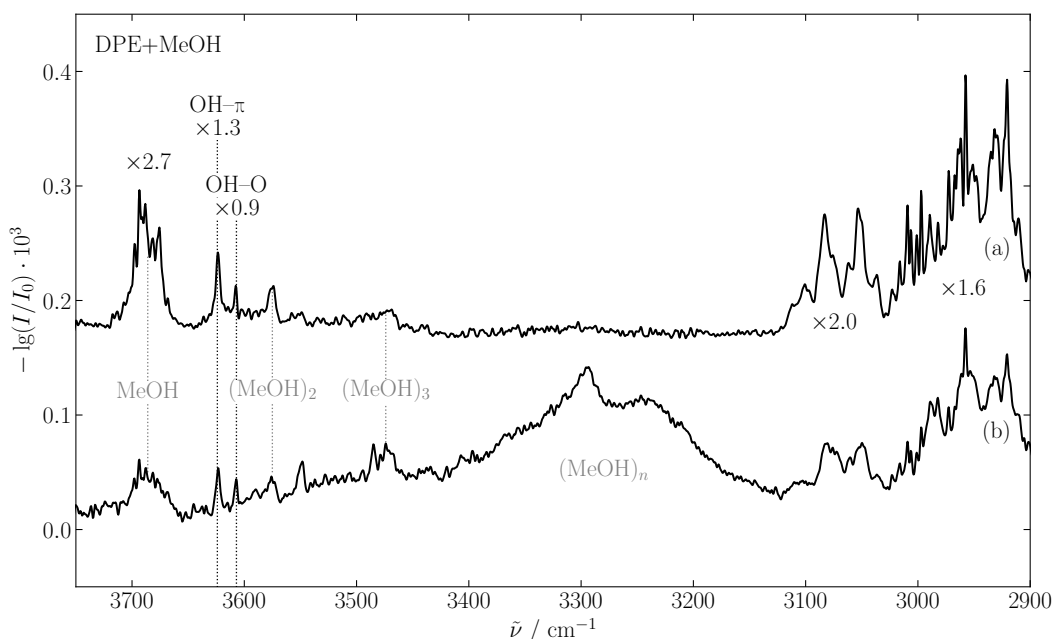


Figure 2.2.4: Comparison of the IR Spectra of diphenyl ether-methanol using the V-nozzle and the double-slit nozzle.

(a) V-nozzle (DPE: 110 °C, MeOH: -20 °C, V-nozzle (conical): 130 °C);

(b) double-slit nozzle (DPE: 110 °C, MeOH: -20 °C, double-slit nozzle: 130 °C).

ment, the V-nozzle is substantially more flexible in the independent choice of nozzle and sample temperatures. Hence, the figure only demonstrates lower bounds of the achievable improvements. The use of the V-nozzle is therefore in no way inferior to the double-slit nozzle and is set as the new standard.

Some effort on optimizing the dimer signal has been made in course of the Master's thesis of M. Lange.⁶² Two variants of the V-nozzle have been tested without the conical shaping of the nozzle area and slit widths of 0.2 mm and 0.5 mm, respectively. These include threaded holes at the top and bottom to include flow barriers if necessary. Unfortunately, the gas throughput of the metal frit in the sample compartment seems to limit the use of the 0.5 mm version. Changing the opening pressure of the second check valve from 690 mbar to 350 mbar increased the dimer signal of the test substance ethylene glycol approximately by a factor of 10. This encourages extension of the setup to further applications as described in the next section. The monomer signal was much less affected.

Extension to two low-volatility compounds

To enable the measurement of gas mixtures with two low-volatility substances a supplementary experiment is needed. As the concentration of the low-volatility substance in the *popcorn*-jet is determined by temperature, filling the sample compartment with two different substances is only possible in fortuitous cases, where both substances have similar vapor pressures. The mixture of benzyl alcohol and cyclohexyl methanol is an example of such a case.^{31,60}

For mixtures not fulfilling these requirements a setup has been developed, where both substances are melted onto molecular sieve in the desired composition. Fast laser heating then evaporates the whole sample at once, so that the composition of the solid phase is retained in the gas phase. This *falafel*-jet ('fast laser-heated individually fed lump')⁶⁰ prototype is currently hosted in a second experiment port, which was added to the setup in course of this thesis.

Several setup components are shared for both parts including the spectrometer, the buffer volume and the gas reservoir. Others, like the detector chamber, are designed as compatible as possible with the *popcorn*-jet side. The gate valves are identical, so is the design of the vacuum containers for the mirrors and the adjustable beam duct. The IR beam optics include two CaF₂ lenses ($\varnothing = 50$ mm, $f = 105$ mm) and windows ($\varnothing = 50$ mm \times 5 mm) as well as two gold coated mirrors ($\varnothing = 3$ in, Edmund Industrial Optics). The mirror mounts (Newport Ultima) are identical to those installed at the *popcorn*-jet side. Because of the shared components, measurements are only possible for one experiment at a time. Switching between the ports would require no further optical adjustments, if a pre-aligned detector was present in each detector chamber. With only one detector available, the port switching might involve minor adjustments of the IR beam.

A main problem of the *falafel*-jet design is the low substance concentration in the expansion,⁶⁰ which may perhaps be further intensified when combining the *falafel*-jet with the longer nozzle geometry. Therefore, a different approach to measuring two low-volatility compounds using the basic heating technique of the *popcorn*-jet has been designed. Instead of two parallel individually heatable sample compartments as proposed by J. Altnöder⁶⁰, the method which needs the least altering of the present *popcorn*-jet-setup is a sequential double pick-up. The more volatile compound is

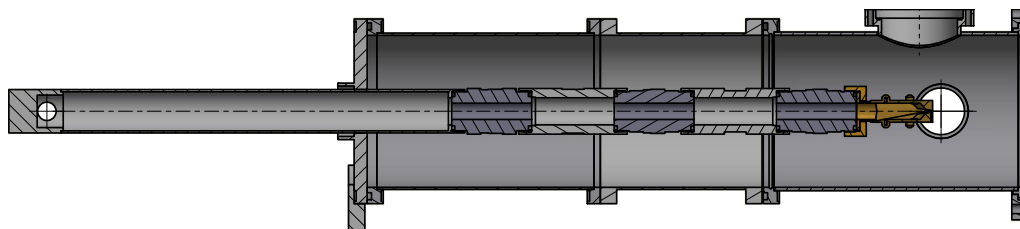


Figure 2.2.5: Side view of the double pick-up design. The two sample compartments are depicted in gray, the three check valves in darker color. The heating sleeves are not shown. The depicted nozzle is the hollow V-nozzle (0.2 mm).⁶⁵

kept in the current sample compartment, while a second sample compartment is added downstream in series with a further check valve (see Fig. 2.2.5). Each one is individually heatable^a to regulate the concentrations. To avoid thermal bridges and condensation of the first sample, the sample compartment further downstream always has to have a higher temperature than the first one. Testing of this double pick-up design has not yet been carried out. A possible complication could be the insertion of a second metal frit, reducing the gas throughput. Furthermore, graded opening pressures of the three check valves might not be possible with the maximum at 350 mbar, leaving it open if a sufficient substance uptake can be achieved.

The second port could be used to build two identical double pick-up experiments to compensate for longer preparation times, as one side could be loaded while a measurement is running on the other. Of course this needs sufficient comparability of those two ports and switching needs to be easy.

Minor setup adjustments

Some minor changes to the setup have been made to the *popcorn*-jet since the work of J. Altnöder⁶⁰:

- In course of a new IR beam alignment, the lenses were changed to two identical plano-convex CaF₂ lenses with a focal length of 105 mm. The convex side is facing outwards of the jet chamber. Furthermore, the beam duct between the two alignment mirrors connecting the spectrometer to the jet chamber was replaced with an adjustable one.

^aFor this purpose the 15 cm jet-chamber adapter has been equipped with a cable feed-through.

- The gate valve separating the jet chamber from the buffer volume was replaced due to malfunctioning, including a change of the adapter pieces due to the different flange geometry. The new valve (VAT, 12146-PA44) is again pneumatic. To ensure the maximum pressure difference of ≤ 30 mbar during opening, the jet chamber has to be evacuated *via* the bypass first.
- Tubing was added to enable evacuating the saturator without emptying the reservoir.
- For safety reasons a residual-current circuit breaker (RCCB) has been added to the power supply of the nozzle heating that is now provided by the three-phase electric power system. The load can thereby be divided on three phases, each has four C13 connectors to allow for further setup adjustments.
- The former practice of baking out the molecular sieve before usage was abandoned, as it is assumed to account for water traces in the expansion.
- New glass sample tubes have been designed with a glass frit (porosity 0, $160\ \mu\text{m}$ to $250\ \mu\text{m}$ ⁶⁶) at one side to eliminate the glass wool as a possible source for spikes (see Sec. 2.2.1). Leaving more room for sample coated molecular sieve, the maximum scan amount with one filling could be slightly enhanced. Unfortunately, the gas throughput seems insufficient, hence the glass wool is still used. A larger porosity (00, $250\ \mu\text{m}$ to $500\ \mu\text{m}$ ⁶⁶) could be tested.
- As a future error prevention, the TRS method could be altered to include a check for the correct reservoir pressure, as in the TRS method of the *filet-jet*⁶⁷ (see Sec. 2.2.2).

Data Post-Processing

Single corrupt scans can influence the whole spectrum. Two main problems arise: Spikes in the probe interferogram, that result in an oscillation in the spectrum, and baseline steps. A macro for removing scans where the probe interferogram contains spikes has been introduced by J. Altnöder⁶⁰. It calculates the differential interferogram of the probe and background wherein the user has to identify spikes. However, the users judgment when to consider a spike as such, seems somewhat arbitrary, hence, a new macro has been developed (see App. B).

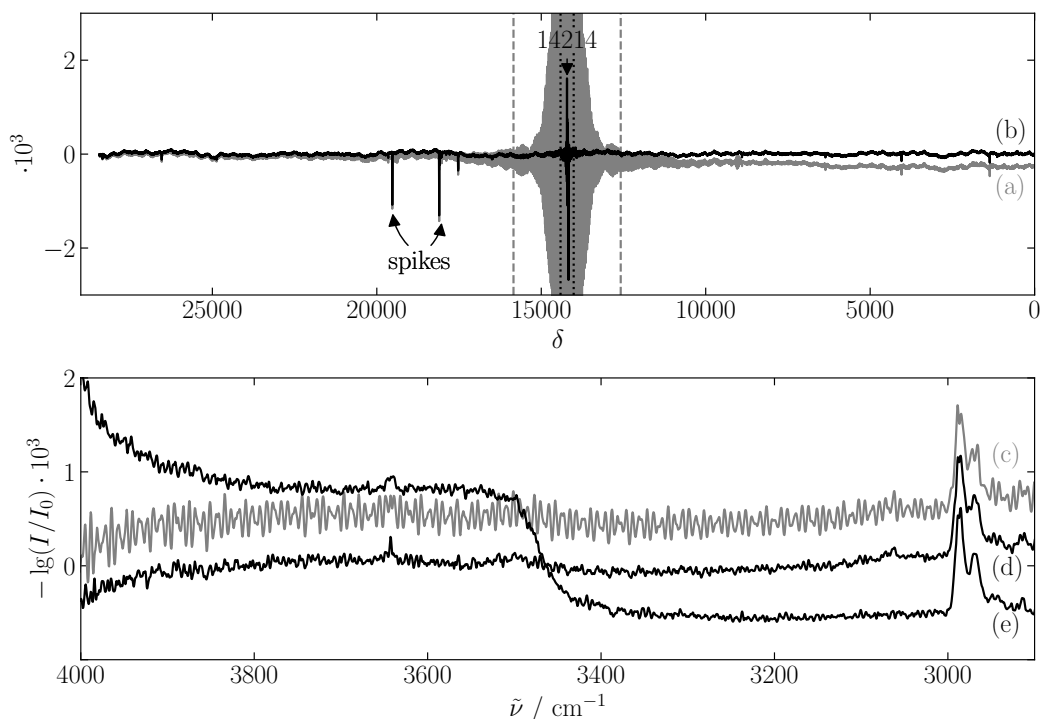


Figure 2.2.6: A probe (a) and the corresponding differential interferogram (b) showing two spikes. The margins for the peak search are depicted by vertical lines. Below are the resulting single-scan spectra with the spikes (c) and without (d). Spectrum (e) is an example of a scan with a baseline step. The spectra are taken from measurements of dibenzofuran-*tert*-butyl alcohol.

The user's decision for a spike is replaced by the OPUS-function 'PeakPick'⁶¹ with an adjustable threshold (e.g. 0.0001). This searches both sides of the differential interferogram for spikes, leaving out the center from 14014 to 14414. If a spike is found, it is removed from the probe interferogram and replaced by a straight line (OPUS-function 'StraightLine'), as the artificial oscillation can thereby be eliminated (see Fig. 2.2.6) and the scan can be used for averaging, in contrast to the former macro.

As replacing the spikes with a straight line can lead to artifacts when the spike is close to the centerburst, a second threshold (e.g. 0.00005) can be set for spikes between 12584 and 15844, for which the scans are omitted completely from the averaging.

The second problem, the steps in the baseline, is treated by the OPUS-function ‘QualityTest’. The spectrum for every single scan is calculated (after spike removal) and tested for quality criteria, that can be defined in a QT-file. As the baseline steps occur in between 3400–3550 cm^{-1} (see Fig. 2.2.6 (e)), the maximal absorption difference in this area may not exceed a certain value (e.g. 0.0003). However, one has to be careful as spectral bands may lay in this region, hence the spectral range for this criterium and/or the threshold might need to be adjusted.

Summarized, these are the steps done for every single scan:

1. Calculate the differential interferogram.
2. Find spikes in the differential interferogram (without center burst) and replace them by a straight line in the probe interferogram.
3. Find spikes in the differential interferogram (center burst only) and sort out corrupt ones.
4. Fourier-transform the interferogram to a spectrum.
5. Quality test for single scan spectrum, sort out corrupt scans.
6. Average satisfactory spectra.

2.2.2 *filet-Jet*

The *filet-jet* (‘fine, but lengthy’) has an analogous working principle to the *popcorn-jet*. It is optimized for volatile compounds, which is why the sample chamber in front of the nozzle is omitted and nozzle heating is not needed. Hence, a much longer slit nozzle (factor ≥ 10) enhances the absorption path, resulting in a far superior signal-to-noise-ratio. Therefore, the *filet-jet* is preferable whenever the substances are volatile enough. A boiling point below 200 °C is a rough estimate. Ethylene glycol with a boiling temperature of 197 °C⁶⁸ is an example where a better signal-to-noise ratio is obtained with the *popcorn-jet*.⁶⁹ Details about the *filet-jet* setup can be found elsewhere.^{70–72} Three gas lines are available to fill the gas reservoir (67 L), two of them containing saturators to introduce the analyte compounds. Apart from the saturator temperatures, the opening and closing times of the solenoid valves controlling the gas throughput can be used to optimize the sample concentrations.

Each gas pulse through the 600 mm \times 0.2 mm slit nozzle is probed by a Bruker IFS 66v/S FTIR spectrometer. The measuring scan sequence is identical to that of the *popcorn*-jet apart from being measured only single-sided. The background pressure is upheld by a buffer volume of 23 m² and a pumping system of two rotary vane and four roots pumps with a rate of up to 2500 m³ h⁻¹. The waiting time between pulses is generally shorter than for the *popcorn*-jet, approximately 30 s. More experimental parameters in comparison to the *popcorn*-jet can be found in App. A.

2.3 Microwave Setup

Microwave spectroscopy offers a way to discriminate between conformers, that are indistinguishable in FTIR spectroscopy. The interpretation of the spectra can be challenging,⁷⁴ but when the rotational constants have been found, the assignment to a cluster is usually unambiguous.

Spectra of some of the clusters in this thesis have been obtained in cooperation with the Schnell group in Hamburg. The setup, acronymed COMPACT ('compact-passage acquired coherence technique'), is depicted in Fig. 2.3.1, a detailed description can be found in Refs. 73,75,76.

The COMPACT setup makes use of the chirped-pulse Fourier transform microwave (CP-FTMW) technique. A 4 μ s microwave chirp is created by a 24 GS/s arbitrary waveform generator. It spans 2–8 GHz, a frequency range suited for larger molecules and clusters. After amplification, it is transmitted to the jet chamber by a horn antenna, where it crosses the supersonically expanded sample. Whenever a frequency coincides with a rotational transition, the cluster is polarized and thus a macroscopic dipole moment is formed, that decays over time. A second horn antenna records this free induction decay (FID). It is then Fourier-transformed into a rotational spectrum. Every gas pulse is probed by eight microwave chirps. With a pulse rate of 3 Hz to 4 Hz this results in an effective repetition rate of 24 Hz to 32 Hz. Approximately 2 million FIDs are averaged to obtain a sufficient signal-to-noise-ratio.

Low-volatility samples are introduced in a sample compartment directly at the nozzle and can be heated up to 200 °C for vapor pressure control. For more volatile compounds a sample compartment further upstream is used, for which part of the carrier gas stream is branched off. Its concentration can be reduced by attenuating

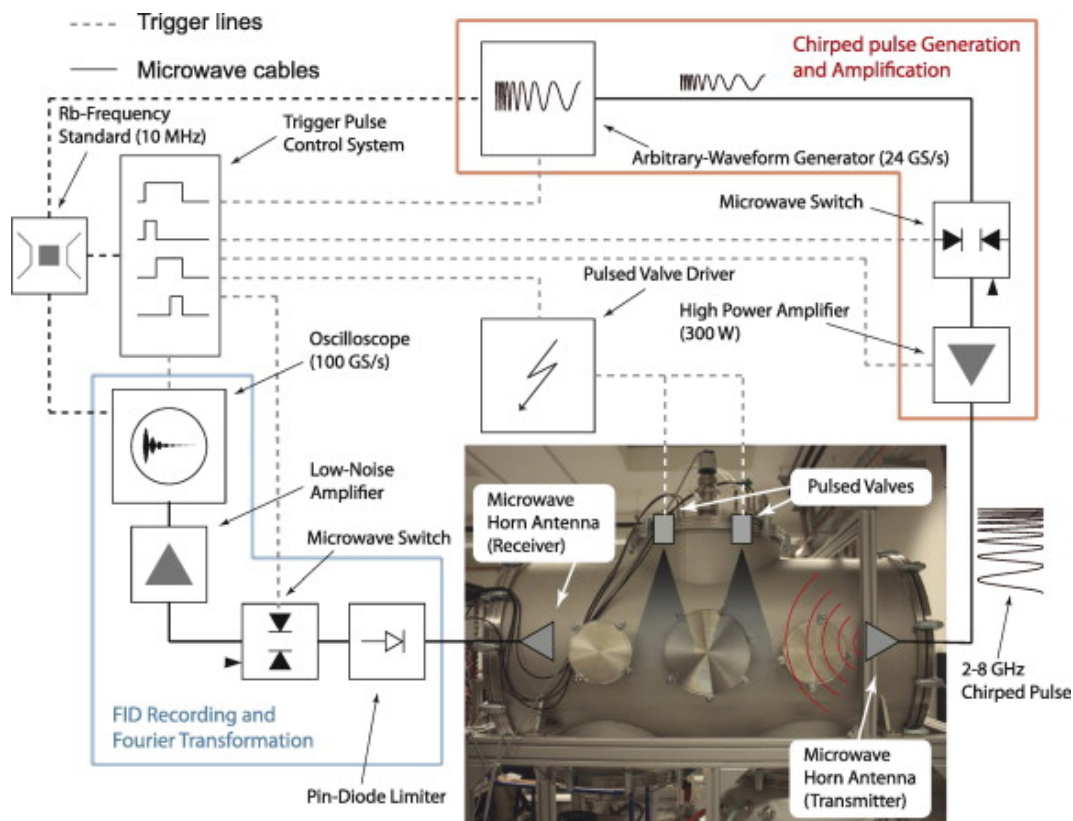


Figure 2.3.1: Representation of the COMPACT setup in Hamburg. For the spectra obtained in this thesis, only one gas nozzle was used. Reprinted from Ref. 73, with permission from Elsevier.

the gas flow portion flowing through the sample compartment. Commonly, neon is used as a carrier gas. If different expansion conditions are desired, helium is used as well.

Microwave spectroscopy is rather unrestrictive to the molecular systems in study, as it only requires a permanent dipole moment. However, it can be blind for larger clusters forming in the expansion, when the transitions are out of the spectral region. The main advantage of the technique is the measurement of first order structural quantities most quantum chemical calculations yield with sufficient accuracy for a reliable assignment.

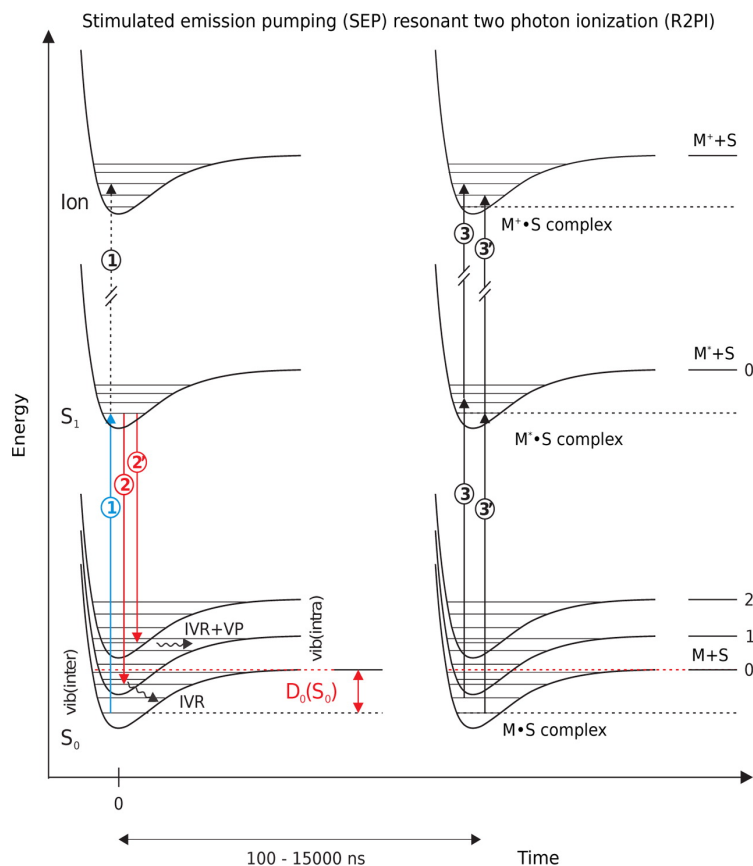


Figure 2.4.1: Schematic level diagram of the SEP-R2PI experiment. Reprinted with permission from Ref. 77. Copyright 2016 American Chemical Society.

2.4 SEP-R2PI Setup

The methods described so far are able to quantitatively or qualitatively measure the binding energy differences ΔE_0 of two or more complexes. However, experimentally determining the absolute dissociation energy D_0 of a complex is even more challenging.⁷⁷ One of the methods for determining cluster binding energies is the stimulated emission pumping resonant enhanced two photon ionization technique (SEP-R2PI), which was developed in the 1990s by the Leutwyler group.^{29,77,78} It is applicable for clusters of strong UV chromophores (M) and small solvent molecules (S). The clusters are prepared in a supersonic expansion, just as in the previously described

methods. A detailed description of the experimental method can be found in Ref. 77–79.

The first step is the measurement of a resonance enhanced two photon ionization (R2PI) spectrum, to determine the electronic origin transition of the cluster. UV/UV hole-burning techniques can be applied in this step to separate different isomers. The spectral shift from the monomer (M) transition can give hints for the structural assignment.⁷⁹

Once the electronic origin transition is known, the actual SEP-R2PI experiment can be applied. The energy level diagram is shown in Fig. 2.4.1. Three lasers are needed. The first (pump) laser (1) is fixed, typically on the electronic origin of the cluster and pumps the clusters to the S_1 state. A small fraction might absorb a second photon in an R2PI scheme, eliminating these clusters from the further process. The second laser’s frequency is scanned, dumping the clusters to vibrationally excited ground state levels. Intramolecular vibrational energy redistribution (IVR) of these hot M–S clusters leads to vibrational predissociation, if the remaining energy is larger than the dissociation energy (2’). Otherwise, the vibrationally excited cluster will stay intact (2) and can be probed by the third laser (3), fixed on a hot band of M–S, with an R2PI experiment. Thereby, a lower boundary to the dissociation energy can be determined by the last band visible in this hot-band probed SEP spectrum.

The upper boundary can be determined by the simultaneous detection of the decrease in the ion signal of the pump R2PI process (1), whenever the dump laser is in resonance with a vibrational energy level above or below the dissociation energy (‘dump spectrum’), depopulating the S_1 state for the second step of the R2PI. As another option, the probe laser can be set to the electronic origin (3’), detecting the population decrease in the ground state, when the dump laser is in resonance (‘origin probed SEP spectrum’). Alternatively, a fluorescence spectrum can be recorded. D_0 is thereby bracketed between the last band of the hot-band probed SEP spectrum and the first band only observed in the dump, origin probed SEP or fluorescence spectrum, respectively. Thus, the accuracy of this technique depends on the gap between these two bands.

An advantage compared to other techniques for the determination of dissociation energies is that it does not depend on thermodynamic cycles. Furthermore, the

vibrational predissociation takes place on the potential energy surface of the ground state. Therefore, the problem of a geometry change with the electronic excitation can be avoided.⁷⁷ Additionally, the excited state dissociation energy $D_0(S_1)$ can be determined *via* a thermodynamic cycle using the spectral shift of the cluster's electronic origin transition $\tilde{\nu} = D_0(S_0) - D_0(S_1)$.⁸⁰

2.5 Multi-spectroscopic Approaches

Every method has its own advantages and drawbacks in detecting, identifying and quantifying molecular balance clusters. Open questions left by a certain technique may be answered by an other in a multi-spectroscopic approach. The combination of different methods for studying the same molecular system can lead to valuable results, not only for the particular system used for the multi-spectroscopic approach, but it enhances the general reliability of each individual technique. If all results can be combined in an overall picture, errors made in the analysis of a single method can be ruled out. Thus, multi-spectroscopic approaches can be used as common ground to start from, before each technique can explore the chemical space individually and resort to other methods if needed.

For benchmarking purposes, the measurement of one system with various techniques is especially fruitful, since different observables are available to compare to theory. Computational methods, that excel in the prediction of one specific molecular property, might fail in the description of another. For example B3LYP-D3 was shown to satisfactorily predict energy differences⁸⁶, but is less suited for the calculation of absolute dissociation energies.⁸⁷ Thereby, fortuitous error cancellation can be identified in computational methods. The application of multi-spectroscopic approaches to molecular balance systems has been reviewed in Ref. 88.

With its broad applicability and comparably fast spectral overview, linear FTIR spectroscopy is well suited to initiate the search for interesting molecular balance systems. In the collaborations of this thesis, IR/UV double resonance spectroscopy by the group of M. Gerhards (Kaiserslautern) is used for verification of the band assignment, adding information on the cluster mass. Microwave spectroscopy by the group of M. Schnell (Hamburg) offers structural information and SEP-R2PI spectroscopy by the group of S. Leutwyler (Bern) provides absolute binding energies.

2 Experimental and Theoretical Methods

Table 2.5.1: Comparison of the methods used in the multi-spectroscopic approaches of this work. Note that these specifications are not necessarily the setup’s limits, but give an order of magnitude for the values employed for the studies related to this thesis.

	FTIR	MW	IR/UV	SEP-R2PI
Expansion type	Free slit jet	Free pinhole jet	Molecular beam	Molecular beam ⁸¹
Nozzle geometry	0.2–0.5 mm × 10–600 mm	∅ = 1 mm ⁸²	∅ = 0.5 mm ⁷⁵	∅ = 0.4 mm ⁸¹
Nozzle area	10–120 mm ²	≈ 0.4 mm ²	≈ 0.2 mm ²	≈ 0.1 mm ²
Nozzle temperature	20–200 °C	80–150 °C ⁸³	20–35 °C ⁸⁴	≈ 80 °C
Opening time	300 ms	380 μs ⁷⁶	220–300 μs ^{84,85}	125–250 μs ⁸¹
Gas pulse repetition rate	1–2 min ⁻¹	180–240 min ⁻¹ ⁷⁵	600 min ⁻¹ ^{84,85}	
Spectral scans/gas pulse	1	8 ^{75,85}	≪1 ⁸⁴	≪1
Scans for final spectrum	50–1000	≈ 2 × 10 ⁶ ⁷⁵	<50 ⁸⁴	≤10
Backing pressure	0.4–1.5 bar	2–3 bar ^{75,83}	2.5–3 bar ^{75,83}	1.2–1.5 bar ⁸¹
Carrier gas	He(+Ar)	Ne(He) ⁷⁵	Ne(He) ⁸³	Ne ⁸¹
Sample consumption	5–10 g	1 g	mg	mg
Sample restrictions	Distinct IR shift, few monomer conformations, proper volatility, low cost	Permanent dipole moment, few internal rotors	UV chromophore	Strong UV chromophore, ⁷⁸ few internal rotors ⁸⁰
Mass identification	no	<i>via</i> moment of inertia	yes	yes
Assignment tools	IR shift, analogies, deuteration	Structure prediction, ¹³ C, dipole moment components	IR shift, S ₁ ←S ₀ spectral shift, ⁷⁵ IR/IR/UV ⁸³	S ₁ ←S ₀ spectral shift, holeburning ⁷⁹
Energy ranking	IR intensity, He/He+Ar	Intensity Ne/He	UV+IR intensity, Ne/He	Absolute dissociation energy

For a multi-spectroscopic study, a good comparability between the experiments is required. Tab. 2.5.1 lists different parameters of the setups from the groups collaborating for the multi-spectroscopic approaches of this thesis. All setups use pulsed supersonic expansions for the cluster preparation. However, the nozzle geometries, that largely influence the cluster formation, vary substantially. Ideally, one would look at the same expansion with different methods simultaneously, but as the spectral methods have different requirements, this is effectively not possible. The largest nozzle is used for the linear FTIR measurements as required by the Lambert-Beer law. It is the only setup type equipped with slit nozzles, which can be expected to enhance the cluster formation.⁴⁸ Pinhole expansions on the other hand allow for better rotational cooling and are thus applied for microwave spectroscopy. The UV techniques, using mass spectrometers for the detection, skim free pinhole jet expansions to molecular beams. The lower propensity for cluster formation in the pinhole expansions is countered by larger stagnation pressures. The opening times for a gas pulse depend on the acquisition time of the spectroscopic method and are also largest for FTIR setups. As the carrier gas, neon is used for most methods, which would be desirable for FTIR spectroscopy, too, but due to the higher gas throughput, helium is used for economic reasons. This leads to warmer expansion conditions. The nozzle temperatures are similar, depending on the volatility of the substances, except for the *filet-jet*, which does not allow for nozzle heating.

Selecting a molecular system that can be studied with multiple setups requires the consideration of each experiment's constraints. UV techniques are the most restricting in terms of molecular classes, as they depend upon a (strong) UV chromophore, making it ideal to study clusters of aromatic compounds. FTIR spectroscopy is more widely applicable, but in need of a characteristic IR shift upon complexation, which can discriminate between the different clusters. It profits from rigid monomer units, as the complexity can be largely reduced (see Sec. 3.3.1), so do the other spectroscopic methods. Microwave spectroscopy is equally widely applicable, since only a permanent dipole moment is required. Few internal rotors are favorable though, in order to diminish complexity. The same is true for the SEP-R2PI method, since energy storage in such modes which are only weakly coupled to the dissociative vibrations might lead to vibrational levels with a longer lifetime than used in the experiment and thus weak bands above the dissociation limit.^{80,89} Shallow potential

energy surfaces may also complicate the measurements,^{77,78} due to possible spectral overlap of multiple minimum structures. Additionally, the fluorescence quantum yield of the $S_0(v'=0)$ state needs to be sufficient.⁷⁸

The identification of the species in the jet expansion is least ambiguous in microwave spectroscopy. If the cluster geometry cannot directly be derived from the observation of ^{13}C isotopologues in natural abundance, rotational constants from quantum chemical calculations usually differ sufficiently for a reliable assignment. Furthermore, the dipole moment components can be compared to the experimental band intensities. By using the ion mass channels for detection, the UV techniques are inherently size selective, as opposed to FTIR. While the SEP-R2PI method is not primarily designed to identify the clusters interaction type, IR/UV, like FTIR, compares the spectral downshift in the infrared upon complexation. Additionally, the $S_1 \leftarrow S_0$ spectral shift can provide valuable information in the UV based techniques. For the differentiation between clusters spectral holeburning can be applied.⁸³ FTIR needs concentration variations to distinguish between cluster sizes (see Sec. 3.2). Apart from the plain IR downshift, deuteration experiments help in assigning the clusters, as described in Sec. 3.2.

A strength of linear FTIR spectroscopy is evident for the energy differences between the clusters. By using heavier or lighter carrier gas and thus cooling or warming the expansion conditions, microwave and IR/UV spectroscopy can determine which cluster is more stable, but a more quantitative analysis is more challenging. In contrast to IR/UV spectroscopy, the band intensities are recorded simultaneously using FTIR, preventing complications such as source instabilities. In IR/UV nonlinear saturation effects might also influence the band intensities. Further difficulties may arise from fragmentation and fast processes in the excited state. Adding to this, more accurate quantification relies on computational cross sections, which are more robust if the values are larger. In order to observe IR transitions, the dipole moment derivatives need to be large, thus the calculated values seem more reliable. More so when only the ratio $\frac{\sigma_{\text{IR}}}{\sigma_{\text{O}}}$ is needed, since the computational deficiencies tend to cancel out. Apart from quantification, the simultaneous measurement of all clusters in linear FTIR spectroscopy is especially useful for plausibility checks. It serves as a bridging technique for the measurement of aromatic and non-aromatic compounds. In many cases, the sequence of finding a suitable system, detect, assign

and quantify the clusters can be accomplished individually, with occasional checks by other techniques.

2.6 Theoretical Methods

For the interpretation of the infrared spectra comparison to quantum chemical calculations is indispensable. The computed electronic and zero-point corrected energies as well as the vibrational frequencies and band strengths are taken into account when assigning the observed bands.

2.6.1 Geometry Optimization

If not stated otherwise, input structures for the geometry optimization have been chosen manually such that several structures for different (hydrogen bond) interaction types were tested. For related clusters, e.g. change of the donor molecule, the optimized geometries of one were used as starting geometries for the other. Binding types found in one cluster were also checked in related clusters.

As the final standard method B3LYP-D3(BJ, abc)/def2-TZVP computed with ORCA 4.0⁹⁰ has been used, all structures computed previously by other methods have been re-optimized at this level. This method implies the dispersion-corrected DFT functional B3LYP^{91,92}-D3⁹³ including Becke-Johnson damping⁹⁴ (BJ) as well as the three-body (Axilrod-Teller-Muto) term of the dispersion correction, indicated by 'abc'. The keywords for the convergence criteria were 'VERYTIGHTSCF' for the SCF convergence and 'TIGHTOPT' for the geometry optimization. The corresponding criteria can be found in Tab. C.1. The DFT grid used was defined by the keywords 'grid5' and 'NoFinalGrid', meaning that ORCA's default multigrid feature is turned off, so that the SCF iterations and final energies are calculated using the same grid (grid 5). Furthermore, the 'UseSym' keyword was generally included to check for symmetry. The geometry optimization was followed by a frequency calculation in double harmonic approximation, serving as a verification for a minimum structure as well as providing the OH stretching frequencies to be compared to the FTIR spectra.

Unfortunately, ORCA does not provide rotational constants for the clusters (yet) and the dipole moment components given depend on the orientation of the cluster in

Table 2.6.1: Comparison of the rotational constants for dibenzofuran–methanol dimers obtained by different quantum mechanical programs.

Dimer		<i>A</i>	<i>B</i>	<i>C</i>	μ	$\mu_x/\mu_y/\mu_z$	
		/MHz	/MHz	/MHz	/D	/D	
OH–O ^p	ORCA ^a	740.1	515.9	318.3	2.702	1.799/	1.629/–1.187
	Gaussian ^b	740.1	515.9	318.3	2.704	1.799/	1.631/–1.189
	Turbomole ^b	739.6	515.5	318.1	2.701	1.798/	1.629/–1.187
	Turbomole ^c	739.7	515.6	318.2	2.702	1.798/–1.634/	1.183
OH–O ^t (<i>C_s</i>)	ORCA ^a	835.7	523.3	382.6	2.845	0.000/	2.814/–0.421
	Gaussian ^b	835.7	523.3	382.6	2.847	0.000/	2.816/–0.422
	Turbomole ^b	835.2	522.9	382.3	2.846	0.000/	2.815/–0.420
	Turbomole ^c	381.5	523.2	832.1	2.851	–0.437/–2.818/	0.000
OH– π	ORCA ^a	1000.6	439.9	419.6	2.051	1.358/–1.472/	0.446
	Gaussian ^b	1000.6	439.9	419.6	2.053	1.359/–1.473/	0.447
	Turbomole ^b	1000.0	439.6	419.3	2.054	1.358/–1.474/	0.447
	Turbomole ^c	999.8	439.6	419.3	2.052	1.146/	1.684/–0.250
CH–O	ORCA ^a	691.2	568.3	331.9	2.565	0.617/–2.349/	0.828
	Gaussian ^b	691.2	568.3	331.9	2.566	0.617/–2.349/	0.828
	Turbomole ^b	690.8	567.9	331.7	2.567	0.616/–2.350/	0.829
	Turbomole ^c	690.9	567.9	331.7	2.567	–0.513/	2.372/ 0.836

^a Single point calculation at B3LYP-D3(BJ, abc)/def2-TZVP level of the aligned geometry obtained by ORCA, rotational constants derived from ChemCraft moments of inertia, as described in the text.

^b Single point calculation at B3LYP-D3(BJ)/def2-TZVP level of the geometry obtained by ORCA.

^c Optimization at B3LYP-D3(BJ)/def2-TZVP level.

the coordinate system and thus do not provide relevant information. The rotational constants given in this thesis were therefore obtained by aligning the optimized geometries in the ChemCraft⁹⁵ program to their principal axes. This outputs the moments of inertia *I*, which are then manually transformed into rotational constants by

$$B = \frac{h}{8\pi^2 c I},$$

with *h* the Planck constant and *c* the speed of light. To obtain meaningful dipole moment components a single point calculation of this aligned structure has been done with ORCA, omitting the 'UseSym' keyword, since it alters the coordinates, but otherwise using the same keywords as above. This method has been tested by single

point calculations of the same geometry using `Gaussian09`⁹⁶ for the dibenzofuran–methanol dimers (see Tab. 2.6.1). The rotational constants are identical, while the overall dipole moment and its components agree within 0.002 D. Thus, the procedure for obtaining the rotational constants and dipole moments from the calculations with `ORCA` is well-founded. Additionally, the values are compared to a single point calculation and a geometry optimization using `Turbomole`⁹⁷. The rotational constants agree within 1 MHz, while the dipole moment component calculations differ slightly in case of the geometry optimization, probably due to a deviation in the optimized geometry. The values in Tab. 2.6.1 are provided following the program output, which reveals a minor deficiency of `Turbomole` in case of OH–O^t (C_s), where the rotational constants and dipole moment components are not given in proper order.

B3LYP-D3(BJ) has been chosen as the computational method, since it has been shown to have an acceptable accuracy with relatively low computational cost for the related anisole–methanol complex.⁸⁶ Starting using the aug-cc-pVTZ⁹⁸ (aVTZ) basis set as proposed in Ref. 86, it could not be upheld for larger clusters, due to recurrent imaginary frequencies. Thus, the basis set was changed to def2-TZVP⁹⁹. This has the added advantage of using the basis set family the D3 correction was originally parametrized for.⁹³

At the start of this thesis the input structures were pre-optimized at the B97D/TZVP^{100,101} level using `Gaussian09`⁹⁶ and then computed at B3LYP-D3(BJ)/def2-TZVP level using `Turbomole`⁹⁷ as has been done by J. Altnöder.⁶⁰ To unify the computational method with the work of H. C. Gottschalk the program was changed to `ORCA 4.0`, omitting the pre-optimization step and including the three-body term.

2.6.2 Transition State Search

Computing transition states generally not being a straightforward task, it reveals its own challenges for the interconversion of two non-covalent dimer complexes. There are multiple ways to obtain barrier heights.¹⁰² When regarding the interconversion of monomer conformations scanning of a dihedral angle is commonly used.⁴⁹ But normally there is no such distinct reaction coordinate to scan for the interconversion of two dimer conformations. Alternatively, Quasi-Newton algorithms can be used.

However, they only succeed if the initial guess is sufficiently close to the transition state geometry. Thus, finding a suitable initial guess is the true challenge.

For finding an initial geometry, two different methods have been used. In favorable cases a pseudo reaction coordinate can be defined and a relaxed surface scan of this coordinate applied. ORCA can combine these two steps, but this has not been tested in this thesis. For the hydrogen bonded clusters studied in this thesis one can try scanning the H–O distance, when changing from one binding type to the other, preferably starting from the less defined binding type (OH– π) to the well defined (OH–O). For the flexible acceptor molecule diphenyl ether, a relaxed scan of the conversion from one monomeric enantiomer to the other has been successful.

If no suitable pseudo reaction coordinate to scan was apparent, the `woelfling` module of `Turbomole` has proven to be a useful tool. It creates an initial guess of the reaction path by a modified linear synchronous transition (LST) method¹⁰³ before optimizing it assuming a quadratic potential with the constraint of equal spacing of structures along the path.¹⁰⁴ Thorough attention has to be paid to the atom labeling. Therefore, running a test stopping after the LST step and checking for a reasonable first path is always worthwhile. Although, `woelfling` has a keyword for aligning the input structures, the use of pre-aligned input structures (and possibly disable the automatic alignment) might help. Furthermore, symmetry of the monomer molecules has to be taken into consideration. Starting from the same 'educt' geometry, the lowest energy path is generally different for the conversion into two enantiomeric 'product' structures. Thereby, the atom numbering can also be used to force `woelfling` to try another pathway. Additionally, a stepwise reaction path, including a local minimum as an intermediate structure should be considered, especially when determining the reaction path for other than the two lowest energy structures.⁸³ Having obtained a plausible reaction path, the maximum energy structure can be taken as the initial guess transition state.

Since ORCA was used as the standard method for geometry optimization in this thesis, if not stated otherwise, the final transition states have also been obtained by this program at B3LYP-D3(BJ, abc)/def2-TZVP level. It utilizes a quasi-Newton like Hessian mode following algorithm.¹⁰⁵ The same keywords stated previously have been used, with 'OptTS' added to specify the optimization to a transition state. This includes the 'FREQ' keyword for the frequency calculation to verify that

the obtained geometry has exactly one imaginary frequency, its mode connecting the two equilibrium structures. Additionally, plotting an overlay of the start, end and transition state geometries helps to check for plausibility. A second run of `woelfling`'s LST step for an initial path might also help to visualize the reaction path *via* the determined transition state. Recalculation of the Hessian matrix every 5 steps improved the geometry convergence.

Furthermore, the transition state search methods of the `Gaussian` program⁹⁶ have been tested. `Gaussian` offers the QST (quadratic synchronous transit) methods, which combine an initial quadratic synchronous transit approach followed by a quasi-Newton optimization. Two variants can be used, QST2 and QST3, depending if an initial guess for the transition state is available. For the tested conformer interconversions only the QST3 method with an initial guess from `woelfling` was able to provide a transition state. Besides, the TS option is available to optimize to a transition state instead of an equilibrium structure using the Berny algorithm.

A more general guide on which method to apply for finding transition states can be found in Ref. 102. Further approaches mentioned therein potentially suitable for dimer complexes are a normal symmetry-constrained geometry optimization if the transition state can be defined by symmetry or the use of a transition state obtained for a related cluster as the initial guess.

3 Clusters of Furans and Alkyl Alcohols

As a heterocycle, furan offers two acceptor sites for hydrogen bonding with a protic solvent. The π system would usually be regarded inferior to an oxygen atom acceptor for an OH hydrogen bond, but as the latter is part of the π system, the situation is at level, since the electron density of the oxygen atom is also distributed. Furans are therefore well suited as molecular balances for these two different hydrogen bond types.^{37,38,106,107} Furthermore, their rigidity allows for only a small amount of conformers and thus simplifies the IR spectrum. Linear FTIR spectroscopy is especially suited for measuring this class of compounds as it is not affected by the ultrafast photodynamics of the electronically excited state.¹⁰⁸

Furan and its derivatives have been studied thoroughly for their complexation behavior. The furan dimer itself presents a molecular balance between weak CH–O and CH– π interactions. In a theoretical study using DFT methods, the combination of two CH–O contacts has been found superior. However, dispersion corrections were not applied.¹⁰⁹ Microwave spectroscopy has been used to study van-der-Waals clusters of furan. As can be expected, the argon(2) cluster^{110–112} as well as the CO cluster¹¹³ exhibit binding to the π face. Line splitting indicated a hindered internal rotation of CO above the furan plane. SO₂ is also bound to the π face of furan.¹¹⁴ Furthermore, excited complexes of furan derivatives with aromatic hydrocarbons in solution have been investigated using fluorescence spectroscopy.^{115,116}

The most systematically studied class of complexes are those of hydrogen halides and their analogues with furan and its derivatives. They have been investigated both theoretically^{36,117–120} and experimentally¹²¹. An early study recorded IR band shifts and formation enthalpies of HF with furan and 2,5-dimethylfuran in solution.¹²² Later studies confirmed the proposed binding to the oxygen site using microwave spectroscopy¹²³, although the structure assignment is more ambiguous when going down the halogen group. For furan–HCl, an oxygen-bound conformer was identified using microwave spectroscopy¹²⁴, while both docking variants were found by FTIR spectroscopy.¹²⁵ The rotational spectrum of furan–HBr revealed a

face-on conformation, but the hydrogen is pointed towards the oxygen atom.¹²¹ An evenly balanced case has also been found for the furan–acetylene dimer prepared by helium nanodroplets spectroscopy experiments,¹²⁶ while the preparation in argon matrix was found to favor the oxygen-bound species.^{36,127} As the π system of this donor forms secondary interactions with the *ortho* CH group breaking the C_{2v} symmetry, these types of complexes have been the subject of a theoretical study.³⁶ The furan–ethylene dimer has also been studied by microwave spectroscopy, revealing a T-shaped dimer structure, that compromises CH–O and CH– π interactions.¹²⁸

Hydrogen bonded complexes with NH donors have also shown to form complexes with the oxygen as an acceptor as well as π -bound complexes,^{37,106} whereas only oxygen-bound conformers have been identified for the OH donor formic acid measured in argon matrix¹⁰⁷. A very recent matrix isolation study¹²⁹ also found a single oxygen-bound conformer for furan–water, which was already predicted by theory.^{130,131} The same holds true for methanol as reported by a matrix isolation study, that was published during this project.¹³² However, the band assignment was based on DFT calculations without dispersion correction, whose inclusion reverses the predicted stability sequence. Furthermore, the applied argon matrix might influence the band shifts, as indicated by the offset of 20 cm^{-1} of the methanol monomer band¹³³ compared to gas phase as well as the relative cluster abundance. This emphasizes the relevance of an independent study of this cluster using supersonic jet FTIR spectroscopy.

The competition between oxygen and π binding in furan has also been investigated for clusters with metal cations.^{134–136} π binding is preferred throughout all metals under study, while the hapticity varies from η^5 to η^2 and η^1 . The experimental binding energies range from 113 kJ mol^{-1} to 255 kJ mol^{-1} and are lower than for benzene. Larger M:furan clusters have been investigated for Mn and Zn.¹³⁷

Moreover, furans can serve as dienes for Diels–Alder cycloadditions. In favorable cases, transition metal catalysts promote these reactions by disrupting the aromaticity. However, the reaction is strongly dependent on the equilibrium of 3,4- η^2 and 4,5- η^2 isomers, which is most favorable for the 2,5-dimethylated furan.¹³⁸

In this chapter furan and several alkylated as well as polycyclic derivatives are studied for their complexation behavior with small alkyl alcohols, namely methanol and *tert*-butyl alcohol. The latter are chosen as they are among the most simple

OH-hydrogen bond donors and their rigidity reduces the complexity of the conformational space. At first, the overarching geometry patterns are introduced and the corresponding nomenclature is defined. The smallest clusters, furan and its methylated derivatives with methanol, form the starting point. To possibly increase the relevance of π binding, the alkyl moieties are then enlarged in Sec. 3.3. A slightly different approach to favor π binding is attempted in Sec. 3.4, where the size of the π system is enhanced by annulating one or two benzene rings to furan.

3.1 Binding Geometries and Nomenclature

As the binding geometries of the furan clusters discussed in the following sections are very similar, a nomenclature for the clusters shall be established first.

The complexes are named by their main type of interaction, most commonly a hydrogen bond to an oxygen atom (OH–O) or a π system (OH– π), less often a CH–O or CH– π interaction. For the latter two, the alcohol molecule is not necessarily the proton donor. Based on this primary classification, the predicted structures for the dimers of the furan derivatives with alcohol donors can be grouped into different structural types, as depicted in Fig. 3.1.1. All clusters are arranged such that the hydroxy group of the alcohol is positioned in front of the plane defined by the furan ring. There are three different OH–O structure types, which can be distinguished by the angle in which the methanol docks to the furan. The most bent hydrogen bond is found in the OH–O^t structure (‘on-top’, as established in Ref. 139, see Fig. 3.1.1a), due to a compromise between the linearity of the hydrogen bond and a supplementary interaction of the alkyl moiety of the alcohol with the π system of the furan ring. For symmetrical acceptor molecules C_s symmetry is possible. The other OH–O structures have more linear hydrogen bonds and deviate from each other by the orientation of the alkyl moiety of the alcohol. In the OH–O^p structure (‘in plane’) the alkyl moiety is directed towards the furan ring, the alcohol being on one side of the furan plane exclusively. Contrarily, in the OH–O^b structure it is turned to the opposite direction, such that the hydroxyl and alkyl moieties are on opposite sides of the furan plane. Often, but not necessarily, this distinction is related to a secondary CH–O interaction with an alkyl moiety of the acceptor in case of OH–O^b and with an aromatic C–H bond in case of OH–O^p, respectively. For example, the investigated purely aromatic derivatives of furan all have a stable

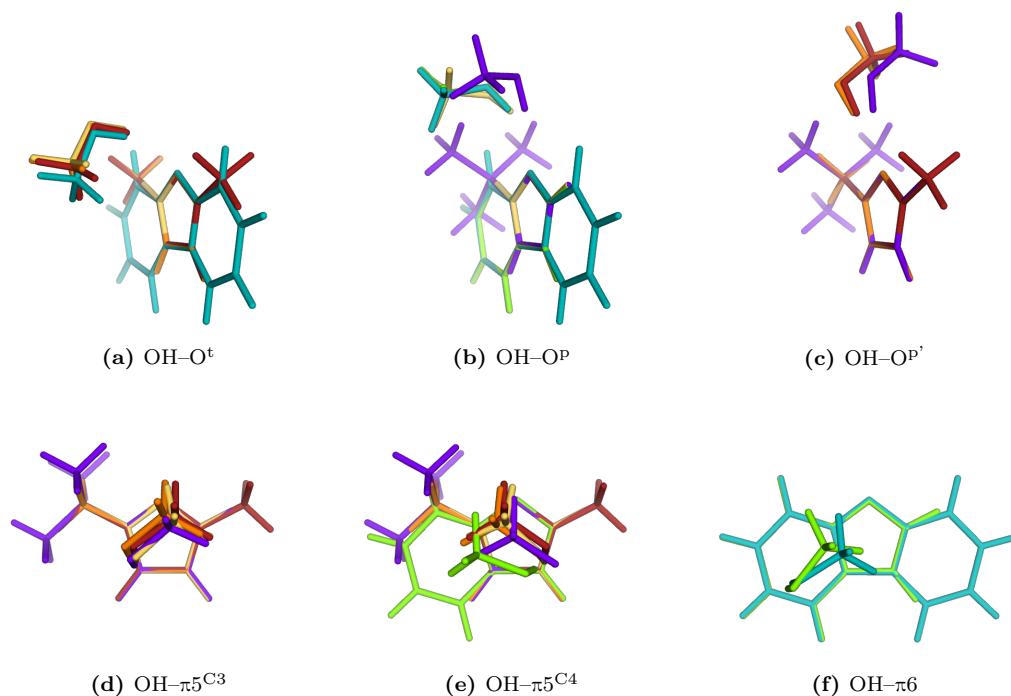


Figure 3.1.1: Binding types of the most stable dimers of methanol and furan derivatives calculated at B3LYP-D3(BJ, abc)/def2-TZVP level.

OH-O^P structure with methanol as a hydrogen bond donor, where the methanol is tilted sideways to profit from a CH-O interaction with an aromatic C-H bond. This behavior has already been proposed for dimers of furan with acetylene and fluoroacetylene³⁶ and is somewhat similar to the proposed structure of the furan homodimer¹⁰⁹. The distinction between the three OH-O structural types is more blurred for the *tert*-butyl alcohol clusters, where intermediate structures between OH-O^t and OH-O^P are somewhat arbitrarily classified by resemblance.

As seen in Fig. 3.1.1d and Fig. 3.1.1e the alcohol profits from several interactions with the furan π system in the OH- π conformers. The hydroxyl is directed towards the C3 or C4 atom (indicated as a superscript), resulting in two possible minimum structures for unsymmetrically substituted furans. A natural population analysis of furan at the MP2/aVTZ level provides an explanation. The charge on the oxygen atom was found to be $-0.41 e$, and that on the C3 and C4 atoms $-0.31 e$, while the charge on the C2 and C5 atoms is positive with $0.09 e$.^{36,117} Similar structures have been computed for π -bound dimers of hydrogen halides.^{36,117} In case of annulated

benzene rings, a further OH- π conformer is possible by binding to the benzene π system (see Fig. 3.1.1f). To discriminate these geometries in the nomenclature, the π is followed by the ring size. Further classifications are added when necessary, *e.g.* 'in' and 'out' for the position of the alkyl group or numbering in order of decreasing stability. For clarity, all additions to the nomenclature are omitted for a system if they are not needed for differentiation.

3.2 Methylation: Furan, MFuran and DMFuran

Methylation offers a slight variation to a chemical system without severely perturbing the electronic structure. The effect of adding one or two methyl groups to the furan in a complex with methanol shall be explored in this section. The results are part of the double-blind 'goebench' challenge¹³⁹, where theoreticians were invited to predict the preferred binding site for the three systems furan, 2-methylfuran and 2,5-dimethylfuran with methanol, while the experiments were done without mutual knowledge. The experimental part was done in collaboration with H. C. Gottschalk. Preliminary measurements for 2,5-dimethylfuran-methanol have been published previously.¹⁴⁰

Methylated furans have gained interest as possible second generation biofuel additives in recent years, as they can catalytically be derived from fructose.^{141,142} They are superior to the first generation biofuel ethanol regarding the production from non-food cellulosic biomass and their hydrophobicity. 2,5-Dimethylfuran seems especially promising due to its high energy density and octane number as well as low oxygen content and optimal boiling point.¹⁴²⁻¹⁴⁴ In its synthesis, larger alcohols may be used as solvents.¹⁴⁵ Therefore, the understanding of the interaction between alcohols and furan derivatives is of a wider interest.

The monomer structures of all three furan derivatives have been studied by microwave spectroscopy, revealing planar heavy atom skeletons.¹⁴⁶⁻¹⁴⁹ The barriers for the internal rotation of the methyl groups were determined to approximately 5 kJ mol⁻¹.¹⁴⁷⁻¹⁴⁹ Vibrational transitions of the monomers have been assigned for furan (*e.g.* Refs. 150-152 and references therein), 2-methylfuran (*e.g.* Refs. 151,153,154 and references therein) and 2,5-dimethylfuran (*e.g.* Refs. 151,154,155 and references therein) using IR and Raman spectroscopy.

Table 3.2.1: Dissociation energies of the dimers of furan, 2-methylfuran and 2,5-dimethylfuran with methanol with (D_0) and without (D_{el}) harmonic zero-point vibrational energy calculated at B3LYP-D3(BJ, abc)/def2-TZVP level in kJ mol^{-1} . Energies relative to the $\text{OH}-\pi^{\text{C3}}$ dimer (ΔE_{el} and ΔE_0) are given in kJ mol^{-1} , harmonic OH stretching wavenumbers (ω_{OH}) and shifts ($\Delta\omega_{\text{OH}}$) from the corresponding monomer vibrational wavenumber in cm^{-1} , band intensities (I_{OH}) in km mol^{-1} ; see also Ref. 139,140. Conformers used for further analysis in Sec. 6 are marked in bold.

Dimer	ΔE_{el}	ΔE_0	D_{el}	D_0	ω_{OH}	$\Delta\omega_{\text{OH}}$	I_{OH}
Furan + MeOH							
OH-O^t	0.4	0.9	18.7	14.8	3782	28	135
OH-O ^p	-0.4	0.4	19.5	15.3	3776	34	175
OH- π	0	0	19.1	15.7	3760	50	190
Furan + MeOD							
OH-O^t	0.4	0.7	18.7	15.2	2752	22	79
OH-O ^p	-0.4	0.1	19.5	15.9	2748	25	104
OH- π	0	0	19.1	15.9	2737	37	112
2-Methylfuran + MeOH							
OH-O^t	-0.8	-0.1	23.5	18.9	3770	40	134
OH-O ^p	2.1	2.4	20.6	16.5	3763	47	260
OH-O ^{p'}	0.5	1.2	22.1	17.7	3748	61	322
OH-π^{C3}	0	0	22.6	18.8	3745	65	192
OH- π^{C4}	0.9	0.8	21.7	18.0	3750	60	194
2-Methylfuran + MeOD							
OH-O^t	-0.8	-0.3	23.5	19.5	2743	30	80
OH-O ^p	2.1	2.1	20.6	17.1	2739	35	151
OH-O ^{p'}	0.5	0.9	22.1	18.3	2729	45	185
OH-π^{C3}	0	0	22.6	19.2	2726	47	114
OH- π^{C4}	0.9	0.9	21.7	18.3	2730	44	113
2,5-Dimethylfuran + MeOH							
OH-O^t	-0.9	-0.3	25.7	21.2	3760	50	168
OH-O ^{p'}	0.8	1.1	24.1	19.9	3735	74	389
OH- π	0	0	24.9	20.9	3736	74	203
2,5-Dimethylfuran + MeOD							
OH-O^t	-0.9	-0.5	25.7	21.8	2736	38	98
OH-O ^{p'}	0.8	0.8	24.1	20.5	2719	54	221
OH- π	0	0	24.9	21.3	2720	54	119

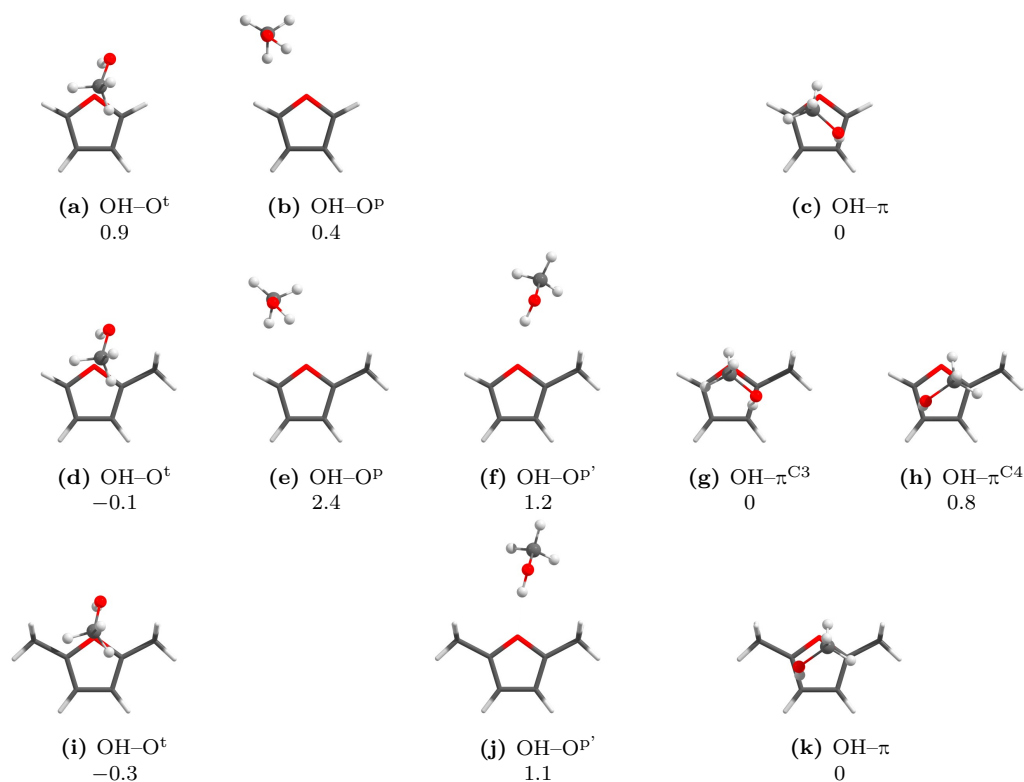


Figure 3.2.1: Structures and relative ZPVE-corrected energies (ΔE_0) in kJ mol^{-1} of the most stable dimers of methylated furan derivatives with methanol calculated at B3LYP-D3(BJ, abc)/def2-TZVP level.

B3LYP-D3(BJ, abc)/def2-TZVP predicts very subtle energy differences (lower than 0.5 kJ mol^{-1} , see Tab. 3.2.1) between the two docking sites for the dimers of methylated furans and methanol, making these complexes a suitable benchmarking system. The conformers obtained by geometry optimization are depicted in Fig. 3.2.1. Keeping the OH- π conformer as a reference point, the stability of the OH-O^t conformation is predicted to increase with the methylation of the furan acceptor, ranging from being 0.9 kJ mol^{-1} less stable in case of furan to being 0.3 kJ mol^{-1} more stable in case of 2,5-dimethylfuran. The disfavoring of OH-O^t in case of furan is probably due to the lack of the alkylic CH-O interaction. Fig. 3.2.2 illustrates the corresponding binding energies. An OH-O^P conformation can only be found for furan and 2-methylfuran, as there is no aromatic *ortho*-hydrogen in

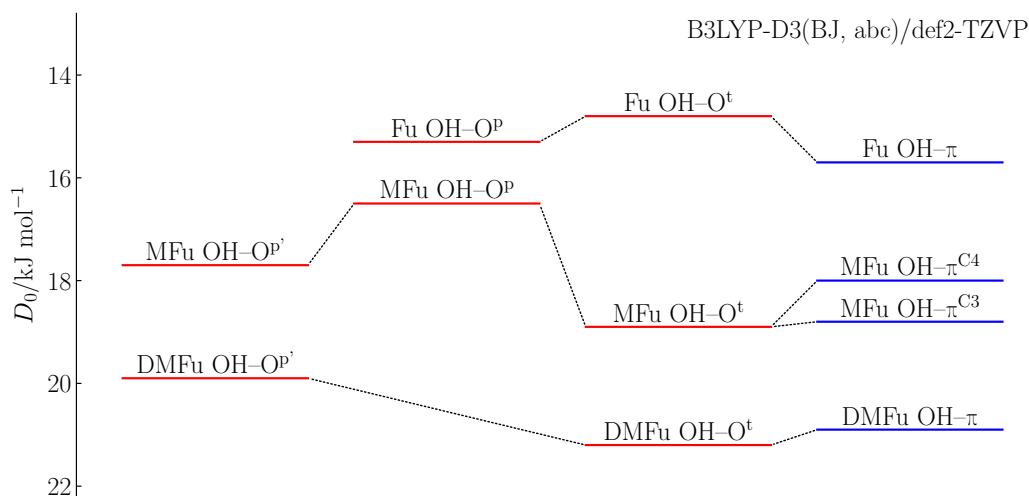


Figure 3.2.2: Illustration of the ZPVE-corrected binding energies of the dimers of furan, 2-methylfuran and 2,5-dimethylfuran with methanol calculated at B3LYP-D3(BJ, abc)/def2-TZVP level.

2,5-dimethylfuran to form the corresponding secondary CH–O interaction. The binding energy of this conformer is least enhanced with methylation. In contrast, the OH–O^p conformer, which is not found for the unmethylated furan, behaves more similar to the OH–O^t and OH– π conformations when a second methyl group is added to the furan ring. Thus, the relative energy compared to the OH– π conformer does not change much. Except for 2-methylfuran, only one π coordinated structure was found, due to the symmetry of the other two acceptors. Zero-point energy also seems to play an important role, as the energetic sequence of the two favored furan–methanol complexes is reversed when going from ΔE_{el} to ΔE_0 .

The mixture of 2,5-dimethylfuran with methanol serves as the starting point for the experimental analysis. Fig. 3.2.3 provides a spectral overview ranging from the OH- to the CH-stretching region measured with the *filet*-jet setup. Spectra (a) to (d) have decreasing concentrations, obtained by adding more helium to the gas mixture.

The CH-stretching region shows an overlap of different aliphatic CH bands originating from all cluster types and provides a rough estimate for the overall concentration. Two distinct bands are observed at 3127 cm^{-1} and 3118 cm^{-1} , corresponding to the symmetric and antisymmetric stretching vibration of the aryllic CH-groups

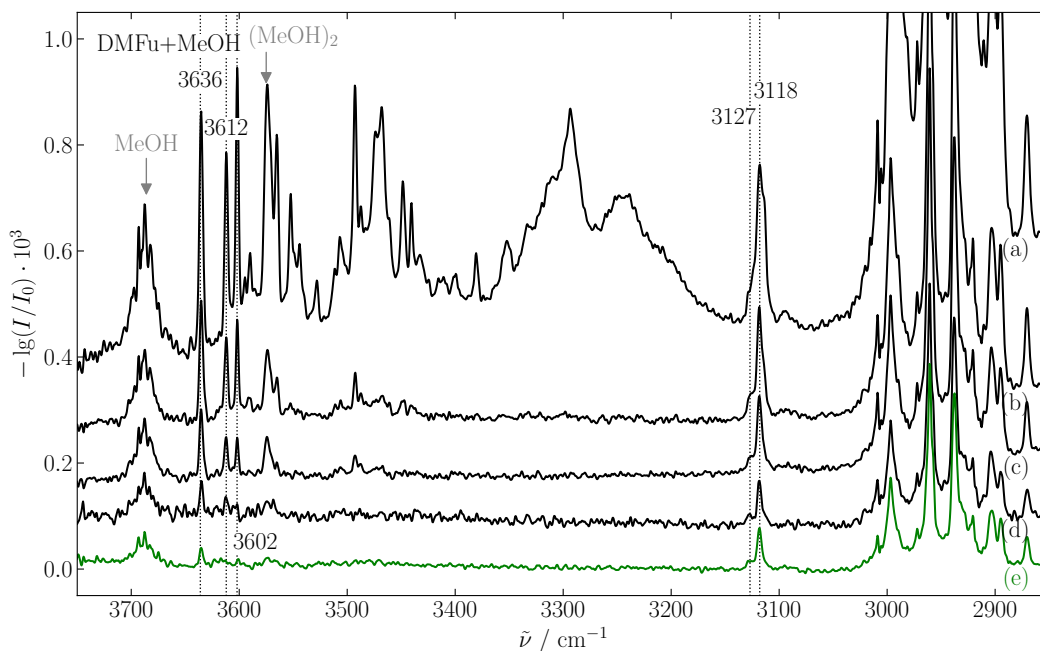


Figure 3.2.3: IR Spectra of 2,5-dimethylfuran with methanol at different concentrations. Percentages are roughly estimated.

- (a) 0.14 % DMFu, 0.15 % MeOH (DMFu: -20°C , 0.95/0.10 s^a, MeOH: -25°C , 0.46/0.49 s);
 (b) 0.07 % DMFu, 0.04 % MeOH (DMFu: -20°C , 0.15/0.89 s, MeOH: -25°C , 0.10/1.14 s, helium: 0.85–0.99/0.25–0.10 s);
 (c) 0.06 % DMFu, 0.02 % MeOH (DMFu: -20°C , 0.15/1.48–2.46 s, MeOH: -25°C , 0.10/1.45–2.46 s, helium: 1.53–2.52/0.10 s);
 (d) 0.02 % DMFu, 0.01 % MeOH (DMFu: -20°C , 0.12/4.92 s, MeOH: -25°C , 0.12/4.92 s, helium: 5.04/0.08 s);
 (e) 0.03 % DMFu, 0.02 % MeOH 4 % Ar (DMFu: -20°C , 0.16/4.92 s, MeOH: -25°C , argon, 0.20/4.96 s, helium: 4.96/0.11 s);
 see also Ref. 140.

^a These values denote the on-/offtime of the solenoid valves filling the reservoir.

of 2,5-dimethylfuran, respectively. The intensity of these bands was taken to estimate the 2,5-dimethylfuran concentration with reference to a spectrum of pure 2,5-dimethylfuran shown in Fig. E.1.

Clusters are identified by their OH-stretching vibration. The spectroscopic range for the OH-stretching vibration of dimers is bracketed by the methanol monomer band at 3686 cm^{-1} and the donor band of the homodimer at 3575 cm^{-1} as hydrogen bonds to furans are expected to be weaker.^{133,156} Between these two bands three prominent bands are visible at 3636 cm^{-1} , 3612 cm^{-1} and 3602 cm^{-1} . The latter is most likely attributed to a trimer, probably containing two 2,5-dimethylfuran molecules, as its intensity is more sensitive to dilution. In spectrum (a) the band is more intense than both of the others, in spectrum (b) less intense than the least shifted band, in spectrum (c) leveled with the second band and reduced to noise level in spectrum (d). To distinguish the underlying cluster stability of the two remaining dimer bands, a spectrum with approximately 4% argon added to a gas mixture similar to spectrum (d) was recorded (spectrum (e)). The band at 3612 cm^{-1} is reduced to noise level in this spectrum, leaving the band at 3636 cm^{-1} as the band of the most stable dimer.

Comparing to the calculated band positions in Fig. 3.2.4, this band matches best to the OH-O^t conformer. The depicted calculated band positions are scaled by a factor of 0.9675 to reproduce the band position of methanol monomer. For the further downshifted band, two conformers are predicted at almost identical position. Regarding the energetic preference, it is most likely associated with the OH- π conformer, which is favored over the OH-O^p conformer by about 1 kJ mol^{-1} (see Tab. 3.2.1).

A spectrum with deuterated methanol was recorded to exclude a band overlap and thus verify this assignment experimentally. It is plotted in the upper panel of Fig. 3.2.4. The position of the OD-stretching band of deuterated methanol (2718 cm^{-1} ¹³³) is aligned with the OH-stretching band of the undeuterated methanol and the wavenumbers are stretched by a factor of $\sqrt{2}$. Two effects can be observed: (1) the intensity of the more downshifted dimer band decreases relatively to the other and (2) the band position of the proposed OH-O band is slightly further shifted in the deuterated case than the scaling of $\sqrt{2}$ would suggest.

3.2 Methylation: Furan, MFuran and DMFuran

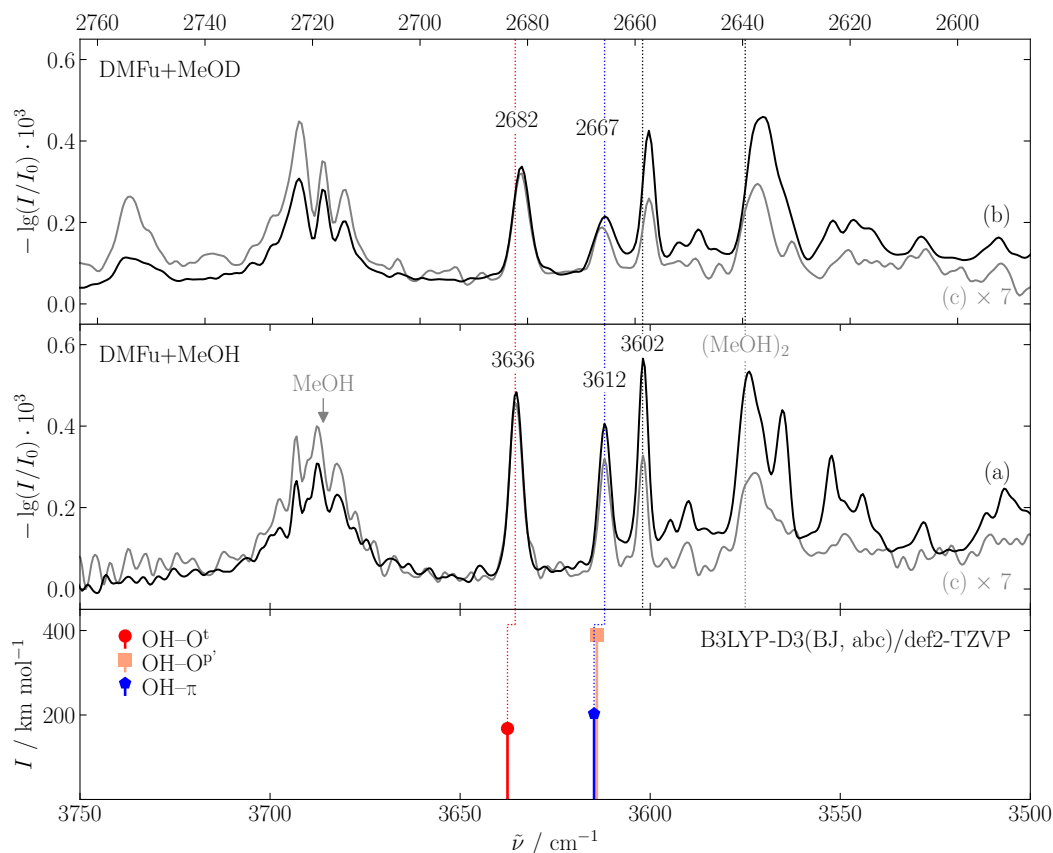


Figure 3.2.4: IR Spectra of 2,5-dimethylfuran with methanol(-d1) compared to theoretical predictions at B3LYP-D3(BJ, abc)/def2-TZVP level. For MeOD (upper panel) wavenumbers are scaled to the methanol monomer and stretched by $\sqrt{2}$. The calculated frequencies are scaled (factor 0.9675) to the experimental MeOH monomer value (3686 cm^{-1}). OH-O conformers are denoted in red, OH- π in blue. Darker colors indicate the most stable conformer of each binding type.

- (a) same as Fig. 3.2.3 (a) (DMFu: $-20\text{ }^{\circ}\text{C}$, 0.95/0.10 s, MeOH: $-25\text{ }^{\circ}\text{C}$, 0.46/0.49 s);
 (b) methanol-d1 (DMFu: $-20\text{ }^{\circ}\text{C}$, 1.04/0.10 s, MeOD: $-25\text{ }^{\circ}\text{C}$, 0.45/0.49 s);
 (c) 1:2 MeOH:MeOD mixture (DMFu: $-10\text{--}20\text{ }^{\circ}\text{C}$, 0.10–0.50/0.50–5.1 s, MeOH+MeOD (1:2): $-22\text{--}25\text{ }^{\circ}\text{C}$, 0.10/0.94–7.5 s, helium: 10.2/0.10 s);
 see also Ref. 139,140.

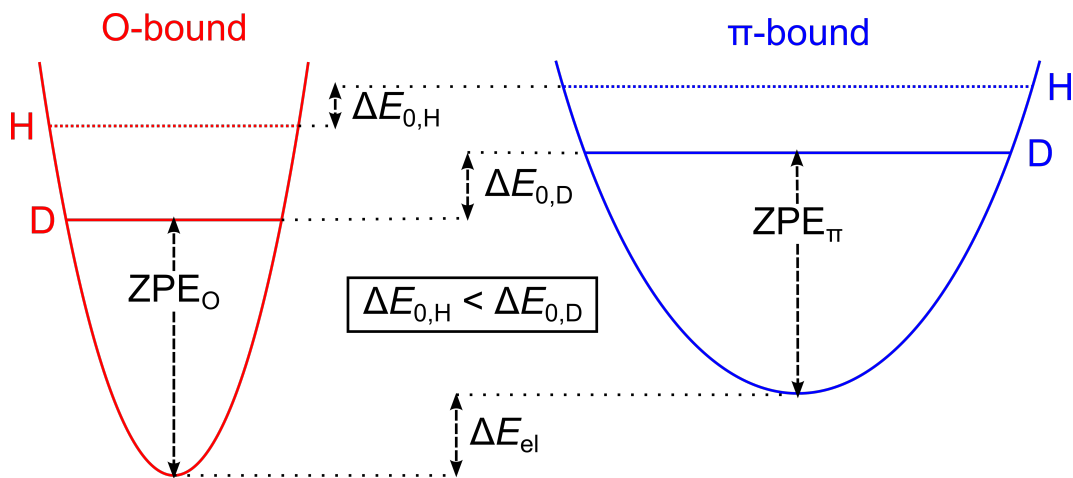


Figure 3.2.5: Schematic explanation of the deuteration effect.

The change in relative intensity can be understood by looking at Fig. 3.2.5. A shallow potential energy surface, like the one for the π -bound conformer, leads to a larger coupling of librational modes to the OH(D)-stretching vibration and thus less zero-point energy is accumulated.⁸⁶ Substituting deuterium for the hydride hydrogen is assumed to leave the conformer structure unaffected, but lowers the vibrational ZPE and hence reduces the relative OH- π stabilization and its relative abundance in the expansion. Applied to the 2,5-dimethylfuran-methanol example, the energy difference between oxygen and π binding is increased, as the OH-O conformer is more stable ($\Delta E_{0,H} = 0.3 \text{ kJ mol}^{-1}$ compared to $\Delta E_{0,D} = 0.5 \text{ kJ mol}^{-1}$, see also Tab. 3.2.1). If the π -bound conformer is the more stable one, the energy difference is lowered with deuteration, such that the relative abundance of the clusters levels out, also reducing the relative intensity of the OH- π band (e.g. BFu+MeOH, see Sec. 3.4.1).

The second effect is due to the different anharmonicities of the OH(D)-stretching mode for oxygen and π -bound clusters. If not for anharmonicity, the scaling of factor $\sqrt{2}$ would result in aligned OH and OD stretching bands in Fig. 3.2.4 corresponding to

$$\omega_{\text{OH/D}} = \frac{1}{2\pi} \sqrt{\frac{k}{\mu_{\text{H/D}}}}$$

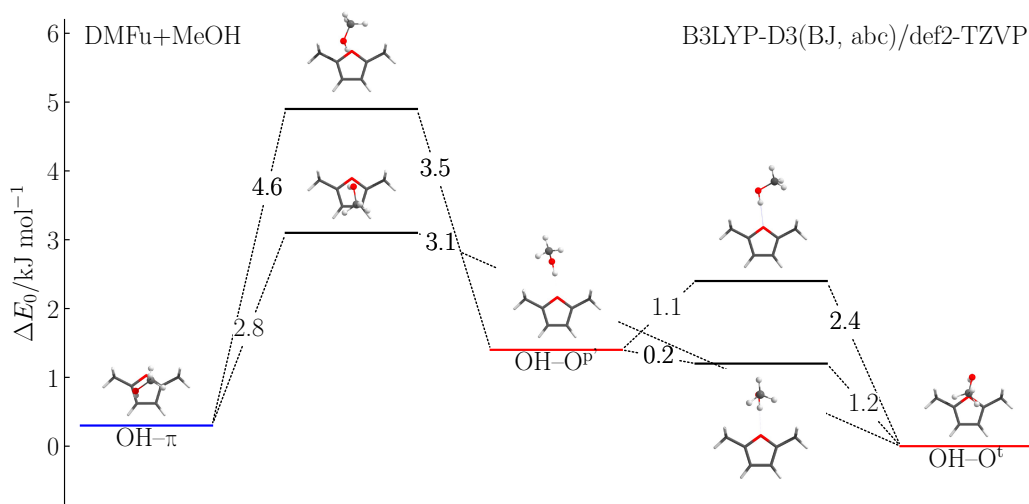


Figure 3.2.6: Calculated transition states (black bars, including harmonic ZPVE for all real modes) for the interconversion of the most stable dimer conformations of 2,5-dimethylfuran–methanol at B3LYP-D3(BJ, abc)/def2-TZVP level.

with an infinite oxygen mass. However, the OD-stretching vibration of the methanol homodimer is further downshifted than this equation would suggest, even after aligning the monomer transitions to compensate for the finite O mass and anharmonic differences in the monomer. Similarly, the OH–O band of the mixed cluster is also further shifted, in contrast to the OH– π band, supporting the assignment. Besides, the proposed trimer band also shows this shift, tentatively hinting for an oxygen-bound conformation. To verify that none of these effects is due to small deviations in the experimental conditions, a spectrum of a 1:2 mixture of MeOH and MeOD has been measured (Fig. 3.2.4 (c)) under more diluted conditions. Both effects are confirmed, the OH– π band being even slightly less shifted than the ideal harmonic shift.

In order to rule out kinetic trapping of the metastable complex, calculations of the barrier height for the interconversion of the most stable conformers have been carried out using the `woelfling` module from `Turbomole` and reoptimizing at B3LYP-D3(BJ, abc)/def2-TZVP level with `ORCA` as described in Sec. 2.6.2. The results are shown in Fig. 3.2.6. Amounting to 2.8 kJ mol^{-1} , the barrier between the OH– π conformer and the global minimum OH–O^t is predicted to be sufficiently low to allow for interconversion in the supersonic expansion.⁵⁰ Thus, kinetic trapping

is unlikely. The relaxation of the OH-OP' conformer into the global minimum is predicted to have no barrier when taking zero-point energy into account. This seems to be a deficiency from treating ZPE only harmonic, rather than a reliable result. Nevertheless, it can be concluded, that the barrier is very shallow when cleaving the alkylic CH-O interaction in favor of a CH- π interaction, pulling down the methanol by the dispersion interactions. A mechanism involving a rotation of the methanol has also been tried, resulting in a barrier height of 1.1 kJ mol⁻¹.

Removing the methyl groups, the qualitative features of the spectrum are conserved, as can be seen in Fig. 3.2.7. The spectra of 2-methylfuran (MFu) with methanol were measured at much lower concentrations. Therefore, uncompensated bands of atmospheric water molecules in the optical path are potentially more problematic. Again, spectra with the pure substances as well as a 1:1 mixture of MeOH and MeOD have been measured. The cluster bands are observed at 3645 cm⁻¹ and 3623 cm⁻¹. Additionally, a small feature at 3617 cm⁻¹ and a band shoulder at 3626 cm⁻¹ can be identified. Both were confirmed by measurements with higher concentrations,⁸² while a shoulder observed in spectrum (d) at 3649 cm⁻¹ is due to water.¹⁵⁷

For the unmethylated furan a spectrum with a 1:2 mixture of methanol and methanol-d1 was measured (Fig. 3.2.7 (a)), averaging as much as 1000 scans because of the low concentration. Furthermore, a spectrum without the deuterated methanol was recorded (Fig. 3.2.7 (b)), revealing the cluster hydride stretching bands at 3654 cm⁻¹ and 3636 cm⁻¹ with increased signal-to-noise ratio. Though the absolute band positions are offset by 20 cm⁻¹, the downshifts of the cluster bands are in good agreement with those observed by matrix isolation spectroscopy.¹³² In the OD region a combination mode of two furan scissoring modes was identified at 2668 cm⁻¹¹⁵², yet there is no overlap with the mixed dimer bands at 2695 cm⁻¹ and 2685 cm⁻¹. In order to obtain a better signal to noise ratio, a spectrum without the deuterated methanol was recorded, while keeping the overall methanol concentration.

Comparing the three acceptors, there is a pair of two bands for every system, shifting further away from the monomer position with methylation. The separation of these bands also increases from 18 cm⁻¹ to 24 cm⁻¹. Upon deuteration, this separation shrinks relative to the absolute shift, the less shifted band shifting slightly

further than the factor of $\sqrt{2}$ and the further shifted band slightly less. This uniform behavior strongly suggests a consistent band assignment. Keeping aside the aforementioned assignment for 2,5-dimethylfuran, in principle three assignments are possible: two π -bound complexes, two oxygen-bound complexes or one of each type. The first two would not evoke a significant change of the relative intensities with deuteration, which would be in agreement with the spectra at very high dilution. However, especially two π -bound complexes are very unlikely. First of all, only for the unsymmetrical case of 2-methylfuran two π -bound structures were found in the geometry optimization. Also, the difference in the spectral shifts seems too large and the opposed band shifting with deuteration would be improbable. For two oxygen-bound clusters this behavior seems more plausible, as at least two OH–O structures were found for each of the three systems, one of OH–O^t and one of OH–O^p or OH–O^{p'} type. The predicted band positions for OH–O^t and OH–O^{p'} are separated enough to match the observed band positions, but the latter was not found as a minimum structure for furan. Assigning different structural types for one band series would conflict the similarity between the three systems. Moreover, the anharmonicity could in principle differ between the two OH–O conformers, but the effect would be expected to be the opposite. The further downshifted band should correspond to the more linear and more anharmonic band, thus showing a larger downshift upon deuteration in resemblance to the homodimer of methanol. Lastly, it would be hard to explain why no OH– π conformer would be present, given the statistical preference for it. Overall, the assignment of one OH–O and one OH– π conformer as proposed for 2,5-dimethylfuran remains the most reasonable.

The OH–O^t conformation being the only oxygen-bound geometry optimized as a minimum structure for all three acceptors, it is the most probable assignment for the less shifted band. This results in a uniform slight underestimation of the spectral downshift and is in agreement with the energetic ordering by calculations at B3LYP-D3(BJ, abc)/def2-TZVP level, except for furan. Since the OH–O^t structure is predicted to be only slightly less stable in this case, and more sophisticated quantum mechanical methods even predict it to be more stable,¹³⁹ the assignment is still conceivable. Microwave experiments by the Schnell group further support this assignment, as the much larger *A* rotational constant of the OH–O^p conformer is inconsistent with observation.⁸² They identified the OH– π as well as the OH–O^t

3 Clusters of Furans and Alkyl Alcohols

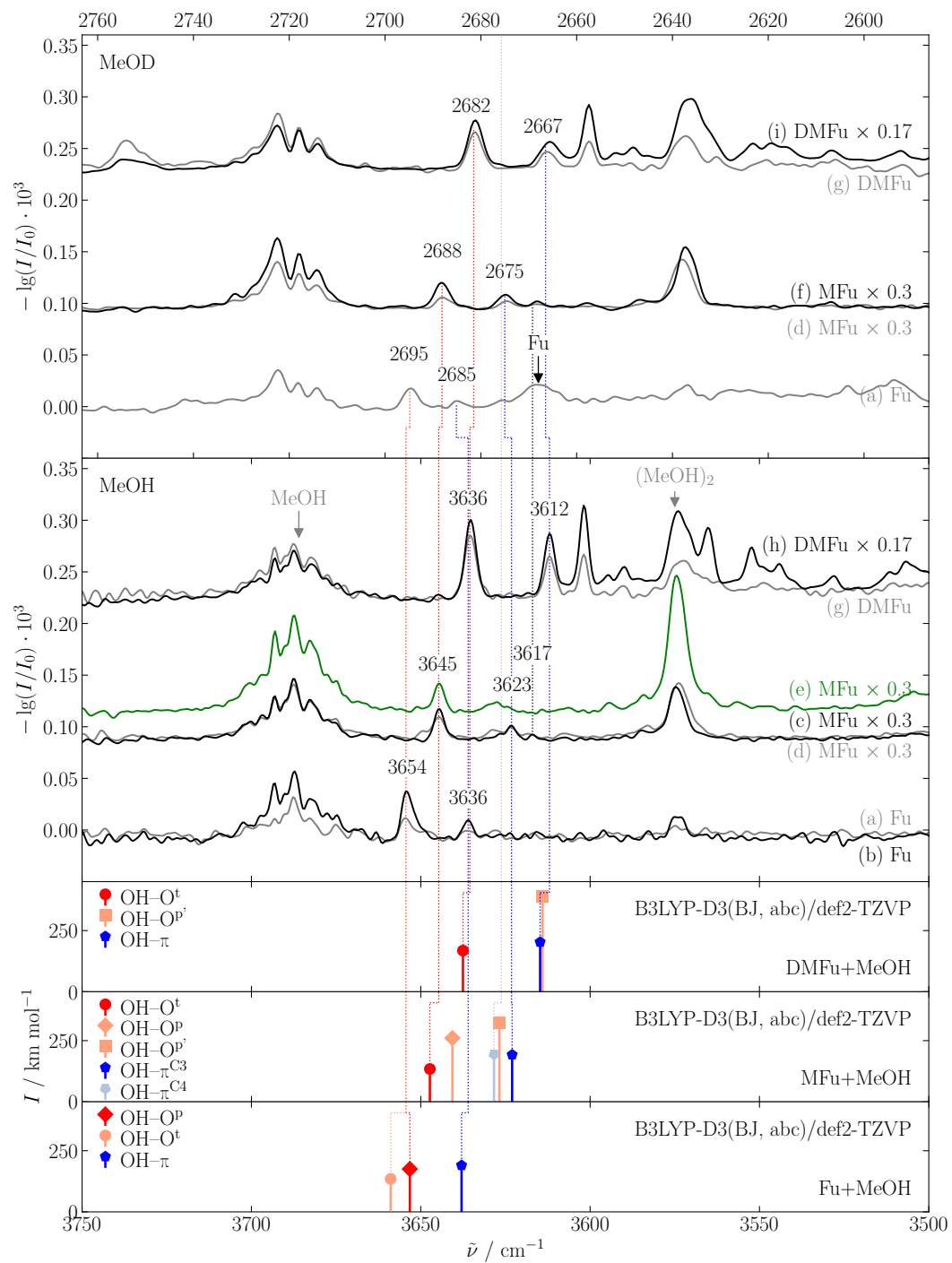


Figure 3.2.7: (Left.) IR Spectra of 2,5-dimethylfuran, 2-methylfuran and furan with methanol compared to theoretical predictions at B3LYP-D3(BJ, abc)/def2-TZVP level. The calculated frequencies are scaled (factor 0.9675) to the experimental MeOH monomer value (3686 cm^{-1}). OH–O conformers are denoted in red, OH– π in blue. Darker colors indicate the most stable conformer of each binding type.

(a) Fu–MeOH/D (Fu: $-28\text{ }^\circ\text{C}$, 0.10/5.1 s, MeOH+MeOD (1:2): $-22\text{ }^\circ\text{C}$, 0.10/7.6 s, helium: 10.2/0.10 s);

(b) Fu–MeOH (Fu: $-28\text{ }^\circ\text{C}$, 0.10/7.4 s, MeOH: $-22\text{ }^\circ\text{C}$, 0.10/7.5 s, helium: 10.1/0.10 s);

(c) MFu–MeOH (MFu: $-28\text{ }^\circ\text{C}$, 0.10/10.2 s, MeOH: $-22\text{ }^\circ\text{C}$, 0.10/10.0 s, helium: 10.1/0.10 s);

(d) MFu–MeOH/D (MFu: $-28\text{ }^\circ\text{C}$, 0.10/2.46 s, MeOH+MeOD (1:1): $-22\text{ }^\circ\text{C}$, 0.10/1.22 s, helium: 10.2/0.10 s);

(e) MFu–MeOH +Ar (MFu: $-28\text{ }^\circ\text{C}$ argon, 0.10/2.52 s, MeOH: $-22\text{ }^\circ\text{C}$, 0.10/1.22 s, helium: 10.2/0.10 s);

(f) MFu–MeOD (MFu: $-28\text{ }^\circ\text{C}$, 0.10/10.3 s, MeOD: $-21\text{--}22\text{ }^\circ\text{C}$, 0.10/9.9 s, helium: 10.1/0.10 s);

(g) DMFu–MeOH/D, same as Fig. 3.2.4 (c) (DMFu: $-10\text{--}20\text{ }^\circ\text{C}$, 0.10–0.50/0.50–5.1 s, MeOH+MeOD (1:2): $-22\text{--}25\text{ }^\circ\text{C}$, 0.10/0.94–7.5 s, helium: 10.2/0.10 s);

(h) DMFu–MeOH, same as Fig. 3.2.4 (a) (DMFu: $-20\text{ }^\circ\text{C}$, 0.95/0.10 s, MeOH: $-25\text{ }^\circ\text{C}$, 0.46/0.49 s);

(i) DMFu–MeOD, same as Fig. 3.2.4 (b) (DMFu: $-20\text{ }^\circ\text{C}$, 1.04/0.10 s, MeOD: $-25\text{ }^\circ\text{C}$, 0.45/0.49 s);

see also Ref. 139,140.

conformer, in agreement with the FTIR data. Furthermore, the analysis of ^{13}C in natural abundance hints to an effective C_s symmetry of the OH–O^t structure. This finding supports the assignment of the OH–O^t conformer to the less shifted band, not only in furan itself, but by analogy also for the methylated derivatives. However, though more unlikely, the presence of other oxygen-bound structures contributing to this band cannot be ruled out, especially taking into account the commonly observed downshift overestimation of oxygen-bound clusters by the B3LYP functional.^{86,158}

Taking a closer look on the OH– π complexes, some ambivalence for the assignment in the 2-methylfuran case is revealed. It is the only acceptor where the distinction between two OH– π structures has to be made. Relying on the energetic ordering, the assigned OH– $\pi^{\text{C}3}$ conformer does not show an underestimation of the downshift at B3LYP-D3(BJ, abc)/def2-TZVP level of theory as for the other two acceptors, contrary to the OH– $\pi^{\text{C}4}$ conformer, which would however be the most underestimated. The energetic difference of 0.8 kJ mol^{-1} is not beyond doubt. More so in the light of the double blind challenge, where two entries using symmetry adapted perturbation theory (SAPT) found the OH– $\pi^{\text{C}4}$ structure as the most stable π -bound conformer.¹³⁹ However, these computational approaches are not among the best per-

Table 3.2.2: OH–O hydrogen bond angles (θ) and shortest (C)H–O distances (d) in Å for the conformers optimized at B3LYP-D3(BJ, abc)/def2-TZVP level.

	OH–O ^t		OH–O ^P		OH–O ^{P'}	
	θ_{OHO}	$d_{\text{H-O}}$	θ_{OHO}	$d_{\text{H-O}}$	θ_{OHO}	$d_{\text{H-O}}$
Furan + MeOH	150°	3.40	146°	2.81	–	–
2-Methylfuran + MeOH	150°	2.70	153°	2.97	165°	2.79
2,5-Dimethylfuran + MeOH	154°	2.95	–	–	170°	3.00

forming results.^{82,139} Furthermore, the shoulder at 3626 cm^{-1} could potentially be caused by the second OH– π conformation, which would also be in better agreement with the corresponding shift underestimation. When adding argon to the expansion mixture, this shoulder is even more pronounced (see Fig. 3.2.7 (e)). However, this could also be due to argon complexation on the opposite side of the furan ring,¹¹² withdrawing electron density and thus weakening the OH– π hydrogen bond. Additionally, the interconversion barrier of the OH– $\pi^{\text{C}4}$ complex to the OH– $\pi^{\text{C}3}$ dimer is predicted as low as 0.1 kJ mol^{-1} and the presence of both conformers seems unlikely. All in all, the OH– $\pi^{\text{C}3}$ conformer remains the more probable assignment for the band at 3623 cm^{-1} . For the small band at 3617 cm^{-1} a plausible explanation would be a trimer origin, similar to the band at 3602 cm^{-1} for 2,5-dimethylfuran. Both bands show a further downshift with deuteration. Therefore, an assignment of this band to an oxygen-bound cluster is most likely. However, the more concentrated spectra have shown, that this band behaves, at least partially, like a dimer.⁸² If so, the most probable assignment would be the OH–O^{P'} dimer, as it is the closest in both relative energy and spectral shift, but the downshift underestimation would be comparably large.

An interesting aspect of these furan–methanol systems is the fact that the oxygen-bound conformers are less downshifted than the π -bound ones. This seems to be less caused by strongly shifted OH– π clusters, but rather only small shifts of the OH–O clusters, due to the strongly bent hydrogen bonds with OH–O angles as low as 150° in the OH–O^t type (see Tab. 3.2.2). The hydrogen bond angles of the OH–O^P conformations are of similar magnitude, though the bending direction differs, laying approximately in the furan plane. The spectral shifts are predicted slightly larger,

Table 3.2.3: Band integral ratios I_O/I_π of the methylated furans with methanol and corresponding energetic difference $\Delta E_0^{\pi-O}$ based on calculations at B3LYP-D3(BJ, abc)/def2-TZVP level; see also Ref. 139.

	Furan	2-Methylfuran	2,5-Dimethylfuran
$I_O/I_\pi(\text{OH})^{139}$	3.3 ± 1.1	2.8 ± 1.5	1.5 ± 0.2
$I_O/I_\pi(\text{OD})^{139}$	3.3 ± 1.0	1.9 ± 0.5	2.1 ± 0.3
$\Delta E_0^{\pi-O}(\text{OH})/\text{kJ mol}^{-1}$	0.8 ± 0.6	0.7 ± 0.6	0.3 ± 0.2
$\Delta E_0^{\pi-O}(\text{OD})/\text{kJ mol}^{-1}$	0.8 ± 0.6	0.5 ± 0.4	0.5 ± 0.4

while the shifts and hydrogen bond angles of the OH–O^p conformations are predicted significantly larger. With methylation the hydrogen bonds appear to be slightly more linear for each structure type. The more bent hydrogen bonds correspond to the more stable conformations, highlighting the importance of the secondary interactions. Apparently, the dispersive methyl– π interaction in the presumably observed OH–O^t conformations wins energetically over the CH–O interactions in the OH–O^p conformations as well as the more linear hydrogen bonds in the OH–O^p conformations. Thus, these systems feature a second intermolecular balance system between CH– π and CH–O interactions.

Concerning the energy difference between the observed conformers, the Boltzmann distribution provides

$$\frac{c_\pi}{c_O} = \frac{g_\pi}{g_O} \exp\left(-\frac{\Delta E_0^{\pi-O}}{RT_c}\right)$$

as a measure of the abundance ratio c_π/c_O .⁸⁸ The symmetry weight ratio g_π/g_O is equal to one, if both isomers have the same symmetry. Substituting the abundance ratio with the experimental band intensities I and the theoretical absorption cross sections σ leads to

$$\Delta E_0^{\pi-O} = RT \ln\left(\frac{g_\pi}{g_O} \frac{\sigma_\pi}{\sigma_O} \frac{I_O}{I_\pi}\right).$$

Given the experimentally observed band integral ratio (see Tab. 3.2.3, details can be found in Ref. 139), the IR cross section ratio computed at B3LYP-D3(BJ, abc)/def2-TZVP level (using the OH–O^t structure) and assuming a conformational temperature of $T_c = (60 \pm 40)$ K an energetic preference for the oxygen-bound conformer by (0.8 ± 0.6) kJ mol⁻¹, (0.7 ± 0.6) kJ mol⁻¹ and (0.3 ± 0.2) kJ mol⁻¹ for furan, 2-methylfuran and 2,5-dimethylfuran, respectively, can be derived. This

conclusion depends on the IR cross sections provided by B3LYP-D3(BJ, abc)/def2-TZVP. Without inclusion of theoretical data and even using IR cross sections provided by anharmonic calculations, the derived energy differences are in qualitative agreement, but the oxygen preference is not certain.¹³⁹ Upon deuteration this oxygen preference is preserved. The stronger oxygen preference with methylation predicted at B3LYP-D3(BJ, abc)/def2-TZVP level of theory is not confirmed in experiment.

The combination of methylated furans with methanol has been shown to be a suitable intermolecular balance for OH–O and OH– π interactions, though the energetic preference remained on the ‘classical’ oxygen-bound side. Attempts to tip the balance to the π side are made in the following sections. For confirming the cluster assignment, especially the deuteration of the donor has been shown to be useful. A relative decrease in the intensity hints at a π -bound conformer, as does a reduced downshift compared to the ideal deuteration value, while oxygen-bound clusters are slightly further downshifted. These two effects can be used as tools for the band assignment of similar clusters.

3.3 π Preference by Enlarging the Alkyl Group

As discussed in the previous section, methylated furan derivatives form clusters of both binding types. However, the oxygen binding remains preferred over π binding. There are many more examples for oxygen-bound cluster formation with a π system present and even a large variety of systems where clusters with both binding sites could be identified.^{38,75,83,159} However, it is more challenging to find systems with a clear π preference despite the presence of oxygen as an intrinsically attractive hydrogen bond acceptor. For diphenyl ether–MeOH the π -bound conformer is more favorable (see Sec. 4 and Ref. 83), but the energy difference is subtle enough (1.8 kJ mol^{-1}) that the presence of the second conformer depends on the experimental conditions. The related case of furan–indole dimer was the first where only the π -bound conformer (NH– π in this case) was identified using IR/UV double resonance, but the energy difference to the other conformers is still subtle ($<0.5 \text{ kJ mol}^{-1}$).³⁷ For substituted anisoles the largest energy difference reported in favor of π binding was 2.4 kJ mol^{-1} (calculated at B3LYP-D3/aVTZ level), where

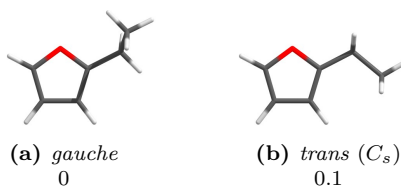


Figure 3.3.1: Monomeric structures and relative ZPVE-corrected energies (ΔE_0) in kJ mol^{-1} of 2-ethylfuran calculated at B3LYP-D3(BJ, abc)/def2-TZVP level.

the oxygen-bound conformer was still detected in the supersonic expansion.¹⁵⁸ Even though a preference for the π binding site has been predicted most probable without methylation of the furan at B3LYP-D3(BJ, abc)/def2-TZVP level, enlarging the alkyl group seems a suitable way to search for clusters showing a clear π preference. Taking 2-methylfuran as a reference, with predictedly almost isoenergetic binding sites, a larger alkyl group could induce a higher electron density in the aromatic ring and thereby tilt the balance towards π coordination. The next sections will explore 2-ethylfuran as well as 2-*tert*-butylfuran as acceptor molecules.

3.3.1 2-Ethylfuran

2-Ethylfuran is the first non-rigid carbon skeleton under study in this thesis. To search for stable conformations, a relaxed scan of the dihedral angle between the C–O bond of the furan and the C–C bond of the ethyl moiety has been carried out from 180° to 0° in steps of 10° . Two almost isoenergetic conformations, *gauche* (60°) and *trans* (180°) have been found and are depicted in Fig. 3.3.1. An early study using LCAO SCF molecular orbital theory was not able to predict this result, as torsional angles between 0° and 90° have not been considered.¹⁶⁰ The conformers are separated by an energy barrier of 4.6 kJ mol^{-1} (ΔE_{el}), thus freezing out of both conformers cannot be ruled out in a supersonic expansion.^{49,50} The barrier for the direct interconversion of the two *gauche* enantiomers is even larger, amounting to 7.9 kJ mol^{-1} . The presence of three monomer conformations (counting the enantiomeric *gauche* conformations as separate conformers, because they make the two furan faces diastereotopic) leads to a large variety of dimers when adding methanol as a hydrogen bond donor, as shown in Fig. 3.3.2. The monomer conformation of the 2-ethylfuran in the cluster is denoted with a *g*, *g'* or *t* subscript. In order to find stable dimer conformations for 2-ethylfuran–methanol, the dimer interaction patterns

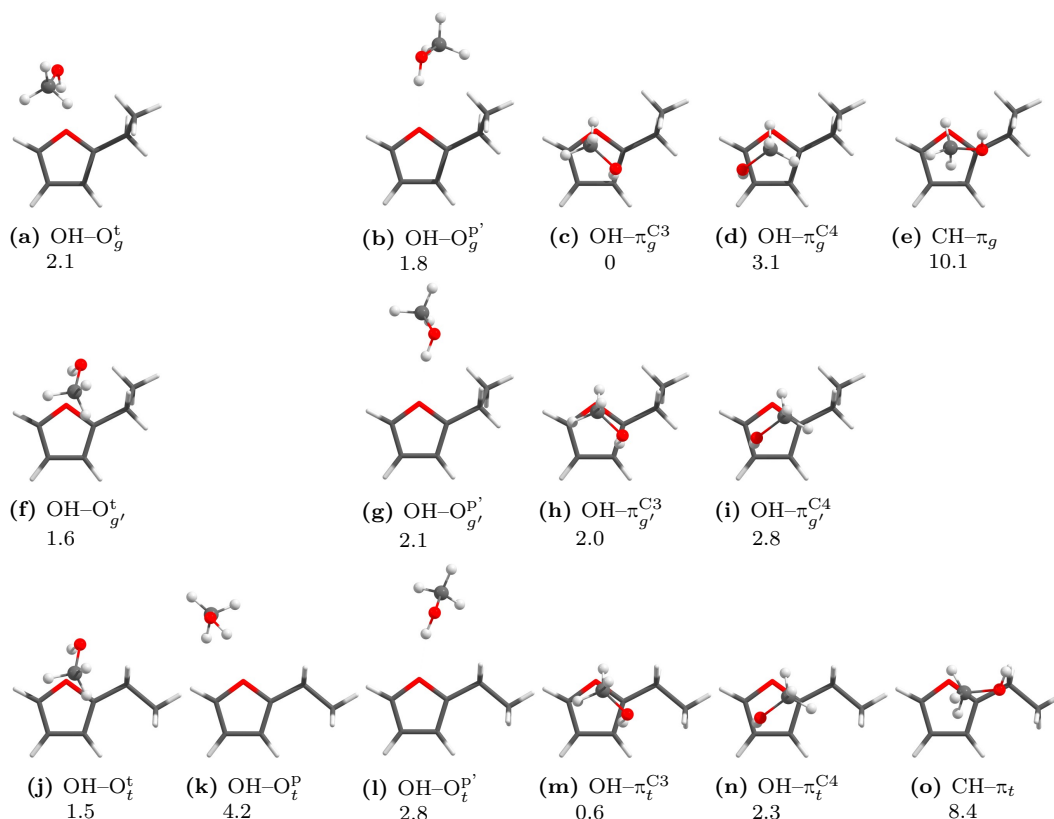


Figure 3.3.2: Structures and relative ZPVE-corrected energies (ΔE_0) in kJ mol^{-1} of the most stable 2-ethylfuran–methanol dimers calculated at B3LYP-D3(BJ, abc)/def2-TZVP level.

of 2-methylfuran–methanol (see Fig. 3.2.1) have been combined with all monomer conformations. The enantiomeric structures of g and g' have been attributed such that the methanol hydroxy group is in front of the furan plane, as established in Sec. 3.1, thus being on the same side as the ethyl moiety for g . The global minimum structure (Fig. 3.3.2e) is a π coordinated one with the 2-ethylfuran monomer in *gauche* conformation (see Tab. 3.3.1). All combinations of π coordination and monomer conformation result in local minima. The $\text{OH}-\pi^{\text{C}3}$ dimers are generally more stable than their counterparts with the methanol hydroxy group directed at the C4 carbon. The smallest difference is predicted for the g' 2-ethylfuran conformation, *i.e.* $\text{OH}-\pi_{g'}^{\text{C}3}$ and $\text{OH}-\pi_{g'}^{\text{C}4}$, due to $\text{OH}-\pi_{g'}^{\text{C}3}$ being disproportionately high in energy compared to the other 2-ethylfuran conformations. An explanation could be the secondary CH–O interaction of the ethyl moiety. It is strongest for $\text{OH}-\pi_g^{\text{C}3}$

3.3 π Preference by Enlarging the Alkyl Group

Table 3.3.1: Dissociation energies of the 2-ethylfuran dimers with (D_0) and without (D_{el}) harmonic zero-point vibrational energy calculated at B3LYP-D3(BJ, abc)/def2-TZVP level in kJ mol^{-1} . Energies relative to the most stable dimer (ΔE_{el} and ΔE_0) are given in kJ mol^{-1} , harmonic OH stretching wavenumbers (ω_{OH}) and shifts ($\Delta\omega_{OH}$) from the corresponding monomer vibrational wavenumber in cm^{-1} , band intensities (I_{OH}) in km mol^{-1} .

	ΔE_{el}	ΔE_0	D_{el}	D_0	ω_{OH}	$\Delta\omega_{OH}$	I_{OH}
2-ethylfuran							
<i>gauche</i>	0	0	–	–	–	–	–
<i>trans</i> (C_s)	0.0	0.1	–	–	–	–	–
2-ethylfuran + MeOH							
OH–O $_g^t$	1.9	2.1	23.6	18.9	3749	61	261
OH–O $_g^p$	1.5	1.8	24.0	19.2	3740	70	358
OH– π_g^{C3}	0	0	25.5	21.0	3738	71	193
OH– π_g^{C4}	3.8	3.1	21.7	17.9	3745	64	196
CH– π_g	11.2	10.1	14.3	10.9	3810	0	27
OH–O $_{g'}^t$	1.6	1.6	23.9	19.4	3766	44	150
OH–O $_{g'}^p$	2.3	2.1	23.2	18.9	3745	65	345
OH– $\pi_{g'}^{C3}$	2.7	2.0	22.8	19.1	3743	67	205
OH– $\pi_{g'}^{C4}$	3.5	2.8	21.9	18.2	3751	58	187
OH–O $_t^t$	1.5	1.5	24.0	19.6	3767	42	138
OH–O $_t^p$	4.6	4.2	20.8	16.8	3762	48	272
OH–O $_t^p$	2.9	2.8	22.6	18.2	3746	63	327
OH– π_t^{C3}	1.2	0.6	24.3	20.4	3735	74	210
OH– π_t^{C4}	3.0	2.3	22.5	18.7	3752	58	178
CH– π_t	9.8	8.4	15.7	12.6	3810	–1	27

with the shortest CH–O distance among the OH– π^{C3} dimers of 2.68 Å. Despite this distance being longer for the *trans* conformer, its energy penalty is rather small, because it interacts in a bifurcated manner with both the CH₂ and CH₃ moieties. In the OH– $\pi_{g'}^{C3}$ structure the closest CH–O distance is 3.23 Å (similar to the OH– π^{C3} structure of 2-methylfuran–methanol (3.16 Å) see Sec. 3.2) and thus least favorable. The directed secondary interaction in the OH– π_g^{C3} conformer also seems to have an effect on the zero-point energy, as all other π -bound structures profit by 0.7 kJ mol^{-1} when adding ZPE relative to the OH– π_g^{C3} conformer, see Tab. 3.3.1. To a smaller degree this influence of the alkyl group is also observed for the OH–O^t conformers. In the *g* conformation the CH–O interaction is provided by the CH₃

moiety of 2-ethylfuran, opposed to the g' and t conformations, where a hydrogen of the CH_2 moiety is closest. Thereby, the methanol CH_3 group is tilted away from the ethyl moiety in OH-O_g^t and ZPE disfavors this conformer slightly, analogous to the $\text{OH-}\pi^{\text{C}3}$ conformations. The OH-O^p conformations are the least systematic. Again, the g conformation differs from the other two, first in energy sequence of the oxygen-bound conformers and second in ZPE disfavoring this complex. g' and t are more similar in this regard, despite the methanol CH_3 group pointing in opposite directions. The *trans* configuration is the only one where a OH-O^p structure was found to be stable, but its energy is the highest among the oxygen- and π -bound clusters. As test cases, two conformers with $\text{CH-}\pi$ interactions have been computed, but were found to be uncompetitive. Overall, the computed energy difference between the most stable π - and oxygen-bound conformers amounts to 1.5 kJ mol^{-1} in favor of π binding. Thus, both coordination types are probable to be observed in experiment.

Fig. 3.3.3 shows the FTIR spectra of the 2-ethylfuran–methanol mixture measured with the *filet-jet*. The aromatic CH stretching modes of 2-ethylfuran are observed at 3162 cm^{-1} and 3127 cm^{-1} , the alkylic CH stretching modes overlap with those of methanol (see also Fig. E.1). Most likely, the broader band at 3127 cm^{-1} results from two asymmetric and the one at 3162 cm^{-1} from the symmetric stretching vibration. Three mixed cluster bands are present at 3616 cm^{-1} , 3629 cm^{-1} and 3643 cm^{-1} in the OH stretching region. With the large variety of clusters within 3 kJ mol^{-1} energy difference, the assignment of those bands is rather difficult and ambiguous. Comparing to the spectrum of 2-methylfuran–methanol (Fig. 3.3.3 (c)), the least shifted band can be assigned to an oxygen-bound cluster, as the band positions differ by only 2 cm^{-1} . Furthermore, compared to the analogous OH-O^t dimer of 2-methylfuran–methanol (see Fig. 3.2.7) a slight underestimation of the downshift prediction of the most stable OH-O structure (OH-O_t^t) also compares well. The other two bands fall within the region of the observed frequencies for the π -bound complexes of the methylated furans with methanol (3636 cm^{-1} to 3612 cm^{-1}), however they are more difficult to assign, regarding the overlap of the predictions for the oxygen and π -bound clusters of 2-ethylfuran. Additionally, a shoulder at the higher wavenumber side of the methanol dimer band is observed. As no dimer bands are predicted in this region, and methanol trimer is also present in the expansion,

3.3 π Preference by Enlarging the Alkyl Group

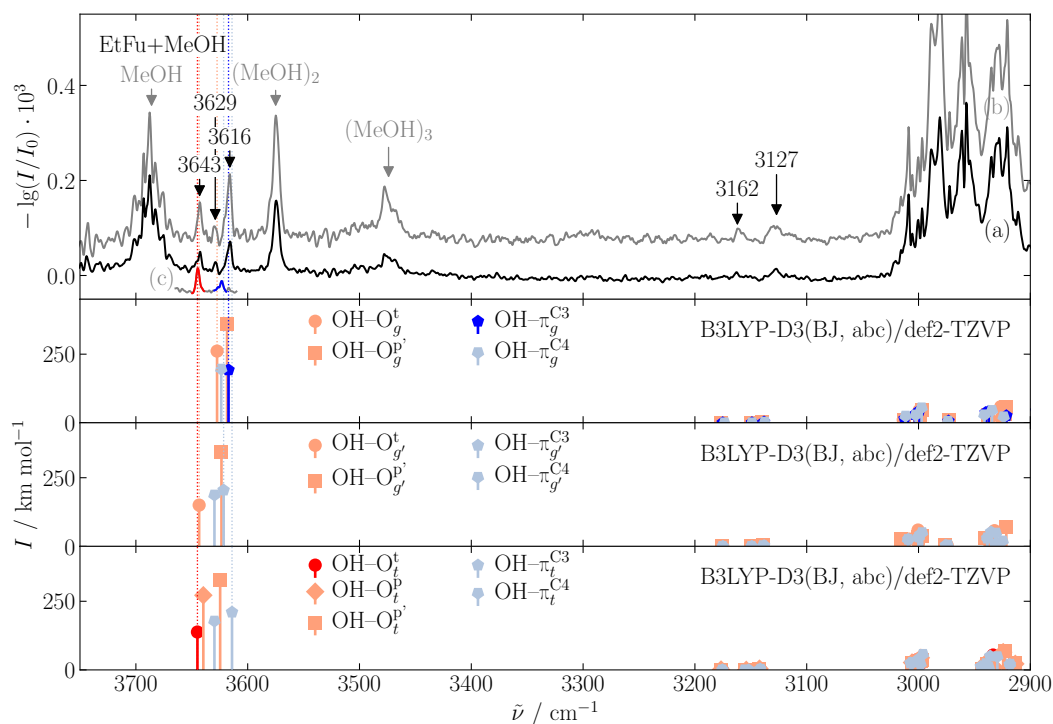


Figure 3.3.3: IR Spectra of 2-ethylfuran with methanol compared to theoretical predictions at B3LYP-D3(BJ, abc)/def2-TZVP level. The calculated frequencies are scaled (factor 0.9675) to the experimental MeOH monomer value (3686 cm^{-1}). OH-O conformers are denoted in red, OH- π in blue. Darker colors indicate the most stable conformer of each binding type.

(a) low methanol concentration (EtFu: $-28\text{ }^\circ\text{C}$, 0.10/5.20 s, MeOH: $-22\text{ }^\circ\text{C}$, 0.10/9.80 s, helium: 10.0/0.10 s);

(b) higher methanol and overall concentration (EtFu: $-28\text{ }^\circ\text{C}$, 0.10/5.16 s, MeOH: $-22\text{ }^\circ\text{C}$, 0.10/4.84 s, helium: 5.12/0.10 s);

(c) 2-methylfuran-methanol, same as Fig. 3.2.7 (c) (MFu: $-28\text{ }^\circ\text{C}$, 0.10/10.2 s, MeOH: $-22\text{ }^\circ\text{C}$, 0.10/10.0 s, helium: 10.1/0.10 s).

it is most likely due to a trimer consisting of one 2-ethylfuran and two methanol molecules. This indicates the additional possibility of overlapping trimer bands.

Three types of barrier heights have to be taken into account for the assignment: The interconversion of the 2-ethylfuran monomer conformations, the barrier heights for the interconversion of OH–O and OH– π binding types and of the same binding type within the same 2-ethylfuran conformation (t , g and g'). The latter is expected to be sufficiently low to be overcome in the supersonic expansion, as no two conformers of the same binding type have been explicitly observed for the methylated furans in the preceding section. Thus, up to six different clusters would be present in the spectrum. The number of observed dimers might be lower if oxygen– π -relaxation within one monomer conformation is possible. Furthermore, the added methanol might influence the interconversion of the 2-ethylfuran conformations and relaxation between the g and g' structures, especially for the oxygen-bound clusters, could potentially be present.

The bands of all OH– π dimers could overlap to form the band at 3616 cm^{-1} , which would also explain the shoulder at higher wavenumber. The band at 3643 cm^{-1} can be assigned to the OH–O ^{t} dimers of t and g' . Again, a small shoulder is observed at higher frequencies, hinting at a band overlap. The oxygen-bound dimer of g is the most ambiguous. The smaller band in between at 3629 cm^{-1} fits well with the OH–O ^{g} structure, but as the OH–O ^{g'} structure is predicted more stable and the shift would be in reasonable agreement, an assignment to this structure would also be plausible. Keeping in mind the microwave results for furan–methanol (see Sec. 3.2), the predicted frequency was more reliable for the IR band assignment than the relative energy, which would support an assignment of the OH–O ^{g} conformer to the band at 3629 cm^{-1} . Keeping aside this weak band, a rough picture analogous to other furan–methanol complexes emerges: 2 OH–O conformations at higher wavenumber and 2–3 OH– π conformations at lower wavenumber. As the IR visibility of the relevant π structures is slightly higher, a roughly similar population of both docking types can be concluded from experiment. The computed energy difference of 1.5 kJ mol^{-1} between the overall most stable oxygen (OH–O ^{t}) and π -bound (OH– π ^{$C3$}) dimers, see Tab. 3.3.1, is in reasonable agreement given that the stability of the π conformations tends to be overestimated.⁸⁶

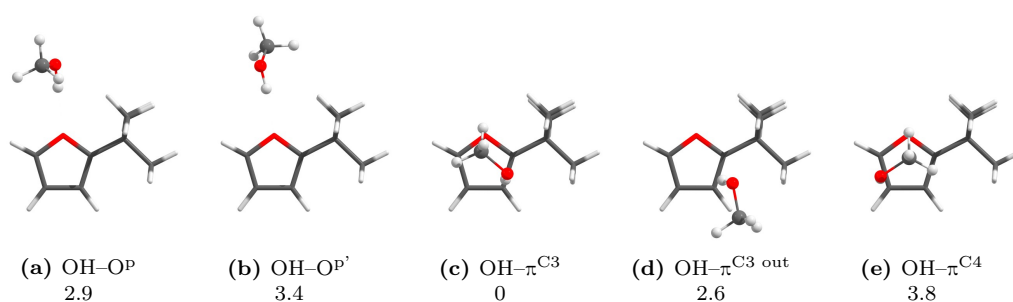


Figure 3.3.4: Structures and relative ZPVE-corrected energies (ΔE_0) in kJ mol^{-1} of the most stable 2-*tert*-butylfuran-methanol dimers calculated at B3LYP-D3(BJ, abc)/def2-TZVP level.

However, all conclusions largely depend on the abundance of the 2-ethylfuran monomer conformations in the supersonic expansion and the relaxation processes, which might also be influenced by the cluster formation. As long as there is no measure for the abundance of the monomer conformations (*e.g.* from the investigation of the monomer fingerprint spectrum in the jet), the significance of the conclusions drawn from these spectra remains limited. Quantum mechanical calculations for the barrier heights would also be desirable. Nevertheless, the general picture is in good agreement with the previous observations and thus substantiates them, but the large variety of conformations prevents a more quantitative analysis inhibiting the use as a benchmarking system.

3.3.2 2-*tert*-Butylfuran

The predicted π preference is even larger for 2-*tert*-butylfuran as the acceptor. It has one stable monomer conformation with a methyl group in *trans* configuration to the oxygen atom, which was confirmed by a scan of the dihedral angle from 180° to 0° in steps of 10° . The rotation barrier for the *tert*-butyl moiety was calculated to be 7.9 kJ mol^{-1} . In case of methanol as a hydrogen bond donor π -coordination is predicted to be 2.9 kJ mol^{-1} more stable than the most favorable OH-O conformer. For *tert*-butyl alcohol the energy difference amounts to as much as 4.3 kJ mol^{-1} (see Tab. 3.3.2). These two systems are thus promising to tilt the molecular balance to OH- π docking and can thus serve as a test for the limiting case of pure π coordination. The outcome is not trivial as evidenced by molecular scales between

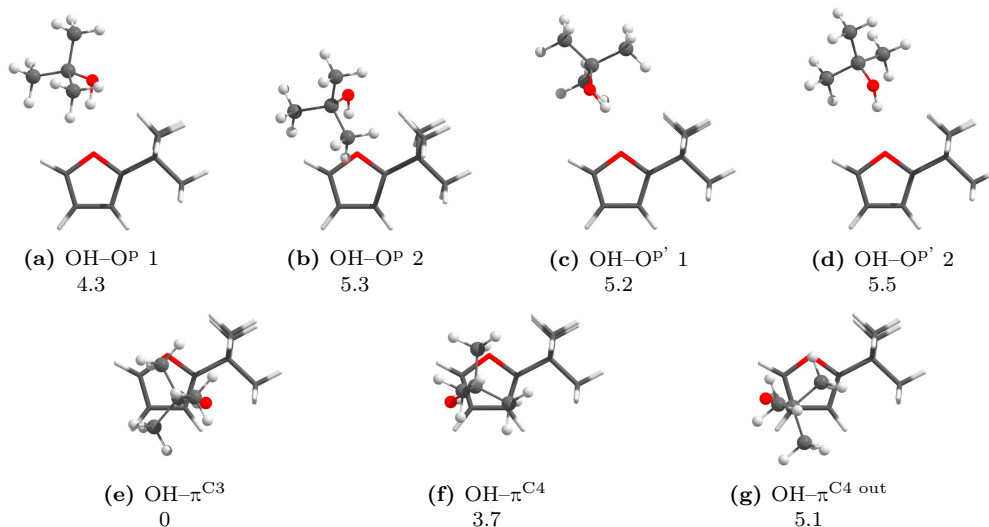


Figure 3.3.5: Structures and relative ZPVE-corrected energies (ΔE_0) in kJ mol^{-1} of the most stable dimers of *tert*-butanol and 2-*tert*-butylfuran calculated at B3LYP-D3(BJ, abc)/def2-TZVP level.

Table 3.3.2: Dissociation energies of the 2-*tert*-butylfuran dimers with (D_0) and without (D_{el}) harmonic zero-point vibrational energy calculated at B3LYP-D3(BJ, abc)/def2-TZVP level in kJ mol^{-1} . Energies relative to the most stable dimer (ΔE_{el} and ΔE_0) are given in kJ mol^{-1} , harmonic OH stretching wavenumbers (ω_{OH}) and shifts ($\Delta\omega_{OH}$) from the corresponding monomer vibrational wavenumber in cm^{-1} , band intensities (I_{OH}) in km mol^{-1} ; see also Ref. 82,88. Conformers used for further analysis in Sec. 6 are marked in bold.

Dimer	ΔE_{el}	ΔE_0	D_{el}	D_0	ω_{OH}	$\Delta\omega_{OH}$	I_{OH}
2-<i>tert</i>-butylfuran + MeOH							
OH-OP	2.9	2.9	24.0	19.4	3741	68	341
OH-OP'	3.3	3.4	23.5	18.9	3740	69	377
OH-π^{C3}	0	0	26.8	22.3	3733	77	205
OH- $\pi^{C3 out}$	3.2	2.6	23.7	19.7	3722	88	248
OH- π^{C4}	4.5	3.8	22.3	18.5	3740	69	220
2-<i>tert</i>-butylfuran + <i>t</i>-BuOH							
OH-OP 1	4.6	4.3	25.0	21.0	3729	56	287
OH-OP 2	5.1	5.3	24.4	20.0	3742	43	226
OH-OP' 1	5.9	5.2	23.6	20.0	3741	44	274
OH-OP' 2	5.9	5.5	23.7	19.8	3730	55	314
OH-π^{C3}	0	0	29.5	25.2	3707	79	219
OH- π^{C4}	4.2	3.7	25.3	21.6	3724	62	205
OH- $\pi^{C4 out}$	6.0	5.1	23.5	20.1	3721	64	234

two π acceptors, where the applied level of theory may have failed by as much as 1.7 kJ mol^{-1} (see Sec. 6.2).¹⁶¹

The pronounced stability of the π -bound complex is the result of a favorable interplay between three intermolecular interactions. The combination of a primary hydrogen bond with a cooperative secondary CH–O interaction between the *tert*-butyl moiety of the acceptor and the oxygen atom of the donor can be found with both coordination types (see Fig. 3.3.4 and Fig. 3.3.5). The distances from the oxygen atom of the alcohol to the closest hydrogen atom of 2-*tert*-butylfuran are also comparable: 2.64 \AA for OH– $\pi^{\text{C}3}$ and 2.61 \AA for OH–O^P 1 in case of *tert*-butyl alcohol, respectively, even more so for methanol as a donor with an O–H distance of 2.66 \AA for both conformers. Unexpectedly, an additional stabilizing interaction of the alkyl group of the donor with the furan π system seems only possible in the OH– π conformations. Optimizing OH–O^t structures for *tert*-butyl alcohol converged into several other OH–O^P conformers varying in the OH–O angle from 169.98° to 171.98° , the former being the most stable and hence the one shown in Fig. 3.3.5. OH–O^t structures with methanol also converged to the OH–O^P conformer. This indicates a very shallow potential energy surface for the oxygen-bound conformer, which might lead to a less localized hydrogen bond compared to the well embedded OH– $\pi^{\text{C}3}$ hydrogen bond. This may switch the rigidity of the structural types compared to the methylated furans, where the π binding site has the more localized hydrogen bond, as indicated by the difference in zero-point energy (see Tab. F.2). A deuteration experiment as described in Sec. 3.2 might hence be more ambiguous to interpret.

Two spectra with different methanol concentrations (spectrum (a) containing more methanol than spectrum (b)) have been measured using the *filet*-jet for the 2-*tert*-butylfuran–methanol mixture and are shown in Fig. 3.3.6. The results have been published in Ref. 88. There is only one mixed cluster band visible at 3612 cm^{-1} , which can be unambiguously assigned to the OH– $\pi^{\text{C}3}$ dimer, as neither of the two spectra show hints at the presence of a second conformer. The predicted energy difference of 2.6 kJ mol^{-1} to the next conformer is large enough not to expect a second conformer in the experiment. Furthermore, the predicted shift of the OH– $\pi^{\text{C}3}$ conformer fits well to the values for the methylated furan derivatives. The fact that the band is still observed in the more diluted expansion, even though methanol trimer is not, excludes a mixed trimer contribution. A deuteration experiment could

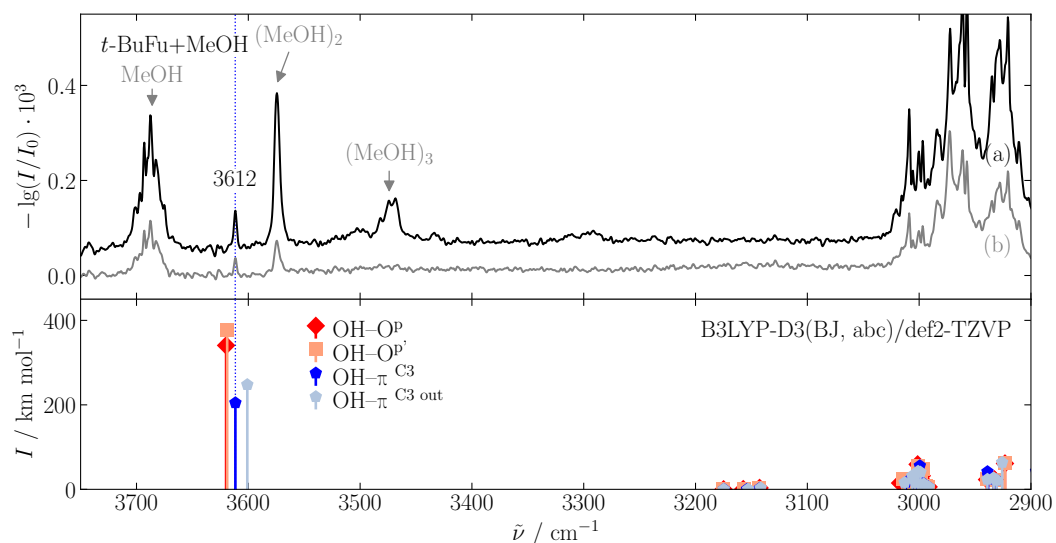


Figure 3.3.6: IR Spectra of 2-*tert*-butylfuran with methanol compared to theoretical predictions at B3LYP-D3(BJ, abc)/def2-TZVP level. The calculated frequencies are scaled (factor 0.9675) to the experimental MeOH monomer value (3686 cm^{-1}). OH-O conformers are denoted in red, OH- π in blue. Darker colors indicate the most stable conformer of each binding type. (a) high methanol concentration (*t*-BuFu: $-25\text{ }^{\circ}\text{C}$, 0.10/1.14 s, MeOH: $-25\text{ }^{\circ}\text{C}$, 0.10/0.96 s, helium: 10.4/0.10 s); (b) reduced methanol concentration (*t*-BuFu: $-25\text{ }^{\circ}\text{C}$, 0.10/1.14 s, MeOH: $-25\text{ }^{\circ}\text{C}$, 0.10/3.00 s, helium: 10.4/0.10 s); see also Ref. 88.

further substantiate the assignment, but was omitted in favor of a measurement with *tert*-butyl alcohol, given the already quite clear assignment and the costly chemicals.

A similar spectrum is observed for the 2-*tert*-butylfuran-*tert*-butyl alcohol mixture, shown in Fig. 3.3.7 (see also Ref. 82). The bands at 3642 cm^{-1} and 3497 cm^{-1} are the monomer and dimer band of *tert*-butyl alcohol, respectively.¹⁶² A negative band marked with an asterisk is due to poorly compensated bands of atmospheric water. The spectrum also shows two small bands at 3128 cm^{-1} and 3132 cm^{-1} which can be assigned to the aromatic C-H stretching modes of the 2-*tert*-butylfuran. They are within noise level in the spectra of the 2-*tert*-butylfuran-methanol mixture. Measuring a spectrum of the pure 2-*tert*-butylfuran for verification was also omitted. Again, only one mixed cluster band is observed at 3565 cm^{-1} . The assignment to the OH- $\pi^{\text{C}3}$ dimer is even more obvious, as both the calculated energy

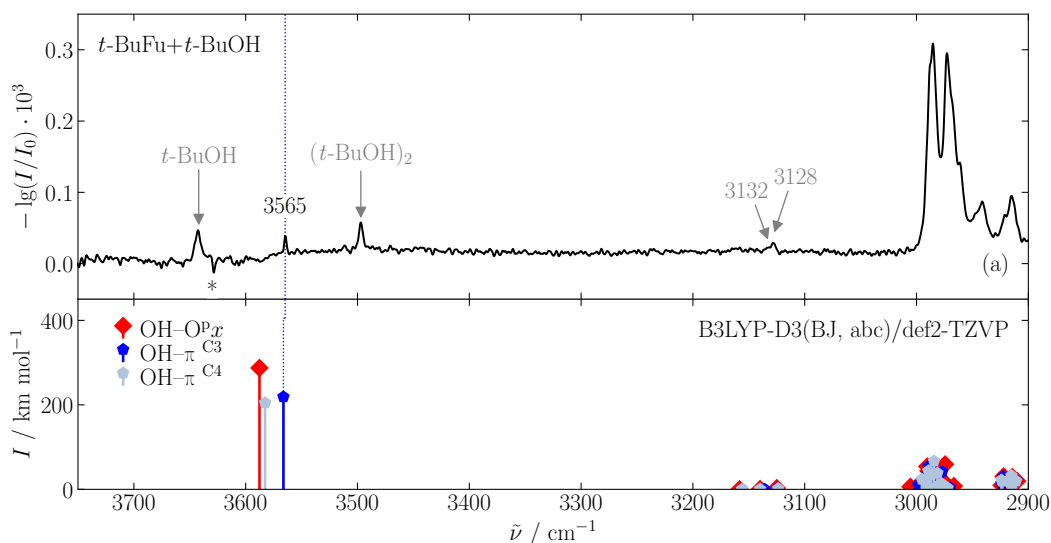


Figure 3.3.7: IR Spectra of 2-*tert*-butylfuran with *tert*-butyl alcohol compared to theoretical predictions at B3LYP-D3(BJ, abc)/def2-TZVP level. The calculated frequencies are scaled (factor 0.9621) to the experimental *t*-BuOH monomer value (3642 cm^{-1}). OH-O conformers are denoted in red, OH- π in blue. Darker colors indicate the most stable conformer of each binding type.

(a) (*t*-BuFu: $-25\text{ }^{\circ}\text{C}$, 0.10/1.14 s, *t*-BuOH: $-10\text{ }^{\circ}\text{C}$, 0.10/3.00 s, helium: 10.4/0.10 s); the asterisk marks a poorly compensated band of atmospheric water; see also Ref. 82.

difference and the spectral shift between O- and π -bound conformers are larger than in the methanol case.

The measurement of these two systems enhances the reliability of benchmarking approaches like sigmoidal Boltzmann plots^{88,158} and frequency shift correlation (see Sec. 6.2) by extending the data space to the whole range of energy preferences. The observation of only one conformer indicates an energy difference of at least 1 kJ mol^{-1} between the docking sites, in consistency with the predictions. Furthermore, it rules out kinetic trapping.⁸⁸

3.4 Annulated Benzene: 2,3-Benzofuran and Dibenzofuran

Attempting to find more cluster systems where π binding is preferred over oxygen binding, the π system of the acceptor has been extended by annulating benzene

rings. This offers a third binding site to hydrogen bond donors, as the enlarged π system can be distinguished between the furan ring ($\pi 5$) and the benzene ring ($\pi 6$) acceptor sites.

3.4.1 2,3-Benzofuran

2,3-Benzofuran, also known as coumarone, is a C_s -symmetric heterocycle. Its planar structure has been confirmed by rotational spectroscopy.^{52,163} Because of its extended π system it is accessible to UV spectroscopy.¹⁶⁴ Its complexation was investigated in a theoretical study for the homodimer,¹⁶⁵ while exciplexes with other aromatic molecules were studied by different UV techniques.¹⁶⁶ Clusters of 2,3-benzofuran with water and methanol have been studied by Sasaki *et al.* using fluorescence-detected infrared spectroscopy and dispersed fluorescence spectroscopy.³⁸ For each donor molecule they observed two clusters, one bound *via* the oxygen atom and one *via* the benzene ring. The assignment was confirmed by applying dispersed fluorescence spectroscopy and comparing the intermolecular vibrational modes to calculated stick spectra. However, the frequency ordering of the bands, the π -bound complex being more downshifted than the oxygen-bound one, was unconventional and worth verifying with linear FTIR spectroscopy. Furthermore, a conformer displaying binding to the π system of the furan ring has not been discussed. Hence, a new conformational search of the 2,3-benzofuran–methanol cluster has been carried out. The results presented in this section have already been published in Ref. 140.

Three oxygen-bound conformers were found for the 2,3-benzofuran–methanol dimer (Fig. 3.4.1): one OH–O^t and two OH–O^p conformers. Each of the three has a secondary interaction, tilting the hydrogen bond from a linear arrangement. The interaction of the methyl moiety with the π system results in an energy ranking of the OH–O^t conformer between the other two (see Tab. 3.4.1), which differ by the aromatic hydrogen (furan or benzyl) that is involved in the secondary CH–O interaction. As the CH–O distance is smaller for the benzyl hydrogen (2.65 Å) than the furan hydrogen (2.78 Å), it results in the most stable oxygen-bound conformation. The other oxygen-bound conformations are each about 1 kJ mol⁻¹ higher in energy. Comparing the CH–O interaction to a screening of crystallographic data for CH–O contacts by Veljković *et al.*¹⁶⁷, a C–H–O angle of 125.5° for OH–O^{p6} is generally

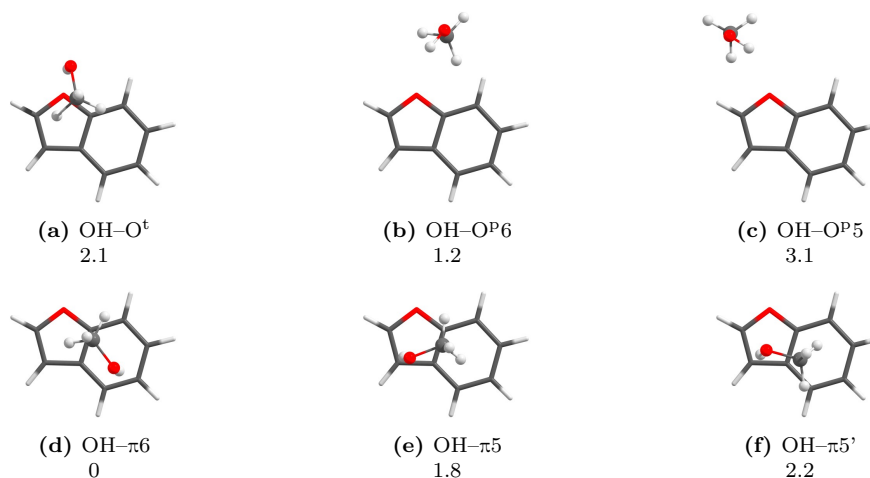


Figure 3.4.1: Structures and relative ZPVE-corrected energies (ΔE_0) in kJ mol^{-1} of the most stable dimers of 2,3-benzofuran and methanol calculated at B3LYP-D3(BJ, abc)/def2-TZVP level; see also Ref. 140.

Table 3.4.1: Dissociation energies of the 2,3-benzofuran dimers with (D_0) and without (D_{el}) harmonic zero-point vibrational energy calculated at B3LYP-D3(BJ, abc)/def2-TZVP level in kJ mol^{-1} . Energies relative to the most stable dimer (ΔE_{el} and ΔE_0) are given in kJ mol^{-1} , harmonic OH stretching wavenumbers (ω_{OH}) and shifts ($\Delta\omega_{\text{OH}}$) from the corresponding monomer vibrational wavenumber in cm^{-1} , band intensities (I_{OH}) in km mol^{-1} ; see also Ref. 140. Conformers used for further analysis in Sec. 6 are marked in bold.

Dimer	ΔE_{el}	ΔE_0	D_{el}	D_0	ω_{OH}	$\Delta\omega_{\text{OH}}$	I_{OH}
2,3-benzofuran + MeOH							
OH-O ^t	1.7	2.1	21.2	17.4	3780	30	139
OH-OP6	0.0	1.2	23.0	18.3	3766	43	197
OH-OP5	2.6	3.1	20.4	16.4	3774	35	213
OH-π6	0	0	23.0	19.5	3776	34	137
OH-π5	1.5	1.8	21.4	17.7	3768	42	140
OH-π5'	1.9	2.2	21.1	17.3	3771	38	134
2,3-benzofuran + MeOD							
OH-O ^t	1.7	1.8	21.2	17.8	2750	23	80
OH-OP6	0.0	0.8	23.0	18.9	2741	32	115
OH-OP5	2.6	2.8	20.4	16.9	2747	26	126
OH-π6	0	0	23.0	19.7	2749	25	82
OH-π5	1.5	1.7	21.4	18.0	2742	31	83
OH-π5'	1.9	2.1	21.1	17.6	2745	28	80

in good agreement. The angle of 109.1° for OH–OP5, however, has not been considered as a sign of CH–O interaction in that study. The possibility of simultaneous hydrogen bonding has only been analyzed for chlorine as an acceptor, for which the C–H–O angle tends to be larger. The CH–O interaction of the model system benzene and methanol has been theoretically determined to amount to 6.8 kJ mol^{-1} in that study (MP2/cc-pVTZ). It is thereby of similar magnitude as the interaction of the methyl group with the aromatic ring, for which the interaction energy of methane and benzene can serve as a model. Its value of 4 kJ mol^{-1} has been experimentally determined using mass analyzed threshold ionization (MATI).¹⁶⁸

Concerning the π -bound conformers, three structures were found as well. The OH– π 6 conformer has the methanol bound to the benzene ring and is the most favorable π conformation. The preference for benzene over furan binding also reflects in the calculated binding energies of methanol to the separate rings ($D_0(\text{furan}) = 15.7 \text{ kJ mol}^{-1}$ (see Tab. 3.2.1) *versus* $D_0(\text{benzene}) = 17.3 \text{ kJ mol}^{-1}$). The two conformers for the OH– π 5 structure do not vary by the carbon atom the hydroxy group is directed to as in case of the methylated furan derivatives, but by the hydrogen atom of the methyl moiety which is more interacting with the benzene π system (see Fig. 3.4.1). A geometry optimization of an initial structure with the methanol pointing at the C3 atom converts to the OH– π 6 conformer.

The cluster has been studied using the *filet*-jet. A spectral overview of the OH and CH stretching regions is given in Fig. 3.4.2. The spectrum of the pure 2,3-benzofuran has been measured in the liquid and gas phase previously by Collier *et al.*^{169,170} and assigned by Singh.¹⁷¹ The observed band positions in Fig. 3.4.2 (d) (see also Fig. E.1) of 3049 cm^{-1} , 3068 cm^{-1} , 3078 cm^{-1} and 3097 cm^{-1} are in good agreement with the assignment to the CH stretching vibrations ν_6 to ν_3 , which correspond to the CH stretching of the benzene ring. Furthermore, the symmetric and antisymmetric stretching of the furan CH bonds are visible at 3160 cm^{-1} and 3126 cm^{-1} , respectively, in accordance with Ref. 170. Two smaller bands are observed at 3107 cm^{-1} and 3085 cm^{-1} , which have not been reported previously. The latter could correspond to the overtone of ν_9 , whose fundamental has been observed at 1543 cm^{-1} in a gas-phase Raman spectrum.¹⁷⁰

Spectrum (a) of Fig. 3.4.2 shows a relatively concentrated mixture of 2,3-benzofuran and methanol in helium. In the dimer region two distinct bands are

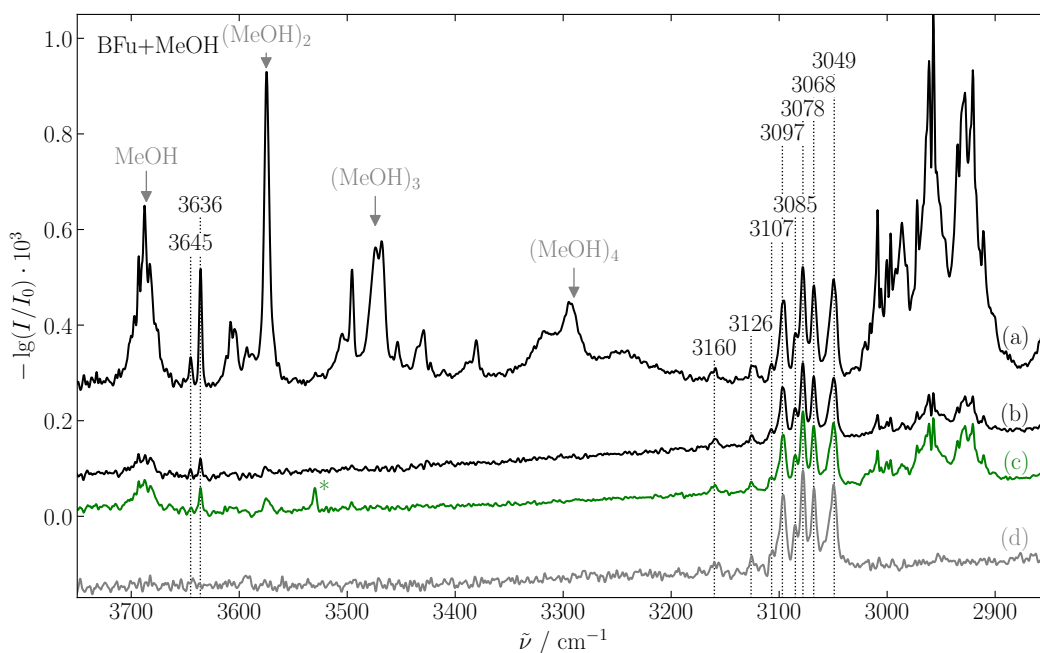


Figure 3.4.2: IR Spectra of 2,3-benzofuran with methanol.

- (a) high concentration (BFu: 20 °C, 1.00/0.10 s, MeOH: -20 °C, 0.10/0.94 s);
 (b) reduced methanol concentration (BFu: 10 °C, 1.00/0.10 s, MeOH: 0.05 % in helium, 0.50/0.47 s);
 (c) acetone added (BFu: 10 °C, 1.00/0.10 s, MeOH: 0.05 % in helium, 0.51/0.46 s, acetone: -20 °C, 0.10/10.0 s once every 10 Scans), the asterisk marks the acetone-methanol band;
 (d) pure 2,3-benzofuran (BFu: 10 °C);
 see also Ref. 140.

observed at 3636 cm^{-1} and 3645 cm^{-1} among broader spectral features possibly attributed to larger clusters. To confirm the dimer origin, much more diluted conditions have been chosen (Fig. 3.4.2 (b)). The fact that both bands are still visible, even though the methanol dimer signal is almost reduced to noise level, verifies the dimer assignment. Regarding the relative stability of the corresponding clusters, a first hint is given by the stronger absorption of the further downshifted band, indicating a larger abundance of the corresponding cluster. More evidence comes from a spectrum, with an added portion of acetone (Fig. 3.4.2 (c)), which has otherwise similar conditions as spectrum (b). Here, the already smaller band is suppressed to noise level. The acetone may act as a better collisional cooling agent in a similar way as argon (see also Sec. 3.2). Furthermore, a relaxation process is

conceivable, where acetone serves as an intermediate binding partner in a solvent exchange mechanism.^{51,172} The band at 3636 cm^{-1} therefore corresponds to the most stable dimer.

For the cluster type assignment spectrum (a) from Fig. 3.4.2 is enlarged and compared to theory in Fig. 3.4.3. The less shifted band has been assigned to the OH–O complex by Sasaki *et al.*³⁸ The band position predicted at the B3LYP-D3(BJ, abc)/def2-TZVP level shows a very good agreement in this case. However, for the OH– π complex, the spectral downshift is underestimated by 13 cm^{-1} . Since this OH– π complex is bound to the benzene ring rather than the furan, this difference to the previously discussed furan OH– π complexes is conceivable. A similar underestimation has been observed in the related OH– π clusters of anisole derivatives (cf. Sec. 6.2).¹⁵⁸ Interestingly, this leads to a crosswise assignment of the predicted and the observed dimer bands.

To confirm this unusual prediction, a deuteration experiment has been carried out. The result is shown in the upper part of Fig. 3.4.3, where two spectra of the deuterated complex are plotted, such that the MeOD monomer band is vertically aligned to the MeOH monomer band and the scale is multiplied by factor $\sqrt{2}$ to account for the harmonic deuteration shift. The two mixed cluster bands are observed at 2688 cm^{-1} and 2684 cm^{-1} , respectively. As described in Sec. 3.2, there are two spectral features changing with deuteration. First, the intensity of the further downshifted band is decreasing relatively to the other, hinting at an OH– π assignment. Secondly, the band positions are closer together, which can be associated with a difference in the anharmonicities of the two clusters. As the band at 3645 cm^{-1} is shifted in the same direction as the methanol dimer with deuteration, it is likely that the clusters are somewhat similar in nature, confirming the OH–O assignment.

There is no spectral evidence for an OH– π cluster bound to the furan ring, even though it is predicted to be only 0.6 kJ mol^{-1} less stable than the OH–O complex. Disregarding the assignment by Sasaki *et al.* and comparing to the previously discussed furan clusters, a contribution of this OH– π 5 conformer to the band at 3645 cm^{-1} seems plausible, but the deuteration experiment should have led to a separation of the bands. A pure OH– π 5 assignment of this band would also contradict the different anharmonic behavior. Furthermore, the disfavoring relative to the OH– π 6 complex when adding zero-point energy is too low compared to the OH–O conformer

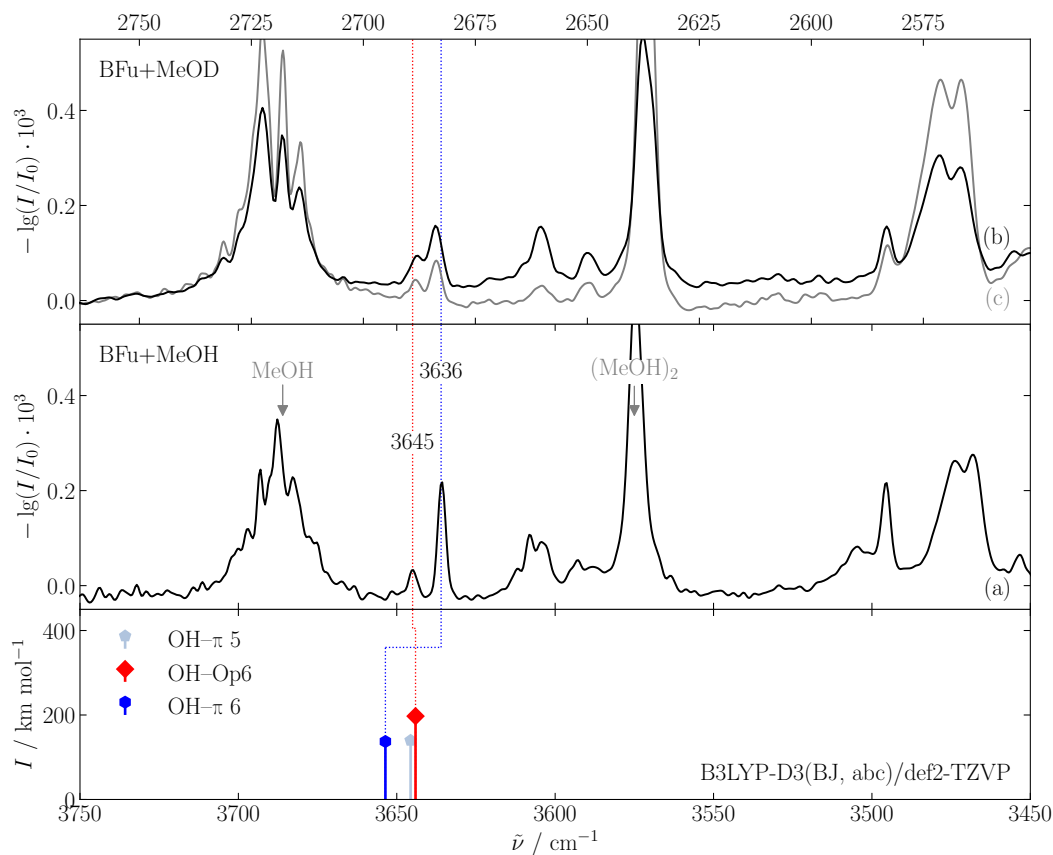


Figure 3.4.3: IR Spectra of 2,3-benzofuran with methanol(-d1) compared to theoretical prediction at B3LYP-D3(BJ, abc)/def2-TZVP level. For MeOD (upper panel) wavenumbers are scaled to the methanol monomer and stretched by $\sqrt{2}$. The calculated frequencies are scaled (factor 0.9675) to the experimental MeOH monomer value (3686 cm^{-1}). OH-O conformers are denoted in red, OH- π in blue. Darker colors indicate the most stable conformer of each binding type. (a) same as Fig. 3.4.2 (a) (BFu: 20°C , 1.00/0.10 s, MeOH: -20°C , 0.10/0.94 s); (b) deuterated methanol (BFu: 20°C , 1.00/0.11 s, MeOD: -20°C , 0.10/0.94 s); (c) deuterated methanol, reduced BFu:MeOD ratio (BFu: 10°C , 0.48/0.51 s, MeOD: -20°C , 0.10/0.94 s); see also Ref. 140.

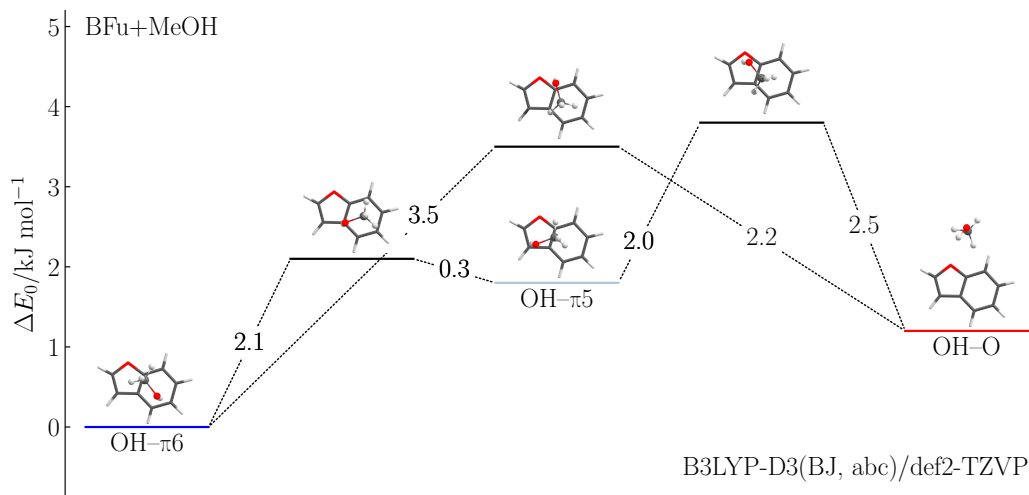


Figure 3.4.4: Calculated transition states (black bars, including harmonic ZPVE for all real modes) for the interconversion of the most stable dimer conformations of 2,3-benzofuran–methanol at B3LYP-D3(BJ, abc)/def2-TZVP level; see also Ref. 140.

(0.3 kJ mol^{-1} versus 1.2 kJ mol^{-1}) to explain the intensity difference with deuteration. Finally, a complete absence of the OH–O cluster seems unrealistic regarding the predicted preference over the OH– π 5 conformer.

For further investigation, the barrier height of the interconversion of the conformers has been calculated and is depicted in Fig. 3.4.4. The conversion of the OH– π 5 conformer into the OH– π 6 has a very low barrier of 0.3 kJ mol^{-1} . The methanol only has to rotate on top of the aromatic plane keeping the major OH– π and CH– π interactions. In contrast, for the conversion of the OH– π 5 conformer into the OH–O conformer, the methanol has to leave the aromatic plane breaking the CH– π interactions in order to form a new CH–O interaction. This results in a barrier height of 2.0 kJ mol^{-1} . The OH– π 5 conformer can therefore be easily transformed into the most stable conformer, while the OH–O might be kinetically trapped.

From the integration of the bands, a relative abundance of 84% of the π -bound cluster can be derived. This portion is lowered to 75% when the methanol is deuterated.⁸⁸ This corresponds to an energetic π preference of $0.8(5) \text{ kJ mol}^{-1}$ for MeOH and $0.5(3) \text{ kJ mol}^{-1}$ for MeOD, respectively, assuming a conformational temperature of $T_c = (60 \pm 40) \text{ K}$, which is in good agreement with the predictions from B3LYP-D3(BJ, abc)/def2-TZVP.

In summary, the band assignment reported by Sasaki *et al.* was confirmed by linear FTIR spectroscopy. Furthermore, the OH- π cluster was identified as the more stable one, while the metastable OH-O conformer is observed due to kinetic trapping. The latter can be overcome by a relaxation process mediated by acetone.

3.4.2 Dibenzofuran

The influence of a further enlargement of the π system by annulating another benzene ring to 2,3-benzofuran is investigated in this section. This has been studied before by the Nibu group.¹⁷³ However, the results of the LIF and fluorescence detected IR spectra of clusters of dibenzofuran with water and methanol remained unpublished. Various spectra of dibenzofuran have been recorded in the condensed¹⁷⁴⁻¹⁸¹ and gas phase¹⁸⁰⁻¹⁸² as well as using supersonic jet expansions¹⁸³⁻¹⁹⁰ with focus on electronic^{174,176,181,182}, vibrational^{175,180,183,184,187} and rotational^{189,190} transitions. The knowledge of its complexation is more limited. The homodimer has been studied by fluorescence spectroscopy^{166,185,191}, as have been mixed dimers with 2,3-benzofuran and fluorene.¹⁶⁶ The binding energy of argon to dibenzofuran has been determined using mass analyzed threshold ionization (MATI) spectroscopy.¹⁹² The position of the argon atom is predicted above the central furan ring.¹⁹³ The dibenzofuran-water dimer has been studied by fluorescence spectroscopy.^{183,184} It is assumed to be bound *via* the oxygen atom, however no detailed analysis has been done. Furthermore, a theoretical study of the binding of an OH-radical has been done.¹⁹⁴

From a more general perspective, clusters of dibenzofuran are interesting in an environmental aspect. Dibenzofuran is the parent molecule of the highly toxic family of polychlorinated dibenzofurans (PCDBs). Methanol is commonly used as a cosolvent for the extraction of such pollutants from soils with supercritical carbon dioxide,¹⁹⁵ whereby the binding of methanol to dibenzofuran is of particular interest. Besides this complex, the cluster of *tert*-butyl alcohol and dibenzofuran is studied in this section to test the dispersion contribution of the larger alkyl moiety. The results are published in Ref. 196, in which the dibenzofuran-water dimer is also revisited.

Even though dibenzofuran has two possible π acceptor sites, only a conformer binding to the benzene ring has found to be stable for a π -bound cluster with me-

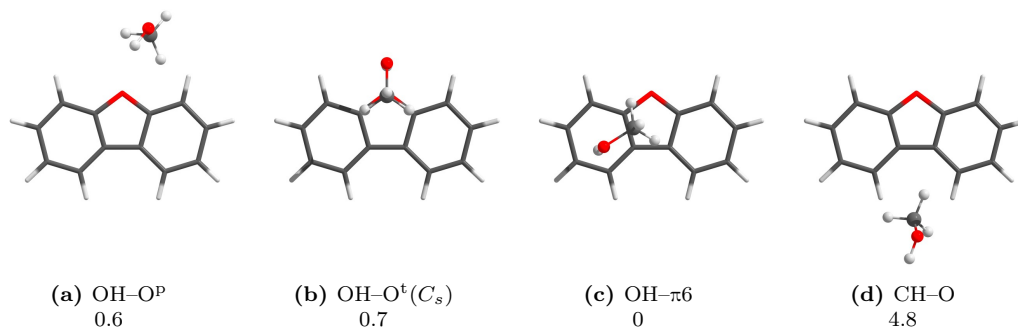


Figure 3.4.5: Structures and relative ZPVE-corrected energies (ΔE_0) in kJ mol^{-1} of the most stable dimers of methanol and dibenzofuran calculated at B3LYP-D3(BJ, abc)/def2-TZVP level.

thanol at B3LYP-D3(BJ, abc)/def2-TZVP level (Fig. 3.4.5). It is similar to the 2,3-benzofuran structure, only slightly tilted on the ring plane and, also as for 2,3-benzofuran, the global minimum structure (see Tab. 3.4.2). The energy gap to the most stable OH-O conformer is smaller, though. An OH-OP conformer was found being slightly favored over a C_s -symmetric OH-O^t conformer. When neglecting zero-point energy, the OH-OP structure is even the global minimum. This zero-point energy stabilization of the OH- π binding site is observed for all methanol clusters in this thesis (see Tab. F.2). However, it is the most pronounced for dibenzofuran-methanol, making it an interesting benchmarking system. Besides these common OH-O and OH- π binding motifs, another structure without an OH-hydrogen bond, but two CH-O interactions, has been optimized. As it is 4.8 kJ mol^{-1} less stable than the global minimum, it will not be discussed further.

Interestingly, enlarging the alkyl moiety of the donor to *tert*-butyl changes the energetic preference. The OH-O conformer is slightly favored over the OH- π conformer, with and without inclusion of zero-point energy. The OH-O structure for dibenzofuran-*tert*-butanol lies somewhere between an OH-O^t and OH-OP structure, as the bulky *tert*-butyl group can better interact with the π system than the methyl group while keeping a secondary CH-O interaction to the alcohol oxygen. A C_s -symmetric OH-O isomer could not be optimized without imaginary frequencies at B3LYP-D3(BJ, abc)/def2-TZVP level and is thus not discussed further. Though, optimizations at other computational levels, among them B3LYP-D3 without three-body term, resulted in a minimum structure competitive in energy.¹⁹⁶ For the OH- π complexes there is again no structure including an OH- π interaction to the furan

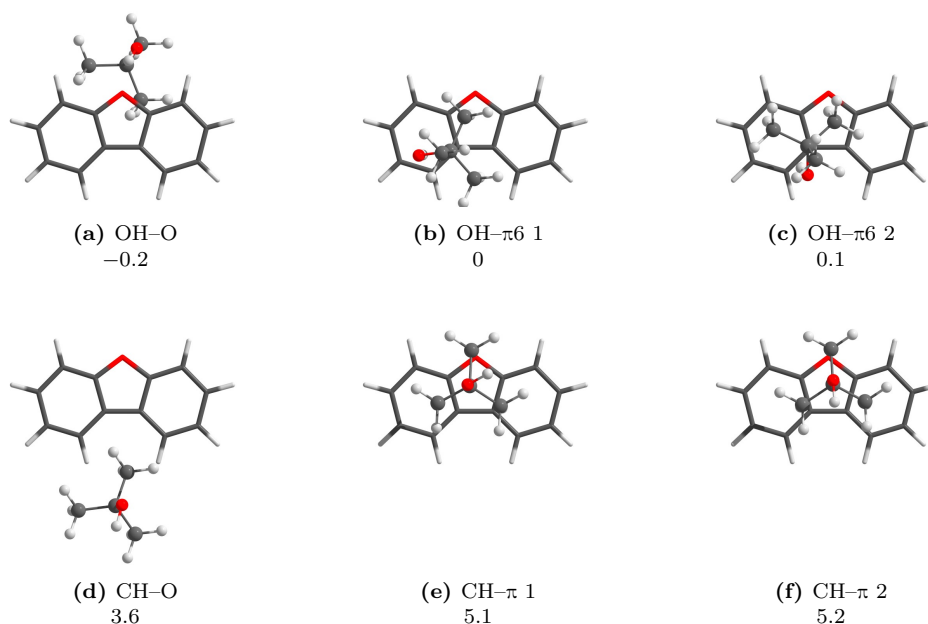


Figure 3.4.6: Structures and relative ZPVE-corrected energies (ΔE_0) in kJ mol^{-1} of the most stable dimers of *tert*-butyl alcohol and dibenzofuran calculated at B3LYP-D3(BJ, abc)/def2-TZVP level.

ring. Two almost isoenergetic OH- π 6 conformers have been found differing by the orientation of the *tert*-butyl moiety. As for methanol as a donor, non-hydrogen-bonded conformers have been tested. Again, a structure containing two CH-O interactions has been found to be stable. Furthermore, two conformers containing CH- π interactions of the *tert*-butyl moiety with the π system have been found. All of these have an energetic penalty of at least 3.9 kJ mol^{-1} with respect to the most stable conformer and will therefore not be discussed further.

With a boiling temperature of $285 \text{ }^\circ\text{C}$ ¹⁹⁷ dibenzofuran is not volatile enough to be measured with the *filet*-jet. A temperature of approximately $100 \text{ }^\circ\text{C}$ is needed to reach a vapor pressure of 2 mbar.¹⁹⁷ Therefore, the *popcorn*-jet was used to obtain spectra at several conditions (see Fig. 3.4.7). For comparison, a spectrum of the pure dibenzofuran has been measured (see Fig. E.1). It contains symmetric as well as antisymmetric CH stretching vibrations between 3110 cm^{-1} and 3030 cm^{-1} , that

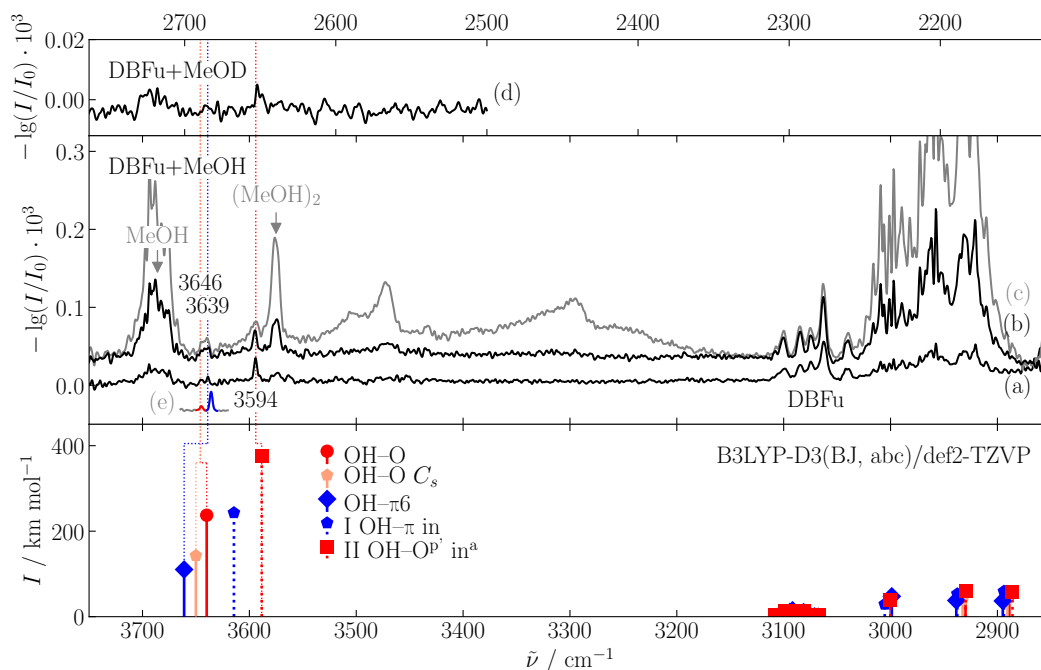


Figure 3.4.7: IR Spectra of dibenzofuran with methanol(-d1) compared to theoretical prediction at B3LYP-D3(BJ, abc)/def2-TZVP level. The calculated frequencies are scaled (factor 0.9675) to the experimental MeOH monomer value (3686 cm^{-1}). OH-O conformers are denoted in red, OH- π in blue. Darker colors indicate the most stable conformer of each binding type. (a) dibenzofuran-methanol (DBFu: $120\text{ }^\circ\text{C}$ ($\approx 0.4\%$), MeOH: 0.15% , double-slit nozzle: $140\text{ }^\circ\text{C}$); (b) dibenzofuran-methanol (DBFu: $110\text{ }^\circ\text{C}$ ($\approx 0.25\%$), MeOH: $-25\text{ }^\circ\text{C}$ ($\approx 0.3\%$), V-nozzle (hollow, 0.2 mm , second check valve at 350 mbar): $130\text{ }^\circ\text{C}$ to $150\text{ }^\circ\text{C}$); (c) dibenzofuran-methanol (DBFu: $110\text{ }^\circ\text{C}$ ($\approx 0.25\%$), MeOH: $-10\text{ }^\circ\text{C}$ ($\approx 1\%$), V-nozzle (hollow, 0.2 mm , second check valve at 350 mbar): $150\text{ }^\circ\text{C}$); (d) deuterated methanol (DBFu: $120\text{ }^\circ\text{C}$ ($\approx 0.4\%$), MeOD: 0.15% , double-slit nozzle: $140\text{ }^\circ\text{C}$); (e) 2,3-benzofuran-methanol, same as Fig. 3.4.2 (a) (BFu: $20\text{ }^\circ\text{C}$, $1.00/0.10\text{ s}$, MeOH: $-20\text{ }^\circ\text{C}$, $0.10/0.94\text{ s}$); see also Ref. 196.

Table 3.4.2: Dissociation energies of the dibenzofuran dimers with (D_0) and without (D_{el}) harmonic zero-point vibrational energy calculated at B3LYP-D3(BJ, abc)/def2-TZVP level in kJ mol^{-1} . Energies relative to the most stable dimer (ΔE_{el} and ΔE_0) are given in kJ mol^{-1} , harmonic OH stretching wavenumbers (ω_{OH}) and shifts ($\Delta\omega_{OH}$) from the corresponding monomer vibrational wavenumber in cm^{-1} , band intensities (I_{OH}) in km mol^{-1} . Trimers are given up to $\Delta E_0 = 5 \text{ kJ mol}^{-1}$, all calculated structures are listed in Tab. D.3. Conformers used for further analysis in Sec. 6 are marked in bold.

Cluster	ΔE_{el}	ΔE_0	D_{el}	D_0	ω_{OH}	$\Delta\omega_{OH}$	I_{OH}
dibenzofuran + MeOH							
OH-O ^P	-0.9	0.6	24.3	19.5	3762	48	237
OH-O^t C_s	0.0	0.7	23.4	19.3	3772	37	143
OH-π 6	0	0	23.4	20.1	3784	26	110
CH-O	4.3	4.8	19.1	15.3	3813	-3	33
(dibenzofuran)₂ + MeOH							
I OH-O ^{P'} out	2.8	2.3	30.7	26.2	3739	70	323
I OH-O ^{P'} out	3.2	2.5	30.3	25.9	3746	64	309
I OH- π in	2.8	2.0	30.7	26.4	3736	74	243
II OH-O ^{P'} in ^a	0	0	33.5	28.4	3709	101	375
II OH-O ^{P'} in ^a	0.4	0.3	33.1	28.1	3709	101	344
II OH-O ^{P'} in ^b	3.6	2.8	29.9	25.6	3738	71	301
dibenzofuran + <i>t</i>-BuOH							
OH-O	-1.1	-0.2	26.6	23.0	3746	39	221
OH-π6 1	0	0	25.5	22.8	3766	19	119
OH- π 6 2	0.0	0.1	25.5	22.7	3758	27	135
CH-O	2.9	3.6	22.6	19.2	3785	0	15
CH- π 1	5.2	5.1	20.3	17.7	3785	0	12
CH- π 2	5.3	5.2	20.2	17.6	3785	0	12

are in agreement with gas-phase IR and Raman data.¹⁸⁰ They are well separated from the methanol CH stretching vibrations as can be seen in Fig. 3.4.7.

Spectrum (a) in Fig. 3.4.7 was measured using the double-slit nozzle at very low methanol concentrations. In the OH stretching region a single band at 3594 cm^{-1} is observed, besides the spectral features of pure methanol. Comparing to the predicted dimer bands however, there is no corresponding structure with such a large downshift. Regarding the excess of dibenzofuran, the most probable assignment seems a mixed trimer of two dibenzofuran units and a methanol. Some trial structures have been calculated, with an OH-O bound structure being the most stable, the most

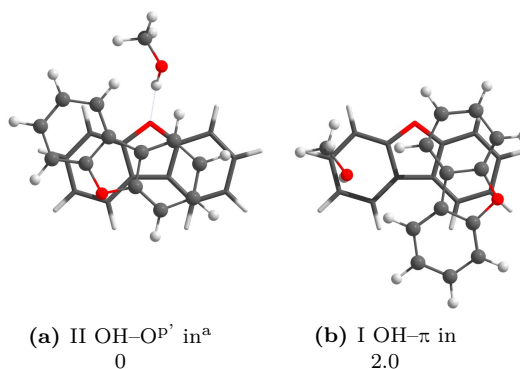


Figure 3.4.8: Structures and relative ZPVE-corrected energies (ΔE_0) in kJ mol^{-1} of the most stable trimers of two dibenzofuran molecules and one methanol calculated at B3LYP-D3(BJ, abc)/def2-TZVP level.

favorable π -bound conformer being 2.0 kJ mol^{-1} higher in energy (see Tab. 3.4.2). These two isomers are depicted in Fig. 3.4.8, further structures in Fig. D.2 and Fig. D.3. Both conformers profit from CH–O interactions of the additional dibenzofuran molecule to the methanol. Despite combining the most stable binding motif of the mixed dimer with the most stable dibenzofuran dimer structure (I, see below), the OH– π conformer is not the global minimum. The OH–O^{P'} motif, which is realized in the oxygen-bound trimer, is not a minimum structure for the dimer. Apparently, it needs the stabilization by the secondary CH–O interaction. A second OH–O^{P'} dimer, differing only in the position of the methyl moiety, is predicted to be only 0.3 kJ mol^{-1} more stable. The large downshift of 92 cm^{-1} would match both binding types, as the π -bound conformer is interacting with the benzene ring, for which a rather large underestimation is probable, as discussed in Sec. 3.4.1. However, the further downshift of the band in the spectrum containing deuterated methanol (Fig. 3.4.7 (d)), which was measured using otherwise the same experimental conditions as spectrum (a), hints to an OH–O binding type in accordance to the methylated furan dimers (see Sec. 3.2). The overestimation of the predicted downshift by 9 cm^{-1} is relatively large compared to the other furan compounds. Though, this might be attributed to the larger absolute shift. For comparison, some trial trimer geometries of one dibenzofuran and two methanol molecule have been optimized at B3LYP-D3(BJ)/def2-TZVP level. The results are shown in Tab. D.4 and Fig. D.4. No structure has been found exhibiting a downshift between 60 cm^{-1} and

120 cm^{-1} , structures with cooperative hydrogen bonding being shifted even further. Thus, the assignment to a (dibenzofuran)₂-methanol trimer is sustained.

Searching for hints of the dimers, one finds very small spectral features at 3639 cm^{-1} and 3646 cm^{-1} , that compare well to the positions of the mixed dimers of 2,3-benzofuran-methanol (see Fig. 3.4.7 (e) and Sec. 3.4.1), but the signal-to-noise ratio of spectrum (a) is too low for a reliable assignment. Another spectrum Fig. 3.4.7 (b) with a larger methanol:dibenzofuran ratio has been measured using the V-nozzle, in an attempt to suppress the trimer in favor of mixed dimer formation. Indeed, a broad spectral feature at 3636 cm^{-1} to 3648 cm^{-1} supports a dimer origin. Unfortunately, it is too broad to decide for the contribution of one or two dimer conformations. Increasing the methanol:dibenzofuran ratio further (Fig. 3.4.7 (c)) only leads to larger methanol clusters, but does not effectively enhance the proposed dimer bands. As the computed geometries are equivalent, an analogous band assignment to 2,3-benzofuran-methanol is probable, tentatively assigning the 3639 cm^{-1} and 3646 cm^{-1} bands to an OH- π and OH-O dimer, respectively. Comparing to the computational results, again this would involve a crossing of experimental and predicted band positions with a large downshift underestimation of the π -bound and overestimation of the oxygen-bound one.

One explanation for the trimer band being more intense than the dimers' is the higher IR visibility. Apart from that, the binding energy of the dibenzofuran homodimer is predicted to be almost twice as high as the mixed dibenzofuran-methanol dimer (see Tab. 3.4.2 and Tab. 3.4.3). The FTIR technique is blind for this dimer, due to the lack of an OH chromophore. Furthermore, the binding energy of a methanol molecule to such a homodimer is also calculated to be larger than for a mixed dimer (with respect to isomer I, see Fig. 3.4.11). Thus, the selective preparation of mixed dibenzofuran-methanol dimers in the supersonic expansion remains challenging.

The binding energy of *tert*-butyl alcohol to dibenzofuran is predicted slightly larger than for methanol. The spectrum measured with the *popcorn*-jet using the V-nozzle is shown in Fig. 3.4.9. It is quite similar to the spectrum containing methanol, though the features possibly belonging to the mixed dimers are somewhat more pronounced. One band is observed at 3607 cm^{-1} and possibly a shoulder at 3613 cm^{-1} . An analogous assignment of the clusters with the two different donor molecules is most

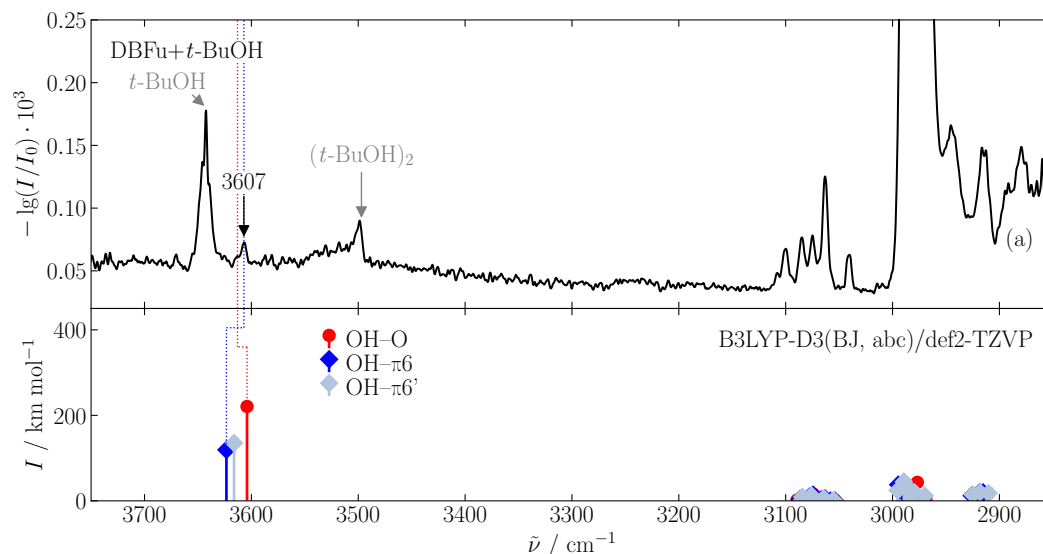


Figure 3.4.9: IR Spectra of dibenzofuran with *tert*-butyl alcohol compared to theoretical prediction at B3LYP-D3(BJ, abc)/def2-TZVP level. The calculated frequencies are scaled (factor 0.9621) to the experimental *t*-BuOH monomer value (3642 cm^{-1}). OH-O conformers are denoted in red, OH- π in blue. Darker colors indicate the most stable conformer of each binding type. (a) dibenzofuran-*tert*-butyl alcohol (DBFu: $110 \text{ }^\circ\text{C}$, *t*-BuOH: $10 \text{ }^\circ\text{C}$, V-nozzle (conical, 0.2 mm): $130 \text{ }^\circ\text{C}$); see also Ref. 196.

likely. Thus, the band at 3607 cm^{-1} is probably due to the OH- π 6 conformer. An underestimation of 16 cm^{-1} would fit to the anisole derivatives (see Fig. 6.2.1). The shoulder at 3613 cm^{-1} could hence be due to the OH-O conformer. The downshift overestimation of 10 cm^{-1} for the OH-O conformer would seem relatively large, but consistent with the methanol complex.

As the spectra measured with the *popcorn*-jet remain elusive, microwave spectra have been recorded and are discussed below.

Microwave data

Microwave spectra of the dibenzofuran clusters have been obtained at the COMPACT setup in Hamburg (see Sec. 2.3) in a cooperation with the group of M. Schnell during a two weeks research stay. An excerpt of the microwave spectrum of the pure dibenzofuran is illustrated in Fig. 3.4.10. It is separately published in Ref. 198. Only b-type lines are observed, confirming the C_{2v} symmetry of the calculated monomer

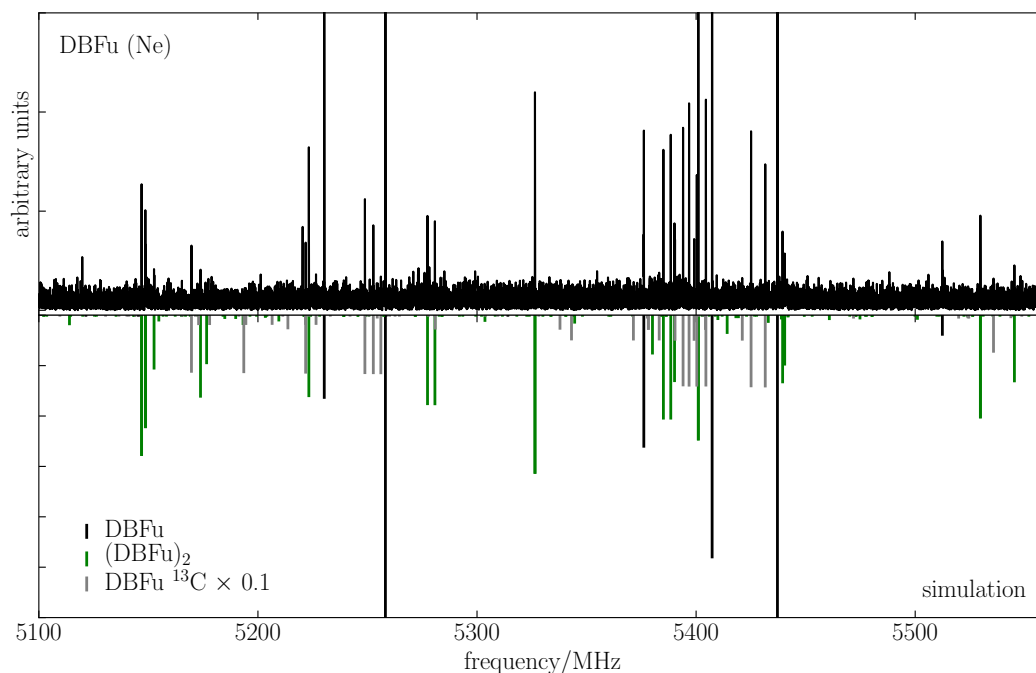


Figure 3.4.10: Excerpt of the microwave spectrum of dibenzofuran using neon (3 bar) as a carrier gas. Experimental data are shown in the upper panel, the lower panel shows the simulated spectra based on the fitted rotational constants; see also Ref. 198.

geometry. The extracted rotational constants are listed in Tab. 3.4.4. They are in excellent agreement with data derived from rotationally resolved fluorescence excitation spectroscopy.^{189,190} Due to the statistical enhancement by the C_{2v} symmetry, bands of the ^{13}C isotopologues in natural abundance could be assigned (grey lines in Fig. 3.4.10). Thus, the structure of the dibenzofuran monomer can be obtained directly from experiment by use of Kraitchman's equations¹⁹⁹. The coordinates obtained by using the KRA program²⁰⁰ are given in Tab. D.2. The deviation of the oxygen atom position between the calculated and experimentally obtained structure is due to the comparison of equilibrium bond lengths r_e with effective bond lengths r_0 (see Fig. D.1).

Dibenzofuran dimer. Besides the monomer transitions, a homodimer of dibenzofuran was identified.¹⁹⁸ It has been studied before using dispersed fluorescence spectroscopy.¹⁸⁵ A displaced sandwich structure was assumed, stabilized by dipole–

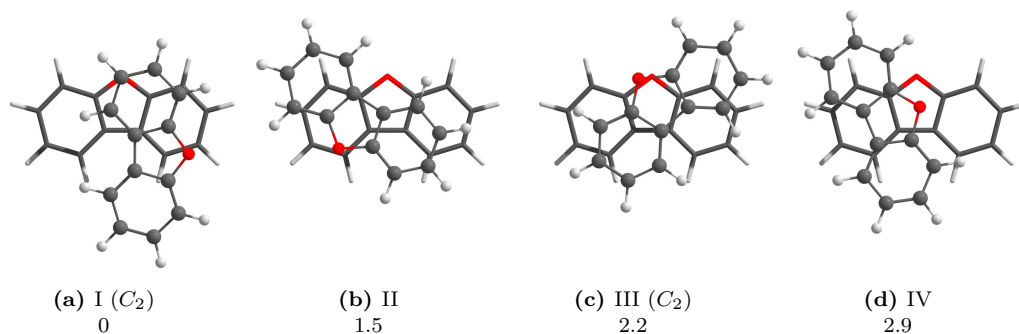


Figure 3.4.11: Structures and relative ZPVE-corrected energies (ΔE_0) in kJ mol^{-1} of the most stable dimers of dibenzofuran calculated at B3LYP-D3(BJ, abc)/def2-TZVP level; see also Ref. 198.

Table 3.4.3: Calculated energies of the dibenzofuran dimers at B3LYP-D3(BJ, abc)/def2-TZVP level. Dissociation energies of the dibenzofuran dimers with (D_0) and without (D_{el}) harmonic zero-point vibrational energy calculated at B3LYP-D3(BJ, abc)/def2-TZVP level in kJ mol^{-1} . Energies relative to the most stable dimer (ΔE_{el} and ΔE_0) are given in kJ mol^{-1} ; see also Ref. 198.

Dimer	ΔE_{el}	ΔE_0	D_{el}	D_0
dibenzofuran dimer				
I (C_2)	0	0	42.6	38.9
II	1.7	1.5	40.8	37.4
III (C_2)	2.8	2.2	39.7	36.7
IV	3.6	2.9	38.9	36.0

dipole interactions of opposed dipoles.^{185,191} However, this geometry was not found to be stable at B3LYP-D3(BJ, abc)/def2-TZVP level. In the most stable geometry (I), the dipoles are oriented perpendicular to each other (see Fig. 3.4.11) while the π systems overlap partially resulting in a C_2 -symmetric structure. The energetically closest geometry (II) is 1.5 kJ mol^{-1} less stable (see Tab. 3.4.3). Two more structures were found, also with parallel π systems. Trial structures for T-shaped geometries did not result in energetic minima. The experimental rotational constants compare best with structure I (see Tab. 3.4.4). Structure IV has very similar rotational constants, but the dipole moment components of IV are of similar magnitude, which would not match to the observation of only b-type lines. Structure I having the dipole aligned along the y-axis, assigns this geometry without ambiguity.

3.4 Annulated Benzene: 2,3-Benzofuran and Dibenzofuran

Table 3.4.4: Calculated rotational parameters of the dibenzofuran dimers at B3LYP-D3(BJ, abc)/def2-TZVP level in comparison to experimental values; see also Ref. 196,198.

Dimer	A /MHz	B /MHz	C /MHz	μ /D	(a/b/c) ^a
dibenzofuran monomer					
C_{2v}	2294	602	477	0.68	0.00/ 0.68/ 0.00
exp	2278.18843(43)	601.12199(14)	475.75313(14)		0/43/0 ^b
dibenzofuran dimer					
I	303	232	193	0.62	0.00/ 0.62/ 0.00
II	357	220	190	0.35	0.31/−0.15/−0.06
III	333	230	201	1.15	0.00/ 0.00/ 1.15
IV	311	231	192	1.04	−0.50/−0.70/−0.58
exp ¹⁹⁸	300.90323(17)	227.98085(17)	190.60573(17)		0/83/0 ^b
dibenzofuran + MeOH					
OH–O ^p	740	516	318	2.70	1.80/ 1.63/−1.19
OH–O ^t C_s	836	523	383	2.85	0.00/ 2.81/−0.42
OH– π 6	1001	440	420	2.05	1.36/−1.47/ 0.45
CH ₂ –O	691	568	332	2.57	0.62/−2.35/ 0.83
exp ^{b196}	987.3953(36)	439.33213(28)	417.58829(26)		49/16/ 0
exp ^{b196}	808.91099(33)	524.58247(15)	375.30332(18)		0/94/28
dibenzofuran + <i>t</i>-BuOH					
OH–O	475	373	244	2.66	−2.11/ 0.40/−1.57
OH– π 6 1	515	353	269	1.89	−1.81/ 0.23/−0.51
OH– π 6 2	497	370	274	1.20	−0.57/ 0.85/−0.62
CH–O	512	315	211	2.77	2.77/ 0.18/ 0.05
CH– π 1	441	395	269	1.80	1.76/−0.37/−0.06
CH– π 2	438	397	268	2.40	1.53/ 0.60/ 1.74
exp ¹⁹⁶	513.73023(20)	351.76117(15)	269.56523(14)		83/36/43

^a Dipole moment components $\mu_x/\mu_y/\mu_z$ in /D for the theoretical data and number of lines assigned for a/b/c-type transitions for experimental data.

^b Thanks to M. Fatima.

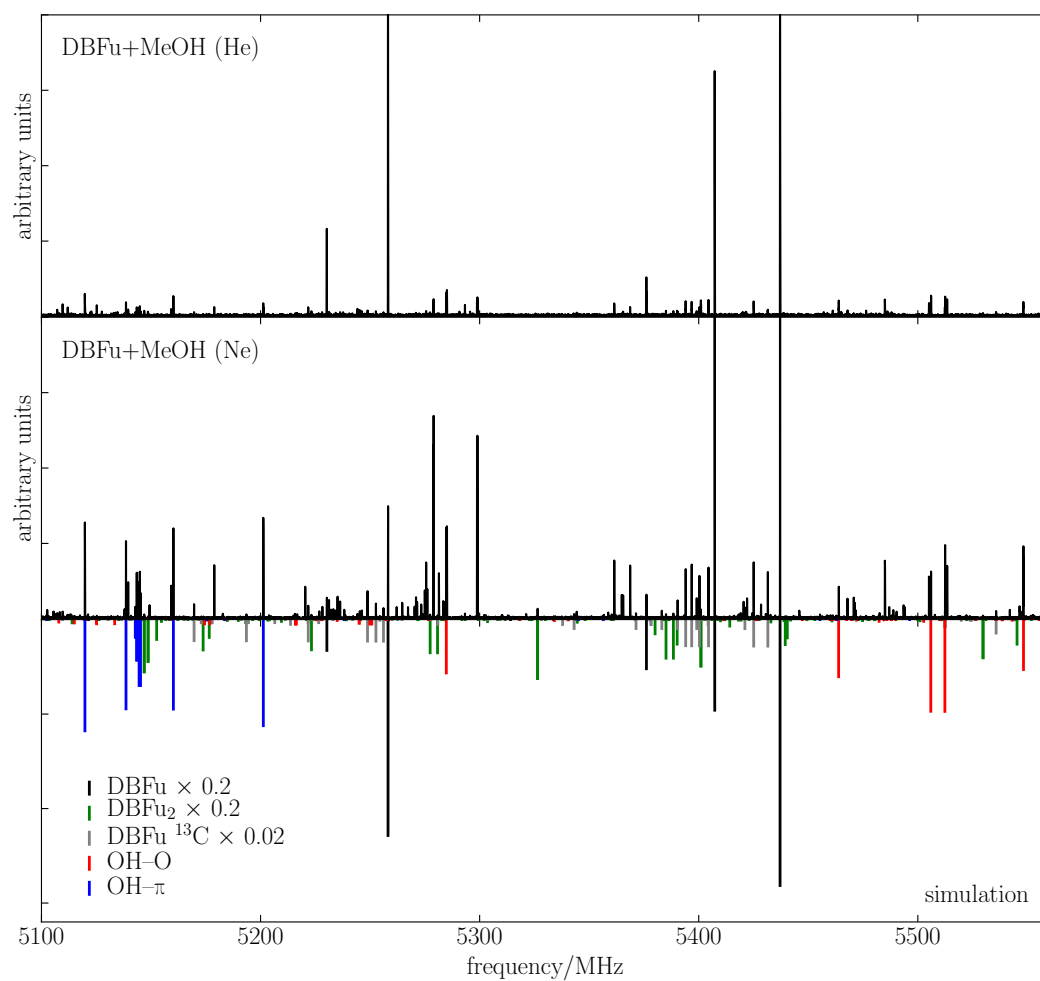


Figure 3.4.12: Excerpt of the microwave spectrum of dibenzofuran–methanol using helium (3 bar, upper panel) and neon (3 bar, middle panel) as a carrier gas. Experimental data are shown in the upper two panels, the lower panel shows the simulated spectra based on the fitted rotational constants.

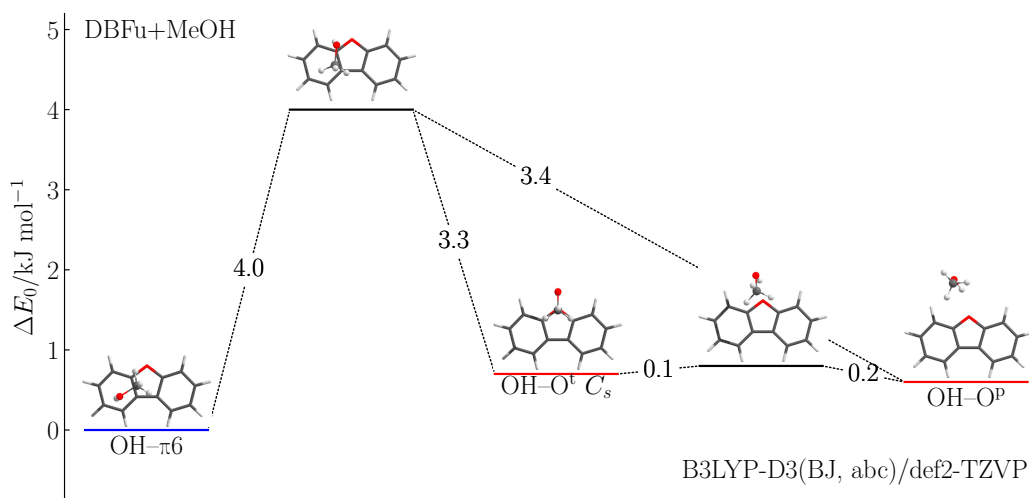


Figure 3.4.13: Calculated transition states (black bars, including harmonic ZPVE for all real modes) for the interconversion of the most stable dimer conformations of dibenzofuran–methanol at B3LYP-D3(BJ, abc)/def2-TZVP level.

Dibenzofuran–methanol. The rotational spectrum of the dibenzofuran–methanol cluster is shown in Fig. 3.4.12. Two spectra were recorded, one using helium (upper panel), one using neon (lower panel) as a carrier gas. Besides the monomer and dimer transitions of dibenzofuran, two clusters could be identified. The nature of the carrier gas does not seem to influence the formation of these two clusters other than in overall abundance. Comparing the resulting rotational constants (see Tab. 3.4.4), the OH– π 6 conformer can be assigned. The maximum deviation is that of the A constant, amounting to 1.4%. The observed line types are also in reasonable agreement with the calculated dipole moment components. The rotational constants of the second observed conformer match best with the C_s -symmetric OH–O^t conformer. However, the unsymmetric OH–O^p conformer would be in reasonable agreement as well. Regarding the observed line types, the symmetric structure is confirmed. The lack of a-type transitions is incompatible with μ_x being the largest dipole moment component in the OH–O^p conformer, but fits well to the OH–O^t (C_s) conformer.

From calculation these two OH–O conformers are almost isoenergetic (see Tab. 3.4.2) with a slight preference for OH–O^p. Interestingly, this is reversed when neglecting the three-body term, see Tab. D.1, resulting in the energetic pre-

ference found by experiment. However, the differences are within the errors of the calculation. The observation of only one OH–O conformer hints to the conversion of the meta stable conformer into the local minimum structure. A low barrier between these conformers is conceivable, since the primary hydrogen bond is the same in both cases and can be retained during the interconversion. Indeed, the barrier is calculated to be as small as 0.2 kJ mol^{-1} , as depicted in Fig. 3.4.13. The conversion to the global minimum OH– π structure requires an energy barrier of 3.3 kJ mol^{-1} , thus the population of one oxygen and one π -bound dimer is conceivable.

Going back to the FTIR spectra and assuming the formation of the same dimers in the supersonic expansion, the OH– π conformer is confirmed, while the less downshifted band is still attributed to an OH–O conformer, but has to be revised. Assigning the OH–O^t results in an underestimation of the spectral downshift by 3 cm^{-1} , which is rather unusual, but compares well to the underestimation of the OH–O^t conformer in case of furan–methanol (see Sec. 3.2). This further supports the inversion of the predicted frequency sequence analogous to the 2,3-benzofuran–methanol clusters, since the underestimation should only be minor.

Adding to this multi-spectroscopic approach, mass selective IR/UV measurements have been done in the group of M. Gerhards.¹⁹⁶ The results of two dimers at 3642 cm^{-1} and 3637 cm^{-1} , respectively, are in reasonable agreement with the data from linear FTIR spectroscopy. The band positions measured by FTIR may be shifted to higher wavenumbers due to the nozzle temperature of $130 \text{ }^\circ\text{C}$ to $150 \text{ }^\circ\text{C}$. The effect is also seen for the methanol homodimer, whose band is shifted by 1 cm^{-1} in spectrum (d) of Fig. 3.4.7. Concerning the assignment, the UV excitation energies also hint for a π coordinated conformer for the further downshifted band, thus further supporting a crosswise band assignment.

Deciding for one side of the molecular balance is especially difficult for this system, regarding the weak and broad bands in the FTIR spectrum. Both are almost equally strong, with a minimal enhancement of the OH– π band. Including the slightly lower IR visibility of the π -bound dimer, a tentative preference for the π binding site can be concluded, which would be in agreement with the prediction by B3LYP-D3(BJ, abc)/def2-TZVP. The independence of the relative abundance from the carrier gas

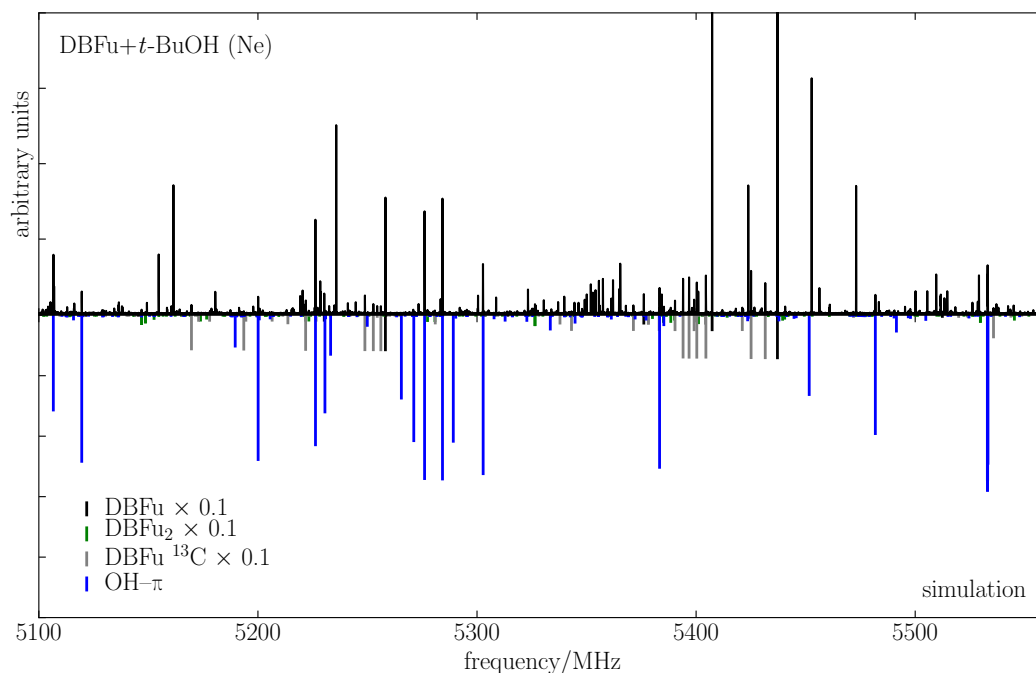


Figure 3.4.14: Excerpt of the microwave spectrum of dibenzofuran-*tert*-butyl alcohol using neon (3 bar) as a carrier gas. Experimental data are shown in the upper panel, the lower panel shows the simulated spectra based on the fitted rotational constants.

in the microwave experiment would be in agreement with a minor energy difference between the conformers.

Dibenzofuran-*tert*-butyl alcohol. Fig. 3.4.14 depicts the microwave spectrum of dibenzofuran-*tert*-butyl alcohol. Only one mixed dimer was found besides the transitions already observed in the pure dibenzofuran spectrum. The rotational constants assign it to the OH- π 6 1 conformer (see Tab. 3.4.4). The observed line types and dipole moment components are also in good agreement. In contrast to the dibenzofuran-methanol spectrum, an oxygen-bound dimer could not be identified. The absence of the second OH- π cluster, despite the fact that it is almost isoenergetic, can again be explained by a low barrier of 0.3 kJ mol^{-1} (calculated at B3LYP-D3(BJ, abc)/def2-TZVP level) for the conversion to the OH- π 6 1 conformation. The transition state search for the conversion to the oxygen-bound conformer did not converge at B3LYP-D3(BJ, abc)/def2-TZVP level, but was determined to

amount to 2 kJ mol^{-1} at B3LYP-D3(BJ)/def2-TZVP level.¹⁹⁶ The barrier is smaller than for dibenzofuran–methanol and thereby a conversion to the most stable conformer seems plausible.

Using this information to the interpretation of the FTIR spectrum, the more pronounced band at 3607 cm^{-1} is most likely attributed to the OH– π 6 1 conformer found in the microwave spectrum, while the shoulder is tentatively assigned to the OH–O dimer. As discussed before, this would be in good agreement with the predicted spectral shift for the OH– π 6 1 conformer, and still reasonable for the oxygen-bound complex. The π -bound complex being further shifted than the oxygen-bound would also be in line with the observations for dibenzofuran–methanol and other furan clusters. As has been done for the methanol cluster, IR/UV measurements have been carried out.¹⁹⁶ Only one cluster band is observed at 3605 cm^{-1} , which is again in good agreement with the FTIR results, bearing in mind the heated nozzle. Based on the electronic excitation energies, an assignment to a π -bound cluster is substantiated. If the shoulder in the FTIR spectrum is caused by the oxygen-bound dimer, the OH– π cluster is approximately four times more abundant, taking into account the computed IR band strength. An OH–O complex being visible in the FTIR spectrum, but neither in the microwave nor in the IR/UV spectrum, could be explained by the use of neon as the carrier gas and hence the more efficient cooling in the setups. The offset between FTIR and IR/UV band positions also hints at warmer expansion conditions in the *popcorn*-jet.

Apparently, the energetic sequence is not predicted properly by B3LYP-D3(BJ, abc)/def2-TZVP. Interestingly, when leaving out the three-body term, the π -bound dimer is indeed predicted as the global minimum (see Tab. D.1). Without the three-body term the absolute binding energies are predicted about 1 kJ mol^{-1} higher for the dibenzofuran–*tert*-butyl alcohol dimers. For the OH–O dimer the effect is smaller, so that the energetic ordering is inverted. This could be due to error compensation in the computational method, that is less fortuitous when the three-body term is included. Unsurprisingly, the effect is larger the more the alkyl group interacts with the π system. Accordingly, for the dibenzofuran–methanol dimers the lowering of the predicted binding energy with three-body term inclusion is smaller, amounting up to 0.5 kJ mol^{-1} .

Studying clusters of dibenzofuran is at the edge of the capability of the *popcorn-jet*. In that way it has triggered some of the experimental developments described in Sec. 2.2.1. Therefore, the application of a multi-spectroscopic approach has been necessary. All spectra are in agreement with the observation of two clusters in case of dibenzofuran–methanol, one oxygen and one π -bound, and a single π -bound cluster in case of *tert*-butyl alcohol, with hints for a second (oxygen-bound) dimer in FTIR. The π -bound cluster is spectroscopically more downshifted than the oxygen-bound one and also the more stable complex in both cases. The π preference is more pronounced for *tert*-butyl alcohol, though the opposite has been predicted by B3LYP-D3(BJ, abc)/def2-TZVP.

4 Clusters of Diphenyl Ether and Alkyl Alcohols

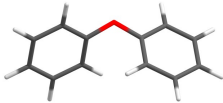
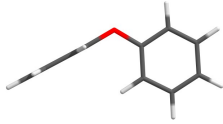
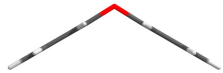
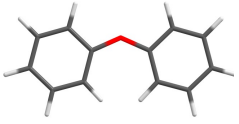
The acceptor molecules investigated so far all contain a furan skeleton, where the oxygen acceptor atom is incorporated in the molecule's π system, tuning down its attractivity. In this chapter, the furan ring of the dibenzofuran molecule of the last section is 'cut open', resulting in diphenyl ether (DPE) as the acceptor molecule. Thereby, the influence of the delocalization of the oxygen's electron density on the competition between π -bound and oxygen-bound cluster formation is investigated.

Clusters of diphenyl ether with methanol and *tert*-butyl alcohol have already been investigated in course of a Master's thesis.³⁴ The remaining open questions are addressed in this thesis by a multi-spectroscopic approach in cooperation with the groups of M. Gerhards in Kaiserslautern and M. Schnell in Hamburg. The results have been published in Ref. 83 and Ref. 75 for diphenyl ether with methanol and *tert*-butyl alcohol, respectively.

Diphenyl ether is non-rigid and rather flexible along the torsion angles of the phenyl rings. Its monomer conformations have been studied previously using resonance enhanced multi photon ionization (REMPI)²⁰¹, nuclear magnetic resonance (NMR)²⁰² and theoretical methods²⁰¹⁻²⁰⁵. The potential energy surface of the two torsional angles reveals four conformations, of which only the *twist* conformation is a minimum structure (see Tab. 4.0.1).^{83,201-205} It has C_2 symmetry and two enantiomeric forms, which are interconnected by the *skew* conformation as the transition state with an energy barrier of about 0.9 kJ mol^{-1} .

Two oxygen and three π -bound dimers were found previously for DPE–MeOH by calculations at B3LYP-D3(BJ)/def2-TZVP level using `Turbomole`,³⁴ which were re-optimized at B3LYP-D3(BJ, abc)/def2-TZVP level (see Tab. 4.0.2 and Fig. 4.0.1). According to these calculations, the most stable dimer conformation is OH– π 1 closely followed by a second π -bound structure OH– π 2 ($\Delta E_0 = 0.3 \text{ kJ mol}^{-1}$), which differs by the orientation of the methyl moiety. The most stable oxygen-bound con-

Table 4.0.1: Relative energies of the diphenyl ether conformers with (ΔE_0) and without (ΔE_{el}) harmonic zero-point vibrational energy calculated at B3LYP-D3(BJ)/def2-TZVP level in kJ mol^{-1} . The structures, point groups, torsional angles (Φ_1 , Φ_2) and number of imaginary frequencies are stated as well.

Conformer		Φ_1	Φ_2	No. im. freq.	ΔE_{el}	ΔE_0	
<i>twist</i>		C_2	40.3	40.3	0	0	0
<i>skew</i>		C_s	91.4	0.0	1	1.1	0.9
<i>gable</i>		C_{2v}	91.2	91.3	1	17.9	16.7
<i>planar</i>		C_{2v}	0.0	0.0	2	26.7	25.3

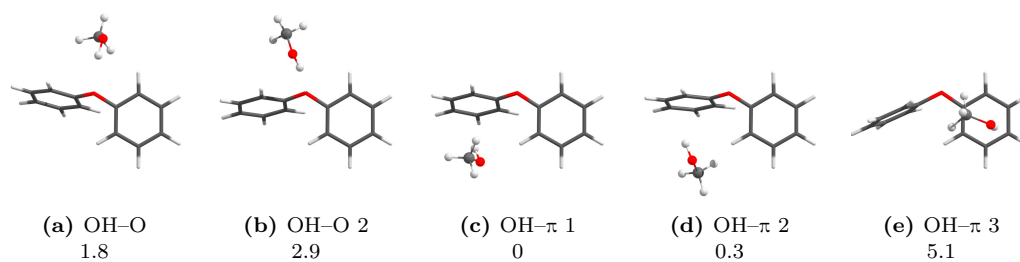


Figure 4.0.1: Structures and relative ZPVE-corrected energies (ΔE_0) in kJ mol^{-1} of the most stable dimers of methanol and diphenyl ether calculated at B3LYP-D3(BJ, abc)/def2-TZVP level.

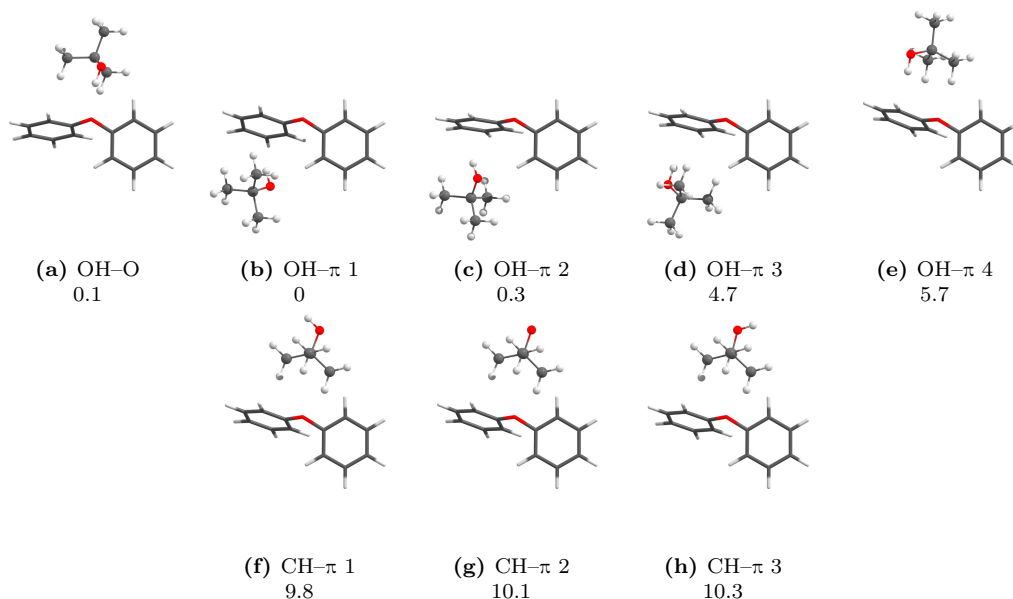


Figure 4.0.2: Structures and relative ZPVE-corrected energies (ΔE_0) in kJ mol^{-1} of the most stable dimers of diphenyl ether and *tert*-butyl alcohol calculated at B3LYP-D3(BJ, abc)/def2-TZVP level.

formation is 1.8 kJ mol^{-1} less stable than the global minimum OH- π . Almost all geometries are stabilized by secondary CH-O interactions of the phenyl *ortho* hydrogen, except for the OH- π 3 conformer, which contains a *skew* like conformation of diphenyl ether. Not generally expected, the competition between oxygen and π binding is even closer for *tert*-butyl alcohol as a donor, despite the larger alkyl moiety. Again, two π -bound conformations with the alkyl group pointing in opposite directions are predicted to be close in energy (see Fig. 4.0.2). However, the oxygen-bound conformer is more competitive in this case, being almost isoenergetic to the most stable OH- π conformation. Stronger interactions between the alkyl group and the phenyl ring when the donor is on the side facing away from the center of mass of DPE is a probable explanation. Further structures with OH- π and CH- π interactions have been found through geometry optimization, but are higher in energy, due to the missing stabilizing CH-O interaction or the weaker primary interaction, respectively.

First IR spectra of diphenyl ether and its complexes with methanol and *tert*-butyl alcohol have been measured previously using the *popcorn*-jet setup.³⁴ One

Table 4.0.2: Dissociation energies of the dimers of diphenylether with methanol and *tert*-butyl alcohol with (D_0) and without (D_{el}) harmonic zero-point vibrational energy calculated at B3LYP-D3(BJ, abc)/def2-TZVP level in kJ mol^{-1} . Energies relative to the most stable dimer (ΔE_{el} and ΔE_0) are given in kJ mol^{-1} , harmonic OH stretching wavenumbers (ω_{OH}) and shifts ($\Delta\omega_{OH}$) from the corresponding monomer vibrational wavenumber in cm^{-1} , band intensities (I_{OH}) in km mol^{-1} ; see also Ref. 34,75,83. Conformers used for further analysis in Sec. 6 are marked in bold.

Dimer	ΔE_{el}	ΔE_0	D_{el}	D_0	ω_{OH}	$\Delta\omega_{OH}$	I_{OH}
diphenyl ether + MeOH							
OH-O 1	0.9	1.8	28.2	23.0	3741	68	206
OH-O 2	2.6	2.9	26.5	21.8	3730	79	345
OH-π 1	0	0	29.1	24.7	3773	37	112
OH- π 2	0.2	0.3	28.8	24.4	3771	38	116
OH- π 3	6.0	5.1	23.1	19.6	3777	33	126
diphenyl ether + <i>t</i>-BuOH							
OH-O	-0.9	0.1	31.6	26.8	3721	64	250
OH-π 1	0	0	30.7	26.9	3755	31	110
OH- π 2	0.4	0.3	30.3	26.6	3748	37	119
OH- π 3	5.0	4.7	25.7	22.2	3743	42	150
OH- π 4	6.3	5.7	24.4	21.2	3747	38	153
CH- π 1	10.6	9.8	20.1	17.1	3785	0	13
CH- π 2	10.8	10.1	19.9	16.8	3785	0	12
CH- π 3	11.2	10.3	19.5	16.6	3784	1	11

band for each binding motif has been assigned for DPE–MeOH at 3623 cm^{-1} and 3607 cm^{-1} , respectively, but other assignments could not be ruled out. Fig. 4.0.3 shows improved jet spectra measured in this work. The high dilution of spectrum (a), realized by preparing a mixed gas bottle containing 0.16% methanol in helium, distinctly shows only the two proposed dimer bands. The band intensities are almost equal, which changes in spectrum (b), which was measured using the V-nozzle. The diphenyl ether concentration is slightly enhanced in this expansion (100°C in spectrum (a) versus 110°C in spectrum (b)) and so is the methanol concentration ($-20^\circ\text{C} \approx 0.5\%^a$). The band intensity of the band at 3623 cm^{-1} is enhanced relative to the other dimer band, suggesting this cluster being more stable. A spectrum measured with the *filet*-jet (Fig. 4.0.3 (c)), further confirms this finding with this

^aThe concentration estimation is in good agreement with the enhancement of the CH band integral by a factor of 5, taking into account the gain in signal by the V-nozzle of factor 1.6 (see Sec. 2.2.1).

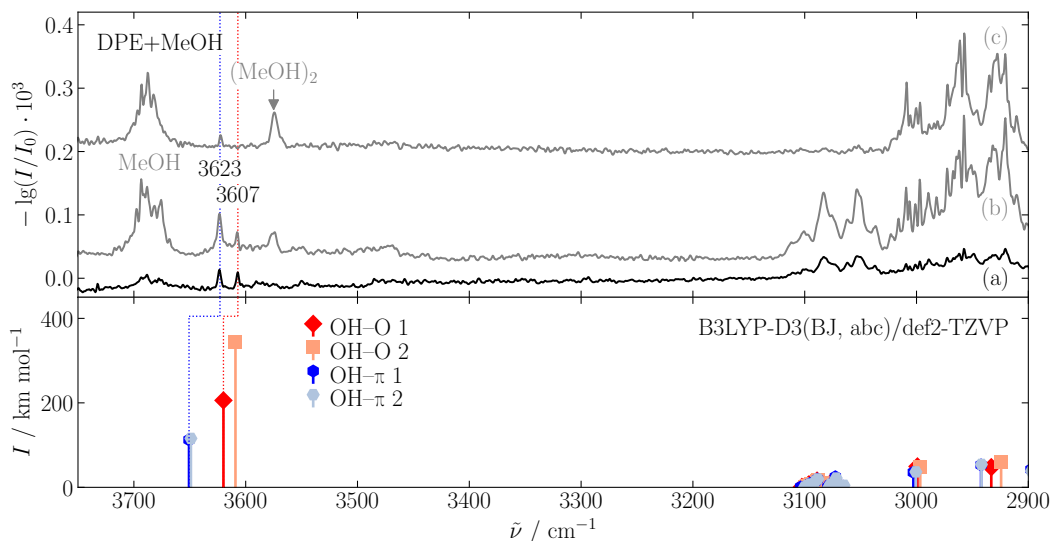


Figure 4.0.3: IR Spectra of diphenyl ether with methanol compared to theoretical predictions at B3LYP-D3(BJ, abc)/def2-TZVP level. The calculated frequencies are scaled (factor 0.9675) to the experimental MeOH monomer value (3686 cm^{-1}). OH–O conformers are denoted in red, OH– π in blue. Darker colors indicate the most stable conformer of each binding type.
 (a) double-slit nozzle (DPE: $100\text{ }^{\circ}\text{C}$, MeOH: 0.16 %, double-slit nozzle: $120\text{ }^{\circ}\text{C}$);
 (b) V-nozzle (DPE: $110\text{ }^{\circ}\text{C}$, MeOH: $-20\text{ }^{\circ}\text{C}$, V-nozzle: $130\text{ }^{\circ}\text{C}$);
 (c) *filet*-jet spectrum (DPE: $24\text{ }^{\circ}\text{C}$, 0.95/0.10 s, MeOH: $-25\text{ }^{\circ}\text{C}$, 0.10/2.20 s);
 see also Ref. 34,83.

band being the only observable mixed cluster band. Apparently, the expansion is colder in the *filet*- than in the *popcorn*-jet and clusters are less easily formed, as has already been proposed by M. Albrecht.⁵⁷ The different rotational band structures of the methanol monomer further support this finding. The calculated energy difference and the sequence of the spectral shifts are in line with the experimental observations, assigning the 3623 cm^{-1} band to a π -bound conformer and the 3607 cm^{-1} band to the oxygen-bound conformer (see Tab. 4.0.2). A contribution of the second OH– π conformer to the band at 3623 cm^{-1} cannot be ruled out. The only conflicting result is the underestimation of the downshift in case of the OH–O complex of as much as 11 cm^{-1} . Neither the furan complexes described previously nor the complexes of methylated anisoles with methanol have shown this behavior (see also Sec. 6.2).¹⁵⁸ Regarding the relative cluster abundance, spectrum (a) rules out an OH–O contribution of more than 35 % to the dimer population, taking into account the calculated infrared visibility. In spectra (b) and (c) it is restricted to

not more than 20%. This is in agreement with an experimental energy difference of 0.5 kJ mol^{-1} to 2 kJ mol^{-1} .¹⁵⁸

Verification for this assignment is provided by a multi-spectroscopic approach as published in Ref. 83. Mass selective IR/UV spectroscopy rules out trimer contributions and reproduces the band positions found *via* FTIR spectroscopy. Furthermore, the energetic ordering proposed by FTIR is confirmed, as the band at 3606 cm^{-1} vanishes when lowering the expansion temperature by using neon as the carrier gas. Further evidence is provided by microwave spectroscopy, where a single π -bound cluster is observed, also using neon as the carrier gas. The differentiation between the two energetically very close π -bound clusters is not straight forward, regarding the similarity of the predicted band positions of the OH stretching vibration as well as the calculated rotational constants. Nevertheless, an unambiguous assignment to the OH- π structure is possible with microwave spectroscopy, taking into account the dipole moment components. The value of 1.9 D for μ_c in OH- π 2 would lead to large c-type transitions, which is inconsistent with observation.

In summary, the proposed preference for π -binding of diphenyl ether-methanol is confirmed by all three applied experimental techniques. However, none could explicitly detect a second π -bound complex, despite its higher stability compared to the lowest OH-O structure, which hints at higher interconversion barriers for the latter.

To investigate the interconversion of the conformers, the barrier heights have been computed at B3LYP-D3(BJ, abc)/def2-TZVP level and are depicted in Fig. 4.0.4. A direct movement of the methanol from oxygen to π coordination without any conformational change of the diphenyl ether seems far from the lowest energy path, as neither the primary nor the secondary intermolecular interactions can be retained. A rough estimate for this barrier height is 10 kJ mol^{-1} .⁸³ The conversion of the less stable OH-O conformer into the global optimum OH- π 1 conformer most likely involves a sequential reaction pathway with the OH- π 2 conformer as an intermediate.⁸³ Switching the bonding site from the OH-O to the OH- π 2 conformer induces a chirality change of the *twist* structure of the diphenyl ether *via* the *skew* conformation, moving the methanol from the outer side of diphenyl ether to the inner cleft. The barrier height for this step is calculated to be 1.4 kJ mol^{-1} . About 0.9 kJ mol^{-1} account for the transition *via* the *skew* conformation (see Tab. 4.0.1).

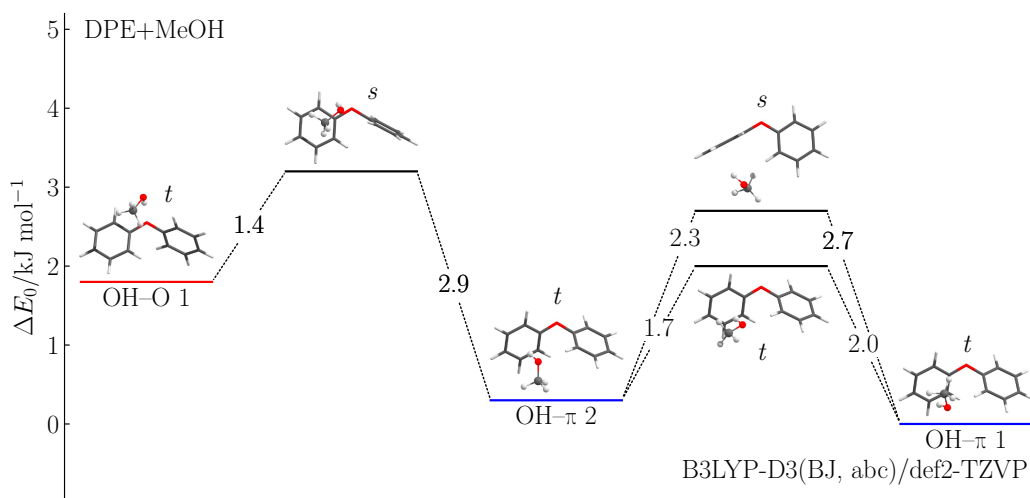


Figure 4.0.4: Calculated transition states (black bars, including harmonic ZPVE for all real modes) for the interconversion of the most stable dimer conformations of diphenyl ether–methanol. The conformation of the diphenyl ether is indicated by $t = \text{twist}$ and $s = \text{skew}$.

For the OH- π 2 to OH- π 1 conversion two pathways have been computed. A simple rotation of the methanol requires 1.7 kJ mol^{-1} . The primary OH- π interaction is maintained, while the accepting lone pair of methanol involved in the secondary CH-O interaction changes. A pathway maintaining both interactions involves another chirality change of the diphenyl ether. This energy barrier is estimated to be higher by 0.6 kJ mol^{-1} . The barrier being predicted to be higher for the interconversion of the π -bound complexes than for O-to- π conversion, raises the question, why the second π -bound conformer is not observed. Given the predicted shift being almost identical, a band overlap of the π -bound clusters in the FTIR and IR/UV spectra is conceivable. The observation of only OH- π dimer in the microwave spectra suggests that a complete relaxation to the most stable conformer has been achieved under the experimental conditions.

The spectrum of the diphenyl ether-*tert*-butyl alcohol is also revisited in this work, as the former study could not assign the bands without ambiguity.³⁴ One major problem was the presence of water in the spectra, which was solved by omitting the heating of the molecular sieve as described in Sec. 2.2.1. A comparison of the former and a newly measured spectrum can be found in the appendix (Fig. E.2). The newly recorded spectra are shown in Fig. 4.0.5. The CH stretching region contains two

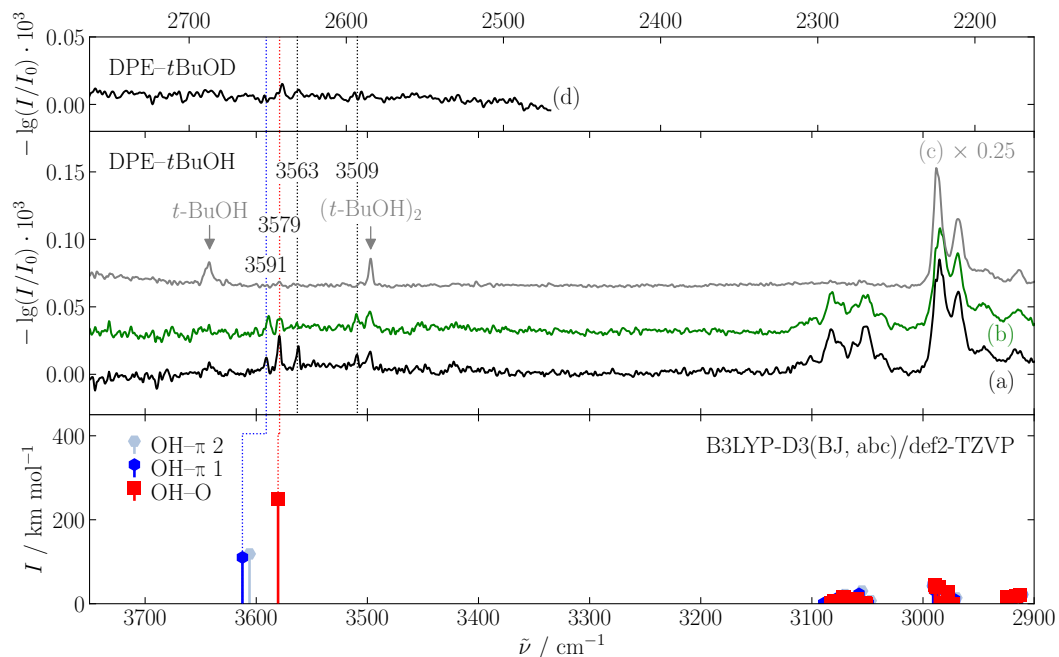


Figure 4.0.5: IR Spectra of diphenyl ether with *tert*-butyl alcohol compared to theoretical predictions at B3LYP-D3(BJ, abc)/def2-TZVP level. The calculated frequencies are scaled (factor 0.9621) to the experimental *t*-BuOH monomer value (3642 cm^{-1}). OH-O conformers are denoted in red, OH- π in blue. Darker colors indicate the most stable conformer of each binding type.

- (a) double-slit nozzle (DPE: $100\text{ }^{\circ}\text{C}$, *t*-BuOH: $-20\text{ }^{\circ}\text{C}$, double-slit nozzle: $120\text{ }^{\circ}\text{C}$);
 (b) argon added (DPE: $100\text{ }^{\circ}\text{C}$, *t*-BuOH: $-20\text{ }^{\circ}\text{C}$, +10% argon, double-slit nozzle: $120\text{ }^{\circ}\text{C}$);
 (c) *filet*-jet spectrum, scaled by factor 0.25 (DPE: $27\text{ }^{\circ}\text{C}$, 0.96/0.10 s, *t*-BuOH: $-10\text{ }^{\circ}\text{C}$, 0.10/2.22 s);
 (d) deuterated (DPE: $100\text{ }^{\circ}\text{C}$, *t*-BuOD: $-20\text{ }^{\circ}\text{C}$, double-slit nozzle: $120\text{ }^{\circ}\text{C}$);
 see also Ref. 34,75.

characteristic band structures for *tert*-butyl alcohol and diphenyl ether. The *tert*-butyl alcohol is diluted such that the monomer band is barely observable in the OH stretching region. Nevertheless, the homodimer band shows up at 3497 cm^{-1} ¹⁶² and so do four mixed cluster bands at 3591 cm^{-1} , 3579 cm^{-1} , 3563 cm^{-1} and 3509 cm^{-1} . Unfortunately, spectrum (a), which is more diluted than the previously recorded spectra, adds little information to the band assignment, besides ruling out water containing clusters. The three less shifted bands were observed before, while the furthest downshifted band was previously hidden among the cluster bands of water-*tert*-butyl alcohol and therefore not assigned. To narrow down the band assign-

ment, a spectrum with an added argon concentration of 10% was measured (see Fig. 4.0.5 (b)). The most intense band at 3579 cm^{-1} persists, however, so do the less and the furthest shifted bands. As no dimer is predicted to have such a large downshift, the band at 3509 cm^{-1} does probably stem from a trimer. Due to the DPE excess in the expansion, a trimer containing two diphenyl ether and one *tert*-butyl alcohol molecules seems most likely, however, the large spectral shift rather indicates two *tert*-butyl alcohol units with cooperative hydrogen bonding effects. The least shifted band has almost no intensity loss when adding argon to the expansion, in contrast to the band at 3579 cm^{-1} , and could thus be attributed to the most stable diphenyl ether–*tert*-butyl alcohol dimer. The band position is slightly more downshifted, which hints at argon complexation. This means that other effects could potentially enhance the intensity and no energetic ordering can be derived. The fact that the band at 3563 cm^{-1} is suppressed in the argon containing spectrum together with its relatively large downshift suggests a trimer origin. The disappearance may be explained by argon complexation competing with the addition of a second diphenyl ether molecule to a dimer. For comparison, a spectrum with the *filet*-jet has also been measured (Fig. 4.0.5 (c)), but since the DPE concentration is too low, even the strongest band can hardly be distinguished from the noise.

Comparison to the predicted band sequence indicates the presence of one OH– π and one OH–O cluster in the same order, which would match the related clusters with methanol as a donor. A measurement with deuterated *tert*-butyl alcohol (see Fig. 4.0.5 (d)) is also in agreement with this, regarding the intensities as well as the further downshifting of the band at 3579 cm^{-1} with deuteration, but the signal-to-noise ratio is not sufficient for a reliable assignment. The energetic ordering of the two dimers cannot be determined, as the difference in intensity is balanced by the difference in the predicted absorption cross section, resulting in a one-to-one ratio in the abundance. At best, a slight preference for the oxygen-bound cluster would be less contradicting, as its band is observable in almost all recorded spectra.

The need for verification of these findings was the start for a second multi-spectroscopic search in cooperation with the groups of M. Gerhards and M. Schnell.⁷⁵ Therein, the two proposed dimer bands were confirmed as such using mass selective IR/UV spectroscopy with neon as a carrier gas. Moreover, the assignment was substantiated by the comparison of the $S_1 \leftarrow S_0$ excitation energy calculated at

SCS-CC2/def2-TZVP level, which is lower for the OH- π complexes. Since the band at 3591 cm^{-1} is observed at an experimental UV excitation of $35\,906\text{ cm}^{-1}$ and the band at 3579 cm^{-1} with a UV excitation of $36\,250\text{ cm}^{-1}$, respectively, the former can be attributed to the π -bound cluster. Furthermore, the calculated difference between the excitation energies matches the experimentally observed transitions in the R2PI spectrum, as well. No further clusters were observed. Concerning the energy difference, a probable preference of the OH-O isomer is proposed from the relative intensities of the ion signal.

Microwave spectroscopy was applied to differentiate between the two π -bound conformers. In an expansion using helium as a buffer gas, the OH-O as well as the OH- π 1 cluster were identified by comparison to the calculated rotational constants. As was the case for diphenyl ether-methanol, the distinction between the π -bound conformers is supported by the dipole-moment components. The large μ_c value of 1.7 D in case of OH- π 2 is incompatible with the lack of c-type transitions in the spectrum. Unexpectedly, regarding the characteristics of the applied techniques (see Sec. 2.5), microwave spectroscopy also provides the most convincing answer to the question of energy sequence. When replacing the buffer gas with neon, the OH- π 1 cluster vanishes, due to the enhanced cooling effect of the heavier collision partner, leaving the OH-O conformer as the most stable complex. Thereby, the theoretical finding that π binding is less favored when enlarging the donor alkyl group has been confirmed experimentally.

The study of diphenyl ether clusters has recently been extended to a series by adding water and adamantanol as donor molecules.²⁰⁶ The not intuitively obvious finding of π binding being less preferred when enlarging the donor moiety upholds. Two main effects were identified: The twisting of the diphenyl ether and the dispersion contribution. With increasing size of the donor the diphenyl ether tends to be less strained from its optimal conformation in the oxygen-bound conformer, while the opposite applies to the π -bound conformer. The dispersion interaction density (DID) plots shown in the SI of Ref. 206, provide an illustrative explanation. While the location of the dispersion contribution of π -bound dimers does not change with larger alcohols, the donor moiety size increases the interaction surface at the phenyl ring for the oxygen-bound conformer and thus the dispersion contribution.

Furthermore, the electronically excited states of the clusters of diphenyl ether with methanol and *tert*-butyl alcohol have been characterized by the Gerhard's group.^{75,207} Both interaction motifs were observed in case of *tert*-butyl alcohol, only the π -bound structure in case of methanol. All structures are almost identical to the ground state ones. The OH stretching vibration is downshifted with respect to the ground state transition for the OH- π complexes, whereas the OH-O complex of DPE-MeOH exhibits an upshift. Both findings are explained by a shift of electron density from the ether oxygen atom to the interacting phenyl ring, strengthening the OH- π hydrogen bond and weakening the OH-O hydrogen bond. The ionized DPE-MeOH complex was also studied, but due to the positive charge on the diphenyl ether, the methanol interacts *via* its electron rich oxygen atom instead of forming hydrogen bonds.²⁰⁷

In summary, changing the size of the donor molecule from methanol to *tert*-butyl alcohol was sufficient to tip the balance slightly from π to oxygen preference. This somewhat counterintuitive behavior is contrary to the dibenzofuran clusters discussed in the previous chapter and explained by the non-planarity of the acceptor molecule. Despite the oxygen atom not being incorporated in the aromatic system, the energy difference between the two docking types is very subtle owing to more flexible secondary interactions. Thus, this provides an optimal test for quantum chemical methods, as will be further discussed in Sec. 6.2.

5 Clusters of Furans and Aromatic Alcohols

Changing the alcohol donor molecule from an alkyl to an aromatic one introduces new interaction possibilities. First of all, π stacking interactions come to mind if both molecules include a π system. Furthermore, the secondary interactions are largely affected, as CH groups are stronger hydrogen bond donors when the carbon is sp^2 hybridized than sp^3 .²⁰⁸ The following sections thus explore the clusters of the more simple acceptors furan and 2,5-dimethylfuran with aromatic alcohols of different π system sizes, namely 1-naphthol and phenol. The former has been thoroughly studied by SEP-R2PI spectroscopy⁷⁸, whereby it offers a test case for a multi-spectroscopic approach for gaining relative and absolute binding energies.

5.1 1-Naphthol

So far, only relative energies have been regarded in this thesis, as absolute dissociation energies of complexes are not easy to obtain.⁷⁷ One of the methods, that is able to do so is the SEP-R2PI experiment of the Leutwyler group in Bern (see Sec. 2.4). In a cooperative study including a three weeks research stay in Bern, complexes of furan and 2,5-dimethylfuran with 1-naphthol have been investigated. 1-Naphthol was chosen as a donor, since it is well studied using the SEP-R2PI setup for its complexation. For example hydrogen bonded solvent molecules with oxygen acceptors^{209–211} and π acceptors²¹² as well as dispersively bound clusters with alkanes^{79,80,87,212} have been investigated. Measurements of complexes of noble gases with 1-naphthol have been started with 1-naphthol–Ar during the research stay.²⁹

1-Naphthol has two rotational isomers, *cis* and *trans*, the latter being more stable by 3.2 kJ mol^{-1} as calculated at B3LYP-D3(BJ, abc)/def2-TZVP level. Experimental values range between 2.6 kJ mol^{-1} and 8.4 kJ mol^{-1} .^{213,214} The *trans* conformer is C_s -symmetric, while the hydroxy group is tilted by 7° out of the plane in the *cis* conformation. The two rotamers are separated by an energy barrier of 10.1 kJ mol^{-1} ²¹⁵,

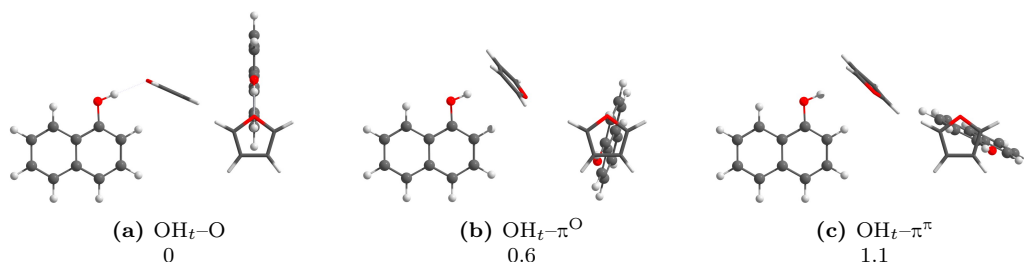


Figure 5.1.1: Structures and relative ZPVE-corrected energies (ΔE_0) in kJ mol^{-1} of the most stable dimers of 1-naphthol and furan calculated at B3LYP-D3(BJ, abc)/def2-TZVP level.

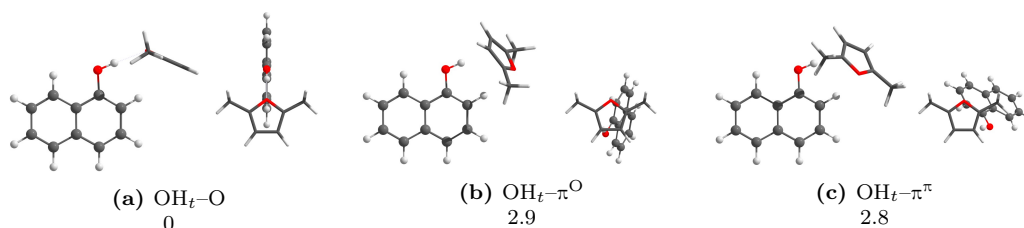


Figure 5.1.2: Structures and relative ZPVE-corrected energies (ΔE_0) in kJ mol^{-1} of the most stable dimers of 1-naphthol and 2,5-dimethylfuran calculated at B3LYP-D3(BJ, abc)/def2-TZVP level.

experimental values for the barrier height are not available.²¹⁶ The monomer conformation of 1-naphthol in the clusters is indicated by a 't' or 'c' subscript, respectively.

The global minimum dimer of furan and 1-naphthol is governed by two interactions: OH–O and CH– π , as shown in Fig. 5.1.1. It is C_s -symmetric and very similar to the benzene–1-naphthol dimer,³⁴ but the angle between the donor O–H bond and the acceptor plane is larger, due to the close interplay between the optimization of the hydrogen bond angle and the CH– π interaction. Only marginally less stable (see Tab. 5.1.1) is an OH– π dimer, with the furan rotated with respect to the 1-naphthol O–H bond. The hydroxy group is directed at C3, as in the π -bound conformers of furan derivatives with methanol (see Sec. 3.2). Here, the additional stabilization is gained by a CH–O interaction of the naphthol *ortho* hydrogen, indicated by the 'O' superscript to the primary interaction label π . This also shortens the distance to the furan plane such that the acceptor angle corresponds to that of the benzene complex. A third conformer was found to be stable with a similar interaction, but the furan oxygen atom does not serve as an acceptor site (' π ' superscript). The interconversion barriers of these conformers are expected to be very low. Conformers

Table 5.1.1: Dissociation energies of the dimers of furan and 2,5-dimethylfuran with 1-naphthol with (D_0) and without (D_{el}) harmonic zero-point vibrational energy calculated at B3LYP-D3(BJ, abc)/def2-TZVP level in kJ mol^{-1} . Energies relative to the most stable dimer (ΔE_{el} and ΔE_0) are given in kJ mol^{-1} , harmonic OH stretching wavenumbers (ω_{OH}) and shifts ($\Delta\omega_{\text{OH}}$) from the *trans*-1-naphthol monomer vibrational wavenumber in cm^{-1} , band intensities (I_{OH}) in km mol^{-1} . Conformers used for further analysis in Sec. 6 are marked in bold.

Dimer	ΔE_{el}	ΔE_0	D_{el}	D_0	ω_{OH}	$\Delta\omega_{\text{OH}}$	I_{OH}
Furan + 1NpOH							
OH_t-O	0	0	26.3	22.7	3698	103	639
OH _t - π^{O}	1.5	0.6	24.8	22.1	3705	96	495
OH _t - π^{π}	1.9	1.1	24.5	21.7	3681	120	589
OH _c - π	5.2	4.3	21.1	18.5	3739	62	228
OH _c - π	7.6	6.6	18.7	16.1	3717	84	226
OH _c -O	6.1	5.5	20.2	17.3	3735	66	278
OH _c -O	8.8	7.0	17.6	15.8	3781	20	44
π_t - π	6.3	4.4	20.0	18.4	3803	-1	66
π_t - π	6.7	5.1	19.6	17.7	3801	0	65
π_t - π	5.8	4.4	20.6	18.4	3799	2	58
π_t - π	7.0	5.1	19.3	17.7	3803	-2	62
2,5-Dimethylfuran + 1NpOH							
OH_t-O	0	0	35.7	31.2	3649	152	746
OH _t - π^{O}	4.0	2.9	31.7	28.3	3666	135	580
OH _t - π^{π}	3.8	2.8	31.9	28.4	3649	152	568
OH _c -O	5.7	5.1	30.0	26.1	3663	138	546
OH _c - π	5.4	4.4	30.3	26.8	3711	91	242
OH _c - π	6.1	4.9	29.6	26.4	3706	95	212
π_t - π	8.8	7.1	26.9	24.1	3801	0	56
π_t - π	9.7	8.1	26.0	23.1	3801	0	64
π_t - π	10.6	8.8	25.1	22.4	3802	-1	65
π_t - π	11.5	10.0	24.2	21.2	3802	-1	64
π_c - π	12.2	10.6	23.4	20.6	3794	7	34

including the *cis* conformation of the 1-naphthol monomer as well as conformers with π stacking being the major interaction are not compatible in energy. They are depicted in Fig. D.5 in the appendix. The most stable of the *cis* dimers is π -bound.

Adding methyl groups to the furan acceptor does not change the most stable conformation, as can be seen in Fig. 5.1.2. However, it affects the structure of the less stable π -bound complexes. The major interactions to C3 remain, but the furan plane is shifted sideways, possibly caused by a dispersive interaction of the methyl group with the naphthol π system. This effect is larger for the doubly π -bound structure $\text{OH}_t\text{-}\pi^\pi$, which further supports the presence of dispersion interactions, given that the methyl group has a more favorable position in this dimer. Thereby, the energy sequence between the two π -bound conformations is reversed with methylation. The relative energy penalty for π binding itself increases significantly with methylation. To a smaller extent, this has also been found for methanol as a donor (see Sec. 3.2). It remains unclear whether this is due to the influence of a destabilization of the π complex or a stabilization of the oxygen-bound complex.

FTIR measurements of these complexes have been the scope of a research internship by M. Lange.²¹⁷ The resulting spectra measured using the *popcorn*-jet are compared to the predicted band positions in Fig. 5.1.3. Furthermore, the spectrum of benzene-1-naphthol is reproduced from Ref. 34. The most intense band in the OH stretching region at 3655 cm^{-1} is attributed to the *trans* configuration of 1-naphthol monomer. In the uppermost spectrum, the *cis* conformer is also detected at 3663 cm^{-1} . These values are in excellent agreement with those obtained by IR dip spectroscopy.²¹⁸ In the spectra of 2,5-dimethylfuran-1-naphthol a second very intense band at 3523 cm^{-1} can be assigned to the DMFu-1NpOH dimer. It is rather broad, possibly resulting from the heating of the nozzle. Unluckily, the predicted band positions for the oxygen and π -bound dimers are identical. Thus, the conformer assignment to the OH-O structure is mainly based on the predicted large energy difference of 2.8 kJ mol^{-1} (see Tab. 5.1.1). The fact that an overestimation of 20 cm^{-1} is commonly observed for oxygen-bound clusters, but rather unusual for π -bound clusters supports this assignment. However, it is worth mentioning that oxygen-bound furan clusters with more weakly bound alkyl alcohols do not show

^aThe intensity difference of the 1-naphthol bands between spectrum (b) and (c) despite identical sample temperatures might be due to a defective solenoid valve.

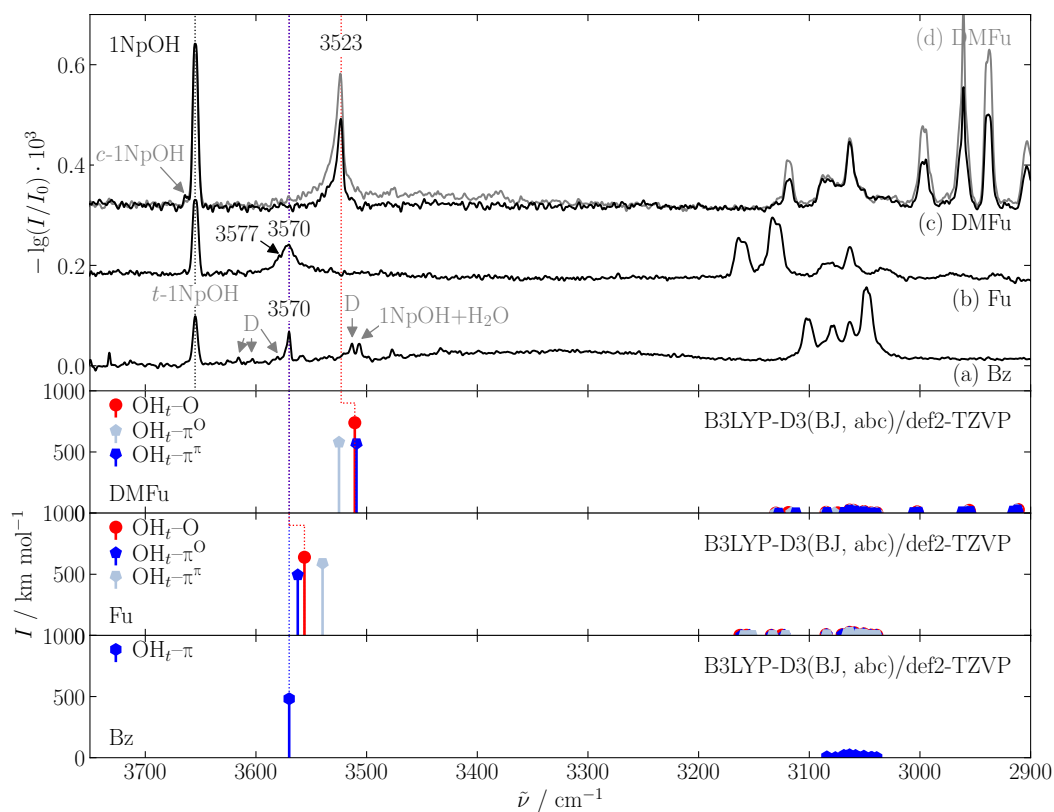


Figure 5.1.3: IR Spectra of 2,5-dimethylfuran, furan and benzene with 1-naphthol compared to theoretical predictions at B3LYP-D3(BJ, abc)/def2-TZVP level. The calculated frequencies are scaled (factor 0.9615) to the experimental 1NpOH monomer value (3655 cm^{-1}). OH-O conformers are denoted in red, OH- π in blue. Darker colors indicate the most stable conformer of each binding type.

- (a) benzene-1-naphthol, reproduced from Ref. 34 (Bz: $-20\text{ }^\circ\text{C}$, 1NpOH: $120\text{ }^\circ\text{C}$, double-slit nozzle $140\text{ }^\circ\text{C}$);
 (b) furan-1-naphthol (Fu: $-25\text{ }^\circ\text{C}$, 1NpOH: $120\text{ }^\circ\text{C}$, V-nozzle $140\text{ }^\circ\text{C}$);
 (c) 2,5-dimethylfuran-1-naphthol (DMFu: $-20\text{ }^\circ\text{C}$, 1NpOH: $120\text{ }^\circ\text{C}$, V-nozzle $140\text{ }^\circ\text{C}$);
 (d) 2,5-dimethylfuran-1-naphthol (DMFu: $-10\text{ }^\circ\text{C}$, 1NpOH: $120\text{ }^\circ\text{C}$, V-nozzle $140\text{ }^\circ\text{C}$).^a

such a large overestimation. Hence, a contribution of π -bound complex to the dimer band cannot be ruled out completely.

The spectral features for the furan–1-naphthol mixture are similar. Again, only one mixed dimer band is observed, here at 3570 cm^{-1} . It is less downshifted than for 2,5-dimethylfuran and even broader. The band shape is more symmetrical than for 2,5-dimethylfuran. Drawing parallels to 2,5-dimethylfuran, the cluster band is assigned to the oxygen-bound dimer conformation. The downshift overestimation of 18 cm^{-1} is in good agreement. With the energy difference between the binding sites being so low for furan–1-naphthol, a contribution of the OH– π dimer has to be discussed. A shoulder at 3577 cm^{-1} could hint at this dimer being present as well. Especially when taking into account the spectrum of benzene–1-naphthol, shown in trace (a) of Fig. 5.1.3. It has been measured using the double slit nozzle. Therefore, the overall band strength is lower and small features of 1-naphthol dimers marked with 'D' at 3616 cm^{-1} , 3604 cm^{-1} , 3579 cm^{-1} and 3513 cm^{-1} are observable. Due to water traces in the expansion mixture, the water–1-naphthol dimer is also identified at 3507 cm^{-1} .²¹⁸ The mixed cluster band coincides with the one for furan–1-naphthol at 3570 cm^{-1} . A similar result has been reported for furan–phenol and benzene–phenol in solution.²¹⁹ The band assignment for benzene–1-naphthol is unambiguous, since the next higher energy conformers are of π -stacking type ($\Delta E_0 = 1.5\text{ kJ mol}^{-1}$ at B3LYP-D3(BJ)/def2-TZVP level) and thus would not show a spectral downshift of the OH stretching vibration.³⁴ Furthermore, this observed spectral downshift compares well to that of benzene–phenol.^{220,221} It is slightly overestimated by 3 cm^{-1} by the predictions at B3LYP-D3(BJ, abc)/def2-TZVP level. This indicates, that the frequency predictions for the π -bound furans should also be in good agreement with experiment. However, a difference in the characteristics of the prediction between five and six membered rings is possible as well, as has been discussed for the 2,3-benzofuran–methanol cluster (see Sec. 3.4.1).

To evaluate the probability of π clusters being present, a transition state search for the three most stable furan–1-naphthol dimers was applied and is shown in Fig. 5.1.4. No transition state could be located between the two π -bound conformers. The optimization led to a geometry almost identical to the OH_t– π^π conformer without any imaginary frequency. This emphasizes the shallow potential energy surface and thus the population of both π -bound clusters is unlikely. In contrast, a surprisingly large

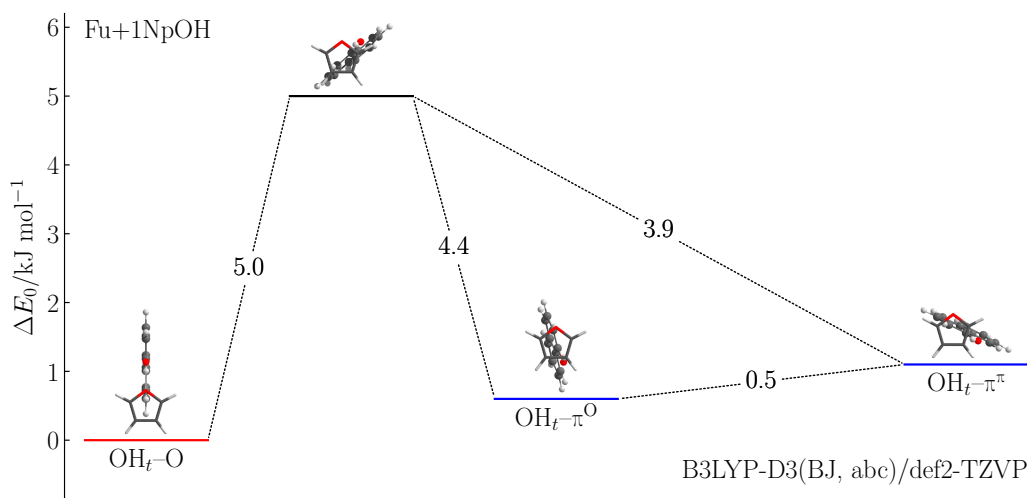


Figure 5.1.4: Calculated transition states (black bars, including harmonic ZPVE for all real modes) for the interconversion of the most stable dimer conformations of furan–1-naphthol at B3LYP-D3(BJ, abc)/def2-TZVP level.

barrier of 4 kJ mol^{-1} is predicted for the conversion from the π - to the oxygen-bound dimer, perhaps enabling the presence of both binding types. The same transition state geometry was optimized for either of the two π structures. Presumably, the conversion of $\text{OH}_t\text{-}\pi^0$ to $\text{OH}_t\text{-O}$ includes $\text{OH}_t\text{-}\pi^\pi$ as an intermediate step. The influence of the methyl groups is difficult to assess, since both a hindered furan rotation and a stabilization of the transition state are conceivable.

As stated at the beginning of this chapter, SEP-R2PI measurements of these clusters have been carried out at the group of S. Leutwyler in Bern. Preliminary results have been obtained during a three weeks research stay. The final results have been published in Ref. 89 and are discussed below. For this technique, as described in Sec. 2.4, first of all, one-color resonant-two-photo ionization (R2PI) spectra need to be measured to find the proper excitation energy for the pump step. These are depicted in Fig. 5.1.5. The large downshift of the origin bands of the clusters compared to the 1-naphthol monomer confirms that the observed clusters mainly interact *via* the hydroxy group and not the π system of the 1-naphthol molecule.⁷⁹ For furan–1-naphthol, two conformers could be identified in the R2PI spectra using UV/UV holeburning, marked with A and B in Fig. 5.1.5. Due to the proximity of the conformers' origin bands, the spectral separation is not possible and thus the dissociation

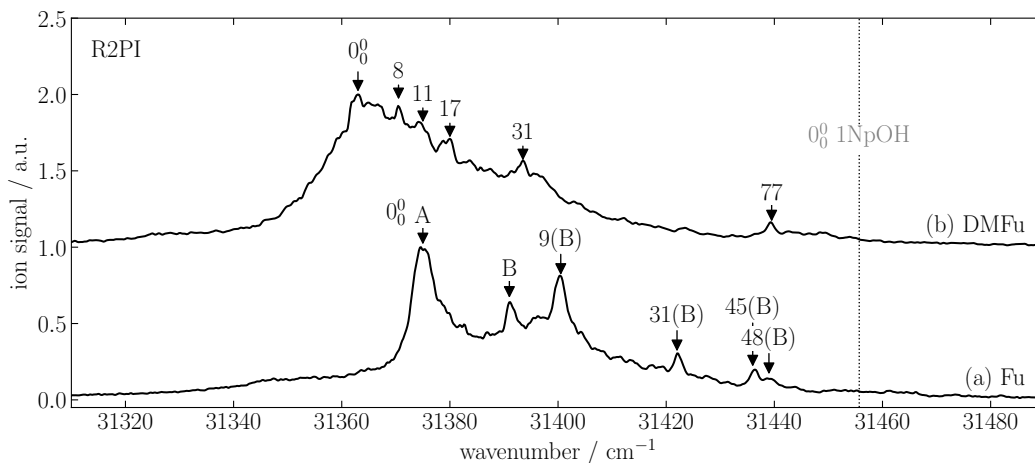


Figure 5.1.5: One-color resonant-two photon ionization (R2PI) spectra of (a) furan–1-naphthol and (b) 2,5-dimethylfuran–1-naphthol. The position of the origin transition of 1-naphthol monomer is indicated by a dashed line. Reproduced from Ref. 89.

energy cannot be determined separately. UV/UV holeburning has also been applied to 2,5-dimethylfuran–1-naphthol, showing no indication for the presence of a second conformer. The band is broader than that of furan–1-naphthol, which can be interpreted as a consequence of a stronger coupling between the $S_1 \leftarrow S_0$ electronic excitation and the low-frequency intermolecular vibrations. This would imply a larger change of the intermolecular coordinates of the 2,5-dimethylfuran–1-naphthol dimer upon electronic excitation than for furan–1-naphthol.⁸⁹ The observation of two conformers in case of furan and a single conformer in case of 2,5-dimethylfuran is in agreement with the FTIR spectra discussed previously. It hints at a lowering of the isomerization barrier when methyl groups are added to furan and/or a larger energy difference between the competing isomers.

To obtain an experimental dissociation energy, first the vibrational levels above and below the dissociation energy need to be known. In case of furan–1-naphthol this is achieved by the dump spectrum, which measures the decrease of the pump laser’s R2PI ion signal when the dump laser is in resonance with a transition to a S_0 vibrational level with significant intensity. The hot-band probed SEP spectrum mirrors this spectrum up to a band observed at 1800 cm^{-1} , giving the lower boundary of the dissociation energy as shown in Fig. 5.1.6. The first band in the dump spectrum, which does not appear in the hot-band probed SEP spectrum is at 1848 cm^{-1} and

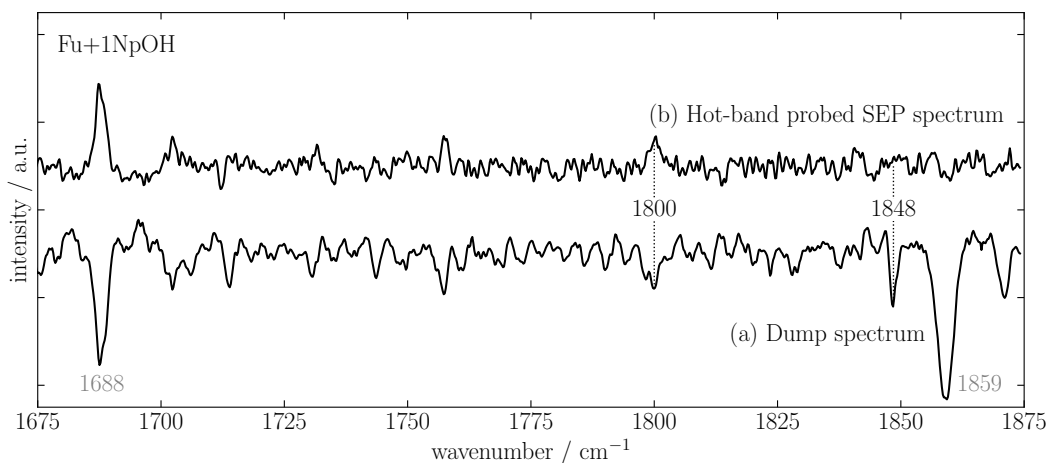


Figure 5.1.6: (a) Dump spectrum and (b) hot-band probed SEP spectrum of furan–1-naphthol. Reproduced from Ref. 89.

thus marks the upper limit for the dissociation energy. The true value is anywhere within this energy window with equal probability. Therefore, the average of these two bands is stated as the experimentally observed value and the uncertainty marks the size of the spectral window. Thus, the dissociation energy obtained for furan–1-naphthol is $(1824 \pm 24) \text{ cm}^{-1}$, corresponding to $(21.8 \pm 0.3) \text{ kJ mol}^{-1}$, for the more stable cluster, as the signal breakoff of the less stable cluster will be unnoticed.

In case of 2,5-dimethylfuran–1-naphthol the dispersed fluorescence spectrum has been used to determine the upper D_0 limit, due to a better signal-to-noise ratio than the dump spectrum. The last band, that is observed in the hot-band probed SEP spectrum is at 3024 cm^{-1} , as shown in Fig. 5.1.7. The next band, that is observed in the fluorescence, but not the hot-band probed SEP spectrum, limits the upper boundary of the dissociation energy to 3243 cm^{-1} . Thereby, the dissociation energy of 2,5-dimethylfuran–1-naphthol is bracketed to $(3134 \pm 110) \text{ cm}^{-1}$ or $(37.5 \pm 1.3) \text{ kJ mol}^{-1}$, respectively.

Comparing to the calculated harmonic dissociation energies, the furan complex shows good agreement with an overestimation by theory of 0.9 kJ mol^{-1} . Given that the calculation is harmonic and the zero-point vibrational anharmonicity along the intermolecular modes can be substantial, the true overestimation is probably significantly larger than 0.9 kJ/mol . Interestingly, other dispersion corrected DFT

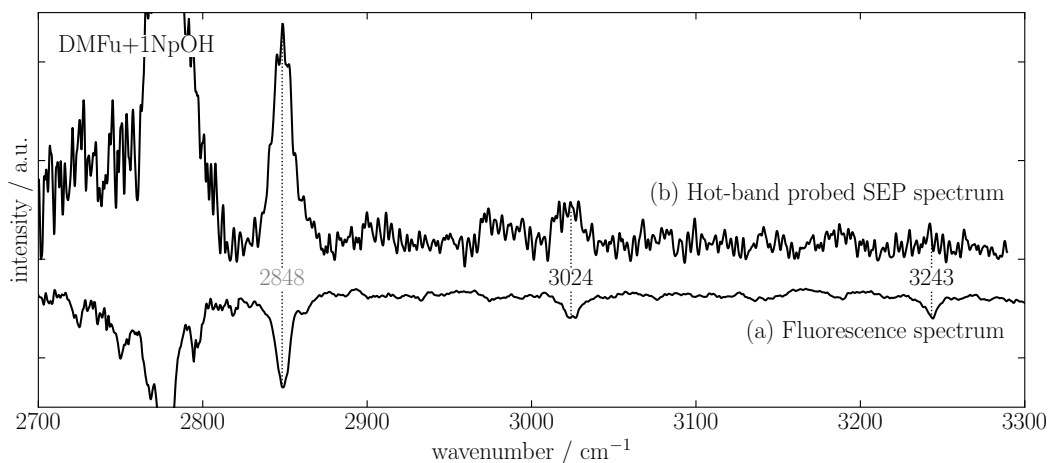


Figure 5.1.7: (a) Fluorescence spectrum and (b) hot-band probed SEP spectrum of 2,5-dimethylfuran–1-naphthol. Reproduced from Ref. 89.

methods tend to slightly underestimate the binding energy.⁸⁹ When neglecting the three-body dispersion term, the binding energy of the most stable furan–1-naphthol dimer is reduced by 0.2 kJ mol^{-1} (see Tab. D.5). As can be expected, this energy difference is largest for the π stacked dimers with up to 1.1 kJ mol^{-1} . The difference between calculated and experimental value is much larger for 2,5-dimethylfuran–1-naphthol. Here, an underestimation of 6.3 kJ mol^{-1} is observed, similar to other DFT methods.⁸⁹ Although some of this discrepancy will likely be reduced if the theoretical calculation includes anharmonicity, this unusually large discrepancy between theory and experiment despite the good prediction in the related furan case necessitates a more detailed investigation. The clusters of methane–1-naphthol and ethane–1-naphthol have shown unusually weak bands in the hot-band probed SEP spectrum, which are proposed to be above the dissociation limit. This is possible by long-lived vibrational states, whose lifetime exceeds the $3 \mu\text{s}$ time frame used in the experiment.⁸⁰ In a similar manner, the methyl groups of 2,5-dimethylfuran could lead to vibrational energy storage in the methyl torsion modes. These are weakly coupled to the modes leading to vibrational predissociation and thus the dissociation is slow. Thereby, the band at 3024 cm^{-1} might actually correspond to the upper limit for the dissociation energy. The lower limit would then be determined by the band at 2848 cm^{-1} , bracketing the dissociation energy to $(2936 \pm 88) \text{ cm}^{-1}$

$(35.1 \pm 1.1) \text{ kJ mol}^{-1}$). This value is closer to the predicted one, but the underestimation of 3.9 kJ mol^{-1} is still significantly larger than for similar complexes.⁸⁹

Regarding the experimentally determined binding energies, the binding of 2,5-dimethylfuran to 1-naphthol is at least 11.9 kJ mol^{-1} stronger than of furan. The predicted difference is smaller (8.5 kJ mol^{-1}), nevertheless, it amounts to 30 % of the total binding energy. The calculated geometries being almost identical, this seems to be a large effect. However, similar values are obtained when comparing the predicted binding energies of the methanol complexes of the two acceptors (see Sec. 3.2), for the oxygen-bound, as well as the π -bound structures. The same holds true for phenol as a donor (see Sec. 5.2), still without major geometry changes. Thus, the main difference will probably be attributed to the change in the electron density of the π system. A corresponding effect can be observed when comparing the spectral downshifts of the OH stretching vibration in the FTIR spectra. The one for the furan cluster amounts to 64 % of that of the 2,5-dimethylfuran cluster for the oxygen-bound complexes with 1-naphthol and methanol and is only marginally larger for the π -bound clusters with methanol. Drawing these close relations between the different donor molecules, experimental data of the binding energies of the methanol and phenol clusters would be helpful to discriminate between shortcomings on the experimental and theoretical side. Unfortunately, these will be more difficult to obtain with the SEP-R2PI setup.

Overall, the usage of this system as a molecular scale seems promising less in the regard of oxygen- π -balances, but more in terms of hydrogen bonding *versus* π interactions ('edge' or 'face' coordination), as has been established by the Leutwyler group. FTIR spectroscopy can help to analyze systems, that are challenging for the SEP-R2PI technique, for example due to π - π -interactions. Such is the case of 2,3-benzofuran-1-naphthol. By enlarging the π system, the preference changes from hydrogen bonding in case of furan to π stacking interactions in case of 2,3-benzofuran (see Tab. D.6 in the appendix). Intrinsically, it will be difficult for FTIR spectroscopy to sense a conformer if the π stacking interactions dominate the cluster formation such that the OH stretching frequency is almost unaffected. This is the case for 2,3-benzofuran-1-naphthol where the downshift of the most stable conformer is predicted to 4 cm^{-1} . Thus, a multi-spectroscopic approach, possibly including microwave spectroscopy, should be aimed for.

Table 5.2.1: Dissociation energies of the dimers of furan and 2,5-dimethylfuran with phenol with (D_0) and without (D_{el}) harmonic zero-point vibrational energy calculated at B3LYP-D3(BJ, abc)/def2-TZVP level in kJ mol^{-1} . Energies relative to the most stable dimer (ΔE_{el} and ΔE_0) are given in kJ mol^{-1} , harmonic OH stretching wavenumbers (ω_{OH}) and shifts ($\Delta\omega_{OH}$) from the monomer vibrational wavenumber in cm^{-1} , band intensities (I_{OH}) in km mol^{-1} . Conformers used for further analysis in Sec. 6 are marked in bold.

Dimer	ΔE_{el}	ΔE_0	D_{el}	D_0	ω_{OH}	$\Delta\omega_{OH}$	I_{OH}
Furan + PhOH							
OH–O	0	0	25.6	21.6	3706	93	502
OH– π^O	1.4	0.5	24.2	21.1	3710	89	388
OH– π^π	1.7	0.9	23.9	20.7	3689	111	473
OH– π	4.7	3.7	20.9	17.9	3709	90	393
π – π	12.2	10.3	13.3	11.3	3799	1	55
2,5-Dimethylfuran + PhOH							
OH–O	0	0	34.5	30.2	3663	136	576
OH– π^O	3.8	2.9	30.8	27.3	3673	126	448
OH– π^π 1	3.5	2.6	31.1	27.6	3655	144	480
OH– π^π 2	3.9	3.2	30.7	27.0	3668	131	395

5.2 Phenol

In course of the research internship by M. Lange the influence of different aromatic donors on the clustering with furans has been explored. Phenol is the smallest aromatic alcohol and many studies regarding its clustering characteristics have been published. These include the homoaggregation^{32,222–225}, van-der-Waals clusters^{26,193,226,227}, as well as hydrogen bonded clusters with water^{193,222,226,228–231}, alcohols^{193,225,228–230,232}, carbohydrates²³³, ethers^{228–230,234} or π acceptors.^{220,221,228,234–237} Even a molecular scale system using anisole as the acceptor has been investigated by REMPI spectroscopy, revealing the oxygen-bound complex as more stable.²³⁸ The furan–phenol complex has been studied theoretically in the context of the interplay between π electron delocalization and hydrogen bonding.¹³¹ However, the possibility of π binding has not explicitly been addressed. Furthermore, an infrared study in carbon tetrachloride solution has suggested, that furan and its methylated derivatives act as π bases in hydrogen bonding with phenol, while dibenzofuran shows similarity to the complexation with polyacenes.²¹⁹

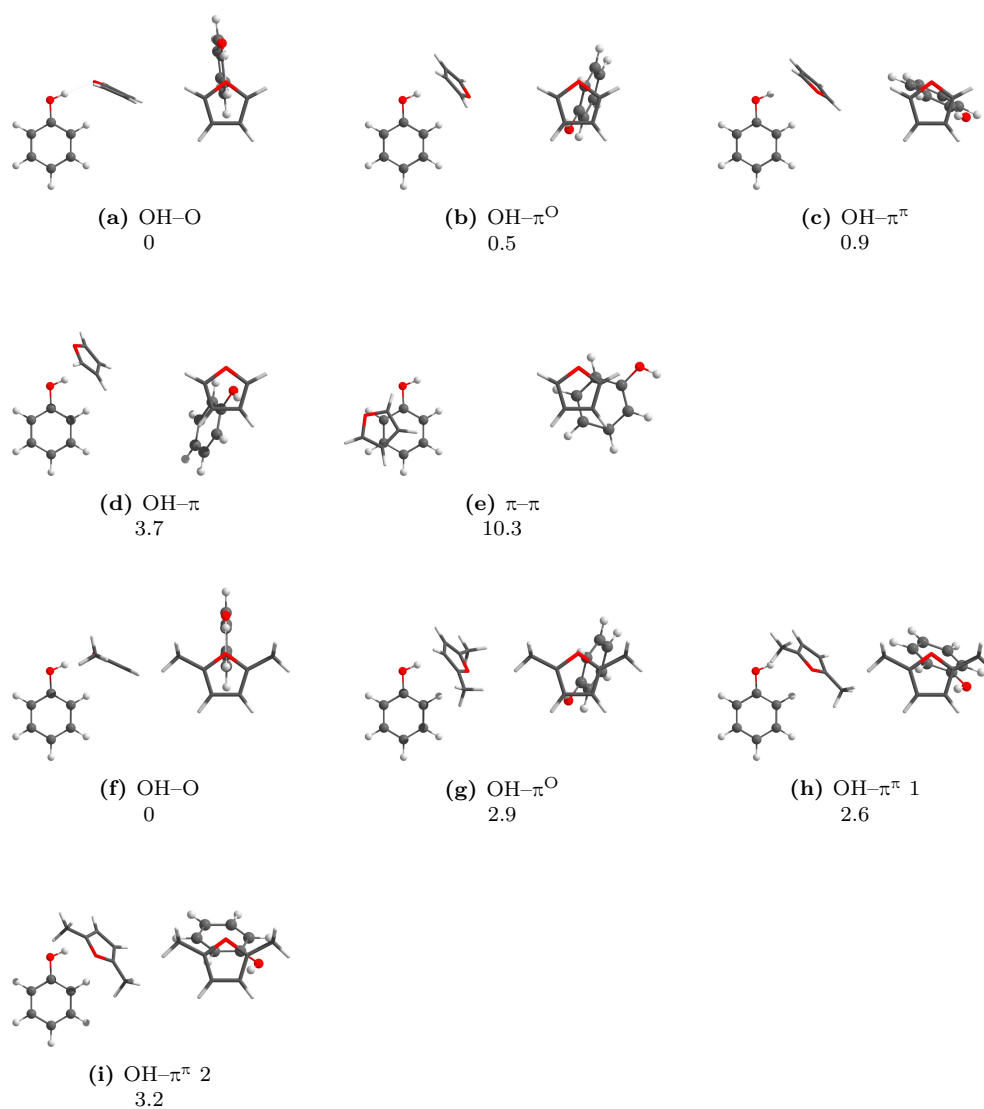


Figure 5.2.1: Structures and relative ZPVE-corrected energies (ΔE_0) in kJ mol^{-1} of the most stable dimers of phenol and furan derivatives calculated at B3LYP-D3(BJ, abc)/def2-TZVP level.

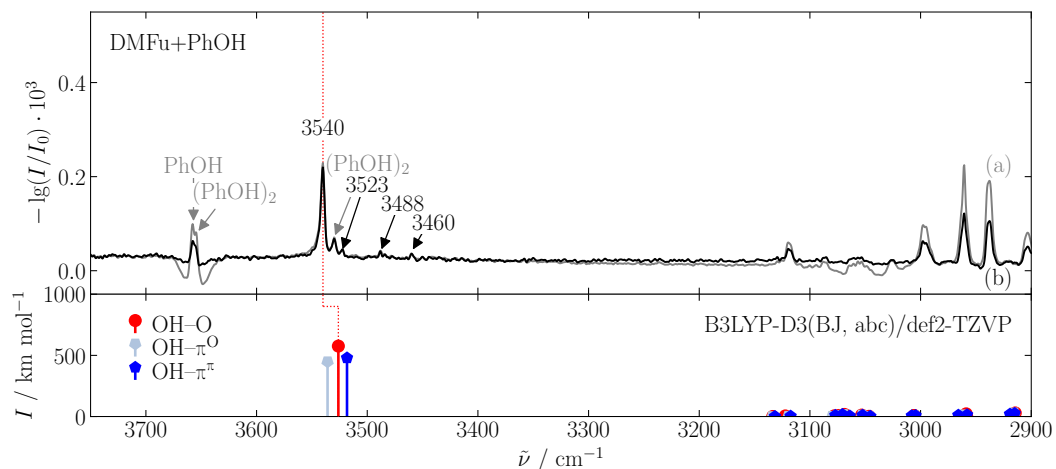


Figure 5.2.2: IR Spectra of 2,5-dimethylfuran and phenol compared to theoretical predictions at B3LYP-D3(BJ, abc)/def2-TZVP level. The calculated frequencies are scaled (factor 0.9626) to the experimental PhOH monomer value (3657 cm^{-1}). OH–O conformers are denoted in red, OH– π in blue. Darker colors indicate the most stable conformer of each binding type. (a) 2,5-dimethylfuran–phenol (DMFu: $-20\text{ }^{\circ}\text{C}$, PhOH: $40\text{ }^{\circ}\text{C}$, V-nozzle $60\text{ }^{\circ}\text{C}$); (b) same spectrum as (a) using the post-scans as background.

As shown in Tab. 5.2.1, the oxygen-bound species of furan–phenol and 2,5-dimethylfuran–phenol have been identified as the most stable using B3LYP-D3(BJ, abc)/def2-TZVP. The three main binding geometries found in the previous section for the dimers involving 1-naphthol are retained when shortening the π system of the donor, as can be seen in Fig. 5.2.1. The energy differences for the clusters containing furan are rather small and similar to those of 1-naphthol–furan, which indicates that the size of the π system does not influence the molecular balance in this case. Two more conformers have been found containing OH– π and π – π interactions, respectively, but are unfavorable. A larger effect might have been expected for the methylated furan, regarding the methyl– π interactions, but apparently the π system does not have a strong influence on the energetic sequence either. The overall picture is generally analogous to the 1-naphthol clusters.

Using the *popcorn*-jet a spectrum of the 2,5-dimethylfuran–phenol mixture has been measured and is shown in Fig. 5.2.2. Monomer and dimer bands of phenol are observed at 3657 cm^{-1} , 3654 cm^{-1} and 3530 cm^{-1} , respectively.^{222,224} The spectrum from the probe-scans (a) has broad negative bands, that probably result from warm phenol molecules in the jet chamber, that are blown out of the absorption path by

the supersonic expansion. These can be compensated using the first post-scans as the background (see Sec. 2.2.1), as shown in Fig. 5.2.2 (b). Since the post-scans still include the monomer signal, the band intensities are not reliable anymore.

The mixed dimer is observed at 3540 cm^{-1} and seems to be quite abundant, even taking into account that the monomer signal might be drastically decreased by the background band. Based on the energy difference to the most stable OH- π conformer of 2.6 kJ mol^{-1} it can be assigned to the OH-O structure. The predicted downshift is also in good agreement, so is the comparison to 2,5-dimethylfuran-1-naphthol. Smaller bands are observed at 3523 cm^{-1} , 3488 cm^{-1} and 3460 cm^{-1} , whose origins remain unclear without further measurements. The one at 3523 cm^{-1} could be the π -bound dimer, but regarding the energy difference, the assignment of larger clusters to all three bands is more probable. Contributions of the phenol homotrimer can be ruled out, as the bands have been reported at 3441 cm^{-1} and 3449 cm^{-1} using IR/UV double resonance.²²⁴

Although the small energy difference between the binding sites makes furan-phenol a promising benchmarking system, so far no FTIR spectrum has been measured, since the small frequency gap of 4 cm^{-1} probably prevents an unambiguous assignment. Microwave spectroscopy or possibly IR/UV double resonance could be better suited for the identification of the most stable complex, but a quantitative analysis of the cluster abundances would be challenging.

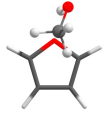
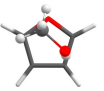
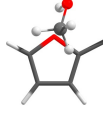
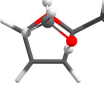
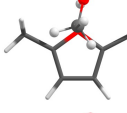
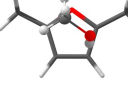
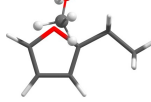
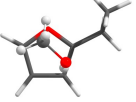
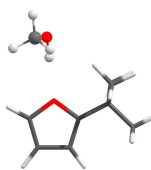
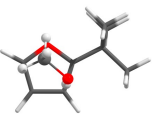
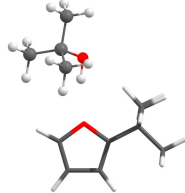
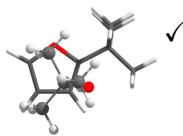
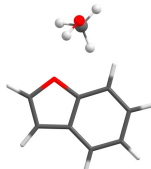
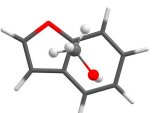
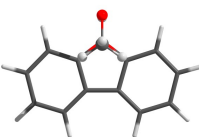
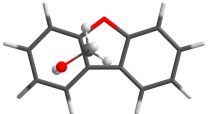
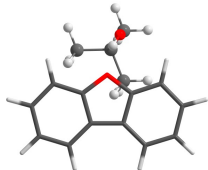
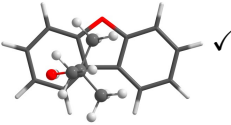
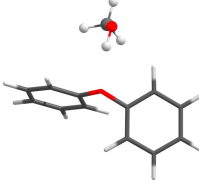
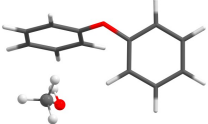
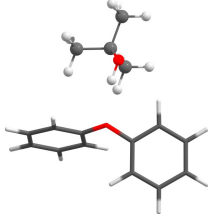
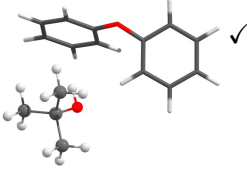
6 Discussion

An overview of the molecular scales studied in this thesis is given in Tab. 6.0.1 for the alkyl alcohols and Tab. 6.0.2 for the aromatic alcohols, respectively. For most systems, clusters with oxygen and π binding could be observed. Exceptions are the *tert*-butylfuran clusters as well as the clusters of the aromatic alcohols. For the dibenzofuran-*tert*-butyl alcohol cluster, hints in the FTIR spectrum for the presence of an oxygen-bound conformer could not be confirmed by IR/UV and microwave spectroscopy.

The experimentally observed docking site preference for the molecular scales is depicted in Fig. 6.0.1 together with the energy difference calculated at B3LYP-D3(BJ, abc)/def2-TZVP level. For methanol as a donor, the π preference seems to increase with alkylation of the furan, as would generally be expected. Interestingly, this is not captured by B3LYP-D3(BJ, abc)/def2-TZVP, which predicts a π preference for the pure furan and its decrease with methylation (see Sec. 3.2). Considering that the OH-O conformer observed by microwave spectroscopy is only the second most stable predicted by B3LYP-D3(BJ, abc)/def2-TZVP, this deficiency is even more evident.

Dibenzofuran is another case where the observed OH-O conformer is not the predicted local minimum structure. However, the energy difference between those conformations is small (see Sec. 3.4.2). Comparing the sequence of benzannulation, the π preference seems most pronounced for 2,3-benzofuran, which may not be expected. Experiment and theory agree on this finding. This might be an intrinsic effect of the binding energies of the docking motifs, as illustrated in Fig. 6.0.2. The only binding motif found uniformly for each acceptor is the OH-O^t conformation. Its binding gets stronger with increasing the π system. The OH-O^p conformation is less affected by the π system size, the CH-O interaction to the benzene side (OH-O^p6) being favored over the furan side (OH-O^p5). π binding to the furan ring has a similar dependence on the π system size as the OH-O^t conformation, while the binding to the benzene ring is least affected. All in all, when comparing the experimentally

Table 6.0.1: Overview of the molecular scale systems including alkyl alcohols. Conformers found in experiment are marked with a check-mark. A question-mark denotes ambiguous assignments.

MeOH		<i>t</i> -BuOH					
O-conformer	exp.	π -conformer	exp.	O-conformer	exp.	π -conformer	exp.
	✓ ^a		✓				
	✓		✓				
	✓		✓				
	?		?				
			✓				✓
	✓		✓				
	✓ ^a		✓		?		✓
	✓		✓		✓		✓

^aExperimentally observed structure type differs from the calculated minimum.

Table 6.0.2: Overview of the molecular scale systems including aromatic alcohols. Conformers found in experiment are marked with a check-mark. A question-mark denotes ambiguous assignments.

PhOH		1NpOH	
O-conformer exp.	π -conformer exp.	O-conformer exp.	π -conformer exp.

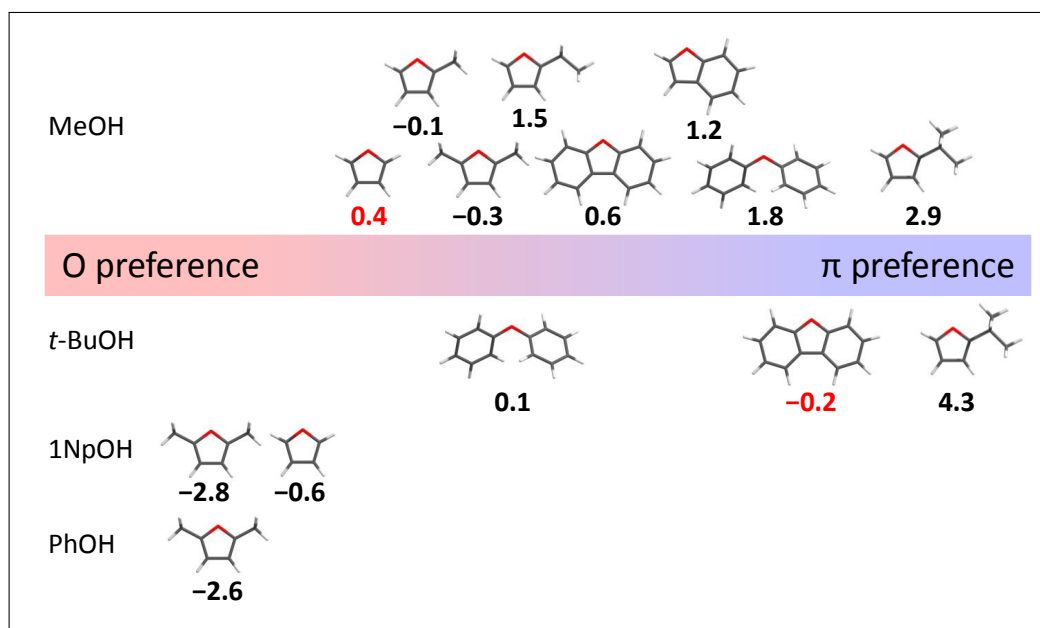


Figure 6.0.1: Experimentally derived ranking of the molecular scale preferences. The energy differences between oxygen and π binding calculated at B3LYP-D3(BJ, abc)/def2-TZVP level are given below each acceptor. Red values are qualitatively conflicting with the experimental observation.

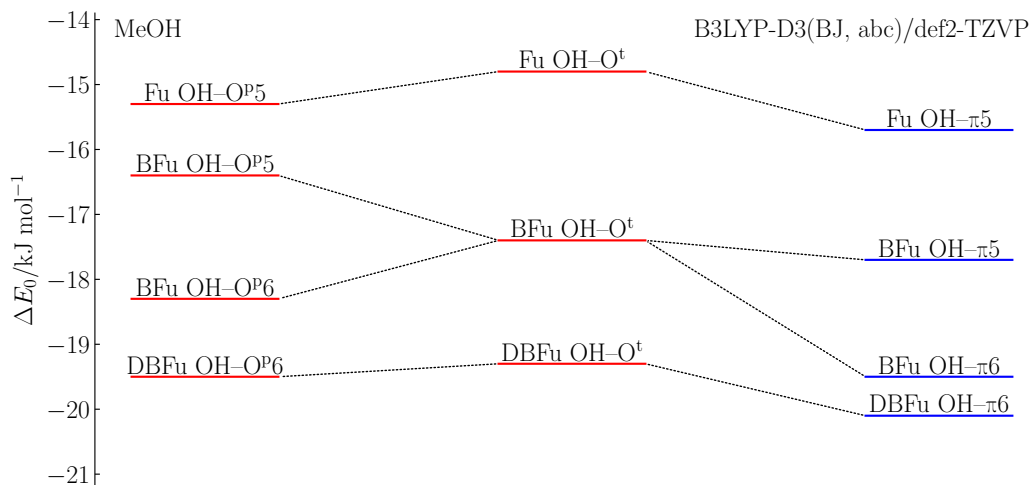


Figure 6.0.2: Illustration of the ZPVE-corrected binding energies of the dimers of furan, 2,3-benzofuran and dibenzofuran with methanol calculated at B3LYP-D3(BJ, abc)/def2-TZVP level.

observed preferences of these three acceptors, the combination of the oxygen and π -bound conformers are different for each molecule, $\text{OH-O}^t/\text{OH-}\pi_5$ for furan, $\text{OH-O}^{\text{P}6}/\text{OH-}\pi_6$ for 2,3-benzofuran and $\text{OH-O}^t/\text{OH-}\pi_6$ for dibenzofuran, respectively. Thus, a non-uniform sequence for the binding preference is plausible.

The binding energies for diphenyl ether are larger than for dibenzofuran, the π site profiting more from the ring opening than the oxygen site, which leads to a pronounced π preference. Unsurprisingly, the oxygen is a better hydrogen bond acceptor if not incorporated in an aromatic system. The secondary interactions are similar to the OH-O^{P} conformer of dibenzofuran. The increase in the binding energy of the π -bound conformer (more than 4 kJ mol^{-1}) can be explained by the additional CH-O interaction, enabled by the gained flexibility of the acceptor.

Changing the donor to *tert*-butyl alcohol leads to an attenuation of the π preference for diphenyl ether, as discussed in Sec. 4, whereas for dibenzofuran the more intuitive increasing π preference with donor alkylation is observed. Surprisingly, the latter is not sufficiently described by B3LYP-D3(BJ, abc)/def2-TZVP, which may be related to the fact that a C_s -symmetric OH-O structure could not be optimized without imaginary frequencies.

The molecular scale systems most useful for benchmarking are those, where both conformers can be observed. At least seven such systems were identified. Extracting a qualitative binding preference from the spectra is possible for most cases, but an exact quantification is more challenging. Major issues arise from weak bands, where an integration can only be done with large error bars, and band overlap. The conformational temperature is not known and adds largely to the uncertainty. Furthermore, the experimental energy difference between the conformers relies on a computational ratio of the IR cross sections. Nevertheless, even a qualitative experimental binding preference is sufficient to identify shortcomings of computational methods, as demonstrated by the dibenzofuran-*tert*-butyl alcohol clusters.

6.1 Dispersion Influence

The identification of the dispersion interaction influence is of special interest in the molecular balance systems of this thesis. OH- π contacts are inherently more dispersion-driven than OH-O hydrogen bonds. However, dispersion also largely contributes to the stability of the analyzed dimers through secondary interactions. The π -bound conformer is therefore not necessarily the one with the larger dispersion component to the binding energy.⁷⁵ One of the secondary interaction motifs commonly observed in the studied clusters are interactions of the donor alkyl moiety with the (furan) π system, which has been shown to add dispersion in dimers of alkyl anisols and methanol.²³⁹ Similarly, the less isotropic alkylic and aromatic CH-O interactions often present in OH-O bound clusters have a dispersion character.^{239,240} Therefore, the presence of these interaction types is regarded as a sign of dispersion contribution to the binding energy.

For the dimers of the methylated furans with methanol the secondary interactions are surprisingly similar. Both, the presumed global minimum OH-O^t and the OH- π structure are stabilized by CH- π interactions and in case of the methylated furans also from alkylic CH-O interactions. This leaves the oxygen-bound conformer as the more stable structure, despite considerable hydrogen bond strain.

The 2-ethylfuran *gauche* conformation (see Sec. 3.3.1) offers a direct comparison of the CH-O interaction influence. Since the electronic structure of the acceptor is the same, the stability of the 2-ethylfuran-methanol dimers at the two sides of the furan

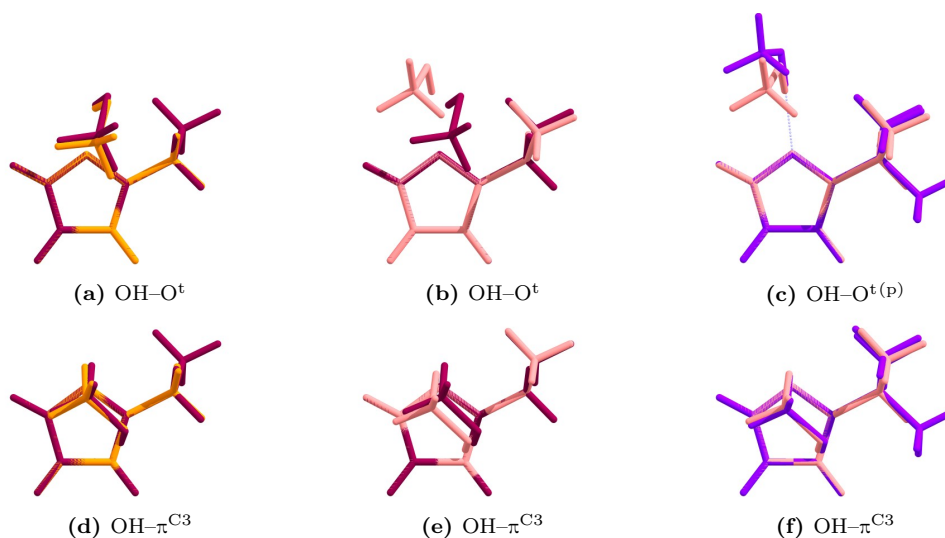


Figure 6.1.1: Overlay of the OH-O^t and $\text{OH-}\pi^{\text{C}3}$ conformers, respectively, of the two *gauche*-2-ethylfuran-methanol conformations (red and light red, center) calculated at B3LYP-D3(BJ, abc)/def2-TZVP level in comparison to 2-methylfuran-methanol (orange) and 2-*tert*-butylfuran-methanol (purple).

ring depends on the way the alkyl moiety interacts with the methanol. If the methanol is on the same side as the ethyl moiety, the surrounding of 2-*tert*-butylfuran is mimicked, otherwise it resembles 2-methylfuran (see Fig. 6.1.1). The π -bound structures are almost identical to the corresponding 2-methylfuran-methanol or 2-*tert*-butylfuran-methanol structures. This indicates that the main $\text{OH-}\pi$ interaction is only slightly influenced by an enlargement of the alkyl group, if the binding site environment is retained. Comparing the two binding site environments (Fig. 6.1.1e), a small displacement of the methanol can be seen. The CH-O contact is shortened from 3.23 Å in the methyl equivalent environment to 2.68 Å in the *tert*-butyl environment, which is reflected in the energetic preference of 2.0 kJ mol^{-1} for the shorter (C)H-O distance, making the latter the global minimum structure. For the OH-O^t conformer, the CH-O contact has a stronger influence on the structure. The (C)H-O distance is similar for both binding environments, but the *tert*-butyl like geometry allows a more linear OH-O hydrogen bond while pulling the methanol away from the furan ring into an almost OH-O^p like conformation. Nevertheless, the strained hydrogen bond is predicted to be energetically preferred by 0.5 kJ mol^{-1} , hinting at a substantial dispersion contribution from the $\text{CH-}\pi$ interaction. Unfortunately, the

experimental data for 2-ethylfuran is not conclusive enough to prove this theoretical prediction. In 2-*tert*-butylfuran–methanol the interplay of the dispersion interactions results in a preference of the OH– π conformation over the almost linear OH–O hydrogen bond (see Sec. 3.3.2).

A preference for π binding is also observed for dimers of methanol with 2,3-benzofuran and tentatively for dibenzofuran, as well. This further indicates the seemingly greater importance of the CH– π dispersion interactions with the aromatic surface, compared to the aromatic CH–O interaction in the oxygen-bound conformations. Especially for *tert*-butyl alcohol as a donor, these seem not to be described sufficiently by B3LYP-D3(BJ, abc)/def2-TZVP.

In the clusters of 1-naphthol with 2,5-dimethylfuran the alkylic CH– π interactions are not strong enough to tilt the acceptor from the symmetry axis, where aromatic CH– π interactions add to its stability. A more detailed insight to the influence of dispersion in these clusters might be achieved by applying SAPT calculations and Dispersion Interaction Density (DID) plots^{8,239}.

6.2 Validation of B3LYP-D3(BJ, abc)/def2-TZVP

The quality of the predictions made by the B3LYP-D3(BJ, abc)/def2-TZVP method, which was used throughout this thesis, shall be investigated in this section. Two aspects are of major interest: The reliability of cluster assignments based on this method and second the ability to predict the energetic sequence correctly. A major issue is, that the experimental interpretation often takes the theoretical predictions into account and is thus not completely independent. This effect has been minimized by different experimental strategies like deuteration and multi-spectroscopic approaches. Furthermore, experimental analogies can be used as an assignment tool without computational input.

For the cluster assignment only harmonic frequencies have been computed in this thesis, as anharmonic frequency calculations can be orders of magnitude more costly and are thus hardly accessible.²⁴¹ Furthermore, anharmonic calculations like VPT2²⁴² are not necessarily better than scaled harmonic values, which are commonly used to account for anharmonicity.²⁴¹ Anharmonic calculations depend on high-level potential energy functions, but if provided can predict frequencies with

good accuracy.²⁴¹ As this increases the computational cost even more, it shall be discussed to what extent the calculated harmonic frequencies can be used as a tool for the cluster assignment, even though they are obviously not directly comparable to anharmonic experimental band positions.

For this purpose, experimental OH stretching vibrations of various hydrogen bonded dimers have been collected in Tab. F.1. Only clusters of the donor molecules from this thesis have been considered, while all chosen acceptors offer oxygen and/or π binding sites. Most (literature) data were measured at the *filet-jet* and *popcorn-jet* setups, others were obtained using different IR/UV combination techniques. All data stem from jet expansion methods, values obtained by matrix isolation experiments were not considered. Generally, no extensive search for conformations has been done, but the stated minimum geometries were reoptimized, if other methods than B3LYP-D3(BJ, abc)/def2-TZVP were applied in the literature.

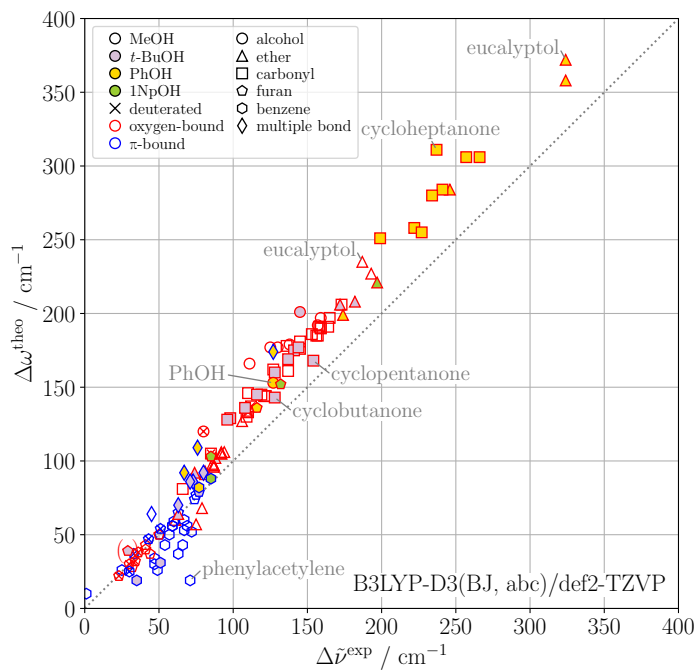
The resulting data is illustrated in Fig. 6.2.1, where the predicted harmonic downshift of the cluster is plotted against the experimentally observed downshift. A similar approach has been investigated for the absolute OH stretching vibration positions of intramolecular hydrogen bonds, where a linear regression was derived as a prediction tool from harmonic B3LYP calculations.^{243,244} The smaller the wavenumber, the larger is the deviation from an ideal prediction. For the hydrogen bonded dimers not the absolute band positions, but the downshifts from the donor monomer are analyzed. 88 oxygen-bound and 36 π -bound dimers are considered, respectively. The majority of the data points seem to correlate nicely with the ideal curve shifted by 20 cm^{-1} to 30 cm^{-1} (see Fig. 6.2.1a). This seems to fail for downshifts in the region below 100 cm^{-1} , in which most data points from this thesis fall. One reason seems to be that these smaller shifts correspond to π -bound clusters (blue), but also oxygen-bound clusters (red) are less overestimated in this region (see Fig. 6.2.1b). A possible explanation are the secondary interactions involved, especially CH- π interactions that bend the hydrogen bond, indicating different anharmonic effects. A uniform treatment with the same scaling factor for all interactions thus does not seem applicable.

To identify patterns in the data points from this thesis, Fig. 6.2.2a and Fig. 6.2.2b show only the dimers containing methanol as a donor and furan as an acceptor, respectively. For the series of the methylated furan derivatives the oxygen-bound

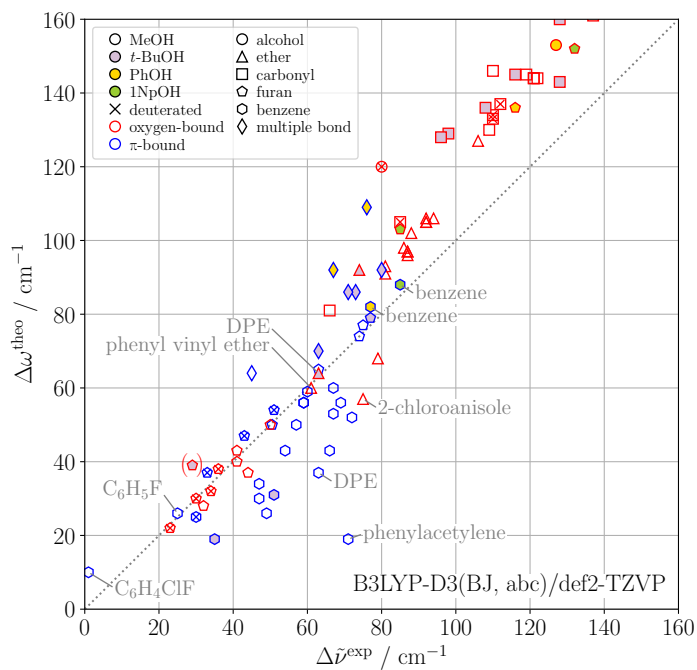
as well as the π -bound clusters are predicted almost ideally. The π -bound *tert*-butylfuran–methanol dimer also fits this trend. The series of furans with annulated benzene rings behave somewhat differently. The oxygen-bound clusters of Fu, BFu and DBFu do not fall on a straight line. This is possibly due to the assignment of different structural types. Especially noticeable are the π -bound dimers of these acceptors, which are significantly underestimated and are among the π -bound complexes of anisole derivatives, framing the data point for pure benzene. This illustrates the distinct behavior for the specific acceptors. Regarding the various donor molecules for the furan acceptors, no significant change is observed when deuterating the methanol. The dimers of *tert*-butyl alcohol are also alike, the only deviating data point being the very tentatively assigned dibenzofuran–*tert*-butyl alcohol dimer. Interestingly, the data points for the oxygen-bound dimers of the aromatic alcohols phenol and 1-naphthol do not fall onto this almost ideal line but show an overestimation, similar to the other oxygen-bound dimers with a large downshift.

The data points from Fig. 6.2.1 can be condensed to a box plot (see App. G) of the theoretical over- and underestimation of the downshifts as shown in Fig. 6.2.3. The divergence $\Delta = \Delta\omega^{\text{theo}} - \Delta\tilde{\nu}^{\text{exp}}$ ranges from $\Delta = -52 \text{ cm}^{-1}$ (underestimation) to $\Delta = 74 \text{ cm}^{-1}$ (overestimation) and is smaller for aromatic donors, where no underestimation is observed. The scattering of the over- and underestimation is similar for oxygen and π -bound clusters, whereby the oxygen-bound clusters tend to be more overestimated.

The π -bound clusters are equally over- and underestimated (π). The largest overestimations stem from donors bound to double and triple bonds ($\pi_{\text{multiple bond}}$). Their range is well separated from the aromatic π acceptors (π_{aromatic}), but for one complex. Only four dimers bound to a six-membered ring are overestimated (π_{benzene}). In fluorobenzene–MeOH ($\Delta = 1 \text{ cm}^{-1}$) the halogen atom might explain the uncommon behavior. This is supported by the *p*-chlorofluorobenzene–MeOH dimer ($\Delta = 9 \text{ cm}^{-1}$), where the addition of a second halogen atom leads to an even larger overestimation. The other two, benzene–PhOH ($\Delta = 5 \text{ cm}^{-1}$) and benzene–1NpOH ($\Delta = 3 \text{ cm}^{-1}$), are both benzene complexes with aromatic alcohols. Their unique binding pattern with an OH– π and a CH– π interaction might give rise to the overestimation. It would be interesting to compare the behavior of π -bound furan to these donors, however, as stated in Sec. 5 none could be identified in experiment. In loose

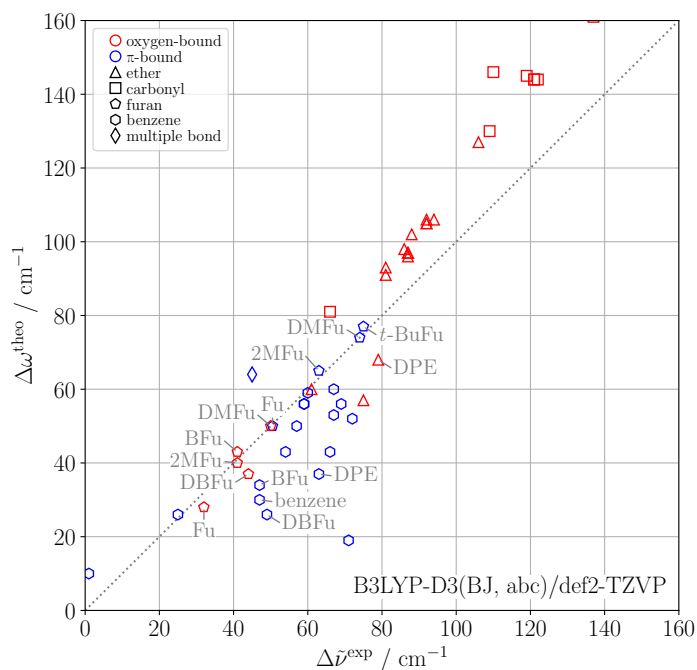


(a)

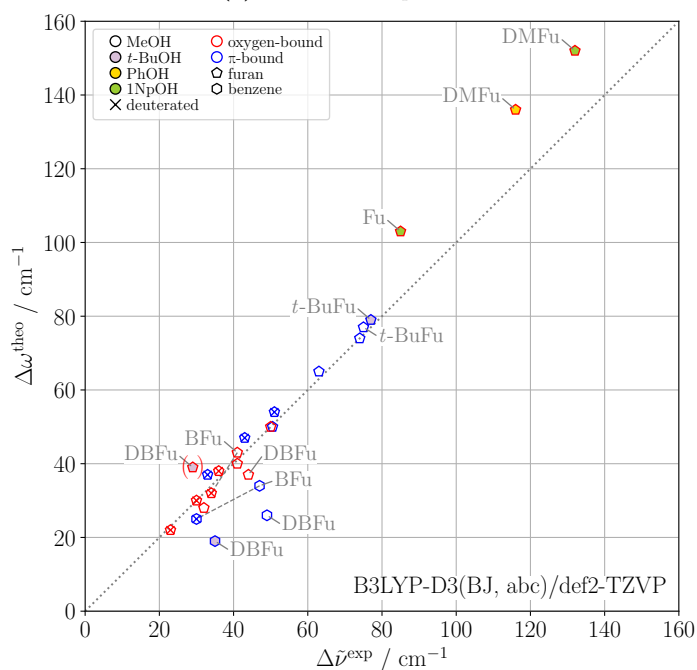


(b)

Figure 6.2.1: Spectral harmonic downshift calculated at B3LYP-D3(BJ, abc)/def2-TZVP level ($\Delta\omega^{\text{theo}}$) against the anharmonic experimental downshift $\Delta\tilde{\nu}^{\text{exp}}$, both in cm^{-1} . (a) full range, (b) extract of the lower left part.



(a) methanol complexes



(b) furan complexes

Figure 6.2.2: Spectral harmonic downshift calculated at B3LYP-D3(BJ, abc)/def2-TZVP level ($\Delta\omega^{\text{theo}}$) against the anharmonic experimental downshift $\Delta\nu^{\text{exp}}$, both in cm^{-1} . (a) methanol donor complexes, (b) furan acceptor complexes.

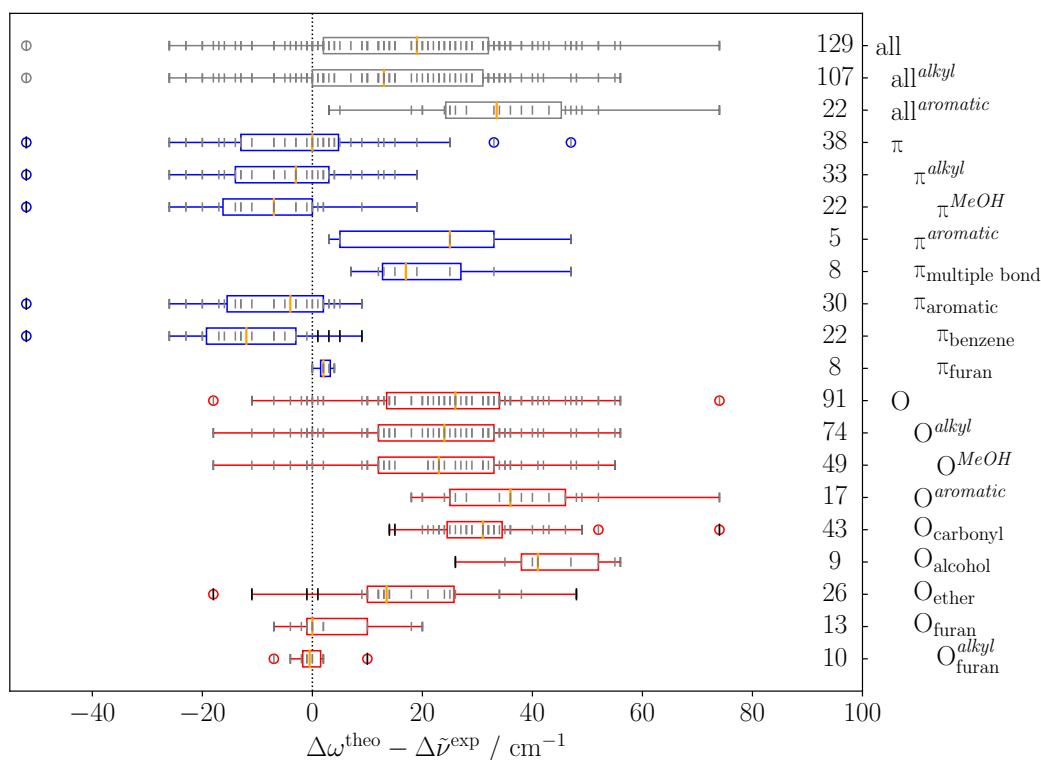


Figure 6.2.3: Box plot visualizing the over- and underestimation at B3LYP-D3(BJ, abc)/def2-TZVP level of the experimental downshift for different structure types. Subscripts denote the acceptor type, superscripts (italic) the donor type. Data subgroups have indented labels, *e.g.* π^{alkyl} and π^{MeOH} . Numbers on the right denote the amount of available data points. Data point positions are marked in grey (overlap is possible, the minimal separation of $\Delta = 1 \text{ cm}^{-1}$ is due to rounding), the median is marked in orange. Data points beyond 1.5 interquartile range are considered as outliers (see App. G). Values explicitly mentioned in the text are marked in black.

correlation is the observation that the π -bound furan clusters (π_{furan}) are also slightly overestimated, regarding that all of them also incorporate CH- π interactions, only of alkylic type instead of aromatic. One outlier is identified for the π -bound clusters with a clear underestimation ($\Delta = -52 \text{ cm}^{-1}$). It corresponds to the phenyl acetylene-MeOH dimer. A revision of the assignment might be worthwhile, especially because the B3LYP-D3(BJ, abc)/def2-TZVP level predicts an acetylene bound conformer to be more stable by 1.7 kJ mol^{-1} .

The oxygen-bound species tend to be overestimated (O). When classified by acceptors, alcohols are overestimated the most (O_{alcohol}), followed by carbonyls

(O_{carbonyl}). Their spreading is similar, except for one data point, corresponding to the cycloheptanone–PhOH dimer ($\Delta = 74 \text{ cm}^{-1}$). As there is no apparent explanation for this outlier, particularly since the related cycloketone–PhOH dimers fit the trend, the assignment might need to be reassessed, more so in light of the second observed band in the spectrum with a larger downshift of 273 cm^{-1} .²⁴⁵ Multiple bands are also observed in the spectra of the least overestimated carbonyl dimers, namely cyclobutanone–*t*-BuOH ($\Delta = 15 \text{ cm}^{-1}$) and cyclopentanone–*t*-BuOH ($\Delta = 14 \text{ cm}^{-1}$), whereby a verification of the assignment seems worthwhile, even though they are not identified as outliers. Furthermore, in both cases the cluster assignment was based on calculations at HF/3-21G level, which cannot describe dispersion interactions.²⁴⁵ The ether acceptors show the widest spread among the classified oxygen acceptors (O_{ether}). One reason is the inclusion of alkylic and aromatic ethers. Overestimations larger than $\Delta = 26 \text{ cm}^{-1}$ are found for alkylic ethers, below are aromatic ethers. The largest overestimation ($\Delta = 48 \text{ cm}^{-1}$) is observed for dimers of eucalyptol with PhOH and MeOH. Interestingly, the dimers of *t*-BuOH with alkylic ethers are less overestimated than those of MeOH and PhOH. Three dimers of aromatic ethers with methanol are even underestimated in their downshift. The largest ($\Delta = -18 \text{ cm}^{-1}$) is 2-chloroanisole–MeOH, where the halogen atom might explain the discrepancy. The second is diphenyl ether–MeOH ($\Delta = -11 \text{ cm}^{-1}$), as already mentioned in Sec. 4. The main difference between this acceptor and the other aromatic ethers (mostly anisole derivatives) is the delocalization of the oxygen electron density in two instead of one aromatic systems, serving as an explanation for the unusual effect. Supporting this hypothesis is the third underestimated dimer ($\Delta = -1 \text{ cm}^{-1}$), namely phenyl vinyl ether with methanol, where the second π system is also withdrawing electron density. In agreement with this finding, the diphenyl ether–*t*-BuOH dimer ($\Delta = 1 \text{ cm}^{-1}$) is also less overestimated than the majority of the dimers with aromatic ethers, so is the phenol homodimer ($\Delta = 26 \text{ cm}^{-1}$) compared to other alcohol acceptors. The scattering of the oxygen-bound furan dimers (O_{furan}) is similar to that of carbonyls and alcohols. It is even smaller when only taking alkylic donors into account ($O_{\text{furan}}^{\text{alkyl}}$). The largest overestimation is then associated with the very tentatively assigned dibenzofuran–*t*-BuOH dimer ($\Delta = 10 \text{ cm}^{-1}$, see Sec. 3.4.2), thus, the assignment seems even less certain. The shifts of the dimers of alkyl alcohols with furan derivatives ($O_{\text{furan}}^{\text{alkyl}}$)

and π_{furan}) are predicted astonishingly well. Obviously, these systems benefit from fortuitous error compensation. Interestingly, the general trend of oxygen over- and π underestimation seems reversed, although not by a large margin.

For the assignment of a band to an oxygen or π -bound dimer it can be concluded, that the harmonically predicted band positions are surprisingly reliable for the furan clusters investigated in this thesis. For other cluster types they provide a range, in which a predicted band should fall for a probable assignment. Larger deviations should have a plausible reason to differ or otherwise point out questionable band assignments. Every interaction type has its own over- or underestimation characteristics. Therefore, a generalized scaling factor for the predicted frequencies does not seem appropriate. This dataset of 129 experimental frequencies might serve as a benchmarking set for anharmonic frequency calculations.

Regarding the relative energy, for most systems B3LYP-D3(BJ, abc)/def2-TZVP predicts the energetic preference correctly, but is at its limit in particularly close cases. One complication at these small energy differences is the vibrational zero-point energy, as it may be sufficient to reverse the electronically predicted stability order.¹³⁹ For furan, the discrepancy is most drastic. Not only is the molecular oxygen- π -binding scale tilted to the wrong side, but the observed OH-O dimer presumably does not match the predicted oxygen-bound minimum structure. Furthermore, the predicted tendency of the methylated furans to prefer π -binding with removal of the methyl groups, was not observed in experiment. When enlarging the basis set to def2-QZVP, the oxygen-bound structures are predicted equally stable, hinting at an effect of the small basis set, but the π -bound conformer is still favored by 0.4 kJ mol^{-1} . Another case is the dibenzofuran-*t*-BuOH dimer, where oxygen binding was predicted to be slightly preferred, but only a π -bound cluster was assigned in experiment. From literature, the phenyl vinyl ether-MeOH dimer is an evident example.²⁴⁰ Experimentally an oxygen-bound dimer was found favored over a structure π -bound to the phenyl side. Contrarily, in the predicted energy sequence this oxygen-bound dimer takes fourth place after a structure π -bound to the vinyl side, the OH- π phenyl dimer and another OH-O dimer. From these cases an error for the predicted relative energy of at least 0.5 kJ mol^{-1} can be derived. When the

energy differences are this subtle, predicted frequencies therefore seem somewhat more reliable for the cluster assignment than energies.

7 Conclusion

Fourteen molecular balance systems between OH–O and OH– π hydrogen bonding were investigated to act as benchmarking systems for the influence of dispersion interactions. In most cases, the energy difference was sufficiently low for the observation of both docking types using FTIR spectroscopy. The largest energy difference predicted at B3LYP-D3(BJ, abc)/def2-TZVP level, where still both conformers were observed, was 1.8 kJ mol^{-1} (diphenyl ether–methanol), while in cases of furan–1-naphthol and dibenzofuran–*tert* butyl alcohol, only one conformer could reliably be assigned, despite a predicted energy difference below 1 kJ mol^{-1} . Having observed different behavior for the docking preference if the donor is enlarged, the investigation of more furan–*tert*-butyl alcohol clusters seems worthwhile. A further enlargement of the donor could be done by using adamantanol, which would require a double pick-up setup design as proposed in Sec. 2.2.1 if the acceptor is also non-volatile.

Dispersion interactions mainly influence the cluster formation by secondary interactions. CH– π and CH–O interactions distort OH–O hydrogen bonds, while OH– π hydrogen bonds profit from their presence. In this context, a secondary molecular balance between OH–O^t and OH–O^p conformers was identified. The interplay of these dispersive interactions excels in the stabilization of the *tert*-butylfuran clusters, where they result in the exclusive observation of π binding. To the best of knowledge, these dimers are the first to favor OH– π binding over an oxygen acceptor. Interestingly, the strain on the OH–O hydrogen bond due to the secondary interactions leads to a smaller spectral downshift for the oxygen-bound dimers of furan derivatives with alkyl alcohols compared to their π -bound dimers. The largest downshift of a π -bound cluster in this thesis amounts to 77 cm^{-1} (*tert*-butylfuran–*tert*-butyl alcohol), while the least shifted oxygen-bound cluster is only shifted 32 cm^{-1} (furan–methanol). A dataset for these downshifts of oxygen and π -bound dimers was collected. It shows that the commonly observed downshift overestimation by B3LYP-D3(BJ, abc)/def2-TZVP of the oxygen-bound clusters is not true for fu-

ran complexes. The variation for dimers bound to a furan π system is surprisingly narrow. The dataset might serve as an assignment tool for the study of further complexes and as a benchmark database for the development of quantum chemical methods.

B3LYP-D3(BJ, abc)/def2-TZVP was shown to be a suitable level of theory for the investigation of molecular balances, with the drawback of potential failing in the energy sequence in very close cases, probably related to vibrational zero-point energy. The design of carbonyl balances could avoid the problem of zero-point energy effects, since the binding site type does not change.^{88,246,247} Additionally, FTIR spectroscopy is especially suited for these compounds, as they do not contain a UV chromophore and can thus not be studied by IR/UV combination techniques. Complexes of aliphatic (bi-)cyclic ethers, such as derivatives of eucalyptol, would similarly be excluded from IR/UV measurements and offer two OH–O binding sites. The spectral shift would be even larger compared to carbonyl balances²⁴⁵, however the amount of commercially available compounds, that are rigid, but asymmetrically substituted seems limited.

For the identification of the clusters deuteration has been shown to serve as a fruitful assignment tool in the FTIR spectra. π -bound complexes are less abundant upon deuteration of the donor hydroxy group. Furthermore, the band shifts seem slightly larger and smaller than the ideal harmonic deuterated counterpart for oxygen and π -bound complexes, respectively. So far, no contradiction to this observation has been found.

Multi-spectroscopic approaches have shown to add to the reliability of the assignments. IR/UV spectroscopy confirmed the dimer origin of the assigned bands, while microwave spectroscopy identified the binding geometry for the most stable OH–O clusters for furan–methanol and dibenzofuran–methanol to differ from the predictions. In the cooperation with the Leutwyler group unfortunately the two conformers of furan–1-naphthol could not be spectroscopically separated, thus a direct comparison of absolute and relative binding energies could not be done.

Regarding 1-naphthol as a hydrogen bond donor, it would be interesting to investigate the molecular see-saw of tilting benzene away from the perpendicular OH– π structure by adding alkyl groups, that could dispersively interact with the naphthol π

system. Particularly the difference between symmetric and asymmetric substitution could have an effect.

In conclusion, the binding preferences of the molecular scales of this thesis may serve as test cases for the performance of quantum mechanical methods for the proper description of dispersion interactions, whose influence has been shown to serve as a design principle in molecular recognition. Hopefully, this thesis can thereby add to a rapprochement of experiment and theory.

A Experimental Parameters

	<i>popcorn-jet</i>	<i>filet-jet</i>
optic parameters		
source	globar (MIR)	tungsten 150 W (NIR)
beam splitter	KBr broadband	KBr / CaF ₂
lenses	KBr / CaF ₂	KBr / CaF ₂
detector	InSb 2mm neu	InSb SW neu
filter	F1, 2860–4000 cm ⁻¹ / F13, 2500–4100 cm ⁻¹	F13, 2500–4100 cm ⁻¹
aperture	4.0 mm	3.5/4.0 mm
acquisition parameters		
acquisition mode	double-sided, fast-return	single-sided, fast-return
resolution	2 cm ⁻¹	2 cm ⁻¹
frequency range	0–15 799.83 cm ⁻¹	
FT-parameters		
apodisation function	Norton-Beer, Medium	Norton-Beer, Medium
phase resolution	16 cm ⁻¹	16 cm ⁻¹
phase correction mode	Mertz	Mertz
zero filling factor	4	4
instrument parameters		
switch gain position	7034	813
gain switch window	150	150
scan time	178 ms	100 ms

B OPUS Macro

Listing B.1: OPUS macro for sorting out single corrupt scans, as described in Sec. 2.2.1.

```
1 VARIABLES SECTION
3 STRING <OpusPath> = '';
4 *STRING <FilePath>= '<FilePath>';
5 *STRING <FileName>= '<FileName>';
6 *STRING <FileEndProbe> = 'p';
7 *STRING <FileEndBackg> = '1';
8 BOOL <SaveSingle> = TRUE;
9 BOOL <SaveSpike> = TRUE;
10 *STRING <QualityFilePath> = 'C:\OPUS_7.0.129\IDENT';
11 *STRING <QualityFileName> = '<QualityFileName>.QT';
12 NUMERIC <ScanCount>;
13 NUMERIC <ScanIndex> = 0;
14 STRING <BackgList> = '';
15 STRING <ProbeList> = '';
16 STRING <GoodScanList> = '';
17 FILE <BackgFile>;
18 FILE <ProbeFile>;
19 FILE <BackgFile_copy>;
20 FILE <ProbeFile_copy>;
21 FILE <DiffFile>;
22 FILE <DiffFile_copy>;
23 FILE <Single>;
24 FILE <AvgFile> = AB;
25 NUMERIC <GoodScan>;
26 NUMERIC <Spike>;
27 *NUMERIC <SpikeMax> = 0.0010000000000000;
28 *NUMERIC <SpikeMaxCenter> = 0.0005000000000000;
29 NUMERIC <SpikePassCenter>;
30 NUMERIC <SpikeCountLeft> = 0;
31 NUMERIC <SpikeCountRight> = 0;
32 NUMERIC <SpikeCount> = 0;
33 NUMERIC <SpikeCountLeftCenter> = 0;
34 NUMERIC <SpikeCountRightCenter> = 0;
35 NUMERIC <SpikeCountCenter> = 0;
36 NUMERIC <SpikeStart> = 0;
37 NUMERIC <SpikeEnd> = 0;
38 NUMERIC <SpikePosition> = 0;
39 NUMERIC <SpikeWidth> = 0;
40 NUMERIC <PeakIndex> = 0;
41 NUMERIC <ArrayIndex> = 0;
42 NUMERIC <ReportIndex> = 0;
43 NUMERIC <StraightLineIndex> = 0;
44 NUMERIC <QualityPass>;
45 NUMERIC <ScanPass>;
46 NUMERIC <Absorption>;
47 NUMERIC <AbsorptionMax>;
48 NUMERIC <AbsorptionPass>;
49 NUMERIC <Noise>;
50 NUMERIC <NoiseMax>;
51 NUMERIC <NoisePass>;
52 NUMERIC <Water>;
53 NUMERIC <WaterMax>;
54 NUMERIC <WaterPass>;
55 NUMERIC <Fringes>;
56 NUMERIC <FringesMax>;
57 NUMERIC <FringesPass>;
58 NUMERIC <GoodScanCount> = 0;
59 NUMERIC <LineCount> = 0;
60 STRING <Line> = '';
61 NUMERIC <LoopIndex> = 0;
```



```

STRING <ScanIndex0> = '';
63 FILE <FinalResult> = AB;

65 PROGRAM SECTION
REM-----delete files in Work directory
67 REM
<OpusPath> = GetOpusPath ();
69 Delete ('<OpusPath>\WORK\*.');
REM
71 REM-----set DisplayLimit
SetDisplayLimits (29000, -200, -0.0015, 0.0015);
73 REM
REM-----UserDialog, load files
75 REM
UserDialog ('Laden mehrerer Spektren', STANDARD, TEXT:'Datenauswahl - FileName ohne Endung
eintragen', EDIT:'<FilePath>', EDIT:'<FileName>', TEXT:'Welche Spektrentypen sollen
verglichen werden? p Probe, l Hintergrund, v Vorscan, n1/n2 Nachscans', EDIT:'<
FileEndProbe>', EDIT:'<FileEndBackg>', TEXT:'Schwellwert (abs) f\"ur Spikes', EDIT:'<
SpikeMax>', BLANK, EDIT:'<SpikeMaxCenter>', EDIT:'<QualityFilePath>', EDIT:'<
QualityFileName>', CHECKBOX:'SaveSpike', TEXT:'VORSICHT: Gleichnamige Spektren im "
removeSpike"-Ordner werden \"uberschrieben!');
77 <BackgList> = ScanPath ('<FilePath>\<FileName>\<FileEndBackg>.*');
<ProbeList> = ScanPath ('<FilePath>\<FileName>\<FileEndProbe>.*');
79 <ScanCount> = GetArrayCount (<ProbeList>);
<ScanIndex> = 0;
81 REM
REM-----TextReport
83 <Line>[<LineCount>] = 'ScanIndex, GoodScan, QualityPass, SpikePass, SpikeCountCenter,
SpikeCount, Absorption, AbsorptionPass, Noise, NoisePass, Water, WaterPass, Fringes,
FringesPass';
TextToFile ('<FilePath>\removeSpike', removeSpike_<FileName>.txt, <Line>[<LineCount>],
REPLACE_TEXT);
85 REM
REM #####
87 REM-----Start Loop
StartLoop (<ScanCount>, 0);
89 REM
REM-----ScanIndex
91 If(<LoopIndex>,.LT.,10);
<ScanIndex0> = '00';
93 Else ();
If(<LoopIndex>,.LT.,100);
95 <ScanIndex0> = '0';
Else ();
97 <ScanIndex0> = '';
Endif ();
99 Endif ();
REM
101 [<BackgFile>:IgSm] = LoadFile ('<FilePath>\<BackgList>[<ScanIndex>]', WARNING);
[<ProbeFile>:IgSm] = LoadFile ('<FilePath>\<ProbeList>[<ScanIndex>]', WARNING);
103 [<BackgFile_copy>:IgSm] = Calculator ([<BackgFile>:IgSm], {FOR='[<BackgFile>:IgSm]'});
[<ProbeFile_copy>:IgSm] = Calculator ([<ProbeFile>:IgSm], {FOR='[<ProbeFile>:IgSm]'});
105 Unload ([<BackgFile>][<ProbeFile>], {});

107 [<DiffFile>:IgSm] = Calculator ([<ProbeFile_copy>:IgSm][<BackgFile_copy>:IgSm], {FOR='[<
ProbeFile_copy>:IgSm]-[<BackgFile_copy>:IgSm]'});
If(<SaveSpike>.EQ.TRUE);
109 SaveAs ([<DiffFile>], {DAP='<FilePath>\removeSpike\spike', OEX='1', SAN='<FileName>\<
FileEndBackg>\<FileEndProbe>_spike.<ScanIndex0>\<LoopIndex>', COF=2, INP='C:\Programme\
OPUS\METHODS', IFP='C:\Programme\OPUS\METHODS', INM='DEFAULT', IFN='DEFAULT', DPA=5,
DPO=5, SEP=',', YON='0', ADP='1'});
Endif ();
111 REM
REM-----spike search without centerburst, delete spikes in probe
113 PeakPick([<DiffFile>:IgSm], {PSM=1, WHR=0, LXP=15844, FXP=29000, PPM=3, QP4=NO, QP5
=0.0005, QP6=NO, QP7=0.0005, QP8=YES, QP9=<SpikeMax>});
PeakPick([<DiffFile>:IgSm], {PSM=1, WHR=0, LXP=0, FXP=12584, PPM=3, QP4=NO, QP5=0.0005,
QP6=NO, QP7=0.0005, QP8=YES, QP9=<SpikeMax>});
115 <SpikeCountLeft> = FromReportHeader ([<DiffFile>:IgSm/Peak], 1, 0, 3, RIGHT);
<SpikeCountRight> = FromReportHeader ([<DiffFile>:IgSm/Peak], 2, 0, 3, RIGHT);
117 <SpikeCount> = <SpikeCountLeft> + <SpikeCountRight>;
REM
119 <ArrayIndex> = 0;
If(<SpikeCountLeft>.>.GT.,0);
121 <PeakIndex> = 0;
StartLoop(<SpikeCountLeft>, 1);
123 <ReportIndex> = <PeakIndex> + 1;
<SpikePosition> = FromReportMatrix ([<DiffFile>:IgSm/Peak], 1, 0, <ReportIndex>, 1);

```

```

125 <SpikeWidth> = FromReportMatrix ([<DiffFile>:IgSm/Peak], 1, 0, <ReportIndex>, 4);
    If(<SpikeWidth>, .GT., 100);
127 UserDialog ('Spikebreite ist gr\o\ss er als 100cm-1', STANDARD, TEXT:'Peakposition:',
    TEXT:'<SpikePosition>', TEXT:'neue Spikebreite eintragen:', EDIT:'<SpikeWidth>',
    BLANK, BLANK, BLANK, BLANK, BLANK, BLANK, BLANK, BLANK, BLANK, BLANK);
    Endif();
129 <SpikeStart>[<ArrayIndex>] = <SpikePosition> - <SpikeWidth>;
    <SpikeEnd>[<ArrayIndex>] = <SpikePosition> + <SpikeWidth>;
131 <PeakIndex> = <PeakIndex> + 1;
    <ArrayIndex> = <ArrayIndex> + 1;
133 EndLoop(1);
    Endif();
135 REM
    If(<SpikeCountRight>, .GT., 0);
137 <PeakIndex> = 0;
    StartLoop(<SpikeCountRight>, 2);
139 <ReportIndex> = <PeakIndex> + 1;
    <SpikePosition> = FromReportMatrix ([<DiffFile>:IgSm/Peak], 2, 0, <ReportIndex>, 1);
141 <SpikeWidth> = FromReportMatrix ([<DiffFile>:IgSm/Peak], 2, 0, <ReportIndex>, 4);
    If(<SpikeWidth>, .GT., 100);
143 UserDialog ('Spikebreite ist gr\o\ss er als 100cm-1', STANDARD, TEXT:'Peakposition:',
    TEXT:'<SpikePosition>', TEXT:'neue Spikebreite eintragen:', EDIT:'<SpikeWidth>',
    BLANK, BLANK, BLANK, BLANK, BLANK, BLANK, BLANK, BLANK, BLANK, BLANK);
    Endif();
145 <SpikeStart>[<ArrayIndex>] = <SpikePosition> - <SpikeWidth>;
    <SpikeEnd>[<ArrayIndex>] = <SpikePosition> + <SpikeWidth>;
147 <PeakIndex> = <PeakIndex> + 1;
    <ArrayIndex> = <ArrayIndex> + 1;
149 EndLoop(2);
    Endif();
151 REM
    If(<SpikeCount>, .GT., 0);
153 <StraightLineIndex> = 0;
    StartLoop(<SpikeCount>, 3);
155 StraightLine ([<ProbeFile_copy>:IgSm], {GFX=<SpikeStart>[<StraightLineIndex>], GLX=<
    SpikeEnd>[<StraightLineIndex>]});
    <StraightLineIndex> = <StraightLineIndex> + 1;
157 EndLoop(3);
    Endif();
159
161 REM-----spike search in difference file (centerburst)
    [<DiffFile_copy>:IgSm] = Calculator ([<DiffFile>:IgSm], {FOR='[<DiffFile>:IgSm]'});
163 PeakPick([<DiffFile_copy>:IgSm], {PSM=1, WHR=0, LXP=12584, FXP=14014, PPM=3, QP4=NO, QP5
    =0.0005, QP6=NO, QP7=0.0005, QP8=YES, QP9=<SpikeMaxCenter>});
    PeakPick([<DiffFile_copy>:IgSm], {PSM=1, WHR=0, LXP=14414, FXP=15844, PPM=3, QP4=NO, QP5
    =0.0005, QP6=NO, QP7=0.0005, QP8=YES, QP9=<SpikeMaxCenter>});
165 <SpikeCountLeftCenter> = FromReportHeader ([<DiffFile_copy>:IgSm/Peak], 1, 0, 3, RIGHT);
    <SpikeCountRightCenter> = FromReportHeader ([<DiffFile_copy>:IgSm/Peak], 2, 0, 3, RIGHT);
167 <SpikeCountCenter> = <SpikeCountLeftCenter> + <SpikeCountRightCenter>;
    If(<SpikeCountCenter>, .EQ., 0);
169 <SpikePassCenter> = 1;
    Else();
171 <SpikePassCenter> = 0;
    Endif();
173 REM
175 REM-----calculate single spectrum
    FFT ([<BackgFile_copy>:IgSm], 0, {FPP=0, FSM='AL', FSR=0, FSY=256, FNE=0.800000, FNC
    =100.000000, FNL=0, FBW=1, FTT=0, FLR=0, FHR=0.000000, FTR=1.000000, FTE=0.000000,
    FTS=15800.000000, FZF='4', FTA='NBM', FHZ='ML'});
    FFT ([<ProbeFile_copy>:IgSm], 0, {FPP=0, FSM='AL', FSR=0, FSY=256, FNE=0.800000, FNC
    =100.000000, FNL=0, FBW=1, FTT=0, FLR=0, FHR=0.000000, FTR=1.000000, FTE=0.000000,
    FTS=15800.000000, FZF='4', FTA='NBM', FHZ='ML'});
177 [<Single>:TR] = Calculator ([<ProbeFile_copy>:IgSm][<BackgFile_copy>:IgSm], {FOR='[<
    ProbeFile_copy>:ScSm]/[<BackgFile_copy>:ScSm]'});
    [<Single>:AB] = ABTR ([<Single>:TR], {CCM=3});
179 If(<SaveSingle>, .EQ., TRUE);
    SaveAs ([<Single>], {DAP='<FilePath>\removeSpike\single', OEX='1', SAN='<FileName>\<
    FileEndBackg>\<FileEndProbe>\_single.<ScanIndex0>\<LoopIndex>', COF=2, INP='C:\Programme
    \OPUS\METHODS', IFP='C:\Programme\OPUS\METHODS', INM='DEFAULT', IFN='DEFAULT', DPA=5,
    DPO=5, SEP=',', YON='0', ADP='1'});
181 Endif();
183 REM-----quality test
    QualityTest ([<Single>:AB], {QQL='<QualityFilePath>', QQM='<QualityFileName>'});
    <QualityPass> = FromReportHeader ([<Single>:AB/Qtest], 1, 0, 1, RIGHT);
185 <Absorption> = FromReportMatrix ([<Single>:AB/Qtest], 1, 0, 1, 4);
    <AbsorptionMax> = FromReportMatrix ([<Single>:AB/Qtest], 1, 0, 1, 3);
187

```

```

189 If(<Absorption>,.LTEQ.,<AbsorptionMax>);
<AbsorptionPass> = 1;
Else ();
191 <AbsorptionPass> = 0;
Endif ();
193 <Noise> = FromReportMatrix ([<Single>:AB/Qtest], 1, 0, 2, 4);
<NoiseMax> = FromReportMatrix ([<Single>:AB/Qtest], 1, 0, 2, 3);
195 If(<Noise>,.LTEQ.,<NoiseMax>);
<NoisePass> = 1;
197 Else ();
<NoisePass> = 0;
199 Endif ();
<Water> = FromReportMatrix ([<Single>:AB/Qtest], 1, 0, 5, 4);
201 <WaterMax> = FromReportMatrix ([<Single>:AB/Qtest], 1, 0, 5, 3);
If(<Water>,.LTEQ.,<WaterMax>);
203 <WaterPass> = 1;
Else ();
205 <WaterPass> = 0;
Endif ();
207 <Fringes> = FromReportMatrix ([<Single>:AB/Qtest], 1, 0, 8, 4);
<FringesMax> = FromReportMatrix ([<Single>:AB/Qtest], 1, 0, 8, 3);
209 If(<Fringes>,.LTEQ.,<FringesMax>);
<FringesPass> = 1;
211 Else ();
<FringesPass> = 0;
213 Endif ();
REM
215 REM-----sorting , average
<ScanPass>=<SpikePassCenter>+<QualityPass>;
217 If(<ScanPass> .EQ. 2);
If(<GoodScanCount>,.EQ.,0);
219 [<FinalResult>:AB] = Average (0, 0, 0, {QA0=1, QA2=1, QAE='NO', QAF='NO', QAL='FIL', QAM
='<FilePath>\removeSpike\single', QAN='<FileName>\<FileEndBackg>\<FileEndProbe>\_single
.<ScanIndex0>\<LoopIndex>', QAO=4111});
REM
221 Else ();
[<FinalResult>:AB] = Average (0, [<FinalResult>:AB], 0, {QA0=1, QA2=1, QAE='NO', QAF='YES
', QAL='FIL', QAM='<FilePath>\removeSpike\single', QAN='<FileName>\<FileEndBackg>\
FileEndProbe>\_single.<ScanIndex0>\<LoopIndex>', QAO=4111});
223 Endif ();
<GoodScan> = 1;
225 <GoodScanCount> = <GoodScanCount>+1;
Else ();
227 <GoodScan> = 0;
Endif ();
229 REM
REM-----report
231 <Line>[<LineCount>] = '<ScanIndex>, <GoodScan>, <QualityPass>, <SpikePassCenter>, <
SpikeCountCenter>, <SpikeCount>, <Absorption>, <AbsorptionPass>, <Noise>, <NoisePass
>, <Water>, <WaterPass>, <Fringes>, <FringesPass>';
TextToFile ('<FilePath>\removeSpike', removeSpike_<FileName>.txt, <Line>[<LineCount>],
APPEND_TEXT);
233 REM
REM-----End Loop
235 <ScanIndex> = <ScanIndex> +1;
<LineCount> = <LineCount> +1;
237 <LoopIndex> = <LoopIndex> +1;
Unload ([<DiffFile>][<DiffFile_copy>][<ProbeFile_copy>][<BackgFile_copy>][<Single>], {});
239 EndLoop (0);
REM #####
241 REM
REM-----warning
243 If(<GoodScanCount>,.EQ.,0);
Message('Kein Spektrum erf\ "ullt das Kriterium, der cutoff muss angepasst werden.',
ON_SCREEN, NO_TIMEOUT);
245 Goto(End);
Endif ();
247 REM
REM-----save
249 SaveAs ([<FinalResult>:AB], {DAP='<FilePath>\removeSpike', OEX='1', SAN='<FileName>\<
FileEndBackg>\<FileEndProbe>.<GoodScanCount>', COF='2'});
REM
251 REM-----unload spectra and show averaged spectrum
Unload ([<FinalResult>], {});
253 SetDisplayLimits (4050, 2850, -0.0001, 0.0007);
[<AvgFile>:AB] = LoadFile ('<FilePath>\removeSpike\<FileName>\<FileEndBackg>\<FileEndProbe
>.<GoodScanCount>', WARNING);
255 REM

```

```
REM-----write report
257 <Line>[0] = 'Anzahl guter Scans: <GoodScanCount>, SpikeMax: <SpikeMax>, SpikeMaxCenter: <
      SpikeMaxCenter>';
      TextToFile ('<FilePath>\removeSpike ', removeSpike_<FileName>.txt, <Line>[0], APPEND_TEXT);
259 REM
      REM
261 Label(End);

263 PARAMETER SECTION

265 QFC='';
      QFB='';
267 FPP=0;
      FNE=0.800000;
269 FNC=100.000000;
      FNL=0;
271 FBW=1;
      FTT=0;
273 FLR=0;
      FTR=1.000000;
275 FTE=100.000000;
      FTS=5000.000000;
277 FHR=0.000000;
```

C Computational Parameters

Table C.1: Convergence criteria used in the final standard method B3LYP-D3(BJ, abc)/def2-TZVP computed with ORCA 4.0 using the 'VERYTIGHTSCF' and 'TIGHTOPT' keywords.

Convergence Tolerance Geometry Optimization:				
Energy Change	TolE	1.0000×10^{-6}	E_h
Max. Gradient	TolMAXG	1.0000×10^{-4}	$E_h a_0^{-1}$
RMS Gradient	TolRMSG	3.0000×10^{-5}	$E_h a_0^{-1}$
Max. Displacement	TolMAXD	1.0000×10^{-3}	a_0
RMS Displacement	TolRMSD	6.0000×10^{-4}	a_0
Convergence Tolerance SCF:				
Convergence Check Mode	ConvCheckMode	Total+1el-Energy	
Convergence forced	ConvForced	0	
Energy Change	TolE	1.000×10^{-8}	E_h
1-El. energy change		1.000×10^{-5}	E_h
Orbital Gradient	TolG	1.000×10^{-5}	
Orbital Rotation angle	TolX	1.000×10^{-5}	
DIIS Error	TolErr	5.000×10^{-7}	

D Complementary Structure Calculations

Table D.1: Dissociation energies of the dibenzofuran complexes with (D_0) and without (D_{el}) harmonic zero-point vibrational energy calculated at B3LYP-D3(BJ)/def2-TZVP level in kJ mol^{-1} . Energies relative to the most stable dimer (ΔE_{el} and ΔE_0) are given in kJ mol^{-1} , harmonic OH stretching wavenumbers (ω_{OH}) and shifts ($\Delta\omega_{OH}$) from the corresponding monomer vibrational wavenumber in cm^{-1} , band intensities (I_{OH}) in km mol^{-1} .

Cluster	ΔE_{el}	ΔE_0	D_{el}	D_0	ω_{OH}	$\Delta\omega_{OH}$	I_{OH}
dibenzofuran + MeOH							
OH-OP	-0.5	1.0	24.4	19.6	3762	47	237
OH-O ^t C_s	0.0	0.8	23.8	19.7	3773	37	143
OH- π 6	0	0	23.9	20.5	3784	26	110
CH-O	4.6	5.1	19.3	15.5	3813	-3	33
dibenzofuran + <i>t</i>-BuOH							
OH-O	-0.8	0.2	27.4	23.6	3746	39	212
OH- π 6	0	0	26.5	23.8	3766	19	119
OH- π 6'	0.0	0.1	26.5	23.7	3759	26	135
CH-O	3.5	4.2	23.1	19.6	3785	0	15
CH- π	5.1	5.0	21.4	18.8	3785	0	12
CH- π	5.2	5.1	21.4	18.7	3785	0	12

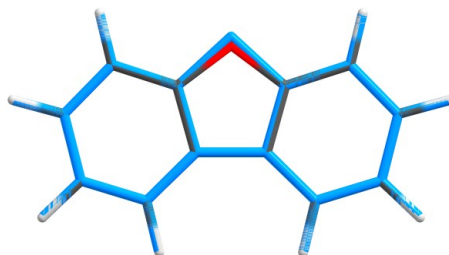


Figure D.1: Overlay of the dibenzofuran geometries obtained from calculations at B3LYP-D3(BJ, abc)/def2-TZVP level and microwave experiment (blue).

Table D.2: Experimental structure coordinates of dibenzofuran.

	x	y	z
C	-1.715 69	0.000 00	-1.534 32
C	-0.704 03	0.000 00	-0.550 27
C	-1.088 68	0.000 00	0.795 79
C	-2.412 73	0.000 00	1.229 31
C	-3.392 76	0.000 00	0.227 10
C	-3.051 33	0.000 00	-1.126 37
C	1.715 69	0.000 00	-1.534 32
C	0.704 03	0.000 00	-0.550 27
C	1.088 68	0.000 00	0.795 79
C	2.412 73	0.000 00	1.229 31
C	3.392 76	0.000 00	0.227 10
C	3.051 33	0.000 00	-1.126 37
O	0.000 00	0.000 00	1.799 68
H	-1.472 82	0.000 00	-2.537 34
H	-2.658 12	0.000 00	2.231 71
H	-4.389 13	0.000 00	0.495 95
H	-3.798 84	0.000 00	-1.837 89
H	1.472 82	0.000 00	-2.537 34
H	2.658 12	0.000 00	2.231 71
H	4.389 13	0.000 00	0.495 95
H	3.798 84	0.000 00	-1.837 89

Table D.3: Dissociation energies of the (dibenzofuran)₂-methanol trimers with (D_0) and without (D_{el}) harmonic zero-point vibrational energy calculated at B3LYP-D3(BJ, abc)/def2-TZVP level in kJ mol^{-1} . Energies relative to the most stable dimer (ΔE_{el} and ΔE_0) are given in kJ mol^{-1} , harmonic OH stretching wavenumbers (ω_{OH}) and shifts ($\Delta\omega_{OH}$) from the corresponding monomer vibrational wavenumber in cm^{-1} , band intensities (I_{OH}) in km mol^{-1} .

Cluster	ΔE_{el}	ΔE_0	D_{el}	D_0	ω_{OH}	$\Delta\omega_{OH}$	I_{OH}
(dibenzofuran)₂ + MeOH							
I OH-O ^t out	9.2	8.0	24.4	20.4	3768	42	184
I OH-O ^p in	6.2	6.1	27.4	22.3	3741	69	341
I OH-O ^p in	6.8	6.5	26.7	21.9	3744	65	340
I OH-O ^{p'} out	2.8	2.3	30.7	26.2	3739	70	323
I OH-O ^{p'} out	3.2	2.5	30.3	25.9	3746	64	309
I OH- π in	2.8	2.0	30.7	26.4	3736	74	243
I OH- π in	3.5	2.5	30.1	25.9	3753	57	224
I OH- π out	9.1	7.2	24.4	21.2	3779	31	140
I OH- π out	9.7	7.7	23.9	20.7	3785	25	125
I CH-O in	17.7	15.5	15.8	12.9	3814	-5	36
II OH-O ^t out ^a	10.4	9.0	23.2	19.4	3767	43	180
II OH-O ^t out ^b	10.5	9.1	23.1	19.3	3768	42	179
II OH-O ^p in ^b	6.9	5.6	26.7	22.8	3734	75	360
II OH-O ^p in ^a	7.0	6.8	26.6	21.7	3743	67	262
II OH-O ^p in ^b	7.3	6.8	26.3	21.6	3740	69	314
II OH-O ^{p'} in ^a	0	0	33.5	28.4	3709	101	375
II OH-O ^{p'} in ^a	0.4	0.3	33.1	28.1	3709	101	344
II OH-O ^{p'} in ^b	3.6	2.8	29.9	25.6	3738	71	301
II OH- π out ^a	10.4	8.1	23.2	20.3	3780	29	136
II OH- π out ^a	10.6	8.4	23.0	20.0	3780	30	132
II OH- π out ^b	10.7	8.5	22.8	19.9	3781	29	129
II OH- π out ^b	10.5	8.3	23.1	20.1	3779	31	141
OH-O ^p in	7.9	7.8	25.7	20.6	3743	67	263
OH- π in	18.3	17.1	15.2	11.3	3784	25	65
CH-O in	16.4	15.3	17.2	13.1	3814	-4	36

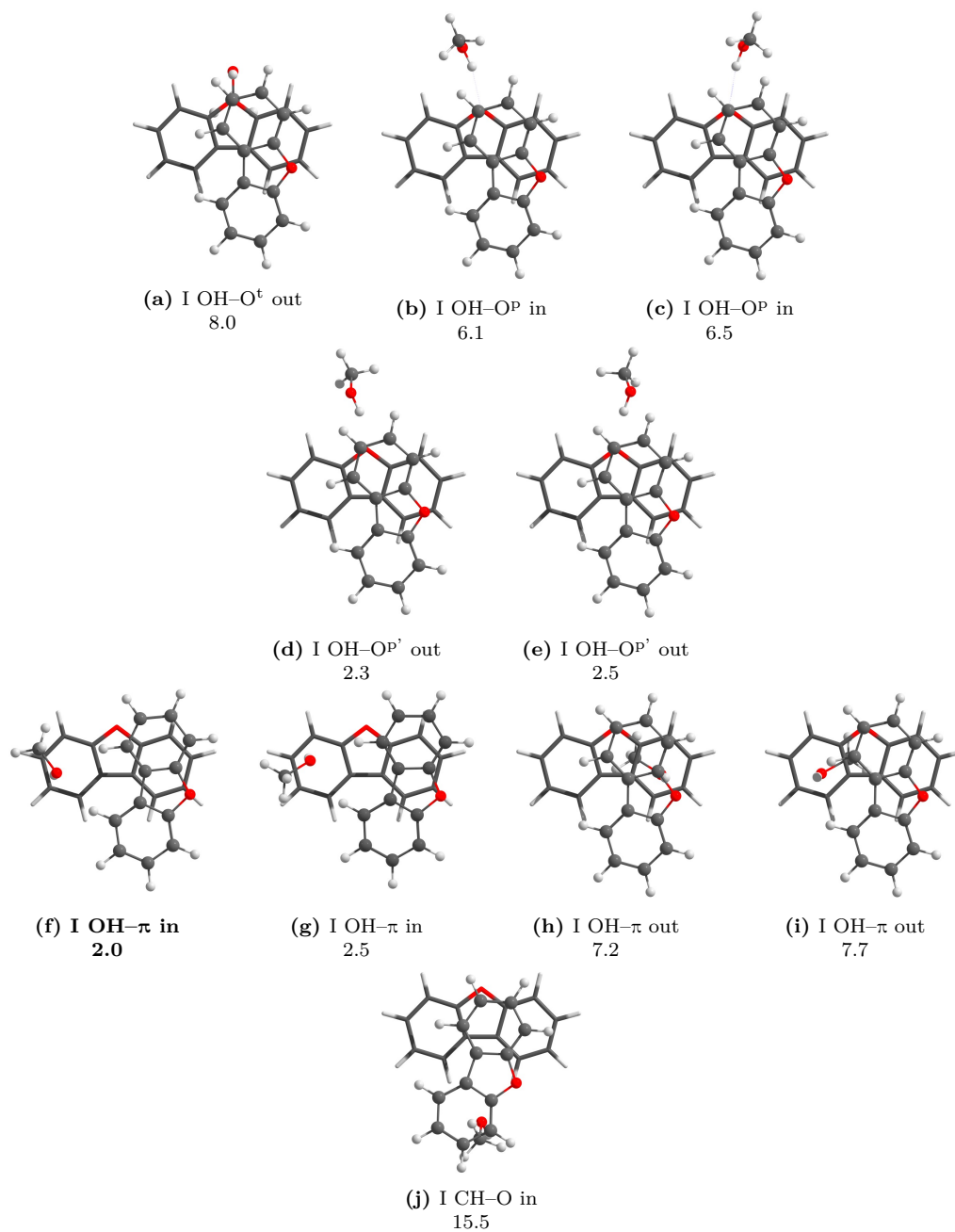


Figure D.2: Structures and relative ZPVE-corrected energies (ΔE_0) in kJ mol^{-1} of trimers of methanol and dibenzofuran including the most stable dibenzofuran dimer structure (I) calculated on B3LYP-D3(BJ, abc)/def2-TZVP level.

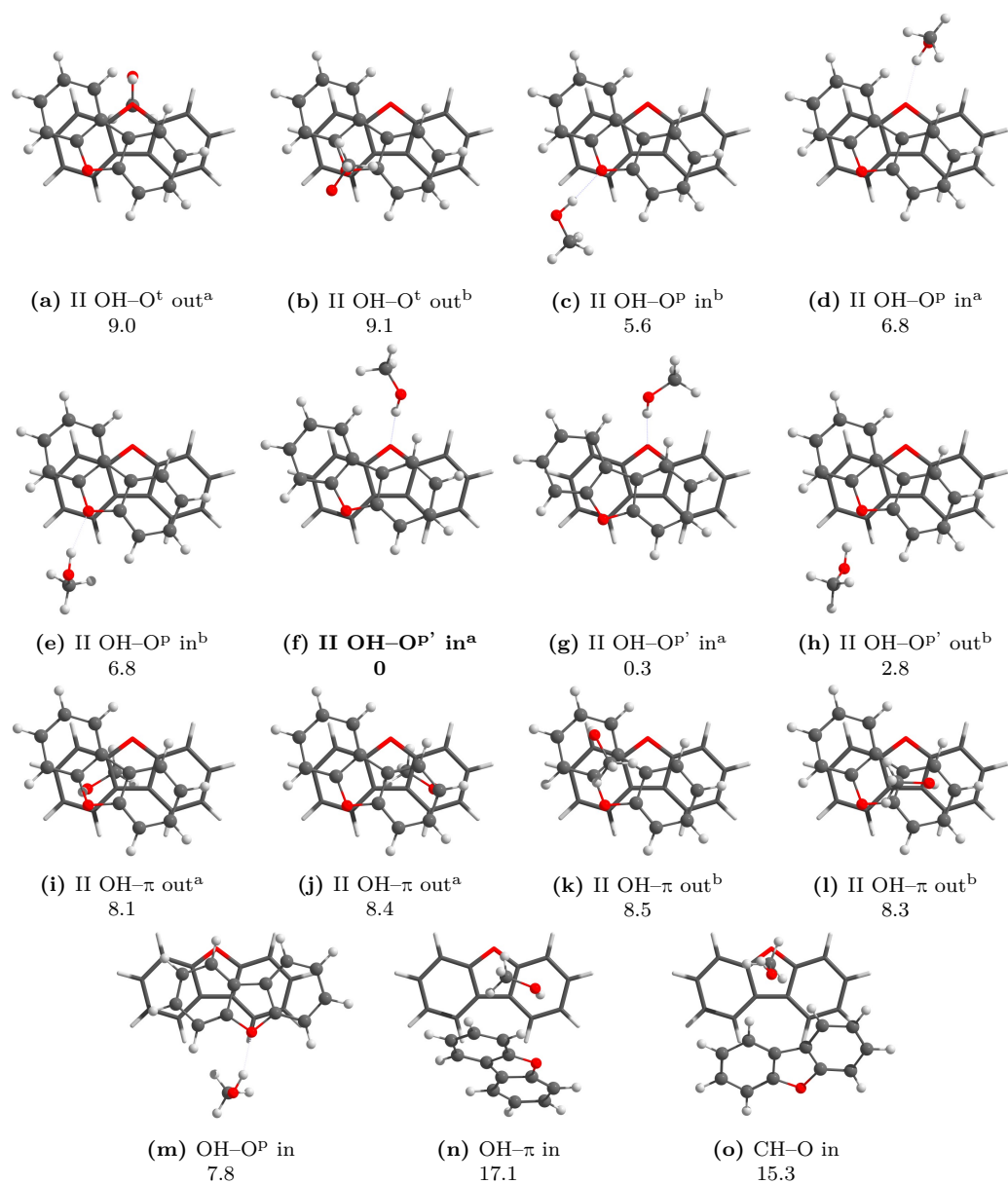


Figure D.3: Structures and relative ZPVE-corrected energies (ΔE_0) in kJ mol^{-1} of trimers of methanol and dibenzofuran including other than the most stable dibenzofuran dimer structure calculated on B3LYP-D3(BJ, abc)/def2-TZVP level.

Table D.4: Energies relative to the most stable trimer of the dibenzofuran–methanol₂ trimers with (ΔE_0) and without (ΔE_{el}) harmonic zero-point vibrational energy calculated at B3LYP-D3(BJ)/def2-TZVP level in kJ mol⁻¹. Energies are given in kJ mol⁻¹, harmonic OH stretching wavenumbers (ω_{OH}) and shifts ($\Delta\omega_{OH}$) from the corresponding monomer vibrational wavenumber in cm⁻¹, band intensities (I_{OH}) in km mol⁻¹.

Cluster	ΔE_{el}	ΔE_0	ω_{OH}	$\Delta\omega_{OH}$	I_{OH}
dibenzofuran + MeOH₂					
OH–OH–O ^t	3.3	4.0	3580	229	437
OH–OH–O ^p	2.8	3.5	3561	249	517
OH–OH– π	9.6	8.7	3614	196	451
OH–OH– π	6.2	5.6	3594	216	482
OH–OH– π	0.0	0.3	3594	216	349
OH–OH– π	0	0	3568	242	494
OH–OH– π	7.1	6.7	3615	195	347
OH–O ^t OH–O ^t o	22.8	20.3	3782	28	244
OH–O ^t OH–O ^p o	23.2	20.8	3774	36	220
OH–O ^t OH– π o	21.9	18.7	3776	33	148
OH–O ^p OH– π o	21.1	18.2	3767	43	232
OH–O ^p OH– π s	20.8	18.3	3767	43	227
OH–O ^p OH– π s	18.9	16.6	3765	45	193
OH–O ^p CH–O o	24.1	22.1	3758	52	261
OH–O ^p CH–O s	24.2	22.3	3757	53	252
OH– π OH– π o	22.6	18.0	3790	20	208
OH– π OH– π s	20.1	16.6	3775	35	123

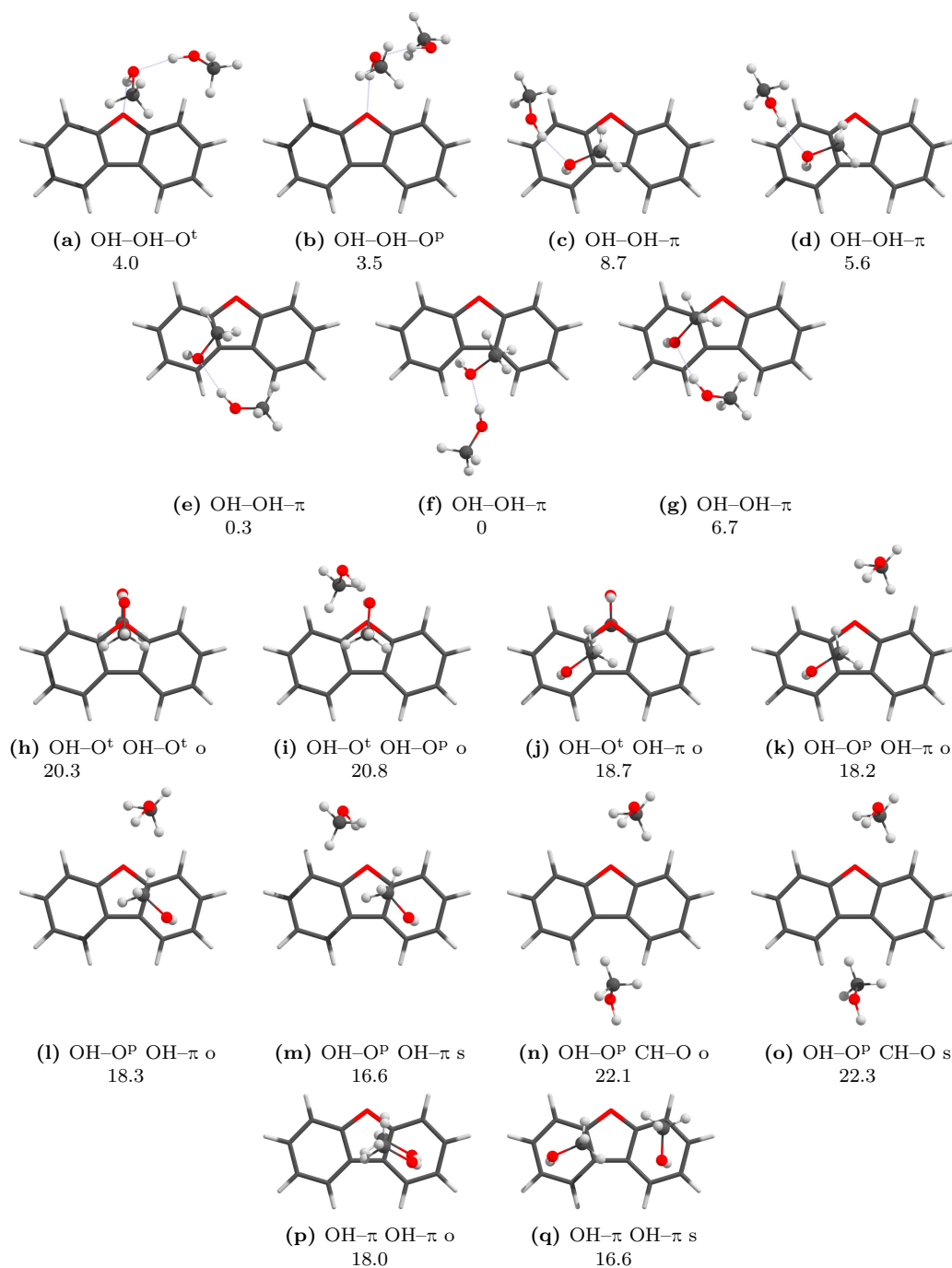


Figure D.4: Structures and relative ZPVE-corrected energies (ΔE_0) in kJ mol^{-1} of trimers of dibenzofuran–methanol₂ calculated on B3LYP-D3(BJ)/def2-TZVP level. 'o' and 's' denote the methanol molecules being on opposite or the same side, respectively.

Table D.5: Dissociation energies of the dimers of furan with 1-naphthol with (D_0) and without (D_{el}) harmonic zero-point vibrational energy calculated at B3LYP-D3(BJ)/def2-TZVP level in kJ mol^{-1} . Energies relative to the most stable dimer (ΔE_{el} and ΔE_0) are given in kJ mol^{-1} , harmonic OH stretching wavenumbers (ω_{OH}) and shifts ($\Delta\omega_{OH}$) from the *trans*-1-naphthol monomer vibrational wavenumber in cm^{-1} , band intensities (I_{OH}) in km mol^{-1} .

Dimer	ΔE_{el}	ΔE_0	D_{el}	D_0	ω_{OH}	$\Delta\omega_{OH}$	I_{OH}
Furan + 1NpOH							
$\text{OH}_t\text{-O}$	0	0	26.4	22.5	3699	103	639
$\text{OH}_t\text{-}\pi^O$	1.5	0.6	24.9	21.9	3705	97	495
$\text{OH}_t\text{-}\pi^\pi$	1.8	1.1	24.5	21.4	3681	120	589
$\text{OH}_c\text{-}\pi$	4.9	3.9	21.5	18.6	3739	63	228
$\text{OH}_c\text{-}\pi$	7.1	6.1	19.2	16.4	3717	84	226
$\text{OH}_c\text{-O}$	6.1	5.5	20.7	17.4	3735	66	278
$\text{OH}_c\text{-O}$	8.0	6.2	18.4	16.3	3781	20	43
$\pi_t\text{-}\pi$	5.5	3.6	20.9	18.9	3803	-1	66
$\pi_t\text{-}\pi$	5.9	4.2	20.5	18.3	3802	0	65
$\pi_t\text{-}\pi$	5.1	3.7	21.2	18.7	3799	2	58
$\pi_t\text{-}\pi$	6.2	4.3	20.2	18.2	3803	-2	62

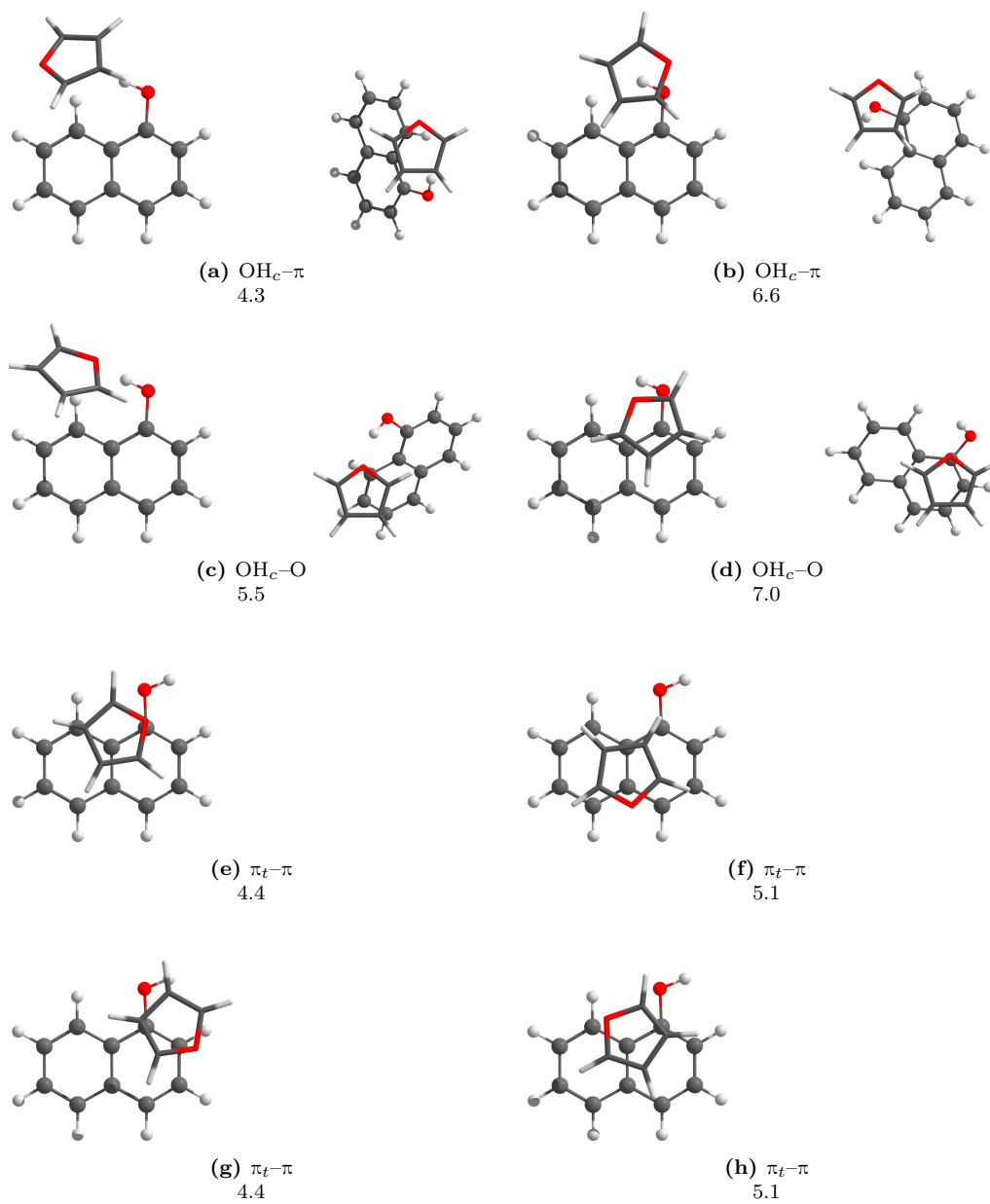


Figure D.5: Structures and relative ZPVE-corrected energies (ΔE_0) in kJ mol^{-1} of the most stable dimers of 1-naphthol and furan calculated at B3LYP-D3(BJ, abc)/def2-TZVP level.

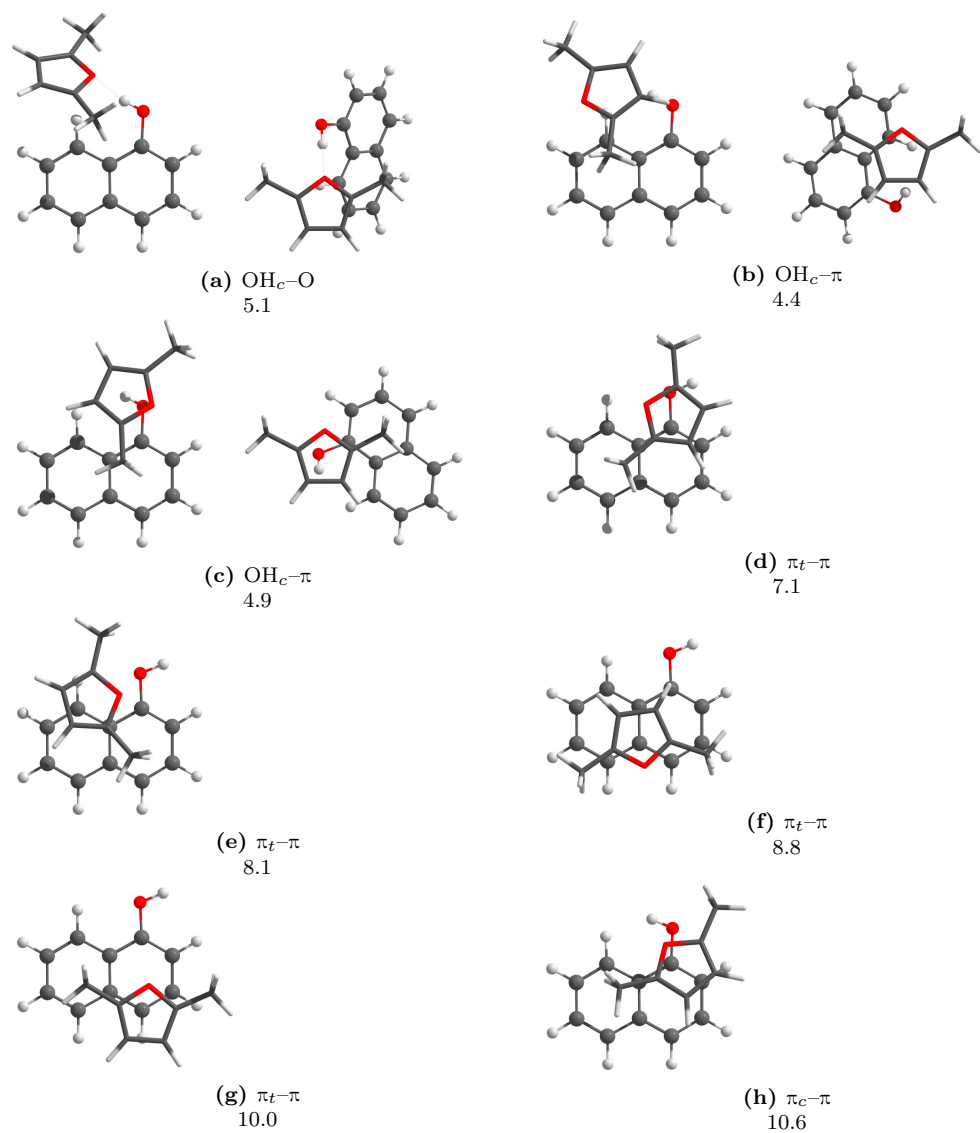


Figure D.6: Structures and relative ZPVE-corrected energies (ΔE_0) in kJ mol^{-1} of the most stable dimers of 1-naphthol and 2,5-dimethylfuran calculated at B3LYP-D3(BJ, abc)/def2-TZVP level.

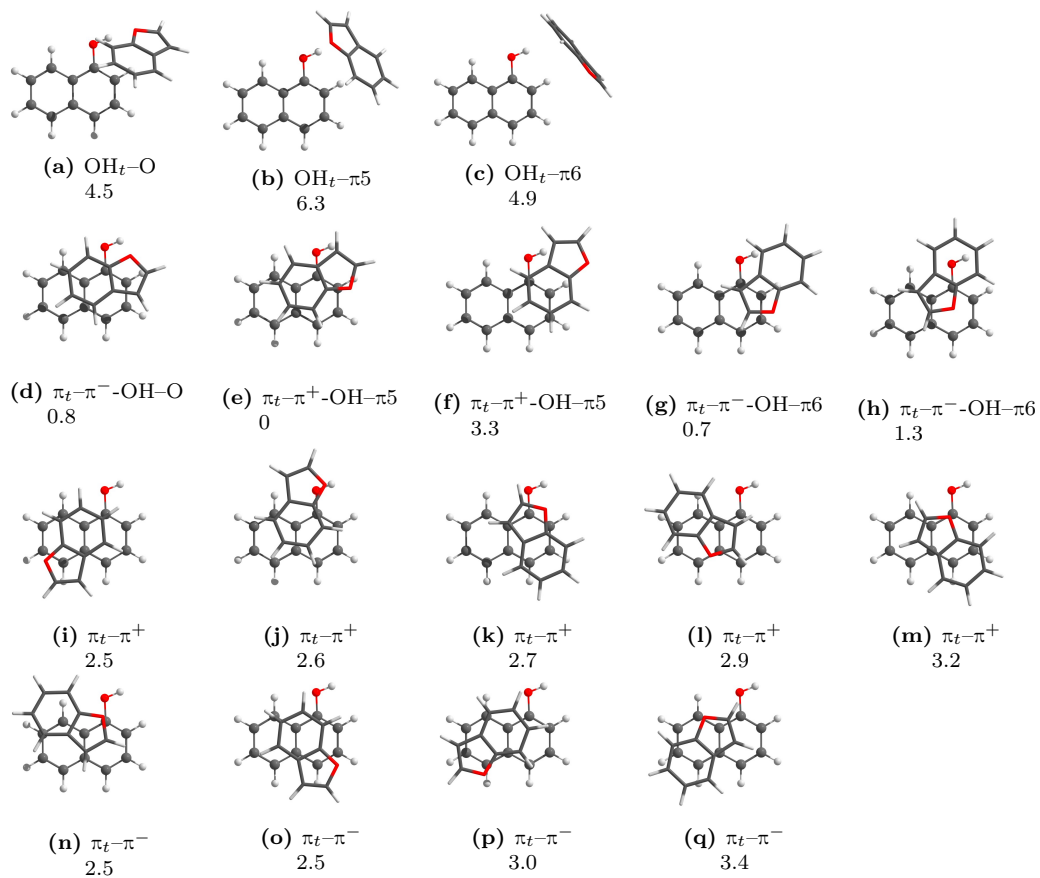


Figure D.7: Structures and relative ZPVE-corrected energies (ΔE_0) in kJ mol^{-1} of the most stable dimers of 2,3-benzofuran and *trans*-1-naphthol at B3LYP-D3(BJ)/def2-TZVP level calculated with Turbomole.

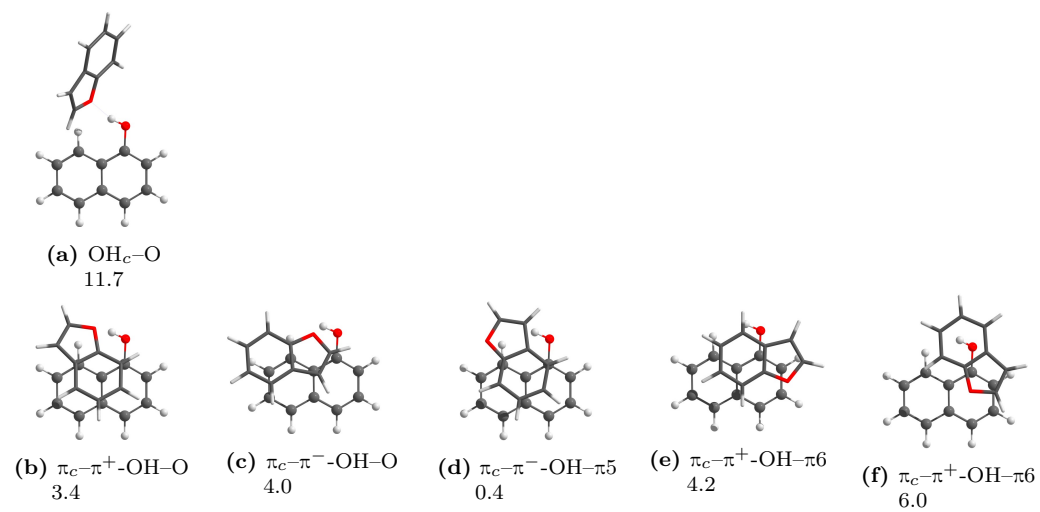


Figure D.8: Structures and relative ZPVE-corrected energies (ΔE_0) in kJ mol^{-1} of the most stable dimers of 2,3-benzofuran and *cis*-1-naphthol at B3LYP-D3(BJ)/def2-TZVP level calculated with Turbomole.

Table D.6: Calculated energies and vibrational wavenumbers of the 2,3-benzofuran–1-naphthol dimers at B3LYP-D3(BJ)/def2-TZVP level calculated with `Turbomole`. Energies are given relative to the most stable dimer. Dissociation energies and frequency shifts are given relative to the *trans*-conformation.

Dimer	ΔE_{el}	ΔE_0	D_{el}	D_0	ω_{OH}	$\Delta\omega_{\text{OH}}$	I_{OH}
2,3-Benzofuran + 1NpOH							
OH _t -O	3.9	4.5	30.2	26.4	3711	90	372
OH _t - π_5	6.1	6.3	28.0	24.7	3746	56	264
OH _t - π_6	5.2	4.9	28.9	26.1	3715	87	455
$\pi_t-\pi^-$ -OH-O	1.1	0.8	33.0	30.1	3801	1	57
$\pi_t-\pi^+$ -OH- π_5	0	0	34.1	31.0	3797	4	51
$\pi_t-\pi^+$ -OH- π_5	3.5	3.3	30.5	27.7	3765	36	97
$\pi_t-\pi^-$ -OH- π_6	0.5	0.7	33.6	30.3	3767	34	92
$\pi_t-\pi^-$ -OH- π_6	2.3	1.3	31.8	29.6	3773	28	86
$\pi_t-\pi^+$	3.0	2.5	31.1	28.5	3802	-1	64
$\pi_t-\pi^+$	3.2	2.6	30.9	28.4	3804	-3	59
$\pi_t-\pi^+$	3.3	2.7	30.7	28.2	3801	0	61
$\pi_t-\pi^+$	3.4	2.9	30.7	28.0	3801	0	63
$\pi_t-\pi^+$	3.8	3.2	30.2	27.8	3803	-2	64
$\pi_t-\pi^-$	3.1	2.5	31.0	28.4	3804	-2	65
$\pi_t-\pi^-$	3.0	2.5	31.1	28.4	3802	-1	63
$\pi_t-\pi^-$	3.7	3.0	30.4	27.9	3802	-1	64
$\pi_t-\pi^-$	3.9	3.4	30.2	27.6	3801	1	67
OH _c -O	11.6	11.7	22.5	19.3	3688	114	640
$\pi_c-\pi^+$ -OH-O	3.6	3.4	30.5	27.6	3753	48	92
$\pi_c-\pi^-$ -OH-O	4.6	4.0	29.5	27.0	3782	19	50
$\pi_c-\pi^-$ -OH- π_5	0.4	0.4	33.7	30.6	3753	49	86
$\pi_c-\pi^+$ -OH- π_6	5.0	4.2	29.1	26.7	3796	5	29
$\pi_c-\pi^+$ -OH- π_6	6.4	6.0	27.6	25.0	3737	64	117

E Complementary Spectra

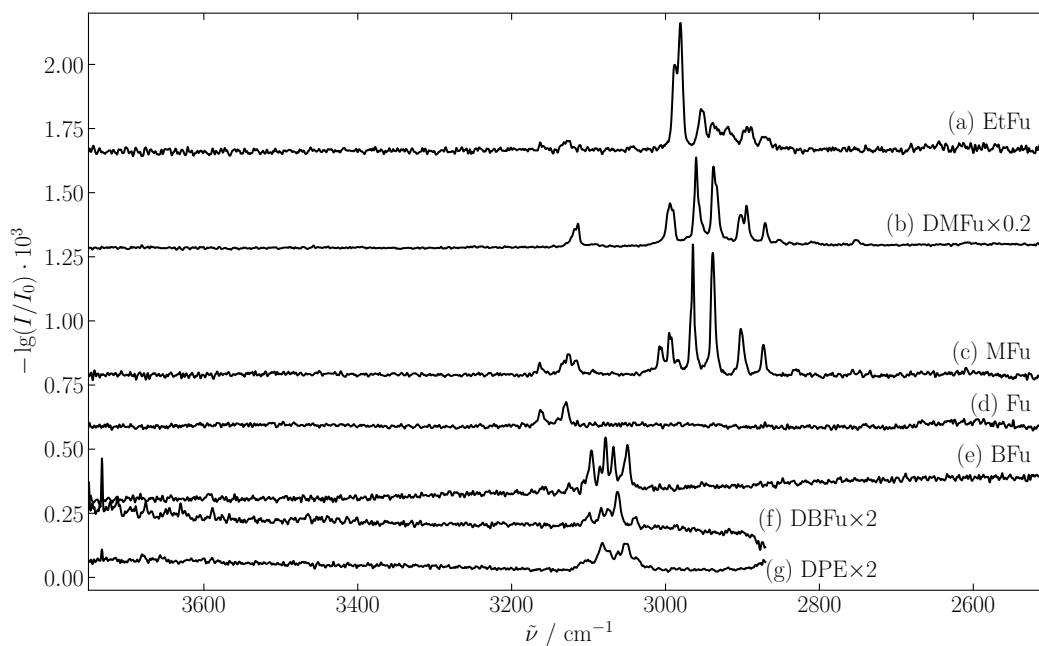


Figure E.1: Complementary IR Spectra of the pure acceptor compounds.

- (a) 2-ethylfuran (*filet-jet*, EtFu: $-28\text{ }^{\circ}\text{C}$, 0.10/2.52 s, helium: 0.10/4.84 s, helium: 5.12/0.10 s);
- (b) 2,5-dimethylfuran (*filet-jet*, DMFu: $-20\text{ }^{\circ}\text{C}$, 1.04/0.10 s, scaled by factor 0.2);
- (c) 2-methylfuran (*filet-jet*, MFu: $-28\text{ }^{\circ}\text{C}$, 0.10/10.2 s, helium: 0.10/9.90 s, helium: 10.1/0.10 s);
- (d) furan (*filet-jet*, Fu: $-28\text{ }^{\circ}\text{C}$, 0.10/5.00 s, helium: 0.10/7.60 s, helium: 10.0/0.10 s);
- (e) 2,3-benzofuran (*filet-jet*, BFu: $10\text{ }^{\circ}\text{C}$, 0.48/0.51 s);
- (f) dibenzofuran (*popcorn-jet*, DBFu: $120\text{ }^{\circ}\text{C}$, double-slit nozzle: $140\text{ }^{\circ}\text{C}$, scaled by factor 2);
- (g) diphenyl ether (*popcorn-jet*, DPE: $100\text{ }^{\circ}\text{C}$, double-slit nozzle: $120\text{ }^{\circ}\text{C}$, scaled by factor 2);

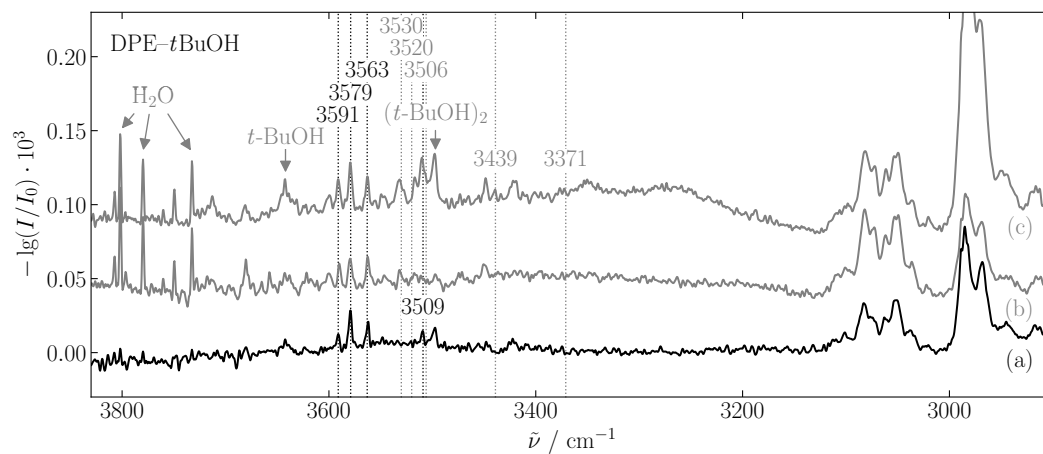


Figure E.2: Complementary IR Spectra of diphenyl ether and *tert*-butyl alcohol. Band positions of *tert*-butyl alcohol–water clusters are marked in gray at 3530 cm^{-1} , 3520 cm^{-1} , 3506 cm^{-1} , 3439 cm^{-1} and 3371 cm^{-1} . The positions were taken from Ref. 248;
 (a) remeasured in this work (DPE: $100\text{ }^{\circ}\text{C}$, *t*-BuOH: $-20\text{ }^{\circ}\text{C}$, double-slit nozzle: $120\text{ }^{\circ}\text{C}$);
 (b) taken from Ref. 34 (DPE: $110\text{ }^{\circ}\text{C}$, *t*-BuOH: $-10\text{ }^{\circ}\text{C}$, double-slit nozzle: $130\text{ }^{\circ}\text{C}$);
 (c) taken from Ref. 34 (DPE: $110\text{ }^{\circ}\text{C}$, *t*-BuOH: $10\text{ }^{\circ}\text{C}$, double-slit nozzle: $130\text{ }^{\circ}\text{C}$);
 see also Refs. 34,75,248.

F Data

Table F.1: Experimental frequencies $\tilde{\nu}^{\text{exp}}$ and shifts $\Delta\tilde{\nu}^{\text{exp}}$ from the donor monomer position, as well as shifts of the harmonic frequency $\Delta\omega_{\text{OH}}^{\text{theo}}$ calculated at B3LYP-D3(BJ, abc)/def2-TZVP level. The reference values for $\Delta\tilde{\nu}^{\text{exp}}$ and $\Delta\omega_{\text{OH}}^{\text{theo}}$ are 3686 cm^{-1} ¹³³ and 3809.63 cm^{-1} for MeOH, 2718 cm^{-1} ¹³³ and 2773.48 cm^{-1} for MeOD, 3642 cm^{-1} ¹⁶² and 3785.28 cm^{-1} for *t*-BuOH, 3657 cm^{-1} ²²² and 3799.08 cm^{-1} for PhOH, 3655 cm^{-1} ²¹⁸ and 3801.17 cm^{-1} for 1NpOH, respectively.

	OH–O			OH– π		
	$\tilde{\nu}^{\text{exp}}$	$\Delta\tilde{\nu}^{\text{exp}}$	$\Delta\omega_{\text{OH}}^{\text{theo}}$	$\tilde{\nu}^{\text{exp}}$	$\Delta\tilde{\nu}^{\text{exp}}$	$\Delta\omega_{\text{OH}}^{\text{theo}}$
MeOH						
furan	3654 ¹³⁹	32	28	3636 ¹³⁹	50	50
2-methylfuran	3645 ¹³⁹	41	40	3623 ¹³⁹	63	65
2,5-dimethylfuran	3636 ¹³⁹	50	50	3612 ¹³⁹	74	74
2- <i>t</i> -butylfuran			68	3612 ⁸⁸	75	77
2,3-benzofuran	3645 ¹⁴⁰	41	43	3636 ¹⁴⁰	47	34
dibenzofuran	3642 ^{196a}	44 ^{196a}	37	3637 ^{196a}	49 ^{196a}	26
diphenyl ether	3607 ⁸³	79	68	3623 ⁸³	63	37
phenyl vinyl ether	3625 ²⁴⁰	61	60			
anisole	3598 ⁸⁶	88	102	3629 ⁸⁶	57	50
2-methyl anisole	3599 ^{158,159}	87	97 ²⁴⁹	3627 ^{158,159}	59	56 ²⁴⁹
3-methyl anisole E	3594 ¹⁵⁹	92	105 ²⁴⁹	3626 ¹⁵⁹	60	59 ²⁴⁹
4-methyl anisole	3594 ^{158,159}	92	106 ²⁴⁹	3627 ^{158,159}	59	56 ²⁴⁹
4- <i>t</i> -butyl anisole	3594 ^{158,159}	92	105 ²⁴⁹	3619 ^{158,159}	67	53 ²⁴⁹
2,3-dimethyl anisole	3599 ^{158,159}	87	96 ²⁴⁹	3620 ^{158,159}	66	43 ²⁴⁹
2,6-dimethyl anisole	3580 ¹⁵⁹	106	127 ²⁴⁹	3617 ¹⁵⁹	69	56 ²⁴⁹
3,5-dimethyl anisole	3592 ^{158,159}	94	106 ²⁴⁹	3619 ^{158,159}	67	60 ²⁴⁹
2,3,5-trimethyl anisole	3599 ^{158,159}	87	97 ²⁴⁹	3614 ^{158,159}	72	52 ²⁴⁹
4-fluoroanisole	3600 ²⁴⁹	86	98 ²⁴⁹			41 ²⁴⁹
2-chloroanisole	3611 ²⁴⁹	75	57 ²⁴⁹			37 ²⁴⁹
4-chloroanisole	3605 ²⁴⁹	81	93 ²⁴⁹			40 ²⁴⁹
4-bromoanisole	3605 ²⁴⁹	81	91 ²⁴⁹			39 ²⁴⁹
ethylene	–	–	–	3641 ²⁵⁰	45	64
benzene	–	–	–	3639 ^{251a}	47	30
fluorobenzene	–	–	–	3661 ^{252a}	25	26
<i>p</i> -chlorofluorobenzene	–	–	–		1 ^{253a}	10
toluene	–	–	–	3632 ⁸⁶	54	43

	OH–O			OH– π		
	$\tilde{\nu}^{\text{exp}}$	$\Delta\tilde{\nu}^{\text{exp}}$	$\Delta\omega_{\text{OH}}^{\text{theo}}$	$\tilde{\nu}^{\text{exp}}$	$\Delta\tilde{\nu}^{\text{exp}}$	$\Delta\omega_{\text{OH}}^{\text{theo}}$
phenylacetylene	–	–	–	3615 ^{161a}	71	19
THF	3493 ²⁴⁵	193	227	–	–	–
eucalyptol	3499 ²⁵⁴	187	235	–	–	–
MeOH	3575 ²⁵⁵	111	166	–	–	–
<i>t</i> -ethanol	3556 ²⁵⁵	130	177	–	–	–
<i>g</i> -ethanol	3548 ²⁵⁵	138	179	–	–	–
<i>t</i> -BuOH	3529 ²⁵⁵	157	192	–	–	–
1-octanol	3561 ²⁵⁶	125	177	–	–	–
1-adamantanol	3527 ²⁵⁶	159	197	–	–	–
acetone	3530 ²⁵⁷	156	185	–	–	–
acetone ((CD ₃) ₂ CO)	3529 ²⁵⁷	157	185	–	–	–
cyclobutanone	3549 ²⁴⁵	137 ²⁴⁵	161	–	–	–
cyclopentanone	3522 ²⁴⁵	164 ²⁴⁵	191	–	–	–
cyclohexanone	3521 ²⁴⁵	165 ²⁴⁵	197	–	–	–
cycloheptanone	3513 ²⁴⁵	173 ²⁴⁵	206	–	–	–
acetophenone Me	3528 ^{88,249}	158 ²⁴⁹	191 ²⁴⁹			
acetophenone Ph	3565 ^{88,249}	121 ²⁴⁹	144 ²⁴⁹			
2-fluoroacetophenone Me		145 ²⁴⁷	176 ²⁴⁷			
2-fluoroacetophenone Ph		109 ²⁴⁷	130 ²⁴⁷			
4-fluoroacetophenone Me		153 ²⁴⁷	186 ²⁴⁷			
4-fluoroacetophenone Ph		119 ²⁴⁷	145 ²⁴⁷			
2,2,2-trifluoroacetophenone Ph		66 ²⁴⁷	81 ²⁴⁷			
acetophenone-d ₃ Me		159 ²⁴⁷	190 ²⁴⁷			
acetophenone-d ₃ Ph		121 ²⁴⁷	144 ²⁴⁷			
acetophenone-d ₅ Me		159 ²⁴⁷	190 ²⁴⁷			
acetophenone-d ₅ Ph		122 ²⁴⁷	144 ²⁴⁷			
isobutyrophenone Alk	3550 ²⁴⁶	136	178 ²⁴⁶			
isobutyrophenone Ph	3576 ²⁴⁶	110	146 ²⁴⁶			
cyclopropylphenone Alk	3541 ²⁴⁶	145	181 ²⁴⁶			
cyclopropylphenone Ph	3559 ²⁴⁶	127	162 ²⁴⁶			
MeOD						
furan	2695 ¹³⁹	23	22	2685 ¹³⁹	33	37
2-methylfuran	2688 ¹³⁹	30	30	2675 ¹³⁹	43	47
2,5-dimethylfuran	2682 ¹³⁹	36	38	2667 ¹³⁹	51	54
2,3-benzofuran	2684	34	32	2688	30	25
MeOD	2638 ¹³³	80	120	–	–	–
acetone	2608 ²⁵⁷	110	134	–	–	–
acetone ((CD ₃) ₂ CO)	2608 ²⁵⁷	110	133	–	–	–
acetophenone Me	2606 ²⁴⁶	112	137 ²⁴⁶			
acetophenone Ph	2633 ²⁴⁶	85	105 ²⁴⁶			
<i>t</i>-BuOH						
2- <i>t</i> -butylfuran			59	3565	77	79

	OH-O			OH- π		
	$\tilde{\nu}^{\text{exp}}$	$\Delta\tilde{\nu}^{\text{exp}}$	$\Delta\omega_{\text{OH}}^{\text{theo}}$	$\tilde{\nu}^{\text{exp}}$	$\Delta\tilde{\nu}^{\text{exp}}$	$\Delta\omega_{\text{OH}}^{\text{theo}}$
dibenzofuran	(3613)	(29)	39	3607	35	19
diphenyl ether	3579 ⁷⁵	63	64	3591 ⁷⁵	51	31
anisole	3568 ²⁴⁵	74	92			
THF	3460 ²⁴⁵	182	208 ^b	–	–	–
eucalyptol	3470 ²⁵⁴	172	206	–	–	–
<i>t</i> -BuOH	3497 ²⁵⁵	145	201	–	–	–
norbornene 5	–	–	–		71 ¹⁶²	86
norbornene 6	–	–	–		63 ¹⁶²	70
cyclopentene	–	–	–		73 ¹⁶²	86
cyclohexene	–	–	–		80 ¹⁶²	92
cyclobutanone	3515 ²⁴⁵	128 ²⁴⁵	143	–	–	–
cyclopentanone	3489 ²⁴⁵	154 ²⁴⁵	168	–	–	–
cyclohexanone	3502 ²⁴⁵	141 ²⁴⁵	175	–	–	–
cycloheptanone	3499 ²⁴⁵	144 ²⁴⁵	177	–	–	–
acetophenone Me	3505 ²⁴⁶	137	169 ²⁴⁶			
acetophenone Ph	3544 ²⁴⁶	98	129 ²⁴⁶			
isobutyrophenone Alk	3534 ²⁴⁶	108	136 ²⁴⁶			
isobutyrophenone Ph	3546 ²⁴⁶	96	128 ²⁴⁶			
cyclopropylphenone Alk	3514 ²⁴⁶	128	160 ²⁴⁶			
cyclopropylphenone Ph	3526 ²⁴⁶	116	145 ²⁴⁶			
PhOH						
2,5-dimethylfuran	3540 ²¹⁷	116	136 ²¹⁷			144 ²¹⁷
ethylene	–	–	–	3580 ^{220a}	76	109
acetylene	–	–	–	3589 ^{220a}	67	92
cyclohexene	–	–	–	3530 ^{234a}	127 ^{234a}	174
benzene	–	–	–	3579 ^{220a}	77	82
anisole	3482 ²⁴⁵	174	199			
dimethyl ether	3410 ^{234a}	247 ^{234a}	284	–	–	–
THF	3332 ²⁴⁵	324	358	–	–	–
eucalyptol	3332 ²⁴⁵	324	372	–	–	–
PhOH	3530 ^{222a}	127 ^{222a}	153			
cyclobutanone	3434 ²⁴⁵	222 ²⁴⁵	258	–	–	–
cyclopentanone	3390 ²⁴⁵	266 ²⁴⁵	306	–	–	–
cyclohexanone	3429 ²⁴⁵	227 ²⁴⁵	255	–	–	–
cycloheptanone	3419 ²⁴⁵	237 ²⁴⁵	311	–	–	–
acetophenone Me	3400 ²⁴⁶	257	306 ²⁴⁶			
acetophenone Ph	3458 ²⁴⁶	199	251 ²⁴⁶			
cyclopropylphenone Alk	3416 ²⁴⁶	241	284 ²⁴⁶			
cyclopropylphenone Ph	3423 ²⁴⁶	234	280 ²⁴⁶			
1-NpOH						
furan	3570 ²¹⁷	85	103			96
2,5-dimethylfuran	3523 ²¹⁷	132	152			152

	OH-O			OH- π		
	$\tilde{\nu}^{\text{exp}}$	$\Delta\tilde{\nu}^{\text{exp}}$	$\Delta\omega_{\text{OH}}^{\text{theo}}$	$\tilde{\nu}^{\text{exp}}$	$\Delta\tilde{\nu}^{\text{exp}}$	$\Delta\omega_{\text{OH}}^{\text{theo}}$
benzene	–	–	–	3570 ³⁴	85	88
anisole	3458 ²¹⁵	197	221			

^a Data from IR/UV double resonance techniques.

^b Geometry differs from reference.

Table F.2: Zero-point energy $D_{\text{el}} - D_0$ calculated at B3LYP-D3(BJ, abc)/def2-TZVP level. The most stable dimer of each binding type is marked in bold.

Dimer	OH-O ^t	OH-O ^p	OH-O ^{p'}	OH- π ^{5 C3}	OH- π ^{5 C4}	OH- π ⁶
MeOH						
furan	3.9	4.2	–	3.4	–	–
2-methylfuran	4.6	4.1	4.4	3.8	3.7	–
2,5-dimethylfuran	4.5	–	4.2	4.0	–	–
2- <i>t</i> -butylfuran	–	4.6	4.6	4.5	4.0	–
2-ethylfuran (<i>t</i>)	4.5	4.1	4.4	3.9	3.8	–
2-ethylfuran (<i>g</i>)	4.7	–	4.8	4.5	3.8	–
2-ethylfuran (<i>g'</i>)	4.5	–	4.3	3.8	3.7	–
2,3-benzofuran	3.8	4.7	4.0	–	3.7	3.8
dibenzofuran	4.1	4.8	–	–	–	3.3
diphenyl ether		5.2	–	–	–	4.4
<i>t</i>-BuOH						
2- <i>t</i> -butylfuran	–	4.0	3.6	4.3	3.7	–
dibenzofuran		3.6	–	–	–	2.7
diphenyl ether		4.8	–	–	–	4.8
1NpOH						
furan	3.6	–	–	2.7	2.8	–
2,5-dimethylfuran	4.4	–	–	3.4	3.5	–
PhOH						
furan	4.0	–	–	3.1	3.2	–
2,5-dimethylfuran	4.4	–	–	3.5	3.5	–

G Box Plot Explanation

A box plot visualizes datasets through their quartiles and highlights possible outliers.^{258,259} An example is shown in Fig. G.1. A box is drawn from the upper ($x_{0.75}$) to the lower ($x_{0.25}$) quartile, which divide the dataset such that 75% and 25% of the data points are below these values, respectively. Thus, the box includes 50% of the data points. A line indicates the median of the dataset. The interquartile range ($IQR = x_{0.75} - x_{0.25}$), is often used to define the size of the whiskers extending from the box.^{258,260} Their ends mark the last data point within $1.5 \times IQR$ of each quartile ($x_{0.75} + 1.5(x_{0.75} - x_{0.25})$ and $x_{0.25} - 1.5(x_{0.75} - x_{0.25})$), respectively. Data beyond is plotted individually and can hence be analyzed in more detail.

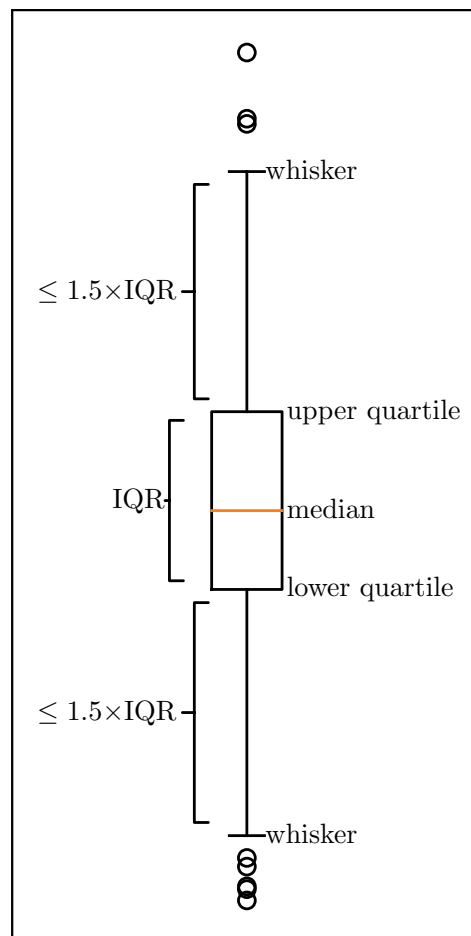


Figure G.1: Example of a box plot.

H List of Spectra

Fig. 2.2.4: Comparison V- and Double-Slit Nozzle: IR Spectra of DPE+MeOH

- a) 170904_cdef_170905_cd_171027_cdef_Diphenylether_110C_MeOH_-20C_130C_0.001.199
- b) 171026_cdefg_Diphenylether_110C_MeOH_-20C_0.001.117

Fig. 2.2.6: Effects of Spikes in the *popcorn*-Jet Spectra

- a) 171117_f_Dibenzofuran_110C_tBuOH_20C_130Cp.011
- b) 171117_f_Dibenzofuran_110C_tBuOH_20C_130C_lp_spike.011
- c) 171117_f_Dibenzofuran_110C_tBuOH_20C_130Cp_single.11
- d) 171117_f_Dibenzofuran_110C_tBuOH_20C_130C_lp_single.011
- e) 171117_b_Dibenzofuran_110C_tBuOH_20C_130C_lp_single.005

Fig. 3.2.3: 2,5-Dimethylfuran + MeOH IR Spectra at Different Concentrations

- a) 150505-ab-MeOH-m25C-25Dimethylfuran-m20C-0,75bar
- b) 150713-ab-MeOH-m25C-25Dimethylfuran-m20C-0,75barpm.150
- c) 150714-ab-MeOH-m25C-25Dimethylfuran-m20C-0,75bar.200
- d) 150714-c-MeOH-m25C-25Dimethylfuran-m20C-0,75barpm.100
- e) 151117-abc-25Dimethylfuran-m20C-He-MeOH-m25C-Ar-0,75bar

Fig. 3.2.4: 2,5-Dimethylfuran + MeOH IR Spectra Compared to Theory

- a) 150505-ab-MeOH-m25C-25Dimethylfuran-m20C-0,75bar
- b) 150519-ab-MeOD-m25C-25Dimethylfuran-m20C-0,75barpm
- c) wghtd_avg_MeOHD+25DMFuran_170628-f+170628-abcde+170227-abcdef-170228-abcdefg-minus-Notch

Fig. 3.2.7: Furan, 2-Methylfuran, 2,5-Dimethylfuran + MeOH IR Spectra Compared to Theory

- a) 170217-abcdefgh-170221-abcdef-MeOHD-m22C-Furan-m28C-0,75barpm.1000
- b) 170214-fghi-MeOH-m22C-Furan-m28C-0,75barpm.250
- c) 170131-bcde-MeOH-m22C-2MFuran-m28C-0,75bar.250
- d) 170206-ghi-170207-abcde-MeOHD-m22C-2MFuran-m28C-0,75barpm.500
- e) 170208-abc-MeOH-m22C-2MFuran-m28C-Ar-3,5prozent-0,75barpm.150
- f) 170202-abc-MeOD-m22C-2MFuran-m28C-0,75bar.250
- g) wghtd_avg_MeOHD+25DMFuran_170628-f+170628-abcde+170227-abcdef-170228-abcdefg-minus-Notch
- h) 150505-ab-MeOH-m25C-25Dimethylfuran-m20C-0,75bar
- i) 150519-ab-MeOD-m25C-25Dimethylfuran-m20C-0,75barpm

Fig. 3.3.3: 2-Ethylfuran + MeOH IR Spectra Compared to Theory

- a) 170123g-170124a-e-MeOH-m22C-2E-Furan-m28C-0,75barpm.300
- b) 170123bcd-MeOH-m22C-2E-Furan-m28C-0,75barpm
- c) 170131-bcde-MeOH-m22C-2MFuran-m28C-0,75bar.250

Fig. 3.3.6: 2-tert-Butylfuran + MeOH IR Spectra Compared to Theory

- a) 170704-a-tBuFuran-m25C-MeOH-m25C-0,75barpm.200
- b) 170704-bcdefghi-tBuFuran-m25C-MeOH-m25C-0,75barpm.300

Fig. 3.3.7: 2-tert-Butylfuran + t-BuOH IR Spectra Compared to Theory

- a) 170705-abcdefghij-tBuFuran-m25C-tBuOH-m10C-0,75barpm.400

Fig. 3.4.2: 2,3-Benzofuran + MeOH IR Spectra at Different Concentrations

- a) 150420-ab-MeOH-m20C-23Benzofuran-20C-0,75barpm.150
- b) 150608-a-MeOH-0,05%-23Benzofuran-10C-0,75barpm.300
- c) MeOH-0,05%-23Benzofuran-10C-Aceton-mitundohneAbsicht.400
- d) 150526-a-23Benzofuran-10C-0,75barpm.52

Fig. 3.4.3: 2,3-Benzofuran + MeOH IR Spectra Compared to Theory

- a) 150420-ab-MeOH-m20C-23Benzofuran-20C-0,75barpm.150
- b) 150520-abc-MeOD-m20C-23Benzofuran-20C-0,75barpm_2
- c) 150526-abc-MeOD-m20C-23Benzofuran-10C-0,75barpm

Fig. 3.4.7: Dibenzofuran + MeOH IR Spectra Compared to Theory

- a) 160811+12_Dibenzofuran_120C_MeOH_0,15%_He_03-10+03-09
- b) 180709_bcdefg_180710_bcdef_180713_bcdefg_Dibenzofuran_110C_MeOH_-25C_130C-150C.387
- c) 180711_bcdefg_180712_bcdef_Dibenzofuran_110C_MeOH_-10C_150C.239
- d) 160819+22_Dibenzofuran_120C_MeOD_0,15%_He_03-08+03-07
- e) 150420-ab-MeOH-m20C-23Benzofuran-20C-0,75barpm.150

Fig. 3.4.9: Dibenzofuran + t-BuOH IR Spectra Compared to Theory

- a) 171115_fgh_171116_cdefgh_Dibenzofuran_110C_tBuOH_10C_130C.175

Fig. 3.4.10: Dibenzofuran Microwave Spectrum

Ne s1-dibenzofuran-150C_500k-avg

Fig. 3.4.12: Dibenzofuran + MeOH Microwave Spectrum

He s4-dibenzofuran-100C-methanol-halfopen-helium_1500k-ft
Ne s2-dibenzofuran-100C-methanol-halfopen_2100k-ft

Fig. 3.4.14: Dibenzofuran + t-BuOH Microwave Spectrum

Ne s1-db-100C-tba-externalhalf_2300k-ft

Fig. 4.0.3: Diphenyl Ether + MeOH IR Spectra Compared to Theory

- a) Diphenylether_100C_MeOH_0,16%_OH_He_151027_04-10v_151028_03-11v
- b) 170904_cdef_170905_cd_171027_cdef_Diphenylether_110C_MeOH_-20C_130C_0.001.199
- c) 151112-b-g-Diphenylether-24C-MeOH-m25C-He-0,75bar

Fig. 4.0.5: Diphenyl Ether + t-BuOH IR Spectra Compared to Theory

- a) 151124+151125_Diphenylether_100C_tBuOH_-20C_He_04-10v+04-12v
- b) 151207+151208_Diphenylether_100C_tBuOH_-20C_He+10%Ar_04-07+09-12+03-10
- c) 160725-b-Diphenylether-27C-tBuOH-m10C-0,75barpm.350
- d) 151209_Diphenylether_100C_tBuOD_-20C_He_04-11

Fig. 5.1.3: Furan + 1-NpOH IR Spectra Compared to Theory

- a) NpOHBenzol_OH_He_120C_sat-20C_Mittel04-11+20+22-25

- b) 180111_defgh_1naphthol_120C_furan_m25C_140C_lp.120
- c) 171212_cdef_1naphthol_120C_dimethylfuran_m20C_140C_lp.71
- d) 171207_abc_171211_cdef_1naphthol_120C_dimethylfuran_m10C_140C_lp.97

Fig. 5.1.5: Furan, 2,5-Dimethylfuran + 1-NpOH R2PI Spectra

- a) Fu-1NpOH_R2PI
- b) DMFu-1NpOH_R2PI

Fig. 5.1.6: Furan + 1-NpOH SEP-R2PI Spectra

- a) Fu-1NpOH_dump
- b) Fu-1NpOH_SEP

Fig. 5.1.7: 2,5-Dimethylfuran + 1-NpOH SEP-R2PI Spectra

- a) DMFu-1NpOH_Fluoreszenz
- b) DMFu-1NpOH_SEP

Fig. 5.2.2: Furan, 2,5-Dimethylfuran + PhOH IR Spectra Compared to Theory

- a) 171213_bcdef_171214_bcdefg_171215_bcdef_phenol_40C_dimethylfuran_m20C_60C_lp.341
- b) 171213_bcdef_171214_bcdef_171215_bcdef_phenol_40C_dimethylfuran_m20C_60C_nlp.279

Fig. E.1: IR Spectra of Pure Acceptors

- a) 170123-e-2E-Furan-m28C-0,75barpm.50
- b) 150519-a-25Dimethylfuran-m20C-0,75barpm.20
- c) 170201-gh-2MFuran-m28C-0,75bar.100
- d) 170216-ik-Furan-m28C-0,75barpm.100
- e) 150526-a-23Benzofuran-10C-0,75barpm.52
- f) 160803_Dibenzofuran_120C_He_04-08v.95
- g) 150922_Diphenylether_100C_OH_He_03-11v

Fig. E.2: Diphenyl Ether + *t*-BuOH Complementary IR Spectra

- a) 151124+151125_Diphenylether_100C_tBuOH_-20C_He_04-10v+04-12v
- b) Diphenylether+tBuOH_OH_He_110C_sat-10C_Mittel05-09+12-20v
- c) Diphenylether+tBuOH_OH_He_110C_sat10C_Mittel07-12+16+18-23v

I List of Figures

2.2.1	<i>popcorn</i> -Jet	8
2.2.2	Pulse Sequence of the <i>popcorn</i> -Jet	9
2.2.3	Technical Drawing of the Conical V-Nozzle	12
2.2.4	Comparison V- and Double-Slit Nozzle: IR Spectra of DPE+MeOH	13
2.2.5	Double Pick-Up Design for the <i>popcorn</i> -Jet	15
2.2.6	Effects of Spikes in the <i>popcorn</i> -Jet Spectra	17
2.3.1	COMPACT Microwave Setup	20
2.4.1	Level Diagram of the SEP-R2PI Experiment	21
3.1.1	Binding Types Structures	36
3.2.1	Furan, 2-Methylfuran, 2,5-Dimethylfuran + MeOH Dimer Structures	39
3.2.2	Furan, 2-Methylfuran, 2,5-Dimethylfuran + MeOH Binding Energy	40
3.2.3	2,5-Dimethylfuran + MeOH IR Spectra at Different Concentrations	41
3.2.4	2,5-Dimethylfuran + MeOH IR Spectra Compared to Theory	43
3.2.5	Schematic Explanation of the Deuteration Effect	44
3.2.6	2,5-Dimethylfuran + MeOH Transition States	45
3.2.7	Furan, 2-Methylfuran, 2,5-Dimethylfuran + MeOH IR Spectra Compared to Theory	49
3.3.1	2-Ethylfuran Monomer Structures	53
3.3.2	2-Ethylfuran + MeOH Dimer Structures	54
3.3.3	2-Ethylfuran + MeOH IR Spectra Compared to Theory	57
3.3.4	2- <i>tert</i> -Butylfuran + MeOH Dimer Structures	59
3.3.5	2- <i>tert</i> -Butylfuran + <i>t</i> -BuOH Dimer Structures	60
3.3.6	2- <i>tert</i> -Butylfuran + MeOH IR Spectra Compared to Theory	62
3.3.7	2- <i>tert</i> -Butylfuran + <i>t</i> -BuOH IR Spectra Compared to Theory	63
3.4.1	2,3-Benzofuran + MeOH Dimer Structures	65
3.4.2	2,3-Benzofuran + MeOH IR Spectra at Different Concentrations	67
3.4.3	2,3-Benzofuran + MeOH IR Spectra Compared to Theory	69
3.4.4	2,3-Benzofuran + MeOH Transition States	70
3.4.5	Dibenzofuran + MeOH Dimer Structures	72
3.4.6	Dibenzofuran + <i>t</i> -BuOH Dimer Structures	73
3.4.7	Dibenzofuran + MeOH IR Spectra Compared to Theory	74
3.4.8	(Dibenzofuran) ₂ + MeOH Trimer Structures	76

3.4.9	Dibenzofuran + <i>t</i> -BuOH IR Spectra Compared to Theory	78
3.4.10	Dibenzofuran Microwave Spectrum	79
3.4.11	Dibenzofuran Dimer Structures	80
3.4.12	Dibenzofuran + MeOH Microwave Spectrum	82
3.4.13	Dibenzofuran + MeOH Transition States	83
3.4.14	Dibenzofuran + <i>t</i> -BuOH Microwave Spectrum	85
4.0.1	Diphenyl Ether + MeOH Dimer Structures	90
4.0.2	Diphenyl Ether + <i>t</i> -BuOH Dimer Structures	91
4.0.3	Diphenyl Ether + MeOH IR Spectra Compared to Theory	93
4.0.4	Diphenyl Ether + MeOH Transition States	95
4.0.5	Diphenyl Ether + <i>t</i> -BuOH IR Spectra Compared to Theory	96
5.1.1	Furan + 1-NpOH Dimer Structures	102
5.1.2	2,5-Dimethylfuran + 1-NpOH Dimer Structures	102
5.1.3	Furan + 1-NpOH IR Spectra Compared to Theory	105
5.1.4	Furan + 1-NpOH Transition States	107
5.1.5	Furan, 2,5-Dimethylfuran + 1-NpOH R2PI Spectra	108
5.1.6	Furan + 1-NpOH SEP-R2PI Spectra	109
5.1.7	2,5-Dimethylfuran + 1-NpOH SEP-R2PI Spectra	110
5.2.1	Furan, 2,5-Dimethylfuran + PhOH Dimer Structures	113
5.2.2	Furan, 2,5-Dimethylfuran + PhOH IR Spectra Compared to Theory	114
6.0.1	Molecular Scale Preference	119
6.0.2	Furan, 2,3-Benzofuran, Dibenzofuran + MeOH Binding Energy	120
6.1.1	Overlap of the OH–O ^t and OH– π^{C3} Conformers	122
6.2.1	Theoretical <i>versus</i> Experimental Spectral Downshift	126
6.2.2	Theoretical <i>versus</i> Experimental Spectral Downshift MeOH Donor and Furan Acceptor Complexes	127
6.2.3	Box Plot of the Over- and Underestimation of the Spectral Downshift	128
D.1	Experimental Dibenzofuran Structure	145
D.2	(Dibenzofuran) ₂ + MeOH Trimer Structures I	147
D.3	(Dibenzofuran) ₂ + MeOH Trimer Structures II	148
D.4	Dibenzofuran + MeOH ₂ Trimer Structures	150
D.5	Furan + 1-NpOH Dimer Structures	152
D.6	2,5-Dimethylfuran + 1-NpOH Dimer Structures	153
D.7	2,3-Benzofuran + <i>t</i> -1-NpOH Dimer Structures	154
D.8	2,3-Benzofuran + <i>c</i> -1-NpOH Dimer Structures	155
E.1	IR Spectra of Pure Acceptors	157
E.2	Diphenyl Ether + <i>t</i> -BuOH Complementary IR Spectra	158
G.1	Example of a Box Plot	163

J List of Tables

2.2.1	Chemicals	7
2.2.2	Available Nozzle Types for the <i>popcorn</i> -Jet	11
2.5.1	Method Comparison for Multi-Spectroscopic Approaches	24
2.6.1	Comparison of Rotational Constants by Different Programs	28
3.2.1	Furan, 2-Methylfuran, 2,5-Dimethylfuran + MeOH Relative Energies	38
3.2.2	Furan, 2-Methylfuran, 2,5-Dimethylfuran + MeOH Hydrogen Bond Angles	50
3.2.3	Furan, 2-Methylfuran, 2,5-Dimethylfuran + MeOH Band Integrals	51
3.3.1	2-Ethylfuran + MeOH Relative Energies	55
3.3.2	2- <i>tert</i> -Butylfuran + MeOH, <i>t</i> -BuOH Relative Energies	60
3.4.1	2,3-Benzofuran + MeOH Relative Energies	65
3.4.2	Dibenzofuran + MeOH, <i>t</i> -BuOH Relative Energies	75
3.4.3	Dibenzofuran Dimer Relative Energies	80
3.4.4	Dibenzofuran + MeOH, <i>t</i> -BuOH Rotational Constants	81
4.0.1	Diphenyl Ether Monomer Conformations Relative Energies	90
4.0.2	Diphenyl Ether + MeOH, <i>t</i> -BuOH Relative Energies	92
5.1.1	Furan, 2,5-Dimethylfuran + 1-NpOH Relative Energies	103
5.2.1	Furan, 2,5-Dimethylfuran + PhOH Relative Energies	112
6.0.1	Overview of the Molecular Scale Systems with Alkyl Alcohols	118
6.0.2	Overview of the Molecular Scale Systems with Aromatic Alcohols	119
C.1	ORCA Convergence Criteria	143
D.1	Dibenzofuran + MeOH, <i>t</i> -BuOH Relative Energies without three-body term	144
D.2	Experimental Dibenzofuran Structure Coordinates	145
D.3	(Dibenzofuran) ₂ + MeOH Trimer Relative Energies	146
D.4	Dibenzofuran + MeOH ₂ Relative Energies	149
D.5	Furan + 1-NpOH Relative Energies without three-body term	151
D.6	2,3-Benzofuran + 1-NpOH Relative Energies	156
F.1	Dataset for Spectral Downshifts	159
F.2	Calculated Zero-Point Energy	162

K Bibliography

- [1] F. London, Zur Theorie und Systematik der Molekularkräfte, *Z. Phys.*, **1930**, *63*, 245–279.
- [2] J. P. Wagner, P. R. Schreiner, London dispersion in molecular chemistry—reconsidering steric effects, *Angew. Chem. Int. Ed.*, **2015**, *54*, 12274–12296.
- [3] M. A. Strauss, H. A. Wegner, Molecular Systems for the Quantification of London Dispersion Interactions, *Eur. J. Org. Chem.*, **2018**.
- [4] D. J. Liptrot, P. P. Power, London dispersion forces in sterically crowded inorganic and organometallic molecules, *Nat. Rev. Chem.*, **2017**, *1*, 0004.
- [5] A. J. Stone, *The Theory of Intermolecular Forces*, Oxford University Press, 2nd edition, **2013**.
- [6] S. Rösel, H. Quanz, C. Logemann, J. Becker, E. Mossou, L. Cañadillas-Delgado, E. Caldeweyher, S. Grimme, P. R. Schreiner, London Dispersion Enables the Shortest Intermolecular Hydrocarbon H··H Contact, *J. Am. Chem. Soc.*, **2017**, *139*, 7428–7431.
- [7] A. A. Fokin, L. V. Chernish, P. A. Gunchenko, E. Y. Tikhonchuk, H. Hausmann, M. Serafin, J. E. P. Dahl, R. M. K. Carlson, P. R. Schreiner, Stable Alkanes Containing Very Long Carbon–Carbon Bonds, *J. Am. Chem. Soc.*, **2012**, *134*, 13641–13650.
- [8] E. Pastorczak, C. Corminboeuf, Perspective: Found in translation: Quantum chemical tools for grasping non-covalent interactions, *J. Chem. Phys.*, **2017**, *146*, 120901.
- [9] L. Goerigk, A. Hansen, C. Bauer, S. Ehrlich, A. Najibi, S. Grimme, A look at the density functional theory zoo with the advanced GMTKN55 database for general main group thermochemistry, kinetics and noncovalent interactions, *Phys. Chem. Chem. Phys.*, **2017**, *19*, 32184–32215.
- [10] R. A. Mata, M. A. Suhm, Benchmarking Quantum Chemical Methods: Are We Heading in the Right Direction?, *Angew. Chem. Int. Ed.*, **2017**, *56*, 11011–11018.
- [11] S. Paliwal, S. Geib, C. S. Wilcox, Molecular Torsion Balance for Weak Molecular Recognition Forces. Effects of "Tilted-T" Edge-to-Face Aromatic Interactions on Conformational Selection and Solid-State Structure, *J. Am. Chem. Soc.*, **1994**, *116*, 4497–4498.
- [12] I. K. Mati, S. L. Cockroft, Molecular balances for quantifying non-covalent interactions, *Chem. Soc. Rev.*, **2010**, *39*, 4195.

- [13] A. B. Lypton, C. S. Wilcox, Synthesis and NMR Analysis of a Conformationally Controlled β -Turn Mimetic Torsion Balance, *J. Org. Chem.*, **2017**, *82*, 898–909.
- [14] L. Yang, C. Adam, G. S. Nichol, S. L. Cockroft, How much do van der Waals dispersion forces contribute to molecular recognition in solution?, *Nat. Chem.*, **2013**, *5*, 1006–1010.
- [15] W. B. Motherwell, J. Moïse, A. E. Aliev, M. Nič, S. J. Coles, P. N. Horton, M. B. Hursthouse, G. Chessari, C. A. Hunter, J. G. Vinter, Noncovalent Functional-Group–Arene Interactions, *Angew. Chem. Int. Ed.*, **2007**, *46*, 7823–7826.
- [16] F.-G. Klärner, Wie antiaromatisch ist planares Cyclooctatetraen?, *Angew. Chem.*, **2001**, *113*, 4099–4103.
- [17] N. O. B. Lüttschwager, M. A. Suhm, Stretching and folding of 2-nanometer hydrocarbon rods, *Soft Matter*, **2014**, *10*, 4885–4901.
- [18] T. Forsting, H. C. Gottschalk, B. Hartwig, M. Mons, M. A. Suhm, Correcting the record: the dimers and trimers of trans-N-methylacetamide, *Phys. Chem. Chem. Phys.*, **2017**, *19*, 10727–10737.
- [19] J. Černý, P. Hobza, Non-covalent interactions in biomacromolecules, *Phys. Chem. Chem. Phys.*, **2007**, *9*, 5291.
- [20] L. M. Salonen, M. Ellermann, F. Diederich, Aromatic Rings in Chemical and Biological Recognition: Energetics and Structures, *Angew. Chem. Int. Ed.*, **2011**, *50*, 4808–4842.
- [21] A. S. Mahadevi, G. N. Sastry, Cooperativity in Noncovalent Interactions, *Chem. Rev.*, **2016**, *116*, 2775–2825.
- [22] H. Mori, H. Kugisaki, Y. Inokuchi, N. Nishi, E. Miyoshi, K. Sakota, K. Ohashi, H. Sekiya, LIF and IR Dip Spectra of Jet-Cooled *p*-Aminophenol–M (M = CO, N₂): Hydrogen-Bonded or Van der Waals-Bonded Structure?, *J. Phys. Chem. A*, **2002**, *106*, 4886–4890.
- [23] K. Yamanouchi, S. Isogai, S. Tsuchiya, Laser induced fluorescence spectroscopy of van der Waals complexes of aniline with N₂, H₂, and CH₄ formed in a supersonic free jet, *J. Mol. Struct.*, **1986**, *146*, 349–359.
- [24] M. Schäfer, D. W. Pratt, Internal rotation in high-resolution ultraviolet spectra. II. Spectrum and structure of the aniline–nitrogen van der Waals complex, *J. Chem. Phys.*, **2001**, *115*, 11147–11156.
- [25] M. F. Hineman, E. R. Bernstein, D. F. Kelley, Excited state vibrational dynamics of 4-ethylaniline (X)₁ clusters (X=Ar, N₂, and CH₄), *J. Chem. Phys.*, **1993**, *98*, 2516–2523.
- [26] M. S. Ford, S. R. Haines, I. Pugliesi, C. E. Dessent, K. Müller-Dethlefs, Rotational band contour analysis in REMPI and ZEKE spectroscopy: elucidating the structures of phenol·X (X=N₂, CO and Ar) complexes, *J. Electron Spectrosc. Relat. Phenom.*, **2000**, *112*, 231–239.

- [27] M. Schmitt, C. Ratzler, W. L. Meerts, The structure of the phenol-nitrogen cluster: A joint experimental and *ab initio* study, *J. Chem. Phys.*, **2004**, *120*, 2752–2758.
- [28] M. Zierhut, W. Roth, S. Dümmler, I. Fischer, Electronic spectroscopy of 1-naphthol/solvent clusters 1-NpOH/S, S=H₂O, Ar and N₂, *Chem. Phys.*, **2004**, *305*, 123–133.
- [29] R. Knochenmuss, R. K. Sinha, S. Leutwyler, Intermolecular dissociation energies of dispersively bound complexes of aromatics with noble gases and nitrogen, *J. Chem. Phys.*, **2018**, *148*, 134302.
- [30] S. Oswald, E. Meyer, M. A. Suhm, Dinitrogen as a Sensor for Metastable Carboxylic Acid Dimers and a Weak Hydrogen Bond Benchmarking Tool, *J. Phys. Chem. A*, **2018**, *122*, 2933–2946.
- [31] J. Altnöder, S. Oswald, M. A. Suhm, Phenyl- vs cyclohexyl-substitution in methanol: implications for the OH conformation and for dispersion-affected aggregation from vibrational spectra in supersonic jets, *J. Phys. Chem. A*, **2014**, *118*, 3266–3279.
- [32] M. Schmitt, M. Böhm, C. Ratzler, D. Krügler, K. Kleinermanns, I. Kalkman, G. Berden, W. L. Meerts, Determining the Intermolecular Structure in the S₀ and S₁ States of the Phenol Dimer by Rotationally Resolved Electronic Spectroscopy, *ChemPhysChem*, **2006**, *7*, 1241–1249.
- [33] M. Saeki, S.-i. Ishiuchi, M. Sakai, M. Fujii, Structure of the jet-cooled 1-naphthol dimer studied by IR dip spectroscopy: cooperation between the π - π interaction and the hydrogen bonding, *J. Phys. Chem. A*, **2007**, *111*, 1001–1005.
- [34] A. Poblitzki, *Regioselektivität der intermolekularen Wasserstoffbrücke in gemischten Dimeren unter Einfluss von Dispersionswechselwirkungen*, Master’s thesis, Georg-August-Universität Göttingen, **2014**.
- [35] E. Arunan, G. R. Desiraju, R. A. Klein, J. Sadlej, S. Scheiner, I. Alkorta, D. C. Clary, R. H. Crabtree, J. J. Dannenberg, P. Hobza, H. G. Kjaergaard, A. C. Legon, B. Mennucci, D. J. Nesbitt, Definition of the hydrogen bond (IUPAC Recommendations 2011), *Pure Appl. Chem.*, **2011**, *83*, 1637–1641.
- [36] E. Sánchez-García, G. Jansen, Competition between H \cdots π and H \cdots O interactions in furan heterodimers, *J. Phys. Chem. A*, **2012**, *116*, 5689–5697.
- [37] S. Kumar, V. Pande, A. Das, π -Hydrogen bonding wins over conventional hydrogen bonding interaction: a jet-cooled study of indole \cdots furan heterodimer, *J. Phys. Chem. A*, **2012**, *116*, 1368–1374.
- [38] H. Sasaki, S. Daicho, Y. Yamada, Y. Nibu, Comparable strength of OH–O versus OH– π hydrogen bonds in hydrogen-bonded 2,3-benzofuran clusters with water and methanol, *J. Phys. Chem. A*, **2013**, *117*, 3183–3189.
- [39] J. Zischang, M. A. Suhm, The OH stretching spectrum of warm water clusters, *J. Chem. Phys.*, **2014**, *140*, 064312.

- [40] J. M. Hayes, G. J. Small, Supersonic Jets, Rotational Cooling, and Analytical Chemistry, *Anal. Chem.*, **1983**, *55*, 565A–574A.
- [41] J. M. Hayes, Analytical spectroscopy in supersonic expansions, *Chem. Rev.*, **1987**, *87*, 745–760.
- [42] M. Herman, R. Georges, M. Hepp, D. Hurtmans, High resolution Fourier transform spectroscopy of jet-cooled molecules, *Int. Rev. Phys. Chem.*, **2000**, *19*, 277–325.
- [43] M. D. Morse, 2. Supersonic Beam Sources, in F. Dunning, R. G. Hulet (editors), *Atomic, Molecular, and Optical Physics: Atoms and Molecules, Experimental Methods in the Physical Sciences*, volume 29, Academic Press, **1996**, 21–47.
- [44] R. E. Smalley, L. Wharton, D. H. Levy, Molecular optical spectroscopy with supersonic beams and jets, *Acc. Chem. Res.*, **1977**, *10*, 139–145.
- [45] D. R. Miller, Free Jet Sources, in G. Scoles (editor), *Atomic and Molecular Beam Methods*, volume I, Oxford University Press, **1988**, 14–53.
- [46] J. Koperski, E. S. Fry, Molecules in the cold environment of a supersonic free-jet beam: from spectroscopy of neutral–neutral interactions to a test of Bell's inequality, *J. Phys. B: At. Mol. Opt. Phys.*, **2006**, *39*, S1125–S1150.
- [47] M. Kappes, S. Leutwyler, Molecular Beams of Clusters, in G. Scoles (editor), *Atomic and Molecular Beam Methods*, volume I, Oxford University Press, **1988**, 380–415.
- [48] M. Sulkes, C. Juvet, S. A. Rice, Theoretical and experimental characterization of supersonic expansions from slit sources, *Chem. Phys. Lett.*, **1982**, *87*, 515–519.
- [49] S. Bocklitz, *Conformational spectroscopy of flexible chain molecules near the folding limit*, Ph.D. thesis, Georg-August-Universität Göttingen, **2017**.
- [50] R. S. Ruoff, T. D. Klots, T. Emilsson, H. S. Gutowsky, Relaxation of conformers and isomers in seeded supersonic jets of inert gases, *J. Chem. Phys.*, **1990**, *93*, 3142–3150.
- [51] C. M. Lovejoy, D. J. Nesbitt, The infrared spectra of nitrous oxide–HF isomers, *J. Chem. Phys.*, **1989**, *90*, 4671–4680.
- [52] A. Maris, B. M. Giuliano, S. Melandri, P. Ottaviani, W. Caminati, L. B. Favero, B. Velino, Structure, dipole moment and large amplitude motions of 1-benzofuran, *Phys. Chem. Chem. Phys.*, **2005**, *7*, 3317.
- [53] M. A. Suhm, Hydrogen Bond Dynamics in Alcohol Clusters, in S. A. Rice (editor), *Advances in Chemical Physics*, volume 142, John Wiley & Sons, Inc, Hoboken, NJ, USA, **2009**, 1–57.
- [54] P. Banerjee, T. Chakraborty, Weak hydrogen bonds: insights from vibrational spectroscopic studies, *Int. Rev. Phys. Chem.*, **2018**, *37*, 83–123.
- [55] A. R. Cooper, C. W. P. Crowne, P. G. Farrell, Gas-liquid chromatographic studies of electron-donor-acceptor systems. Part 2.—Interactions of aromatic hydrocarbons and heterocycles with 2,4,7-trinitrofluorenone, *Trans. Faraday Soc.*, **1967**, *63*, 447–454.

- [56] W. B. Sediawan, S. Gupta, E. McLaughlin, Solid–liquid phase diagrams of binary aromatic hydrocarbon mixtures from calorimetric studies, *J. Chem. Eng. Data*, **1989**, *34*, 223–226.
- [57] M. Albrecht, *Biologisch relevante Wasserstoffbrückensysteme im Überschallstrahl: Steuerung der Aggregation durch Substitution*, Ph.D. thesis, Georg-August-Universität Göttingen, **2009**.
- [58] C. Rice, *Jet-FTIR Spectroscopy of Biomolecular Model Systems*, Ph.D. thesis, Georg-August-Universität Göttingen, **2007**.
- [59] J. Lee, *Adaptive Aggregation über starke Wasserstoffbrücken in der Gasphase*, Ph.D. thesis, Georg-August-Universität Göttingen, **2012**.
- [60] J. Altnöder, *Untersuchungen zum Einfluss von London-Dispersionswechselwirkungen auf die Molekülaggregation*, Ph.D. thesis, Georg-August-Universität Göttingen, **2015**.
- [61] Bruker Optik GmbH, OPUS Version 7.0, **2011**.
- [62] M. Lange, *IR-Studien zur Aggregation und Komplexierung von 1,2-Diolen*, Master’s thesis, Georg-August-Universität Göttingen, **2018**.
- [63] R. Hildebrandt, Technical drawing (adapted): V-Förmiger Düsenaufsatz Popcorn, Suhm-17-03-00, Mechanik-Werkstatt, Institut für Physikalische Chemie, Georg-August-Universität Göttingen, **2017**.
- [64] S. Abraham, *Schwingungsspektroskopie nah und überkritischer Lösungsmittel*, Ph.D. thesis, Georg-August-Universität Göttingen, **2013**.
- [65] R. Hildebrandt, Technical drawing (adapted): Popcorn-Jet mit Double Pickup, Suhm-18-04-00, Mechanik-Werkstatt, Institut für Physikalische Chemie, Georg-August-Universität Göttingen, **2018**.
- [66] F. W. Küster, *Rechentafeln für die Chemische Analytik: Basiswissen für die Analytische Chemie (de Gruyter Studium) (German Edition)*, De Gruyter, 107th edition, **2011**.
- [67] N. Borho, *Chirale Erkennung in Molekülclustern: Maßgeschneiderte Aggregation von α -Hydroxyestern*, Ph.D. thesis, Georg-August-Universität Göttingen, **2005**.
- [68] D. R. Lide (editor), *CRC Handbook of Chemistry and Physics*, CRC-Press, 78th edition, **1997**.
- [69] F. Kollipost, K. E. Otto, M. A. Suhm, A Symmetric Recognition Motif between Vicinal Diols: The Fourfold Grip in Ethylene Glycol Dimer, *Angew. Chem. Int. Ed.*, **2016**, *55*, 4591–4595.
- [70] M. A. Suhm, F. Kollipost, Femtosecond single-mole infrared spectroscopy of molecular clusters, *Phys. Chem. Chem. Phys.*, **2013**, *15*, 10702–10721.
- [71] M. Heger, *Diagonal and off-diagonal anharmonicity in hydrogen-bonded systems*, Ph.D. thesis, Georg-August-Universität Göttingen, **2016**.

- [72] F. Kollipost, *Schwingungsdynamik in O–H···O-verbrückten Aggregaten: FTIR-Spektroskopie vom Nah- bis zum Ferninfraroten*, Ph.D. thesis, Georg-August-Universität Göttingen, **2015**.
- [73] D. Schmitz, V. Alvin Shubert, T. Betz, M. Schnell, Multi-resonance effects within a single chirp in broadband rotational spectroscopy: The rapid adiabatic passage regime for benzonitrile, *J. Mol. Spectrosc.*, **2012**, *280*, 77–84.
- [74] S. A. Cooke, P. Ohring, Decoding Pure Rotational Molecular Spectra for Asymmetric Molecules, *J. Spectrosc.*, **2013**, *2013*, 1–10.
- [75] D. Bernhard, F. Dietrich, M. Fatima, C. Pérez, A. Poblitzki, G. Jansen, M. A. Suhm, M. Schnell, M. Gerhards, Multi-spectroscopic and theoretical analyses on the diphenyl ether–*tert*-butyl alcohol complex in the electronic ground and electronically excited state, *Phys. Chem. Chem. Phys.*, **2017**, *19*, 18076–18088.
- [76] D. Schmitz, *Structural flexibility and chirality of polar molecules elucidated with broadband rotational spectroscopy*, Ph.D. thesis, Universität Hamburg, **2015**.
- [77] J. A. Frey, C. Holzer, W. Klopper, S. Leutwyler, Experimental and Theoretical Determination of Dissociation Energies of Dispersion-Dominated Aromatic Molecular Complexes, *Chem. Rev.*, **2016**, *116*, 5614–5641.
- [78] R. Knochenmuss, S. Maity, G. Féraud, S. Leutwyler, Measuring Intermolecular Binding Energies by Laser Spectroscopy, *Chimia*, **2017**, *71*, 7–12.
- [79] S. Maity, R. Knochenmuss, C. Holzer, G. Féraud, J. Frey, W. Klopper, S. Leutwyler, Accurate dissociation energies of two isomers of the 1-naphthol-cyclopropane complex, *J. Chem. Phys.*, **2016**, *145*, 164304.
- [80] R. Knochenmuss, S. Maity, F. Balmer, C. Müller, S. Leutwyler, Intermolecular dissociation energies of 1-naphthol-*n*-alkane complexes, *J. Chem. Phys.*, **2018**, *149*, 034306.
- [81] T. Droz, T. Bürgi, S. Leutwyler, van der Waals binding energies and intermolecular vibrations of carbazole·R (R=Ne, Ar, Kr, Xe), *J. Chem. Phys.*, **1995**, *103*, 4035–4045.
- [82] H. C. Gottschalk, C. Pérez, A. Poblitzki, M. Schnell, R. A. Mata, M. A. Suhm, *et. al.*, Microsolvation of furans: Bringing theory and experiment together, in preparation.
- [83] C. Medcraft, S. Zinn, M. Schnell, A. Poblitzki, J. Altnöder, M. Heger, M. A. Suhm, D. Bernhard, A. Stamm, F. Dietrich, M. Gerhards, Aromatic embedding wins over classical hydrogen bonding – a multi-spectroscopic approach for the diphenyl ether–methanol complex, *Phys. Chem. Chem. Phys.*, **2016**, *18*, 25975–25983.
- [84] D. Bernhard, personal communication.
- [85] D. Bernhard, *IR/UV-Spektroskopie an einem isolierten Depsipeptid in der Gasphase*, Diploma thesis, Technische Universität Kaiserslautern, **2014**.
- [86] M. Heger, J. Altnöder, A. Poblitzki, M. A. Suhm, To π or not to π – how does methanol dock onto anisole?, *Phys. Chem. Chem. Phys.*, **2015**, *17*, 13045–13052.

- [87] S. Maity, P. Ottiger, F. A. Balmer, R. Knochenmuss, S. Leutwyler, Intermolecular dissociation energies of dispersively bound 1-naphthol-cycloalkane complexes, *J. Chem. Phys.*, **2016**, *145*, 244314.
- [88] A. Poblitzki, H. C. Gottschalk, M. A. Suhm, Tipping the Scales: Spectroscopic Tools for Intermolecular Energy Balances, *J. Phys. Chem. Lett.*, **2017**, *8*, 5656–5665.
- [89] R. Knochenmuss, R. K. Sinha, A. Poblitzki, T. Den, S. Leutwyler, Intermolecular dissociation energies of hydrogen-bonded 1-naphthol complexes, *J. Chem. Phys.*, **2018**, *149*, 204311.
- [90] F. Neese, The ORCA program system, *WIREs Comput Mol Sci*, **2011**, *2*, 73–78.
- [91] A. D. Becke, Density-functional thermochemistry. III. The role of exact exchange, *J. Chem. Phys.*, **1993**, *98*, 5648–5652.
- [92] C. Lee, W. Yang, R. G. Parr, Development of the Colle-Salvetti correlation-energy formula into a functional of the electron density, *Phys. Rev. B*, **1988**, *37*, 785–789.
- [93] S. Grimme, J. Antony, S. Ehrlich, H. Krieg, A consistent and accurate *ab initio* parametrization of density functional dispersion correction (DFT-D) for the 94 elements H-Pu, *J. Chem. Phys.*, **2010**, *132*, 154104.
- [94] S. Grimme, S. Ehrlich, L. Goerigk, Effect of the damping function in dispersion corrected density functional theory, *J. Comput. Chem.*, **2011**, *32*, 1456–1465.
- [95] Chemcraft – graphical software for visualization of quantum chemistry computations, Version 1.8 (build536a), Programming: G. A. Andrienko.
<https://www.chemcraftprog.com>.
- [96] M. J. Frisch, G. W. Trucks, H. B. Schlegel, G. E. Scuseria, M. A. Robb, J. R. Cheeseman, G. Scalmani, V. Barone, B. Mennucci, G. A. Petersson, H. Nakatsuji, M. Caricato, X. Li, H. P. Hratchian, A. F. Izmaylov, J. Bloino, G. Zheng, J. L. Sonnenberg, M. Hada, M. Ehara, K. Toyota, R. Fukuda, J. Hasegawa, M. Ishida, T. Nakajima, Y. Honda, O. Kitao, H. Nakai, T. Vreven, Montgomery, J. A., Jr., J. E. Peralta, F. Ogliaro, M. Bearpark, J. J. Heyd, E. Brothers, K. N. Kudin, V. N. Staroverov, R. Kobayashi, J. Normand, K. Raghavachari, A. Rendell, J. C. Burant, S. S. Iyengar, J. Tomasi, M. Cossi, N. Rega, J. M. Millam, M. Klene, J. E. Knox, J. B. Cross, V. Bakken, C. Adamo, J. Jaramillo, R. Gomperts, R. E. Stratmann, O. Yazyev, A. J. Austin, R. Cammi, C. Pomelli, J. W. Ochterski, R. L. Martin, K. Morokuma, V. G. Zakrzewski, G. A. Voth, P. Salvador, J. J. Dannenberg, S. Dapprich, A. D. Daniels, Ö. Farkas, J. B. Foresman, J. V. Ortiz, J. Cioslowski, D. J. Fox, Gaussian 09, **2009**.
- [97] TURBOMOLE V7.0 2015, a development of University of Karlsruhe and Forschungszentrum Karlsruhe GmbH, 1989–2007, TURBOMOLE GmbH, since 2007; available from
<http://www.turbomole.com>.

- [98] R. A. Kendall, T. H. Dunning, R. J. Harrison, Electron affinities of the first-row atoms revisited. Systematic basis sets and wave functions, *J. Chem. Phys.*, **1992**, *96*, 6796–6806.
- [99] F. Weigend, R. Ahlrichs, Balanced basis sets of split valence, triple zeta valence and quadruple zeta valence quality for H to Rn: Design and assessment of accuracy, *Phys. Chem. Chem. Phys.*, **2005**, *7*, 3297.
- [100] S. Grimme, Semiempirical GGA-type density functional constructed with a long-range dispersion correction, *J. Comput. Chem.*, **2006**, *27*, 1787–1799.
- [101] A. Schäfer, C. Huber, R. Ahlrichs, Fully optimized contracted Gaussian basis sets of triple zeta valence quality for atoms Li to Kr, *J. Chem. Phys.*, **1994**, *100*, 5829–5835.
- [102] D. C. Young, *Computational Chemistry*, John Wiley & Sons, **2001**.
- [103] T. A. Halgren, W. N. Lipscomb, The synchronous-transit method for determining reaction pathways and locating molecular transition states, *Chem. Phys. Lett.*, **1977**, *49*, 225–232.
- [104] P. Plessow, Reaction Path Optimization without NEB Springs or Interpolation Algorithms, *J. Chem. Theory Comput.*, **2013**, *9*, 1305–1310.
- [105] J. Baker, An algorithm for the location of transition states, *J. Comput. Chem.*, **1986**, *7*, 385–395.
- [106] T. Nakanaga, F. Ito, Investigations on the Hydrogen Bond Interaction in the Aniline-Furan Complex and Its Cation by Infrared Depletion Spectroscopy, *J. Phys. Chem. A*, **1999**, *103*, 5440–5445.
- [107] E. Sánchez-García, *Computational Study of Weakly Interacting Complexes*, Ph.D. thesis, Ruhr-Universität Bochum, **2006**.
- [108] T. Fuji, Y.-I. Suzuki, T. Horio, T. Suzuki, R. Mitrić, U. Werner, V. Bonačić-Koutecký, Ultrafast photodynamics of furan, *J. Chem. Phys.*, **2010**, *133*, 234303.
- [109] K. Pei, H. Li, Structure and property of the furan dimer (C₄H₄O)₂: A theoretical study, *J. Mol. Struct.*, **2004**, *693*, 141–144.
- [110] S. G. Kukolich, J. A. Shea, The microwave spectrum and molecular structure of the furan–argon complex, *J. Chem. Phys.*, **1982**, *77*, 5242–5243.
- [111] S. G. Kukolich, Microwave structure measurements on the furan–argon complex, *J. Am. Chem. Soc.*, **1983**, *105*, 2207–2210.
- [112] R. Spycher, L. Hausherr-Primo, G. Grassi, A. Bauder, Rotational spectra of isotopic furan–(argon)_n, *n* = 1, 2, complexes and their vibrationally averaged structures, *J. Mol. Struct.*, **1995**, *351*, 7–17.
- [113] T. Brupbacher, J. Makarewicz, A. Bauder, Microwave spectrum of the furan–CO van der Waals complex, *J. Chem. Phys.*, **1998**, *108*, 3932–3939.

- [114] J. J. Oh, L.-W. Xu, A. Taleb-Bendiab, K. W. Hillig, R. L. Kuczkowski, The microwave spectrum and structure of the furan · sulfur dioxide complex, *J. Mol. Spectrosc.*, **1992**, *153*, 497–510.
- [115] R. S. Davidson, A. Lewis, T. D. Whelan, Excited complex formation between aromatic hydrocarbons and heterocyclic compounds, *J. Chem. Soc., Chem. Commun.*, **1975**, 203.
- [116] R. S. Davidson, A. Lewis, T. D. Whelan, Excited complex formation between heterocyclic compounds and aromatic hydrocarbons and amines, *J. Chem. Soc., Perkin Trans. 2*, **1977**, 1280.
- [117] D.-M. Huang, Y.-B. Wang, L. M. Visco, F.-M. Tao, Theoretical Study of Stable Intermolecular Complexes of Furan with Hydrogen Halides, *J. Phys. Chem. A*, **2004**, *108*, 11375–11380.
- [118] Y. Zeng, X. Li, X. Zhang, S. Zheng, L. Meng, Insight into the nature of the interactions of furan and thiophene with hydrogen halides and lithium halides: *ab initio* and QTAIM studies, *J. Mol. Model.*, **2011**, *17*, 2907–2918.
- [119] Z.-X. Wang, J.-C. Zhang, J.-Y. Wu, W.-L. Cao, Theoretical study on intermolecular interactions between furan and dihalogen molecules XY(X,Y=F,Cl,Br), *J. Chem. Phys.*, **2007**, *126*, 134301.
- [120] J. Li, D. Xie, G. Yan, Theoretical study of the intermolecular hydrogen bond interaction for furan-HCl and furan-CHCl₃ complexes, *Science in China Series B*, **2003**, 113.
- [121] G. C. Cole, A. C. Legon, P. Ottaviani, Are members of the family of hydrogen-bonded complexes formed by furan with the hydrogen halides isostructural? An answer from the rotational spectrum of furan···HBr, *J. Chem. Phys.*, **2002**, *117*, 2790–2799.
- [122] M. Tsuda, H. Touhara, K. Nakanishi, K. Kitaura, K. Morokuma, Calorimetric and molecular orbital studies of hydrogen bonding between hydrogen fluoride and cyclic ethers, *J. Am. Chem. Soc.*, **1978**, *100*, 7189–7196.
- [123] A. Lesarri, J. C. López, J. L. Alonso, Rotational spectrum, H, F nuclear spin–nuclear spin coupling and structure of the furan–HF dimer, *J. Chem. Soc., Faraday Trans.*, **1998**, *94*, 729–733.
- [124] J. A. Shea, S. G. Kukolich, The rotational spectrum and molecular structure of the furan–HCl complex, *J. Chem. Phys.*, **1983**, *78*, 3545–3551.
- [125] P. Asselin, B. Madebène, P. Soulard, P. Reinhardt, M. E. Alikhani, Evidence of an isomeric pair in furan···HCl: Fourier transform infrared spectroscopy and *ab initio* calculations, *J. Chem. Phys.*, **2008**, *128*, 244301.
- [126] A. Metzethin, Özgür Birer, E. Sánchez-García, M. Havenith, High resolution IR spectroscopy of acetylene-furan in ultracold helium nanodroplets, *J. Chem. Phys.*, **2008**, *129*, 114307.

- [127] E. Sánchez-García, A. Mardyukov, A. Tekin, R. Crespo-Otero, L. A. Montero, W. Sander, G. Jansen, Ab initio and matrix isolation study of the acetylene–furan dimer, *Chem. Phys.*, **2008**, *343*, 168–185.
- [128] S. Firth, R. L. Kuczkowski, Microwave spectrum and structure of furan · ethene, *J. Chem. Soc., Faraday Trans.*, **1995**, *91*, 975–981.
- [129] S. P. Lockwood, T. G. Fuller, J. J. Newby, Structure and Spectroscopy of Furan:H₂O Complexes, *J. Phys. Chem. A*, **2018**, *122*, 7160–7170.
- [130] D. Kaur, S. Khanna, Theoretical study on the hydrogen bonding of five-membered heteroaromatics with water, *Struct. Chem.*, **2012**, *23*, 755–764.
- [131] P. Lenain, M. Mandado, R. A. Mosquera, P. Bultinck, Interplay between hydrogen bond formation and multicenter π -electron delocalization: intermolecular hydrogen bonds, *J. Phys. Chem. A*, **2008**, *112*, 7898–7904.
- [132] X. Jiang, S. Liu, N. T. Tsona, S. Tang, L. Ding, H. Zhao, L. Du, Matrix isolation FTIR study of hydrogen-bonded complexes of methanol with heterocyclic organic compounds, *RSC Adv.*, **2017**, *7*, 2503–2512.
- [133] R. Wugt Larsen, P. Zielke, M. A. Suhm, Hydrogen-bonded OH stretching modes of methanol clusters: a combined IR and Raman isotopomer study, *J. Chem. Phys.*, **2007**, *126*, 194307.
- [134] P.-H. Su, C.-S. Yeh, Photofragmentation of the Ag⁺–furan complex in the gas-phase, *Chem. Phys. Lett.*, **2000**, *331*, 420–424.
- [135] P.-H. Su, F.-W. Lin, C.-S. Yeh, Photodissociation Studies of M(Furan)⁺ (M = Cu, Ag, and Au) and Au(C₃H₄)⁺ Complexes, *J. Phys. Chem. A*, **2001**, *105*, 9643–9648.
- [136] R. L. Grimm, J. B. Mangrum, R. C. Dunbar, Complexation of Gas-Phase Metal Ions with Furan: Experimental and Quantum Chemical Binding Energies, *J. Phys. Chem. A*, **2004**, *108*, 10897–10905.
- [137] G. Wu, A. J. Stace, Gas phase studies of metal dimer complexes, M₂L_n⁺, where M=Zn and Mn, and L=pyrrole and furan, for *n* in the range 1–5, *Int. J. Mass Spectrom.*, **2006**, *249-250*, 289–295.
- [138] K. C. Bassett, F. You, P. M. Graham, W. H. Myers, M. Sabat, W. D. Harman, Furan [3 + 2] Dipolar Cycloadditions Promoted by a π -Basic Tungsten Metal Fragment, *Organometallics*, **2006**, *25*, 435–439.
- [139] H. C. Gottschalk, A. Poblitzki, M. A. Suhm, M. M. Al-Mogren, J. Antony, A. A. Auer, L. Baptista, D. M. Benoit, G. Bistoni, F. Bohle, R. Dahmani, D. Firaha, S. Grimme, A. Hansen, M. E. Harding, M. Hochlaf, C. Holzer, G. Jansen, W. Klopper, W. A. Kopp, L. C. Kröger, K. Leonhard, H. Mouhib, F. Neese, M. N. Pereira, I. S. Ulusoy, A. Wuttke, R. A. Mata, The furan microsolvation blind challenge for quantum chemical methods: First steps, *J. Chem. Phys.*, **2018**, *148*, 014301.

- [140] A. Poblitzki, J. Altnöder, M. A. Suhm, Subtle solvation behaviour of a biofuel additive: the methanol complex with 2,5-dimethylfuran, *Phys. Chem. Chem. Phys.*, **2016**, *18*, 27265–27271.
- [141] Y. Román-Leshkov, C. J. Barrett, Z. Y. Liu, J. A. Dumesic, Production of dimethylfuran for liquid fuels from biomass-derived carbohydrates, *Nature*, **2007**, *447*, 982–985.
- [142] E. Nürenberg, P. Schulze, F. Kohler, M. Zubel, S. Pischinger, F. Schüth, Blending real world gasoline with biofuel in a direct conversion process, *ACS Sustainable Chem. Eng.*, **2018**.
- [143] B. Saha, M. M. Abu-Omar, Current Technologies, Economics, and Perspectives for 2,5-Dimethylfuran Production from Biomass-Derived Intermediates, *ChemSusChem*, **2015**, *8*, 1133–1142.
- [144] A. Bohre, S. Dutta, B. Saha, M. M. Abu-Omar, Upgrading Furfurals to Drop-in Biofuels: An Overview, *ACS Sustainable Chem. Eng.*, **2015**, *3*, 1263–1277.
- [145] J. L. da Silva, M. Aznar, Thermophysical properties of 2,5-dimethylfuran and liquid–liquid equilibria of ternary systems water + 2,5-dimethylfuran + alcohols (1-butanol or 2-butanol or 1-hexanol), *Fuel*, **2014**, *136*, 316–325.
- [146] B. Bak, D. Christensen, W. B. Dixon, L. Hansen-Nygaard, J. R. Andersen, M. Schottländer, The complete structure of furan, *J. Mol. Spectrosc.*, **1962**, *9*, 124–129.
- [147] W. G. Norris, L. C. Krisher, Microwave Spectrum of 2-Methylfuran, *J. Chem. Phys.*, **1969**, *51*, 403–406.
- [148] I. A. Finneran, S. T. Shipman, S. L. W. Weaver, Rotational spectroscopy of 2-methylfuran from 8.7 to 960GHz, *J. Mol. Spectrosc.*, **2012**, *280*, 27–33.
- [149] V. Van, J. Bruckhuisen, W. Stahl, V. Ilyushin, H. V. L. Nguyen, The torsional barriers of two equivalent methyl internal rotations in 2,5-dimethylfuran investigated by microwave spectroscopy, *J. Mol. Spectrosc.*, **2018**, *343*, 121–125.
- [150] M. Rico, M. Barrachina, J. Orza, Fundamental vibrations of furan and deuterated derivatives, *J. Mol. Spectrosc.*, **1967**, *24*, 133–148.
- [151] D. W. Scott, A valence force field for furan and pyrrole and their deuterium and methyl derivatives, *J. Mol. Spectrosc.*, **1971**, *37*, 77–91.
- [152] A. Mellouki, J. Liévin, M. Herman, The vibrational spectrum of pyrrole (C₄H₅N) and furan (C₄H₄O) in the gas phase, *Chem. Phys.*, **2001**, *271*, 239–266.
- [153] C. Pouchan, J. Raymond, H. Sauvaitre, M. Chaillet, Étude des modes normaux de vibration du furanne et de dérivés substitués, *J. Mol. Struct.*, **1974**, *21*, 253–279.
- [154] J. Green, D. Harrison, Spectroscopic and thermodynamic properties of furan derivatives—I. 2- and 2,5-substituted compounds, *Spectrochimica Acta Part A: Molecular Spectroscopy*, **1977**, *33*, 843–848.

- [155] P. M. Élkin, E. A. Éрман, O. V. Pulin, Quantum chemical calculation of normal molecular vibrations for substituted five-member chalcogen heterocyclic compounds taking anharmonicity into account, *J. Appl. Spectrosc.*, **2009**, *76*, 156–161.
- [156] F. Kollipost, J. Andersen, D. W. Mahler, J. Heimdal, M. Heger, M. A. Suhm, R. Wugt Larsen, The effect of hydrogen bonding on torsional dynamics: a combined far-infrared jet and matrix isolation study of methanol dimer, *J. Chem. Phys.*, **2014**, *141*, 174314.
- [157] C. Camy-Peyret, J. M. Flaud, G. Guelachvili, C. Amiot, High resolution Fourier transform spectrum of water between 2930 and 4255 cm^{-1} , *Mol. Phys.*, **1973**, *26*, 825–855.
- [158] H. C. Gottschalk, J. Altnöder, M. Heger, M. A. Suhm, Control over the Hydrogen-Bond Docking Site in Anisole by Ring Methylation, *Angew. Chem. Int. Ed.*, **2016**, *55*, 1921–1924.
- [159] H. C. Gottschalk, *Dispersionskontrollierte Regioselektivität in Komplexen zwischen Alkoholen und aromatischen Ethern*, Master's thesis, Georg-August-Universität Göttingen, **2015**.
- [160] I. G. John, L. Radom, Conformations, stabilities, and charge distributions in 2- and 3-monosubstituted furans. An ab initio molecular orbital study, *J. Am. Chem. Soc.*, **1978**, *100*, 3981–3991.
- [161] S. Maity, M. Guin, P. C. Singh, G. N. Patwari, Phenylacetylene: a hydrogen bonding chameleon, *ChemPhysChem*, **2011**, *12*, 26–46.
- [162] R. Medel, M. Heger, M. A. Suhm, Molecular docking via olefinic $\text{OH}\cdots\pi$ interactions: a bulky alkene model system and its cooperativity, *J. Phys. Chem. A*, **2015**, *119*, 1723–1730.
- [163] B. M. Giuliano, W. Caminati, Rotational Spectrum of 2,3-Benzofuran, *Collect. Czech. Chem. Commun.*, **2003**, *68*, 1572–1578.
- [164] J. Hollas, Vapour-phase ultra-violet absorption spectra of indene, indole, coumarone and thionaphthene, *Spectrochim. Acta*, **1963**, *19*, 753–767.
- [165] S. Fomine, M. Tlenkopatchev, S. Martinez, L. Fomina, Local MP2 Study of Naphthalene, Indole, and 2,3-Benzofuran Dimers, *J. Phys. Chem. A*, **2002**, *106*, 3941–3946.
- [166] W. T. Yip, D. H. Levy, Excimer/Exciplex Formation in van der Waals Dimers of Aromatic Molecules, *J. Phys. Chem.*, **1996**, *100*, 11539–11545.
- [167] D. Ž. Veljković, G. V. Janjić, S. D. Zarić, Are C–H \cdots O interactions linear? The case of aromatic CH donors, *CrystEngComm*, **2011**, *13*, 5005.
- [168] K. Shibasaki, A. Fujii, N. Mikami, S. Tsuzuki, Magnitude of the CH/ π Interaction in the Gas Phase: Experimental and Theoretical Determination of the Accurate Interaction Energy in Benzene-methane, *J. Phys. Chem. A*, **2006**, *110*, 4397–4404.

- [169] W. B. Collier, I. Magdó, T. D. Klots, Infrared and Raman spectra of bicyclic molecules using scaled noncorrelated and correlated ab initio force fields, *J. Chem. Phys.*, **1999**, *110*, 5710–5720.
- [170] T. Klots, W. Collier, Heteroatom derivatives of indene Part 3. Vibrational spectra of benzoxazole, benzofuran, and indole, *Spectrochim. Acta, Part A*, **1995**, *51*, 1291–1316.
- [171] V. Singh, Ab initio and DFT studies of the vibrational spectra of benzofuran and some of its derivatives, *Spectrochim. Acta, Part A*, **2006**, *65*, 1125–1130.
- [172] W. Y. Sohn, J. S. Kang, S. Y. Lee, H. Kang, Fluorescence excitation spectrum and solvent-assisted conformational isomerization (SACI) of jet-cooled acetaminophen, *Chem. Phys. Lett.*, **2013**, *581*, 36–41.
- [173] S. Daicho, Y. Yamada, Y. Nibu, Study on intermolecular interaction in solvated clusters of benzofuran and dibenzofuran, in *Pacificchem 2010, International Chemical Congress of Pacific Basin Societies*, American Chemical Society Washington, D. C.
- [174] A. Bree, V. Vilkos, R. Zwarich, Some electronic spectra of dibenzofuran, *J. Mol. Spectrosc.*, **1973**, *48*, 135–147.
- [175] A. Bree, V. Vilkos, R. Zwarich, The vibrational spectra of dibenzofuran, *J. Mol. Spectrosc.*, **1973**, *48*, 124–134.
- [176] A. Bree, A. Lacey, I. Ross, R. Zwarich, Vibronic coupling in the lowest singlet state of dibenzofuran, *Chem. Phys. Lett.*, **1974**, *26*, 329–333.
- [177] K. D. Hoffmann, A. Schmillen, H. Wolff, Prompt and delayed spectrum of the pure dibenzofuran crystal, *Z. Naturforsch. A*, **1977**, *32a*, 105–106.
- [178] C. Taliani, A. Bree, R. Zwarich, Laser-excited fluorescence from dibenzofuran in a biphenyl host, *J. Phys. Chem.*, **1984**, *88*, 2357–2360.
- [179] I. Khasawneh, Luminescence characteristics of dibenzofuran and several polychlorinated dibenzofurans and dibenzo-*p*-dioxins, *Talanta*, **1988**, *35*, 267–270.
- [180] T. Klots, W. Collier, Vibrational spectra, structure, assignment, and ideal-gas thermodynamics of a three-ring molecule: dibenzofuran, *J. Mol. Struct.*, **1996**, *380*, 1–14.
- [181] D. D. Nguyen, J. Trunk, L. Nakhimovsky, J. Spanget-Larsen, Electronic transitions of fluorene, dibenzofuran, carbazole, and dibenzothiophene: From the onset of absorption to the ionization threshold, *J. Mol. Spectrosc.*, **2010**, *264*, 19–25.
- [182] C. A. Pinkham, S. C. Wait, The electronic spectra of fluorene, dibenzofuran and carbazole, *J. Mol. Spectrosc.*, **1968**, *27*, 326–342.
- [183] A. R. Auty, A. C. Jones, D. Phillips, Fluorescence excitation spectra and decay times of jet-cooled dibenzofuran and the dibenzofuran–water complex, *Chem. Phys. Lett.*, **1984**, *112*, 529–533.
- [184] A. R. Auty, A. C. Jones, D. Phillips, Time-resolved fluorescence of jet-cooled carbazoles and their weak complexes, *J. Chem. Soc., Faraday Trans. 2*, **1986**, *82*, 1219.

- [185] T. Chakraborty, E. Lim, Dual fluorescence from the photoexcited van der Waals dimer of dibenzofuran in a supersonic jet. Intermediate-case level structure of the coupling between the dimer excited state and the lower-lying excimer state, *Chem. Phys. Lett.*, **1993**, *207*, 99–104.
- [186] C. Weickhardt, R. Zimmermann, U. Boesl, E. W. Schlag, Laser mass spectrometry of dibenzodioxin, dibenzofuran and two isomers of dichlorodibenzodioxins: Selective ionization, *Rapid Commun. Mass Spectrom.*, **1993**, *7*, 183–185.
- [187] M. Baba, K. Mori, M. Yamawaki, K. Akita, M. Ito, S. Kasahara, T. Yamanaka, Vibronic Structure in the S_1 – S_0 Transition of Jet-Cooled Dibenzofuran, *J. Phys. Chem. A*, **2006**, *110*, 10000–10005.
- [188] D. Q. Hoa, T. Uchimura, T. Imasaka, N. D. Hung, Fluorescence lifetime measurement of dibenzofuran and monochlorodibenzofuran, *Sci. Technol. Adv. Mater.*, **2006**, *7*, 714–717.
- [189] M. Yamawaki, Y. Tatamitani, A. Doi, S. Kasahara, M. Baba, Sub-Doppler high-resolution excitation spectroscopy of the S_1 ← S_0 transition of dibenzofuran, *J. Mol. Spectrosc.*, **2006**, *238*, 49–55.
- [190] J. T. Yi, L. Alvarez-Valtierra, D. W. Pratt, Rotationally resolved S_1 ← S_0 electronic spectra of fluorene, carbazole, and dibenzofuran: Evidence for Herzberg-Teller coupling with the S_2 state, *J. Chem. Phys.*, **2006**, *124*, 244302.
- [191] F. L. Minn, J. P. Pinion, N. Filipescu, Excimer model for fluorene and dibenzofuran, *J. Phys. Chem.*, **1971**, *75*, 1794–1798.
- [192] T. Grebner, R. Stumpf, H. J. Neusser, Mass analyzed threshold ionization of van der Waals complexes: Binding energies of dibenzofuran · Ar and dibenzo-*p*-dioxin · Ar, *Int. J. Mass Spectrom. Ion Process.*, **1997**, *167-168*, 649–660.
- [193] S. Haldar, R. Gnanasekaran, P. Hobza, A comparison of *ab initio* quantum-mechanical and experimental D_0 binding energies of eleven H-bonded and eleven dispersion-bound complexes, *Phys. Chem. Chem. Phys.*, **2015**, *17*, 26645–26652.
- [194] M. Altarawneh, E. M. Kennedy, B. Z. Dlugogorski, J. C. Mackie, Computational Study of the Oxidation and Decomposition of Dibenzofuran under Atmospheric Conditions, *J. Phys. Chem. A*, **2008**, *112*, 6960–6967.
- [195] E. Pérez, A. Cabañas, J. A. R. Renuncio, Y. Sánchez-Vicente, C. Pando, Cosolvent Effect of Methanol and Acetic Acid on Dibenzofuran Solubility in Supercritical Carbon Dioxide, *J. Chem. Eng. Data*, **2008**, *53*, 2649–2653.
- [196] D. Bernhard, M. Fatima, A. Poblitzki, A. L. Steber, C. Pérez, M. A. Suhm, M. Schnell, M. Gerhards, Dispersion-controlled docking preference: multi-spectroscopic study on complexes of dibenzofuran with alcohols and water, *Phys. Chem. Chem. Phys.*, **2019**, *21*, 16032–16046.

- [197] R. Chirico, B. Gammon, S. Knipmeyer, A. Nguyen, M. Strube, C. Tsonopoulos, W. Steele, The thermodynamic properties of dibenzofuran, *J. Chem. Thermodyn.*, **1990**, *22*, 1075–1096.
- [198] M. Fatima, A. L. Steber, A. Poblitzki, C. Pérez, S. Zinn, M. Schnell, Rotational Signatures of Dispersive Stacking in the Formation of Aromatic Dimers, *Angewandte Chemie International Edition*, **2019**, *58*, 3108–3113.
- [199] W. Gordy, R. L. Cook, *Microwave Molecular Spectra*, *Techniques of Chemistry*, volume 18, John Wiley & Sons, Inc., **1984**.
- [200] Z. Kisiel, KRA Version 9.09.2013, <http://info.ifpan.edu.pl/kisiel/prospe.htm>.
- [201] A. Paiva, P. Kistemaker, T. Weeding, A REMPI investigation of the minimum energy conformations of diphenyl ether, *Int. J. Mass Spectrom.*, **2002**, *221*, 107–115.
- [202] K. Aimi, T. Fujiwara, S. Ando, A conformational study of aromatic imide compounds. part 1. Compounds containing diphenyl ether and benzophenone moieties, *J. Mol. Struct.*, **2002**, *602-603*, 405–416.
- [203] M. Guerra, R. Pinto, J. Santos, A. Paiva, Towards the assignment of the REMPI spectrum of Ph₂O using CIS and TD-DFT methods, *Mol. Phys.*, **2013**, *111*, 3311–3319.
- [204] T. Straßner, Diphenylmethane and diphenyl ether — experimental conformations and torsional surfaces calculated with AM1, MNDO, PM3, and density functional theory (Becke3LYP), *Can. J. Chem.*, **1997**, *75*, 1011–1022.
- [205] M. Feigel, Phenyl rotation in diphenylether and diphenylmethane calculated with ab initio methods, *J. Mol. Struct. Theochem*, **1996**, *366*, 83–88.
- [206] F. Dietrich, D. Bernhard, M. Fatima, C. Pérez, M. Schnell, M. Gerhards, The effect of dispersion on the structure of diphenyl ether aggregates, *Angew. Chem. Int. Ed.*, **2018**, *57*, 9534–9537.
- [207] D. Bernhard, C. Holzer, F. Dietrich, A. Stamm, W. Klopfer, M. Gerhards, The Structure of Diphenyl Ether–Methanol in the Electronically Excited and Ionic Ground States: A Combined IR/UV Spectroscopic and Theoretical Study, *ChemPhysChem*, **2017**, *18*, 3634–3641.
- [208] A. Allerhand, P. von Rague Schleyer, A Survey of C–H Groups as Proton Donors in Hydrogen Bonding, *J. Am. Chem. Soc.*, **1963**, *85*, 1715–1723.
- [209] C. Wickleder, D. Henseler, S. Leutwyler, Accurate dissociation energies of O–H···O hydrogen-bonded 1-naphthol-solvent complexes, *J. Chem. Phys.*, **2002**, *116*, 1850–1857.
- [210] T. Bürgi, T. Droz, S. Leutwyler, Accurate hydrogen-bonding energies between 1-naphthol and water, methanol and ammonia, *Chem. Phys. Lett.*, **1995**, *246*, 291–299.
- [211] R. Knochenmuss, S. Leutwyler, Proton transfer from 1-naphthol to water: Small clusters to the bulk, *J. Chem. Phys.*, **1989**, *91*, 1268–1278.

- [212] C. Wickleder, T. Droz, T. Bürgi, S. Leutwyler, Accurate intermolecular binding energies of 1-naphthol to benzene and cyclohexane, *Chem. Phys. Lett.*, **1997**, *264*, 257–264.
- [213] J. Hollas, M. Z. bin Hussein, Evidence for two rotational isomers of 1-naphthol and 2-naphthol from their gas-phase electronic absorption spectra, *J. Mol. Spectrosc.*, **1988**, *127*, 497–508.
- [214] C. Lakshminarayan, J. M. Smith, J. L. Knee, Laser photoelectron spectroscopy of 1- and 2-naphthol: relative stability of the cis and trans cation rotamers, *Chem. Phys. Lett.*, **1991**, *182*, 656–662.
- [215] A. Nejad, *Auf Biegen und Brechen – Anisol als zwischenmolekulare Waage*, Bachelor’s thesis, Georg-August-Universität Göttingen, **2016**.
- [216] K. Chuchev, J. J. BelBruno, Rotation barriers in condensed rings: an extension of Clar’s stability rule, *J. Phys. Org. Chem.*, **2006**, *19*, 115–121.
- [217] M. Lange, *FTIR-spektroskopische Untersuchungen von Wasserstoffbrücken zwischen aromatischen Molekülen und Test einer automatisierten Spektrenauswertung*, Research internship report, Georg-August-Universität Göttingen, **2018**.
- [218] R. Yoshino, K. Hashimoto, T. Omi, S.-i. Ishiuchi, M. Fujii, Structure of 1-Naphthol–Water Clusters Studied by IR Dip Spectroscopy and Ab Initio Molecular Orbital Calculations, *J. Phys. Chem. A*, **1998**, *102*, 6227–6233.
- [219] Z. Yoshida, E. Ōsawa, Hydrogen Bonding of Phenol to π Electrons of Aromatics, Polyolefins, Heteroaromatics, Fulvenes, and Azulenes, *J. Am. Chem. Soc.*, **1966**, *88*, 4019–4026.
- [220] A. Fujii, T. Ebata, N. Mikami, An Infrared Study of π -Hydrogen Bonds in Microsolvated Phenol: OH Stretching Vibrations of Phenol–X (X = C₆H₆, C₂H₄, and C₂H₂) Clusters in the Neutral and Cationic Ground States, *J. Phys. Chem. A*, **2002**, *106*, 8554–8560.
- [221] P. Banerjee, T. Chakraborty, Correlation of ν_{OH} Spectral Shifts of Phenol–Benzene O–H $\cdots\pi$ Hydrogen-Bonded Complexes with Donor’s Acidity: A Combined Matrix Isolation, Infrared Spectroscopy, and Quantum Chemistry Study, *J. Phys. Chem. A*, **2014**, *118*, 7074–7084.
- [222] T. Ebata, A. Fujii, N. Mikami, Vibrational spectroscopy of small-sized hydrogen-bonded clusters and their ions, *Int. Rev. Phys. Chem.*, **1998**, *17*, 331–361.
- [223] T. Ebata, M. Kayano, S. Sato, N. Mikami, Picosecond IR–UV Pump–Probe Spectroscopy. IVR of OH Stretching Vibration of Phenol and Phenol Dimer, *J. Phys. Chem. A*, **2001**, *105*, 8623–8628.
- [224] T. Ebata, T. Watanabe, N. Mikami, Evidence for the Cyclic Form of Phenol Trimer: Vibrational Spectroscopy of the OH Stretching Vibrations of Jet-Cooled Phenol Dimer and Trimer, *J. Phys. Chem.*, **1995**, *99*, 5761–5764.

- [225] M. Kolář, P. Hobza, Accurate Theoretical Determination of the Structure of Aromatic Complexes Is Complicated: The Phenol Dimer and Phenol···Methanol Cases, *J. Phys. Chem. A*, **2007**, *111*, 5851–5854, pMID: 17566991.
- [226] T. Ebata, A. Iwasaki, N. Mikami, Vibrational Relaxation of OH and OD Stretching Vibrations of Phenol and Its Clusters Studied by IR–UV Pump–Probe Spectroscopy, *J. Phys. Chem. A*, **2000**, *104*, 7974–7979.
- [227] A. L. Ringer, M. S. Figs, M. O. Sinnokrot, C. D. Sherrill, Aliphatic C–H/ π Interactions: Methane–Benzene, Methane–Phenol, and Methane–Indole Complexes, *J. Phys. Chem. A*, **2006**, *110*, 10822–10828.
- [228] H. Abe, N. Mikami, M. Ito, Fluorescence excitation spectra of hydrogen-bonded phenols in a supersonic free jet, *J. Phys. Chem.*, **1982**, *86*, 1768–1771.
- [229] A. Courty, M. Mons, I. Dimicoli, F. Piuze, V. Brenner, P. Millié, Ionization, Energetics, and Geometry of the Phenol–S Complexes (S = H₂O, CH₃OH, and CH₃OCH₃), *J. Phys. Chem. A*, **1998**, *102*, 4890–4898.
- [230] S. Parveen, A. K. Chandra, T. Zeegers-Huyskens, Theoretical investigation of the hydrogen bonding interaction between substituted phenols and simple O- and N-bases, *J. Mol. Struct.*, **2010**, *977*, 258–265.
- [231] N. R. Samala, N. Agmon, Structure, spectroscopy, and dynamics of the phenol-(water)₂ cluster at low and high temperatures, *J. Chem. Phys.*, **2017**, *147*, 234307.
- [232] M. Gerhards, K. Beckmann, K. Kleinermanns, Vibrational analysis of phenol/(methanol)₁, *Z. Phys. D: At. Mol. Clusters*, **1994**, *29*, 223–229.
- [233] I. Usabiaga, J. González, P. F. Arnáiz, I. León, E. J. Cocinero, J. A. Fernández, Modeling the tyrosine–sugar interactions in supersonic expansions: glucopyranose–phenol clusters, *Phys. Chem. Chem. Phys.*, **2016**, *18*, 12457–12465.
- [234] Y. Yamada, Y. Katsumoto, T. Ebata, Picosecond IR-UV pump-probe spectroscopic study on the vibrational energy flow in isolated molecules and clusters, *Phys. Chem. Chem. Phys.*, **2007**, *9*, 1170–1185.
- [235] D. Blosler, J. Murphy, J. N. Spencer, Bond Enthalpy for the Phenol–Benzene Complex, *Can. J. Chem.*, **1971**, *49*, 3913–3915.
- [236] M. Böning, B. Stuhlmann, G. Engler, K. Kleinermanns, Isomer-Selective Vibrational Spectroscopy of Jet-Cooled Phenol–Acetylene Aggregates, *J. Phys. Chem. A*, **2013**, *117*, 3214–3220.
- [237] J. L. Knee, L. R. Khundkar, A. H. Zewail, Picosecond photofragment spectroscopy. III. Vibrational predissociation of van der Waals’ clusters, *J. Chem. Phys.*, **1987**, *87*, 115–127.
- [238] G. Pietraperzia, M. Pasquini, F. Mazzoni, G. Piani, M. Becucci, M. Biczysko, D. Michalski, J. Bloino, V. Barone, Noncovalent Interactions in the Gas Phase: The Anisole–Phenol Complex, *J. Phys. Chem. A*, **2011**, *115*, 9603–9611.

- [239] A. Wuttke, R. A. Mata, Visualizing dispersion interactions through the use of local orbital spaces, *J. Comput. Chem.*, **2017**, *38*, 15–23.
- [240] D. Bernhard, F. Dietrich, M. Fatima, C. Pérez, H. C. Gottschalk, A. Wuttke, R. A. Mata, M. A. Suhm, M. Schnell, M. Gerhards, The phenyl vinyl ether–methanol complex: a model system for quantum chemistry benchmarking, *Beilstein J. Org. Chem.*, **2018**, *14*, 1642–1654.
- [241] R. L. Jacobsen, R. D. Johnson, K. K. Irikura, R. N. Kacker, Anharmonic Vibrational Frequency Calculations Are Not Worthwhile for Small Basis Sets, *J. Chem. Theory Comput.*, **2013**, *9*, 951–954.
- [242] V. Barone, Anharmonic vibrational properties by a fully automated second-order perturbative approach, *J. Chem. Phys.*, **2005**, *122*, 014108.
- [243] J. Spanget-Larsen, B. K. Hansen, P. E. Hansen, OH stretching frequencies in systems with intramolecular hydrogen bonds: Harmonic and anharmonic analyses, *Chem. Phys.*, **2011**, *389*, 107–115.
- [244] P. E. Hansen, J. Spanget-Larsen, On prediction of OH stretching frequencies in intramolecularly hydrogen bonded systems, *J. Mol. Struct.*, **2012**, *1018*, 8–13.
- [245] L. Biemann, *Bathochrome Verschiebungen von OH-Streckschwingungen als Sonde für die Güte von Wasserstoffbrückenakzeptoren*, Diploma thesis, Georg-August-Universität Göttingen, **2004**.
- [246] C. Zimmermann, *FTIR-Spektroskopie an Intermolekularen Carbonyl-Waagen*, Master’s thesis, Georg-August-Universität Göttingen, **2018**.
- [247] J. Stachowiak, *Alkohol-Keton-Dimere als zwischenmolekulares Waagensystem*, Bachelor’s thesis, Georg-August-Universität Göttingen, **2018**.
- [248] R. Medel, *Infrarotspektroskopie von Alkohol-Alken-Komplexen: konkurrierende schwache Wechselwirkungen*, Master’s thesis, Georg-August-Universität Göttingen, **2014**.
- [249] H. C. Gottschalk, personal communication.
- [250] M. Heger, R. A. Mata, M. A. Suhm, Soft hydrogen bonds to alkenes: the methanol–ethene prototype under experimental and theoretical scrutiny, *Chem. Sci.*, **2015**, *6*, 3738–3745.
- [251] R. N. Pribble, F. C. Hagemeister, T. S. Zwier, Resonant ion-dip infrared spectroscopy of benzene–(methanol)_m clusters with *m*=1–6, *J. Chem. Phys.*, **1997**, *106*, 2145–2157.
- [252] A. Fujii, S. Okuyama, A. Iwasaki, T. Maeyama, T. Ebata, N. Mikami, Infrared spectroscopy of precursor clusters for nucleophilic substitution reactions: Fluorobenzene–(CH₃OH)_n (*n* = 1 and 2), *Chem. Phys. Lett.*, **1996**, *256*, 1–7.
- [253] C. Riehn, K. Buchhold, B. Reimann, S. Djafari, H.-D. Barth, B. Brutschy, P. Tarakeshwar, K. S. Kim, van der Waals isomers and ionic reactivity of the cluster system para-chlorofluorobenzene/methanol, *J. Chem. Phys.*, **2000**, *112*, 1170.

- [254] P. Raveendran, D. Zimmermann, T. Häber, M. A. Suhm, Exploring a hydrogen-bond terminus: Spectroscopy of eucalyptol–alcohol clusters, *Phys. Chem. Chem. Phys.*, **2000**, *2*, 3555–3563.
- [255] C. Emmeluth, V. Dyczmons, M. A. Suhm, Tuning the hydrogen bond donor/acceptor isomerism in jet-cooled mixed dimers of aliphatic alcohols, *J. Phys. Chem. A*, **2006**, *110*, 2906–2915.
- [256] C. Cézard, C. A. Rice, M. A. Suhm, OH-stretching red shifts in bulky hydrogen-bonded alcohols: jet spectroscopy and modeling, *J. Phys. Chem. A*, **2006**, *110*, 9839–9848.
- [257] F. Kollipost, A. V. Domanskaya, M. A. Suhm, Microscopic roots of alcohol–ketone demixing: infrared spectroscopy of methanol–acetone clusters, *J. Phys. Chem. A*, **2015**, *119*, 2225–2232.
- [258] N. Henze, *Stochastik für Einsteiger*, Springer Fachmedien Wiesbaden, **2013**.
- [259] R. McGill, J. W. Tukey, W. A. Larsen, Variations of Box Plots, *The American Statistician*, **1978**, *32*, 12.
- [260] D. C. Hoaglin, John W. Tukey and Data Analysis, *Statistical Science*, **2003**, *18*, 311–318.